Development of spatiotemporal 1D-CARS for the investigation of hydrogen flame propagation

Castellanos, Leonardo

Important note
To cite this publication, please use the final published version (if applicable).
Please check the document version above.

Development of spatiotemporal 1D-CARS for the investigation of hydrogen flame propagation

Leonardo Castellanos Gonzalez

Development of spatiotemporal 1D-CARS for the investigation of hydrogen flame propagation

Development of spatiotemporal 1D-CARS for the investigation of hydrogen flame propagation

Dissertation

For the purpose of obtaining the degree of doctor
at Delft University of Technology,
by the authority of the Rector Magnificus prof. dr. ir. T.H.J.J. van der Hagen
chair of the Board for Doctorates,
to be defended publicly on
Friday 11 of October 2024 at 10:00 o'clock

By

Leonardo CASTELLANOS GONZALEZ

Master of Science in Mechanical Engineering
Universidade Federal do Rio de Janeiro, Brazil
Born in Bogotá, Colombia

This dissertation has been approved by the promotors.

Composition of the doctoral committee:

Rector Magnificus,	chairperson
Prof. dr. ir. P. Colonna,	Delft University of Technology, *promotor*
Dr. ir. G. A. Bohlin,	Delft University of Technology, *copromotor*

Independent members:

Prof. dr. S. Hochgreb,	University of Cambridge, England
Prof. dr. ir. S. A. Klein,	Delft University of Technology
Dr. N.J. Dam,	Eindhoven University of Technology
Dr. J. Melguizo Gavilanes,	Shell plc
Dr. B. Peterson,	The University of Edinburgh, Scotland
Prof. dr. D.J.E.M. Roekaerts,	Delft University of Technology, *reserve member*

Abstract

This doctoral thesis presents the development and application of spatiotemporal coherent anti-Stokes Raman scattering (CARS) imaging for quantitative measurements of local structures in laminar and turbulent hydrogen flames. The study of spatial-thermochemical scalars in these flames is of paramount importance in advancing the next generation of sustainable combustion systems. The complexities of these environments require high-fidelity scalar measurements, demanding optical diagnostic tools with exceptional spatial and temporal resolution. Ideally, such instruments must be capable of delivering *in-situ* non-intrusive measurements of temperature, as well as species mole fraction in dynamical environments occurring across narrow spatial gradients of typically ~100's μm. Recent developments in ultrafast —femtosecond (fs) and picosecond (ps)— laser technology have enabled the advancement of time-resolved CARS spectroscopy achieving independently, heightened repetition rates (from Hz to kHz), multidimensional imaging (1D and 2D), and multiplex spectroscopic measurements targeting major combustion species. Despite these advancements, there remains a gap in the availability of CARS instruments capable of seamlessly combining all these functionalities.

The primary goal of this research is to combine these advancements in a unique design, that allows for spatiotemporal 1D-CARS measurements of temperature and concentration of N_2, H_2, O_2, and H_2O across the flame front of hydrogen flames. Using a single ultrafast regenerative amplifier laser system (Astrella, coherent) combined with a Second harmonic bandwidth compressor (Light conversion), two-beam fs/ps pure-rotational CARS imaging is achieved across a one-dimensional field-of-view of ~1.5 mm at 1 kHz repetition rate in flames. To detect these signals, a novel polarization-sensitive coherent imaging spectrometer equipped with a high-speed sCMOS camera was designed, achieving an excellent spectral and imaging resolution (<20 μm). The performance of the instrument is demonstrated for cinematographic 1D-CARS gas-phase thermometry (300-2200K) across an unstable premixed methane/air flame-front, achieving a single-shot precision <1% and an accuracy of <3%.

A comprehensive characterization of the spectrochronographic characteristics of the pump/Stokes and the probe pulses is also reported. On the one hand, the spectral response of the CARS instrument is evaluated characterizing the bandwidth of the pump/Stokes pulse as a function of linear chirp introduced by an external grating pulse compressor. On the other hand, the spectral phase of the ps-duration probe pulse generated with the SHBC is experimentally measured employing a new methodology in which the inherently short duration of the non-resonant signal is used to map the relative phase of different spectral components of the probe pulse. This facilitates the modeling of the fs/ps CARS signals in which ps-probe pulses with strong non-linear chirp are employed obviating the need for additional spectral filters.

Furthermore, the thesis introduces a groundbreaking strategy for deducing water vapor concentration from the pure-rotational N_2 CARS signal in the time domain, overcoming the challenge posed by weak H_2O pure-rotational Raman spectra. This is achieved by exploiting the sensitivity of the N_2 rotational Raman coherence to energy transfer during inelastic collisions between N_2-N_2 and N_2-H_2O. The developed technique allows simultaneous measurements of temperature, as well as O_2, H_2, and water vapor concentrations in a laminar H_2/air diffusion flame. These experimental findings are complemented by numerical investigations, underscoring the potential to extend the technique to measure water vapor in more complex ternary collisional systems found in hydrocarbon flames. The further application of these developments in the canonical H3 flame reveals the capability to directly measure molecular transport processes affecting flame structure using spatiotemporal 1D-CARS. A dual-probe CARS approach combined with a polarization-sensitive coherent imaging spectrometer enables simultaneous acquisition of molecular N_2 coherence at short and long probe delays, providing one-dimensional thermometry and concentration measurements for H_2, O_2, and H_2O in a single laser shot.

Samenvatting

Dit proefschrift presenteert de ontwikkeling en toepassing van spatiotemporele coherent anti-Stokes Raman scattering (CARS) beeldvorming voor kwantitatieve metingen van lokale structuren in laminaire en turbulente waterstofflammen. Het bestuderen van ruimtelijk-thermochemische scalairs in deze vlammen is van groot belang voor de vooruitgang van de volgende generatie duurzame verbrandingssystemen. De complexiteit van deze omgevingen vereist nauwkeurige scalar metingen, waarvoor optische diagnostische hulpmiddelen met uitzonderlijke ruimtelijke en temporele resolutie nodig zijn. Ideaal gezien moeten dergelijke instrumenten in staat zijn tot in-situ niet-intrusieve metingen van temperatuur en soorten molfractie in dynamische omgevingen die zich voordoen over smalle ruimtelijke gradiënten van doorgaans ~100 µm. Recente ontwikkelingen in ulrasnelle lasertechnologie hebben de vooruitgang van tijdsopgeloste CARS-spectroscopie mogelijk gemaakt met onafhankelijk verhoogde herhalingsfrequenties (van Hz tot kHz), multidimensionale beeldvorming (1D en 2D) en multiplex spectroscopische metingen die gericht zijn op de belangrijkste verbrandingssoorten. Ondanks deze vooruitgangen blijft er een kloof bestaan in de beschikbaarheid van CARS-instrumenten die al deze functionaliteiten naadloos kunnen combineren.

Het primaire doel van dit onderzoek is om deze vooruitgangen te combineren in een uniek ontwerp dat spatiotemporele 1D-CARS-metingen van temperatuur en concentratie van N_2, H_2, O_2 en H_2O mogelijk maakt over de vlamfronten van waterstofflammen. Met behulp van een enkel ultrasnel regeneratief versterkerlasersysteem (Astrella, coherent) gecombineerd met een second harmonic bandwidth compressor (Light conversion) wordt tweestraals fs/ps puur-rotationele CARS-beeldvorming bereikt over een eendimensionaal gezichtsveld van ~1,5 mm bij een herhalingsfrequentie van 1 kHz in vlammen. Om deze signalen te detecteren werd een nieuwe polarisatiegevoelige coherente beeldspectrometer uitgerust met een hogesnelheid sCMOS-camera ontworpen, waarmee een uitstekende spectrale en beeldresolutie (<20 µm) werd bereikt. De prestaties van het instrument worden gedemonstreerd voor cinematografische 1D-CARS-gasfasethermometrie (300-2200K) over een onstabiel premix-methaan/luchtvlamfront, met een enkelopnamennauwkeurigheid van <1% en een nauwkeurigheid van <3%.

Er wordt ook een uitgebreide karakterisering van de spectrochronografische kenmerken van de pomp/Stokes en de probe pulsen gerapporteerd. Enerzijds wordt de spectrale respons van het CARS-instrument geëvalueerd door de bandbreedte van de pomp/Stokes puls te karakteriseren als functie van lineaire chirp geïntroduceerd door een externe grating-pulscompressor. Anderzijds wordt de spectrale fase van de ps-duur probe-puls die met de SHBC is gegenereerd, experimenteel gemeten met behulp van een nieuwe methode waarbij de inherent korte duur van het niet-resonante signaal wordt gebruikt om de relatieve fase van verschillende spectrale componenten van de probe-puls in kaart te brengen. Dit vergemakkelijkt de modellering van de fs/ps CARS-signalen waarin ps-probe-pulsen met sterke niet-lineaire chirp worden gebruikt, waardoor extra spectrale filters overbodig worden.

Verder introduceert het proefschrift een baanbrekende strategie voor het afleiden van de waterdampconcentratie uit het puur-rotationele N_2 CARS-signaal in het tijdsdomein, waarmee de uitdaging van zwakke $H2O$ puur-rotationele Ramanspectra wordt overwonnen. Dit wordt bereikt door de gevoeligheid van de N_2 rotatie-Ramancoherentie voor energieoverdracht tijdens inelastische botsingen tussen N_2-N_2 en N_2-H_2O te benutten. De ontwikkelde techniek maakt gelijktijdige metingen van temperatuur en de concentraties van O_2, H_2 en waterdamp mogelijk in een laminaire H_2/lucht-diffusievlam. Deze experimentele bevindingen worden aangevuld met numerieke onderzoeken, die het potentieel benadrukken om de techniek uit te breiden voor het meten van waterdamp in complexere tertiaire botsingssystemen die in koolwaterstofvlammen voorkomen. De verdere toepassing van deze ontwikkelingen in de canonieke H3-vlam onthult het vermogen om moleculaire transportprocessen te meten die de vlamstructuur beïnvloeden met behulp van spatiotemporele 1D-CARS. Een dual-probe CARS-aanpak, gecombineerd met een polarisatiegevoelige coherente beeldspectrometer, maakt gelijktijdige acquisitie van moleculaire N2-coherentie mogelijk bij korte en lange probe-vertragingen, waardoor eendimensionale thermometrie- en concentratiemetingen voor H_2, O_2 en H_2O in een enkele laseropname kunnen worden uitgevoerd.

List of publications

Relevant Journal publications

I.   L. Castellanos, F. Mazza, D. Kliukin, A. Bohlin, "Pure-rotational 1D-CARS spatiotemporal thermometry obtained with a single regenerative amplifier system", Opt. Lett. 45, 4662-4665 (2020). [Editor's Pick].

II.   L. Castellanos, F. Mazza, A. Bohlin, "Water vapor in hydrogen flames measured by time-resolved collisional dephasing of the pure-rotational N_2 CARS signal", Proc. Combust. Inst. 39 (2022) [Distinguished paper in Diagnostics]

III.   L. Castellanos, F. Mazza, A. Bohlin, "Spectral phase characterization of SHBC produced picosecond probe pulses used in fs/ps CARS thermometry". [Article in preparation]

IV.   L. Castellanos, F. Mazza, A. Bohlin, "Study of H_2 molecular transport in turbulent flames using spatiotemporal CARS". [Article in preparation]

V.   F. Mazza, L. Castellanos, D. Kliukin, A. Bohlin, "Coherent Raman imaging thermometry with *in-situ* referencing of the impulsive excitation efficiency", Proc. Combust. Inst. 38, 1895-1904 (2020).

VI.   F. Mazza, A. Stutvoet, L. Castellanos, D. Kliukin, A. Bohlin, "Coherent Raman spectroscopy on hydrogen with *in-situ* generation, *in-situ* use, and *in-situ* referencing of the ultrabroadband excitation." Optics Express 30.20, 35232-35245 (2022).

Additional Journal publications

VII.   F. Mazza, N. Griffioen, L. Castellanos, D. Kliukin, A. Bohlin, "High-temperature rotational-vibrational O_2-CO_2 coherent Raman spectroscopy with ultrabroadband femtosecond laser excitation generated *in-situ*", Comb. Flame 237, 111738 (2022).

VIII.   D. Kliukin, F. Mazza, L. Castellanos, A. Bohlin, "Cascaded coherent anti-Stokes Raman scattering for high-sensitivity number density

determination in the gas-phase", J. Raman Spectroscopy; 1-9 (2021). [Special Issue].

IX. F. Mazza, H. Buurmeijer, L. Castellanos, A. Bohlin, "Coherent N_2+ emission mediated by coherent Raman scattering for gas-phase thermometry." Optics Letters 47.23, 6105-6108 (2022).

X. F. Mazza, O. Thornquist, L. Castellanos, A. Bohlin, "The ro-vibrational $v2$ mode spectrum of methane investigated by ultrabroadband coherent Raman spectroscopy." The Journal of Chemical Physics 158.9, 094201 (2023).

Book Chapters

I. F. Mazza, L. Castellanos, D. Kliukin, A. Bohlin, "Coherent Anti-Stokes Raman Spectroscopy (CARS)", D.K. Kumar Mishra, A. Materny. (eds) Raman Spectroscopy. Springer Series in Optical Sciences, vol 248. Springer, Singapore (2024).

Conference contributions

I. L. Castellanos, F. Mazza, A. Bohlin, "Direct measurements of preferential diffusion in turbulent H2 flames using multi-field CARS imaging", Talk at the COMBURA 2022 Symposium, Soesterberg, The Netherlands, 23-24 November 2022.

II. L. Castellanos, A. Vijayaraghavan, F. Mazza, A. Bohlin, "Autocorrelation measurements of the spectral phase of SHBC produced ps-probe pulses for precise CARS imaging thermometry", Poster at the 20th European Conference on Non-linear Optical Spectroscopy (ECONOS)/40th European CARS workshop, Kiruna, Sweden, 25-28 September 2022.

III. L. Castellanos, F. Mazza, A. Bohlin, "N_2 CARS coherence decay-based detection of water vapor in flames dominated by N_2-H_2O (binary) or N_2-H_2O & N_2-CO_2 (tertiary) collisions", Poster at the 39th International Symposium on Combustion, Vancouver, Canada, 24-29 July 2022.

IV. L. Castellanos, F. Mazza, A. Bohlin, "Water vapor in hydrogen flames measured by time-resolved collisional dephasing of the pure-rotational N2 CARS signal", Talk at the 39th International Symposium on Combustion, Vancouver, Canada, 24-29 July 2022.

V. L. Castellanos, F. Mazza, D. Kliukin, A. Bohlin, "Water vapor concentration in hydrogen flames measured by the collisional dephasing of the pure-rotational N2 CARS signal", Talk at the COMBURA 2021 Symposium, Soesterberg, The Netherlands, 10-11 November 2021.

VI. L. Castellanos, F. Mazza, D. Kliukin, A. Bohlin, "Time-domain pure-rotational N_2 CARS signal dephasing as a method for determining water vapor concentration in hydrogen flames", Poster at the 19th European Conference on Non-linear Optical Spectroscopy (ECONOS)/39th European CARS workshop, Karlsruhe, Germany, 26-29 September 2021. [Best poster award]

VII. L. Castellanos, F. Mazza, A. Bohlin, "Time-domain pure-rotational N_2 CARS signal dephasing as a method for determining water vapor concentration in hydrogen flames", Poster at Gordon Research Conference (GRC) Connect Event, 13 – 14 July 2021.

VIII. L. Castellanos, D. Kliukin, A. Bohlin, "On the robustness of space-time CARS imaging thermometry at the study of quasi-laminar premixed flame fronts", Poster at the 38th International Symposium on Combustion, Adelaide, Australia, 24 – 29 January 2021.

IX. L. Castellanos, F. Mazza, D. Kliukin, A. Bohlin, "Development of spatiotemporal CARS for flame diagnostics", Talk at COMBURA 2019 symposium, Soesterberg, Netherlands, October 9-10, 2019.

Supervised Students

Student: A. Krishna
Degree: M.Sc. degree in Aerospace Engineering
Title: Characterizing low frequency laminar flame-front oscillations – an investigation into their origin and their mitigation.

Student: A. Vijayaraghavan
Degree: M.Sc. degree in Aerospace Engineering
Title: Enhanced single-shot flame thermometry with femtosecond/picosecond CARS using a phase-characterized picosecond probe.

Student: T. M. Klijn Velderman
Degree: M.Sc. degree in Aerospace Engineering

Title: Development of pure rotational coherent Raman spectroscopy on hydrogen for applied flame thermometry.

Student: A. Montoya Santamaria

Degree: B.Sc. degree in Aerospace Engineering

Title: Designing and testing a Computed Tomography of Chemiluminescence (CTC) setup for the Swan band of hydrocarbon flames.

Student: A. Sepulcri, E. Radcliff, F. Wilmink, O. Dvořák, S. van den Heuvel, V. Petit

Degree: B.Sc. degree in Aerospace Engineering

Title: Skymaster flying renewable propulsion testbed.

Contents

Chapter 1

Introduction

1.1 Motivation

In recent years, the use of hydrogen (H_2) as an energy carrier has gained much research attention for propulsion and power technologies. Apart from the clear benefits of this fuel to eliminate CO_2 emissions, one of the main advantages of H_2 is its large energy content by weight. The energy density of this molecule is almost three times higher than any other common hydrocarbon fuel (i.e. natural gas, and kerosene). This makes it appealing for applications in which high and fast energy release is required. For instance, hydrogen is a standard propellant for reusable space shuttle vehicles operated by ESA and NASA [1–3]. It is also considered to be used in a wide variety of applications such as fossil-free production of steel [4,5], as a replenisher in the metal combustion cycle [6–8], ammonia synthesis [9], as well as for power generation in terrestrial gas turbines [10–13]. Its potential is perhaps most groundbreaking in the aviation industry, where it's poised to revolutionize aircraft propulsion [14–17]. It is foreseen that within the coming decade, the first aircraft powered by H_2 could potentially be introduced into the aviation market. Commercial aircraft manufacturers such as Airbus have publicly disclosed their intentions to launch the prototypes of long-haul hydrogen-powered aircraft as early as 2035 [18]. According to the International Civil Aviation Organization (ICAO), a profound shift towards this technology is envisioned [19]. It is expected that by 2050, H_2 should be able to cover up to a third of worldwide aviation's energy demand. However, to achieve these goals, radical modifications to the existing aircraft designs are required, particularly in the fuselage which needs to carry containers with liquid hydrogen, but also in the combustion chamber where the chemically stored energy in H_2 needs to be efficiently converted to kinetic energy generating thrust.

Several challenges need to be overcome to use H_2 as fuel in combustion environments. One of them is to mitigate the nitric oxide (NO_x) emissions generated in air-breathing engines. At temperatures above 1800 K, thermal NO_x is usually

produced via an exothermic mechanism and the rate of formation increases with increasing temperature as well as oxygen and nitrogen concentrations [20]. Hydrogen flames have a higher adiabatic flame temperature in comparison to most hydrocarbon flames, consequently, there is a corresponding increase in these emissions. The impact of NO_x emissions on ozone depletion is critical, especially in supersonic aircraft flying above 18,000 m altitude. In such high-altitude, NO_x is generated not only through combustion processes but also via the dissociation of molecular nitrogen (N_2) and oxygen (O_2) due to the substantial velocities encountered at the nose cone of the aircraft [21]. Another challenge is to burn H_2 safely and in a wide range of operability conditions. Hydrogen has a high diffusivity and reactivity, which makes it burn faster than any other fuel [22]. As a consequence, flame instabilities driven by the rapid mixing and fast chemical kinetics reactions (i.e. auto ignition, flashback, deflagration-to-detonation transition) may arise in the combustion chamber [23]. To overcome these issues, fundamental research aiming to describe the propagation of H_2 flames is required.

The experimental assessment of the different scalars involved in the combustion process plays a key role in the investigation of H_2 flame propagation. In particular, the temperature is the main scalar that needs to be accurately quantified. The structure of a flame can be defined as a function of the temperature profile across the different layers of gas between reactants and products. The temperature also influences the rate of consumption and formation of different combustion species (i.e. hydrogen, oxygen, and water vapor) [24]. When the temperature and local concentration of these species are measured, it is possible to investigate directly different molecular transport processes influencing flame propagation. For example, the preferential transport of H_2 from the reactants into the product gases is induced by differences between molecular diffusion coefficients for the fuel, the oxidizer, and the product gases. This phenomenon is also referred to as preferential diffusion. Accurate measurements of these parameters would bring valuable information that can be used for the development and improvement of combustion models. In particular, those in which it is normally assumed that atomic mass fractions are conserved from reactants to fully burnt products [25].

In my doctoral research, I have focused on the development of a laser diagnostic technique that is capable of providing high-fidelity information about the most relevant scalars in H_2 flames. In particular, I defined temperature and local O_2, H_2, and H_2O concentration as the main variables that need to be measured to characterize the structure of an H_2 flame. Laser-based diagnostics techniques are

the most employed tools for measuring flame temperature and concentration of species in chemically reacting flows. The importance of these techniques comes with the capability of performing *in-situ* measurements, in a non-intrusive fashion, which avoids disturbances to the reacting flow [26]. This feature is predominantly important in measurement environments where steep gradients of temperature exist (i.e., in a thermal boundary layer and laminar/turbulent flame-fronts) and in those conditions where physical probes would either fail completely or yield a large systematic deviation from the true condition.

1.2 Challenges of hydrogen combustion diagnostics

To accurately characterize the structure of an H_2 flame-front at a molecular level, I built a tailor-made fs/ps CARS instrument which involved many technical challenges. To describe some of these challenges, let us first consider a stationary laminar premixed flame from a Bunsen burner, as shown in Figure 1.1.
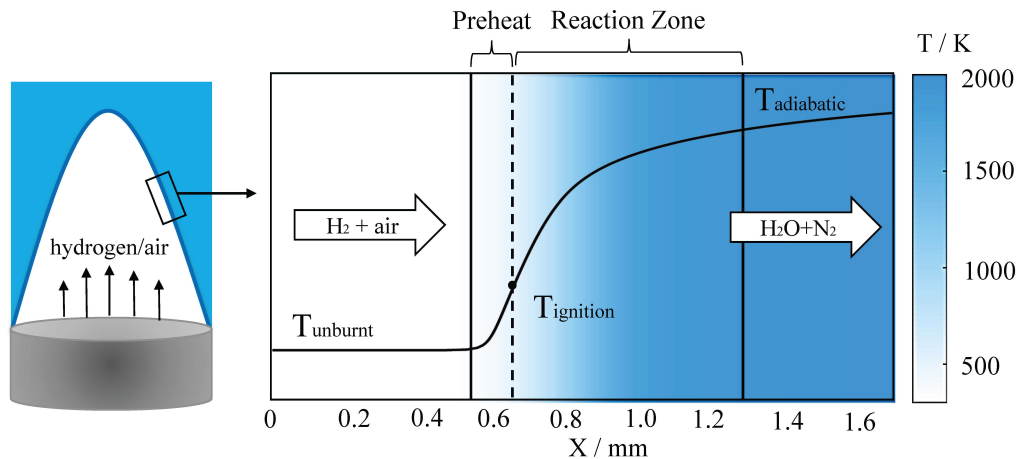
Figure 1.1: The flame-front structure of a typical premixed H_2/air flame, defined by the temperature profile across the reactant and the burnt product gases. Two main areas are identified across the one-dimensional domain, termed the preheat and the reaction layer. In these areas, temperature is raised from 300 K to 2400 K (blue) and the fuel (H_2) reacts with the oxygen present in air to produce mainly water vapour.

This figure displays a very rapid increase in temperature (from 300 K to 2200 K) across a relatively small spatial extent (~0.5 mm) that is needed for a flame to continue to propagate. One of the most well-accepted theories that describe this propagation of laminar premixed flames was developed by the French scientists Mallard and Le Chatelier [27]. They stated that the propagation of heat through different layers of the gaseous flow is the main mechanism that effects flame

propagation. In their description, the flame structure is composed of two main layers of gas, which are delimited by a point where the next layer ignites. The first one is termed the preheat zone, which occurs between the cold boundary (T_u) and the location of the ignition temperature (T_i). In this region, the temperature of the unburnt gas is raised mainly by heat conduction and partly also by convection from the reaction zone. Therefore, no significant chemical reaction occurs in this area. After the gas mixture is ignited, a second region appears, which is denoted as the reaction zone in Figure 1.1. In this spatial region, the temperature keeps rising until it reaches chemical equilibrium, where (in a perfectly thermodynamic isolated system) the adiabatic flame temperature (T_a) is obtained. In this theory, the ignition temperature is a critical parameter as it defines the boundary between the two regions of the flame. In addition to this theory, a more complete description proposed by Bernard Lewis and Guenther von Elbe [28] suggests that molecular diffusion of certain combustion-relevant species (i.e., radicals) also impacts the flame structure. In this description, it is the produced radicals in the flame that diffuse back into the flow with unreacted gases and can drive chain-branching chemical reactions that induce the ignition.

From an experimental point of view, the accurate description of the flame structure relies on the possibility of using non-intrusive laser probing techniques which can obtain *in-situ* data on temperature and species composition across step gradients in space. This endeavour is fraught with challenges, primarily stemming from two crucial factors. Firstly, the scarcity of laser diagnostic techniques versatile enough to serve as comprehensive instruments for multi-scalar measurements in reactive flows poses a substantial hurdle. Classical ways in which light can potentially interact with molecules, such as absorption and fluorescence prove inefficient when dealing with homonuclear diatomic molecules such as N_2, H_2, and O_2 [29], which are critical for characterizing the flame front in hydrogen flames. Consequently, the assessment of thermometry and species concentration relies mostly on the use of more sophisticated techniques based on light scattering, such as spontaneous Raman and coherent Raman scattering (CARS). The second challenge lies in the demand for excellent spatial and temporal resolution, directly influencing the precision and accuracy of the measurements. In the following sections, these challenges are going to be discussed, focusing on temperature for simplicity while acknowledging that similar challenges extend to the measurement of species concentration profiles.

1.2.1 Spatial resolution

The structure of laminar premixed flames fed with H_2 has a very steep temperature gradient and therefore the use of an instrument with a superior spatial resolution is paramount. A coarse spatial resolution would introduce a systematic bias to the measured data caused by spatial averaging [30]. To illustrate this problem, one can consider the freely propagating laminar premixed H_2/air flame displayed in Fig. 1.1. The thickness (δ_L) of a laminar premixed flame is usually derived from the temperature difference between the reactant (T_u) and the product (T_a) gases, according to:

$$\delta_L = \frac{T_a - T_u}{\max\left(\left|\frac{\partial T}{\partial x}\right|\right)} \tag{1.1}$$

In this flame, the local temperature increases very rapidly from 300 K up to 2400 K, in a narrow spatial region $\delta_L \sim 500$ µm. This would require at least ~10 independent spatial segments of ~50 µm to deduce reliable data across this region. In H_2 flames, the width of the preheat zone is even narrower than that in hydrocarbon flames. This means that the effect of spatial averaging becomes even more dramatic. Laser probing is the well-established measurement approach used for this application since the coherence of the electromagnetic radiation enables investigations down to microscopic scales (~50-200 µm for gas-phase thermometry).

In Figure 1.2, a comparison of the retrieval of the flame-front contour obtained for different degrees of spatial blur is presented to illustrate the effect of spatial averaging on temperature measurements. Two temperature profiles corresponding to laminar premixed CH_4/air and H_2/air flames were simulated over a 700 µm-distance using the flame simulation code CHEM1D [31]. These generated temperature profiles were then convoluted with three Gaussian functions with corresponding widths of 20, 100, and 200 µm at full-width-half-maximum (fwhm), respectively, to simulate spatial averaging effects. Spatial averaging effects are common due to the focusing properties of the optics equipment employed or imperfections in general which are merged into the instrumental function slit width. As can be seen in Figure 1.2, the spatial blur clearly impacts the temperature estimation particularly in the preheat zone, when the temperature gradient is at maximum. On the other hand, no significant differences are found where the

temperature profile is more constant, i.e., both on the reactants side and on the product side of the flame front. Moreover, it is remarkable that while the temperature error is below 5% in the case of the laminar premixed CH_4/air flame for all three spatial filters, the temperature of the laminar premixed H_2/air flame is overestimated by 20% in the case of the spatial blur simulated with the 200 µm fwhm Gaussian function. Based on this, it is possible to infer that while the usually employed spatial resolution of ~100's of microns would retrieve accurate temperature information in laminar premixed CH_4/air flames, to resolve the flame structure of premixed flames fed with pure hydrogen, at least 20 µm is needed to avoid spatial averaging effects.
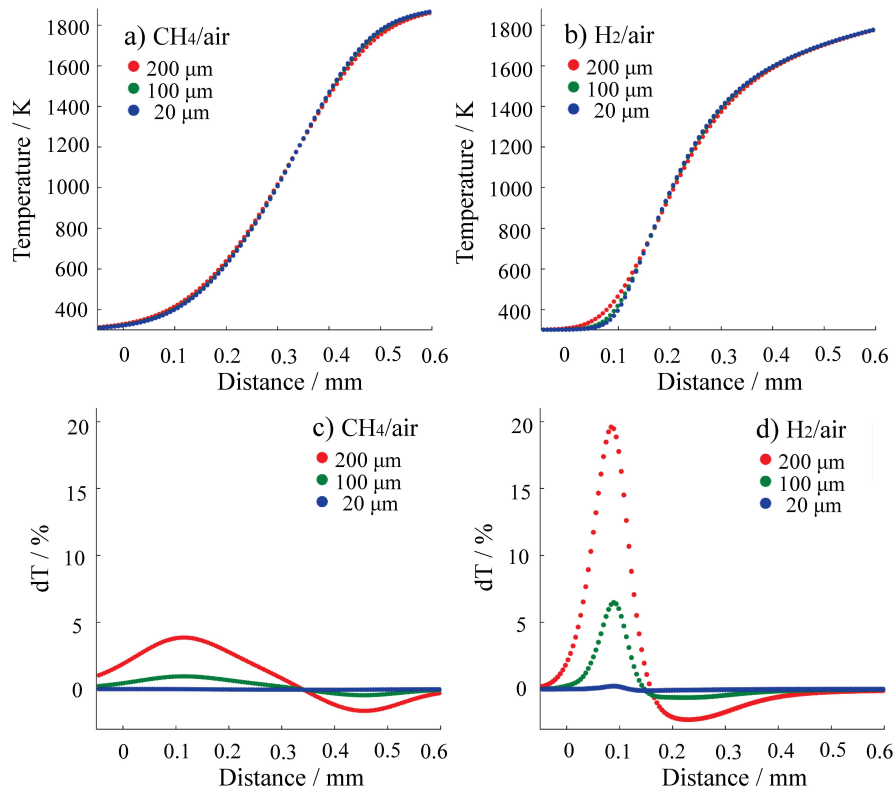
Figure 1.2: Temperature error assessment based on various degrees of image blur for a methane/air flame (left) and a hydrogen/air laminar flame (right). (a,b) The temperature profile of the flame-font obtained with three different spatial resolution of 20, 100, and 200 µm FWHM size, respectively. (c,d) The relative systematic error (%) comparing the real temperature profile with the convoluted ones.

In turbulent flames, the spatial resolution also becomes a potentially limiting factor when the finest turbulence scales are of interest [32]. When a flow becomes turbulent, fluctuations of velocity, temperature, and species concentration affect the

chemical reactions and the flame propagation. The degree to which these scalars influence the flame structure depends upon the characteristics time and length scales associated with each fluctuating component. In turbulent flows, large eddies transport turbulent kinetic energy into the system, cascading it down to smaller eddies where this energy is dissipated. The size of these eddies is defined, respectively, by the integral and the Kolmogorov length scales. While the integral scale is usually on the order of 1-10 mm, the Kolmogorov scale shrinks dramatically to a mere 20-60 µm [33]. In order to effectively measure scalar quantities down to the Kolmogorov scales, the use of laser diagnostic techniques with exceptionally high spatial resolution becomes imperative.

Point-wise (0-D) laser probing has been traditionally employed for the measurement of temperature and species concentration across H_2 flames. However, the ability to acquire single-shot images of the scalars across the flame front is considerably more beneficial. The primary argument for using one-dimensional temperature imaging is that the flame structure is instantaneously acquired (as opposed to a point-wise scanning arrangement), which makes it possible to retrieve the entire flame structure in a single laser shot. Secondly, the direct imaging of species such as hydrogen would allow the follow-up on the evolution of fresh gases and their conversion into burnt products, defining elemental transport processes affecting flame propagation. Finally, with the instantaneous imaging of the flame-front, it is possible to reduce uncertainties that arise specifically from point-wise (0-D) measurements; when 0-D measurements are employed, the flame thickness is discretized in a number of points, enough to resolve the scalar profile. Once the measurement at one of these points is performed, the flame is translated until all the defined points are measured. In this case, the data acquisition may proceed for several hours as a considerably high number of points are necessary to resolve the steep gradients. The point-wise raster scanning process may induce bias in the measured data, firstly because it is likely that boundary conditions of the experiment will drift during the data acquisition, and secondly because when dynamic scenes are probed, it is not possible to completely resolve the flame structure.

1.2.2 Temporal resolution

In addition, to the imaging capability, the experimental technique employed to measure temperature and species concentration should be able to resolve temporal fluctuations of the flame. Laminar flames are usually considered stationary and naturally stable, however, in practice, flames are affected by instabilities that emerge due to difficulties in controlling the boundary conditions of the experiment.

These perturbations may cause harmonic oscillations of the flame-front, which must be considered in the uncertainty analysis [34,35].
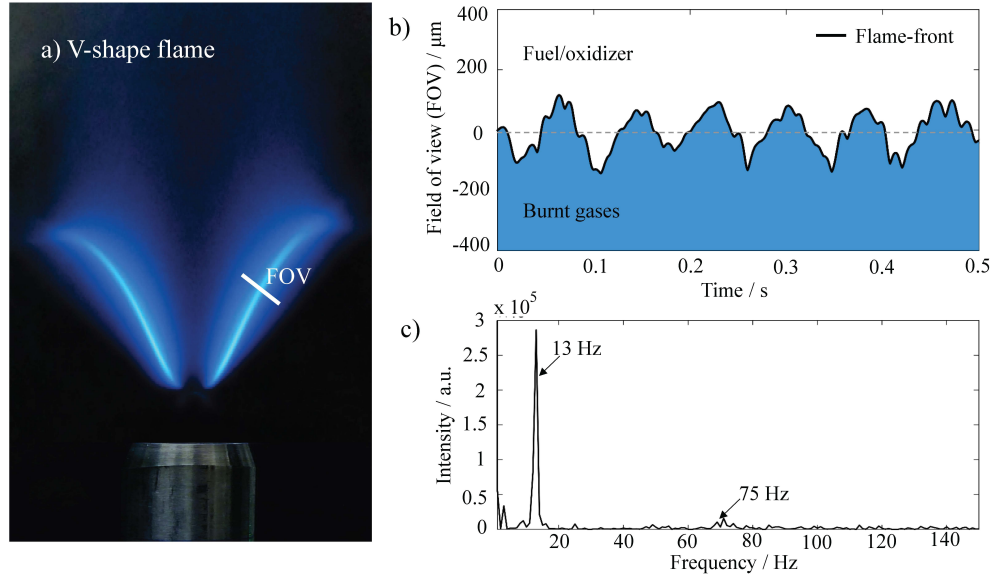
Figure 1.3: Instabilities of a quasi-stationary laminar premixed methane/air flame-front. (a) A snapshot of the flame with indicated location of the analysed region. (b) A spatial shift of the flame-front position as function of time and (c) frequency analysis of the flame flickering within the field of view. The colours of the binary image represent the burnt gases (blue colour) and reactant mixture (white colour).

An assessment of these flame dynamics has been preliminarily performed to show the magnitude of these perturbations. A high-speed sCMOS (scientific-grade complementary metal-oxide-semiconductor) camera was used to capture the chemiluminescence produced by the radicals of a premixed CH_4/air laminar flame. For a specific regime and fuel/oxidizer mixture condition, 1000 images were recorded at a rate of 1000 frames per second. Further, the flame dynamics were analyzed using an image processing algorithm. It consisted of a set of filters in which the position of the flame-front was defined as the pixels with a maximum gradient of brightness. A Fourier transform routine was employed to estimate the frequency of the oscillating position of the flame-front. In Fig. 1.3, it is exhibited the shift in the position of the flame-front as a function of time. A flickering motion is distinguishable as the flame-front oscillates periodically within the acquisition time. Two distinct frequencies of 13 and 75 Hz are discerned. The lowest frequency has the highest amplitude which becomes critical for temperature and species measurements. For instance, for a fixed measurement point, during one period of 13 Hz, the flame position varies up to ~300 µm. If not captured well, this would

yield a significant systematic error in the temperature estimation since this distance represents half of the flame-front thickness.

The origin of the flame flickering motion is debatable and needs to be properly investigated; however, a common explanation can be given based on a frequency band analysis of the flame oscillation. Frequencies ranging from 10 to 20 Hz, are usually attributed to a buoyancy effect that occurs at the interface between hot combustion products and the air at ambient temperature. In this case, accelerated Kelvin-Helmholtz vortices caused by the difference in velocity and density between both fluids can produce flame wavering [36,37]. However, it is also possible that within this frequency band, flame oscillations coexist as a consequence of periodic changes in the equivalence ratio. The cone-angle of a premixed flame provided on a Bunsen burner is highly sensitive to changes in the mixture ratio and the bulk flow. A pulsation of the flow controllers can therefore easily alter the flame position. In the case of frequencies obtained in the band of 50-100 Hz, internal acoustic modes inherent to the design of the burner are identified as the possible source of the flame fluctuation [38,39].

The Nyquist sampling theorem is typically used to determine the minimum sampling rate that is required, to completely resolve these periodic fluctuations [40]. Based on the results obtained from the chemiluminescence study on the current quasi-stationary laminar flame, this sampling frequency must be higher than 200 Hz which is about twice the maximum frequency component observed in the frequency analysis. When spatially correlated data are acquired at this sampling frequency, it can be claimed as space-time resolved information for this flame application. This is the ultimate goal for flame structure measurements. With the simultaneous space-time resolution, it is possible to track the position of the quasi-stationary flame at any moment. If these changes are only mechanical, the precision of the measurement will not be altered by perturbations via the laboratory frame (e.g. vibrations on the platform). Conditional statistics on the entire collected sample can be employed, for instance, deduced at a specific point relative to the inflection point of the flame contour which is representative of every single sample. This is further demonstrated in section 3.3, with correlated space-time resolution for CARS.

1.2.3 Temperature single-shot precision and accuracy

The reliability of the data obtained from optical diagnostics is also a major concern in flame measurements and must be analyzed in the context of experimental

uncertainty. This is usually inferred by quantifying the accuracy and precision of the scalar determination. In reality, measurements are tainted by errors. These errors might be created by the experiment's uncontrolled boundary conditions and lack of robustness of instruments, usually contributing to stochastic errors. However, errors can also be caused by low instrument resolution or by simplifications and assumptions of the models employed to deduce quantities from indirect measurement techniques; in this case, we usually refer to systematic errors.

The uncertainty in the temperature estimation has a dramatic impact on the study of H_2 combustion. In particular, to determine the rate of formation of radicals and pollutants governed by specific chemical reaction mechanisms. One clear example is the direct link between temperature and NO_x emissions. Thermal NO_x is formed by reactions that occur between atmospheric oxygen and nitrogen atoms. The temperature dependence of this reaction is explained by the Arrhenius expression that describes the rate of formation κ assuming equilibrium values as

$$\kappa_{true} \propto \exp\left(-\frac{T_a}{T}\right) \tag{1.2}$$

Where $T_a = E_a/R$ is the activation temperature of the reaction; R=8,314462 J/mol K is the molar gas constant and $E_a = 317$ kJ/mol is the activation energy of the $O + N_2 \leftrightarrow N + NO$ chemical reaction [41]. To include the influence of temperature uncertainty in the rate of formation of NO_x, the flame temperature T in Eq.(1.2), can be expanded to

$$T = T_f + \Delta T \tag{1.3}$$

Where T_f ~2400 K denotes the 'true' value of the flame temperature and ΔT is the experimental uncertainty. Since $\Delta T \ll T$, the exponential term in Eq.(1.3) can be expanded, giving the following expression [32]:

$$\kappa_{\Delta T} \propto \exp\left(-\frac{T_a}{T_f}\right) \exp\left(-\frac{T_a \Delta T}{T_f^2}\right) \tag{1.4}$$

According to Eq. (1.4), it follows that even a slight uncertainty of 4% (i.e. 96 K) in the temperature estimation results in a ~50% error in the expected yield of NO_x as compared to the rate calculated using Eq. 1.2:

$$\kappa_{true} \propto \exp\left(-\frac{38129\ K}{2400\ K}\right) \tag{1.5}$$

$$\kappa_{\Delta T} \propto \exp\left(-\frac{38129\ K}{2400\ K}\right) \exp\left(-\frac{38129\ K\ (96\ K)}{(2400\ K)^2}\right) \tag{1.6}$$

$$\kappa_{error} = \frac{|\kappa_{true} - \kappa_{\Delta T}|}{\kappa_{true}} \sim 0.5 \tag{1.7}$$

This effect is equivalent to that of other radicals of major importance on the flame propagation and therefore is of primary importance to consider when employing a particular diagnostic technique.

The measurement uncertainty in CARS thermometry is the lowest among the different optical techniques available for gas-phase studies. The CARS spectrum indicates, with a high degree of fidelity, the population of a specific energy state in a molecular ensemble. As a result, it might be considered a direct method of measuring the mole fraction and temperature of molecules in the gas-phase. This provides a high degree of reliability as compared to other techniques in which measurements are less direct. Before this research, the precision of state-of-the-art flame CARS thermometry was estimated to be in the order of ~2-3%. For accuracy, similar values of 3-5% were achieved [42,43]. However, making strong claims about the uncertainty of data obtained in flames is particularly problematic due to current limitations in the benchmarking methodologies employed to define what the "true" temperature value is in an experiment. Nonetheless, this thesis introduces attempts to lower the uncertainty of CARS thermometry below 1% percent. In chapter 3, these efforts are discussed.

1.3 Coherent anti-Stokes Raman spectroscopy for thermometry and species concentration measurements

Coherent anti-Stokes Raman scattering (CARS) spectroscopy is a laser diagnostic technique that has been employed in various research fields, both related to solid- and liquid-state physics, and as in this thesis, to investigate molecular systems in the gas-phase. The first experimental work based on this non-linear optical process was reported in 1965 in the seminal study of Maker and Terhune [44], where a pulsed ruby laser was used to generate a coherent Raman signal in a crystalline sample. Years later, the name coherent anti-Stokes Raman scattering was first

introduced by Begley and co-workers [45], who used toluene and benzene mixtures to investigate four-wave mixing. After this, much research was devoted to provide quantitative measurements of temperature and species concentration in gaseous media. The main reason was related to the advantages of CARS over the more commonly applied spontaneous Raman spectroscopy technique. The signals generated with CARS are several orders of magnitude stronger, and due to the enhanced signal throughput, it can favourably be applied in high-temperature environments as well as low-pressure applications where the number density (or the macroscopic susceptibility) is relatively low. Additionally, the coherence properties of the signal can be used to implement effective stray light rejection, which can lead to minimal background interference operating in highly luminous environments such as flames and plasmas. The CARS signal is also upconverted in frequency, which makes it such that it can be easily discriminated from the wavelength of the employed laser [46]. Altogether, this is what makes CARS exceptional in probing combustion processes over a broad range of practical operating conditions.

The first applications of CARS for quantitative measurements in combustion dates to the mid-1970s by Regnier *et al.* [47] who were the first to perform concentration measurements of H_2 in the reaction zone of a hydrocarbon flame. Furthermore, Moya *et al.* [48] proved that CARS could be used to perform thermometry in the product gases of a natural gas flame provided on a Bunsen burner. Both thermometry and species concentration measurements were inferred from the rotational-vibrational spectrum of H_2, here referred to as vibrational CARS. In the first implementations of vibrational CARS in reacting flows, the signal was generated using pulsed laser sources, which usually have a temporal duration of ~10-20 nanoseconds. Nanosecond pulses are inherently narrow in the frequency domain, and with this implementation, the full CARS spectrum was recovered either by scanning the frequency of the pump and the Stokes pulses [49–51] or by employing the broadband emission originating from pumped dye lasers [52]. The latter approach is particularly appealing since it could allow measuring the whole spectrum of the molecule based on a single laser shot. Nonetheless, the application of nanosecond-pulsed vibrational CARS systems is somehow limited by the difficulty of performing measurements of multiple combustion species simultaneously, and the congested rotational-vibrational transitions of the main Q-branch spectra give rise to a poor accuracy obtained at low temperatures below 1000 K [53] and problems with line-mixing at high pressure if vibrational CARS is applied in more realistic combustors.

Pure-rotational CARS spectroscopy was developed to overcome some of the drawbacks of vibrational CARS. The pure-rotational transitions of most of the Raman-active molecules of interest for combustion diagnostics are positioned in the same frequency interval. Therefore, the use of broadband laser sources allows for instantaneous measurements of the major species present in a gas phase mixture with a single laser pulse [53,54]. Additionally, individual rotational spectral lines from a diatomic species are well isolated which makes it easier to interpret data obtained in high-pressure environments where both pressure-broadening and line-mixing effects make the retrieval of spectral information otherwise difficult. The pure-rotational CARS spectra are also more temperature-sensitive below ~1800 K [55]. This feature is important when dynamic environments are investigated; for instance, in turbulent flows, where the temperature can fluctuate between 300 K (unreacted pockets in the flame) and 2400 K (reacted pockets in the flame) from shot-to-shot. Since the first experimental observation of a pure-rotational CARS signal [56], this approach has been vastly expanded to probe a number of diatomic molecules such as nitrogen [52], oxygen [57,58], carbon monoxide [59] and hydrogen [60]. It has been applied also to tri-atomic molecules such as carbon dioxide [61,62] nitrous oxide [63], water vapor [64], and polyatomic molecules such as acetylene [65,66], ethane [67,68] and ethylene [69,70]. This feature has been extensively exploited in the development and characterization of canonical flames.

Some of the drawbacks of time-averaged ns-CARS systems are associated with inherent uncertainties that cannot be avoided using nanosecond laser pulses. The duration of these pulses is relatively long when compared to the typical collisional dephasing time of most molecules relevant to combustion processes. For instance, under atmospheric conditions, nitrogen molecules have a dephasing time of approximately 200 ps. The effect of molecular collisions on the CARS signal can lead to inaccuracy in the evaluated temperature and the assessment of the concentration of molecules. In addition, shot-to-shot mode noise and amplitude variations in the output from pumped dye lasers can directly impact the stability of recording CARS spectra. This effect has limited the thermometric precision of ns-CARS to 4-5% [71,72]. A further disadvantage is the low repetition rate of the laser, which allows data acquisition only at ~5-10 Hz which is too slow to resolve dynamic variations of temperature and species concentration in turbulent flows.

In recent years, the development of laser systems with ultrashort femtosecond laser pulses has been presented as the best alternative to performing measurements

of combustion processes, overcoming many of the above-listed difficulties related to nanosecond-pulsed CARS systems.

In the ultrafast approach, the laser pulse width is on the order of a few femtoseconds to 10's of picoseconds which provides a direct enhancement of the pulse peak-power, and the bandwidth that is required to excite the entire manifold of pure-rotational Raman transitions. The first work in which ultrashort laser pulses were implemented to gas-phase CARS spectroscopy [72] was published in 1995 by Hayden and Chandler [72] who demonstrated the suitability of using fs laser pulses to measure the evolution of molecular coherence in benzene and 1,3,5-hexatriene. Furthermore, Lang *et al*. [73], were the first to employ fs-CARS for gas phase thermometry in heated gas-cell and later also in flames [74] using the detailed beat structures between the thermally populated states of H_2 and N_2 respectively in the time domain. In these cases, the implementation of ultrashort laser pulses in gaseous media was only possible thanks to the advent of the chirp pulse amplification (CPA) scheme that allowed to increase the energy of femtosecond pulses by six orders of magnitude, from nJ to mJ [75]. After that, the multiple benefits that ultrafast laser systems can provide have truly revolutionized CARS and can be summarized as:

High peak-power fs-laser pulses:

- With the high-peak power provided by fs-laser pulses it is possible to drive coherent Raman transitions impulsively, which leads to the generation of the strongest CARS signals. Impulsive excitation is a pre-requisite for single-shot CARS imaging (1D and 2D). With CARS imaging it is possible to achieve spatially correlated measurements of temperature and species concentration simultaneously in high-temperature combustion applications.

Broad bandwidth, near transform-limited fs-laser pulses:

- The broad bandwidth of near transform-limited fs-laser pulses can be used to excite all combustion-relevant species, e.g. N_2, O_2, CO, CO_2, and H_2, obtained with a single laser shot. In addition, with near transform-limited fs-laser pulses, the spectral phase between the different individual spectral components is eliminated, and with this coherent property, the precision of CARS thermometry and multispecies detection can be reduced significantly to below 1 %.

Short-duration fs-laser pulses, and the high repetition-rate:

- The use of laser pulses that are shorter than the collisional dephasing time of the probed molecules practically eliminates the uncertainty caused by

collisional dephasing. This feature of time-resolved spectroscopy provides advantages, especially at high pressure.

- It also provides the ability to measure the CARS signal dephasing rates due to species-specific collisions with perturber molecules.
- The high repetition-rate of commercially available fs-laser systems (1-10 kHz) allows to (a certain extent) resolve flame dynamics in unstable reaction environments.

For pure-rotational CARS, the implementation of these capabilities was possible, much thanks to the advent of hybrid fs/ps CARS [76]. In this approach, broadband fs-laser pulses (pump and Stokes) are used to drive the pure-rotational Raman transitions of the molecule, and the excited states are then sequentially scattered by a ps-probe pulse to generate the CARS signal. The CARS signal is thereafter detected in the frequency domain using a spectrometer. This requires the use of a (relatively) narrowband ps-probe pulse. A short probe pulse also permits the introduction of a time delay between the probe and the pump/Stokes (excitation) pulses, which can be used to suppress the non-resonant background since this signal is only generated with the synchronous temporal overlap of the three input laser fields [77]. Another advantage of time-resolved CARS is the nearly collision-independent measurements, which have been achieved even at pressures as high as 70 atm [78].

The past decade has seen a rapid advance of pure-rotational fs/ps CARS for applied diagnostics in high-temperature reacting flows. One of the most significant breakthroughs was the invention of a two-beam rotational CARS technique in 2013 [79]. Through this technique, Bohlin and Kliewer extended the traditional use of point-measurement CARS to perform coherent imaging simultaneously across a one-dimensional spatial coordinate (1D). In the two-beam CARS technique, both the pump and the Stokes photons originate from a single broadband fs pulse (45 fs) and are therefore automatically overlapped in space and in time. This simplifies the beam alignment and makes the technique more robust against beam steering effects. Additionally, the spatial resolution is enhanced since the interaction length between the two beams can be adjusted even down to ~50 μm. In one of the works demonstrated by Bohlin and Kliewer at Sandia National Laboratories, temperature measurements were performed along a ~6 mm line segment positioned across the flame-front of a premixed CH_4/air flame impinging against a steel wall [80]. This approach (the two-beam phase-matching scheme), was further expanded also to perform CARS measurements simultaneously over a two-dimensional field of ~40 mm^2 [81].

An important consideration for the two-beam pure-rotational fs/ps CARS setup concerns the picosecond probe pulse. To achieve planar imaging with CARS (2D-CARS), extremely high pulse energy of the picosecond probe is required (~30-60 mJ). Therefore, the probe pulse has to be supplied from a separate ps-laser system that is synchronized with the combined pump/Stokes fs-laser excitation pulse. In this case, the current demonstrations of 2D-CARS applied to flames have had a sampling rate of ~20 Hz [82], however, kHz sampling rates have also been achieved for 2D-CARS at probing of oxygen at room temperature [83]. Another possibility is to generate the probe laser pulse directly from the output of the fs-laser system utilizing different pulse-shaping techniques. This process has been implemented by selecting a small portion of the bandwidth of the fs-duration laser pulse, leading to a much narrower bandwidth and a prolonged – picosecond – duration laser pulse. As a result, the ps-probe pulse as well as the fs-excitation pulse can be created from a single laser source, with the benefits of automatic synchronization in repetition rates to achieve increased data sampling rates (1-5 kHz) [84,85]. The limitation in acquisition rate is currently set by commercially available fs-laser systems, however, 100 kHz have been achieved for two-beam CARS implemented with custom-built pulse burst mode lasers [86]. The single laser system approach has a significant impact on pulse energy available for the ps-probe pulse and therefore has been limited to perform only point-wise measurements with CARS. Examples of such techniques include narrowband Lorentzian filters [87], volume Bragg gratings [88,89], and 4-f pulse shapers [90,91]. To date, the most efficient way to produce a narrowband ps-probe pulse from the broadband fs-laser is to use a second harmonic bandwidth compressor (SHBC). This methodology was first introduced in hybrid fs/ps CARS by Kearney *et al.* [92] in 2013. Here, the probe pulse is generated via a nonlinear process termed sum-frequency generation (SFG), in which phase-conjugate linearly chirped fs-laser pulses are combined in a nonlinear crystal to be converted to a "single wavelength" achieved with an efficiency of 30-40%. This means that much of the original fs-pulse energy is recovered in the SHBC "fs-to-ps" pulse conversion process. One of the key-objectives for this thesis, which has also been achieved successfully, is to exploit this "extra" available pulse energy for the ps-probe pulse to achieve spatiotemporal 1D-imaging with CARS obtained with a single laser system.

The use of high-energy SHBC-produced probe pulses is also effective for monitoring the evolution of the CARS signal in the time-domain over a wide pressure range [78]. This capability provides an additional degree of sensitivity that can be used to assess additional scalars. All of this is possible because the dephasing of the CARS signal is highly sensitive to the thermodynamic properties of the

medium (i.e. temperature, pressure, and gas mixture composition). Kearney and Danehy [93] were the first to use the pure-rotational CARS signal's sensitivity in the time-domain for measurements of pressure. They developed a new detection scheme that allows to estimate both temperature and pressure simultaneously from the pure-rotational N_2 CARS spectrum at pressures ranging from 0.4 to 3 atm. Although, during this first attempt, with the sequential probe delay measurements it could not be acquired single-shot statistics of pressure, more recent improvements have demonstrated the feasibility of single-shot temperature/pressure assessments by employing multi-probe schemes [94,95]. However, no previous attempt had been made yet to utilize the sensitivity of the CARS signal in the time-domain for flame diagnostics. The main difficulties are the decreased sensitivity of the collisional dephasing at high temperatures and the requirement for simultaneous monitoring of all combustion species present in the probe volume. In this thesis, it is reported a new development, in which the sensitivity of the N_2 CARS signal in the time-domain is used for measuring water vapor concentration in H_2 flames.

In general, pure-rotational CARS spectroscopy has a few challenges that need to be overcome to be efficiently used in H_2 flames. The first challenge concerns the performance of thermometry directly on hydrogen and to measure the concentration of H_2 and H_2O. The large rotational constant of hydrogen (i.e. ~60 cm^{-1} for H_2 compared to ~2 cm^{-1} for N_2) results in a large dispersion of the rotational spectral lines, which is spread over the spectral region of 350-2200 cm^{-1} (at ~2300 K). The lack of excitation bandwidth of commercially available femtosecond lasers to encompass this entire spectral range has thus precluded the use of CARS spectroscopy to detect more than one, or possibly two, rotational Raman transitions of H_2 simultaneously [96]. To generate efficient excitation bandwidth, additional pulse compression techniques need to be used. For instance, by using an optics combination of a hollow-core fiber and negatively dispersed mirrors to compress the fs-pulse down to sub 10 fs [97,98]. In the case of H_2O, it is the low Raman cross-section that has hampered its detection in high-temperature reacting flows. The Raman cross-section of a molecule is roughly a measure of the coherent Raman scattering susceptibility, and it is typically much smaller for molecules with low polarizability, such as H_2O. This can make it more difficult to detect the CARS signal of such molecules, especially in the presence of other species with larger Raman cross sections, such as N_2. In the only attempt to measure the pure-rotational signal of H_2O with CARS, it was concluded that it is an unsuitable technique to be used in combustion environments [64]. The reason is that the signal intensity is more than five orders of magnitude smaller than that of N_2 CARS at room temperature. The challenge of detecting water vapor—the main product gas of

hydrogen flames—is even greater, as at high temperatures, the intensity of the pure-rotational CARS spectrum is spread over many spectral lines (thermally populated states). Therefore, the new detection method introduced in this thesis (discussed in chapter 5) using pure-rotational CARS spectroscopy on H_2O can be considered a breakthrough.

The second challenge is related to the spatiotemporal resolution obtained with pure-rotational CARS imaging. As it was discussed in the previous sections, performing diagnostics in H_2 flame fronts is very challenging. The lack of spatial and temporal (cinematographic) resolution may impact negatively the precision and accuracy of the measurements. While the use of two synchronized fs- and ps-laser systems has been successfully employed to probe the propagation of both laminar [79] and turbulent [99] hydrogen flames with 1D- and 2D-CARS, respectively, a lateral spatial imaging resolution of ∼40 μm has been reported at these measurements which was dictated by the wavelength of the probe beam (532 nm). In addition, in these previous works of CARS imaging, the refresh-rate was 20 Hz, which is determined by the high-power picosecond regenerative amplifier laser system design. In this thesis, it is developed a new unique architecture for pure-rotational CARS imaging spectroscopy using a single laser system, and with the "blue-shifting" of the probe beam (from 532 nm to 400 nm), it should be possible to achieve an even greater spatial resolution, as well as an increased data acquisition rate (from 20 Hz to 1 kHz). With these new prospects, it means that the spatial averaging effects might become reduced to such an extent, that the retrieval of the hydrogen flame-front contour is nearly exact. Additionally, with the slight possibility of cinematography, it is intended to resolve scalar dynamics and improve the significance of the recorded data in laminar flames.

1.4 Research objectives

As underlined in the former section, a tailor-made diagnostic system has been built to overcome the challenges involved in the experimental characterization of the structure of H_2 flames. I have had two primary objectives for this research. The first one is to expand on the performance of pure-rotational CARS imaging spectroscopy with the ambition to measure temperature and species concentration (i.e. N_2, O_2, H_2, and H_2O) with correlated resolution in space (1D field of view) and in time (∼kHz acquisition rate). The second one is to make use of this new diagnostics tool to study the flame propagation of turbulent diffusion flames. In particular, the effect of differential diffusion of H_2 is investigated. To date, there have been no direct

observations of this molecular transport process in either laminar- or turbulent hydrogen flame environments.

The content of this thesis is thus organized as follows. Chapter two begins with the sufficient theoretical description of the CARS process. It emphasizes on rotational spectroscopy of diatomic molecules and the modeling of the CARS signal in the time-domain. Chapter three describes the outline of the experimental apparatus which includes the design of the laser system and the coherent imaging spectrometer to detect the 1D CARS signal. In chapter four, the procedure for the characterization of the spectral phase of the ps-probe beam and its further optimization is explained. Then, in chapter five, a new detection strategy to measure the concentration of water vapor using the sensitivity of the N_2 CARS signal in the time domain is discussed along with the proof of principle in a laminar diffusion H_2 flame. Finally, in chapter six, the application of the developed instrument is demonstrated in the investigation of the differential diffusion of H_2 in a canonical turbulent flame.

Chapter 2

Theory and modeling of fs/ps pure-rotational CARS

This chapter provides a general overview of the physical principles behind the use of CARS spectroscopy for gas-phase temperature and species concentration measurements. It begins by describing the internal energy structure of diatomic molecules, focusing on their vibrational and rotational quantum states as well as the probability distribution of these states within molecular ensembles, which is strongly temperature-dependent. Following this, a detailed description of the time-domain model used to simulate the fs/ps pure-rotational CARS signal is presented. The aim is to offer the reader insight into how scalars, such as temperature and species concentration, are derived from experimental spectra acquired in flames.

2.1 Spectroscopy of diatomic molecules

A molecule is an assembly of atoms, held together by electrostatic forces created between the positively charged nuclei of the atoms and the negatively charged electrons. In this system, energy is quantized, and therefore, it takes discrete values that are specific for each molecule. To understand this discrete energy distribution, it is useful to divide the nuclei and the electrons' energy into separate parts represented by the electronic, the vibrational, and the rotational motions of the molecule. The Born-Oppenheimer approximation assumes that on extremely short time scales (less than 1 fs), the nuclei may be thought of as fixed in space as compared to the fast motion of the electrons [100]. As a result, the energy associated with the motion of the nuclei and the electrons can be treated as two independent systems. Conveniently, the total Hamiltonian for measuring the total kinetic energy of a diatomic molecule can thus be expressed as a sum of these motions.

$$H_T = H_{el} + H_{nucl} \tag{2.1}$$

$$H_T = H_{el} + H_{vib} + H_{rot} \tag{2.2}$$

This thesis dissertation mostly concerns energy transitions within the manifold of rotational energy states which belong to the first vibrational level of the ground electronic state of a diatomic molecule. Therefore, both the contributions of vibrational and electronic energies are not discussed further. The vibrational motion of a diatomic molecule may, however, induce changes in the rotational moment of inertia leading to centrifugal distortion of the molecule. This means that a coupling between vibrational and the rotational energy states also needs to be considered to simulate the exact positions of the spectral lines.

2.1.1 The rigid rotor

The rotational energy distribution of diatomic molecules is best described by the rigid rotor model [101]. For a rigid rotor, it can be assumed that the bond between two atoms of masses M_1 and M_2 is fixed, so that its length and angle do not change while the molecule rotates about its center of mass (Fig. 2.1a). The kinetic energy associated with this rotational motion of angular velocity ω can be written as

$$K = \frac{1}{2}I\omega^2 \qquad (2.3)$$

Here, the moment of inertia (I) is calculated using the reduced mass of the molecule $\mu = (M_1 M_2/(M_1 + M_2)$ and a fixed internuclear distance $R = r_1 + r_2$ as in the following: $I = \mu R^2$. Consequently, the rotational Hamiltonian operator H_{rot} from Eq. (2.2) may be expressed as

$$H_{rot} = \frac{\vec{J}^2}{2I} = \frac{\vec{J}^2}{2\mu R^2} \qquad (2.4)$$

where $\vec{J}$ denotes the angular momentum operator of the molecule, whose eigenvalues are specified by the rotational quantum number J. The corresponding eigenvalues (energies) are given by the solution of the time-independent Schrödinger equation for H_{rot} according to

$$E_{rot} = \frac{h^2}{8\pi^2 I}J\,(J+1)\;[\mathrm{J}] \qquad (2.5)$$

Since the energy is quantized, J takes only positive integral values (i.e. 0,1,2, etc.). Due to the small energy of rotational transitions expressed in Joule [J], it is

convenient to instead employ wavenumbers units $[\mathrm{cm}^{-1}]$. This is done by dividing E_{rot} in Eq. (2.5) by the Planck constant (h) and the velocity of light (c) according to:

$$E_j = \frac{E_{rot}}{hc} = BJ(J + 1) \ [\mathrm{cm}^{-1}] \tag{2.6}$$

As it can be seen in Eq. (2.6), the moment of inertia is incorporated into the rotational constant $B = h \ / \ 8\pi^2 \ Ic \ [\mathrm{cm}^{-1}]$. The magnitude of this constant defines the rotational level spacing of the molecule and varies with the vibrational quantum level, respectively.
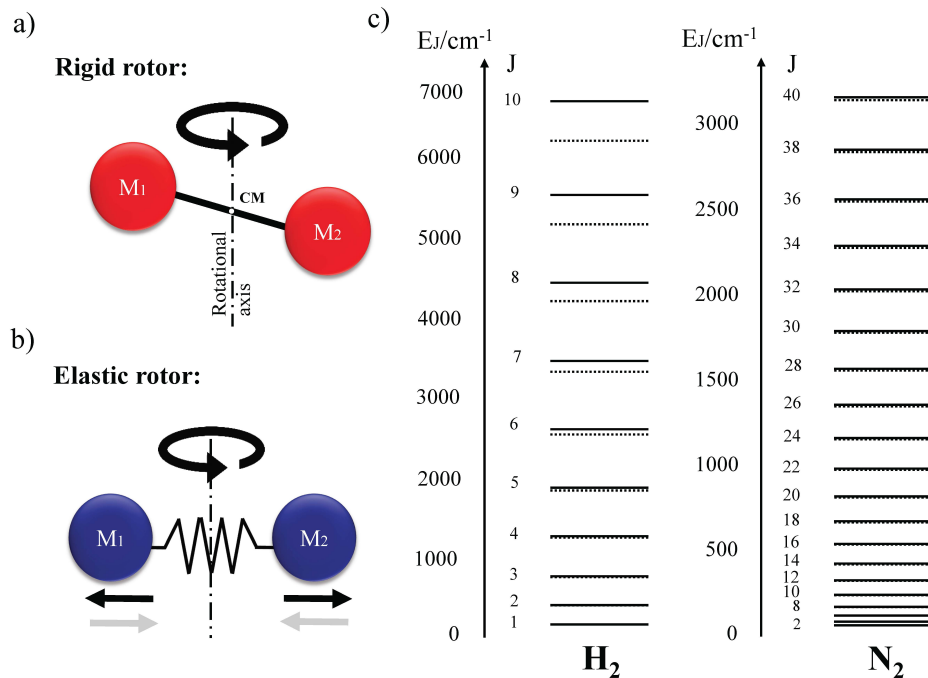
Figure 2.1: Rotational energy of diatomic molecules. A visual representation of a) the rigid rotor and b) the elastic rotor model. c) Comparison of energy states distribution between the two models applied for N_2 and H_2. The solid line represents the rigid rotor and the dashed line the elastic rotor which accounts for centrifugal distortions of the molecules.

2.1.2 Elastic rotor

The rigid rotor model, while simple, approximates well the rotational energy distribution of diatomic molecules with small angular momenta. However, it starts to fail at simulating the rotational energy states corresponding to elevated *J*-quantum numbers, especially in molecules with large rotational constants such as

hydrogen. This is because a more realistic description of the molecule would be to consider it fluidic (more or less), and the centrifugal force acting through the fast-spinning motion leading to its distortion. In this case, the internuclear separation distance changes between the point masses of the atoms, and therefore the rotational and the vibrational motions cannot be considered decoupled anymore. The molecule is thus better described as an elastic rotor. Another depiction of this effect can be seen in Fig.2.1(b) concerning the vibrational motion. Here, the bond between the two atoms of point masses M_1 and M_2 is now represented by an elastic spring that expands due to the strong vibrations. From a mathematical point of view, this is also more complicated, as the energy states of a harmonic oscillator motion with neat analytical solutions are not valid, and instead, numerical solutions need to be applied. A common method, to simulate the energy states of the anharmonic motion is to introduce correction terms to the energy expression in Eq. (2.6) obtained via a Taylor expansion

$$E_J = B_v J(J + 1) - D_v (J^2 (J + 1)^2 - H_v J^3 (J + 1)^3 + \cdots \qquad (2.7)$$

For simplicity, the series can be trunked after the second-order correction term, where D_v is usually referred to as the centrifugal constant and accounts for the additional moment of inertia due to the bond length distortion. Figure 2.1(c) shows the centrifugal correction of the rotational energy ladder for N_2 ($D_v = 5.76 \times 10^{-6} \text{cm}^{-1}$) and H_2 ($D_v = 0.0459 \text{ cm}^{-1}$) [102]. As it can be seen the effect of centrifugal distortion is very small for the nitrogen molecule, at least for $J \leq 40$. On the other hand, these distortions become significant for H_2 due to the flexibility of its single bond, which is affected by the large angular momenta. This effect is important for calculating the line positions of the pure-rotational CARS spectra.

2.1.3 Population distribution

Once the rotational energy states have been calculated, it is of primary importance for thermometry to know how molecules in a thermal ensemble are populated over these quantized states. This explains how the CARS signal is sensitive to temperature.
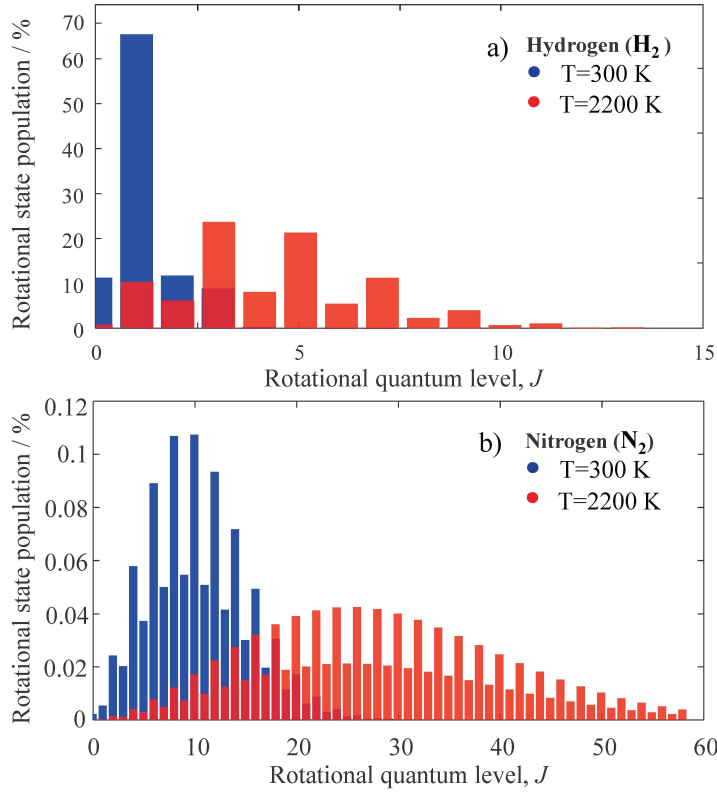
Figure 2.2: Boltzmann population distribution of rotational levels for the N_2 (top) and H_2 (bottom) for 300 K and 2200 K; the usual upper and lower temperature limits seen in flames.

The population distribution is derived from statistical mechanics using the normalized Boltzmann factors;

$$\rho_{v,J} = g_n^k \cdot g_Z \frac{e^{-\frac{\hbar E_J}{k_B T}}}{Z} \tag{2.8}$$

$$Z = \sum_j g_n^k \cdot g_Z \, e^{-\frac{\hbar E_J}{k_B T}} \tag{2.9}$$

where $\rho_{v,J}$ indicates the percentage of molecules in the Jth state of rotational energy E_J; k_B the Boltzmann's constant, and T, is the temperature in Kelvin. Moreover, the denominator in Eq. (2.8) is the partition function Z and represents the sum over all the states used for normalization. The terms g_n^k and g_Z in Eq. 2.8 and 2.9 account for the degeneracy of the quantized rotational states (i.e. individual states with exactly the same energy). On the one hand, the term $g_Z = (2J + 1)$ accounts for the rotational multiplicity of degenerate magnetic sub-states. On the

other hand, g_n^k is the nuclear spin statistical factor. For heteronuclear diatomic molecules, the nuclear spin is constant and equal to 1. In the case of homonuclear diatomics such as N_2, O_2, and H_2, the effect of nuclear spin degeneracy causes alternating populations between even and odd rotational states, depending of specific symmetry properties of the electronic wave function of the molecule.

To better illustrate how temperature is retrieved from this probability distribution, Figure 2.2 depicts the thermal Boltzmann population distribution of the rotational energy states of N_2 and H_2 at 293 K and 2200 K; the upper and lower temperature bounds that are probed in the present study. It can be seen that as the temperature increases, the distribution spreads out and higher rotational energy states get populated. In the most basic sense, this indicates that when temperature increases, the molecule starts to spin faster. Additionally, it is possible to see that the rotational state population distribution is not the same for all species; instead, it varies according to the molecular energy spacing. At room temperature, for instance, only three J-quantum states of hydrogen are significantly populated. About ~65% of the total population is concentrated only in J=1. On the contrary, nitrogen presents a denser manifold of the rotational energy states, and a considerably larger number of these states are occupied even at low temperatures. Therefore, the probability in each state is below 10% overall. What makes CARS excellent for gas-phase thermometry is that the spectrum closely resembles this distribution. The following section presents how to simulate the pure-rotational CARS spectrum of diatomic molecules.

2.2 Two-beam rotational fs/ps CARS

The CARS process is based on the principle of inelastic scattering of light. When a photon is scattered by a molecule, the energy of the scattered photon is different from the energy of the incident photon (Raman scattering), resulting in a change in the wavelength or frequency of the scattered light. This energy difference is equal to the energy of a vibrational or rotational transition of the molecule being probed. In essence, this effect arises from a change in the polarization of the medium induced by the oscillating electric field component of the electromagnetic radiation. The induced polarization is dependent on the nuclei position and is thus modulated by rotational and vibrational motions of the molecule. The frequency shift between the incident and the scattered light is the Raman signal and can thus be interpreted as the beat frequency between incident radiation and nuclear motions [103].

The CARS signal is generated through a third-order induced polarization of the medium created when three incident photons (pump, Stokes, and probe) interact with the quantized energy states of the evaluated molecule, as shown in Figure 2.3(a). In this process, the frequency difference between the pump (ω_{pump}) and Stokes (ω_{Stokes}) photons matches a pure-rotational Raman transition between two observable states of the molecule, resulting in an induced Raman coherence. This molecular coherence is then probed with a third photon (ω_{probe}) thereby generating a coherent signal (ω_{CARS}) from the scattered light. In this process, energy is conserved according to the equation $\omega_{CARS=}\omega_{pump}$- ω_{Stokes} + ω_{probe}. The spectrum of the signal generated resembles the Boltzmann population distribution of a thermal ensemble; this is where the sensitivity of CARS to temperature and chemical gas composition is obtained.
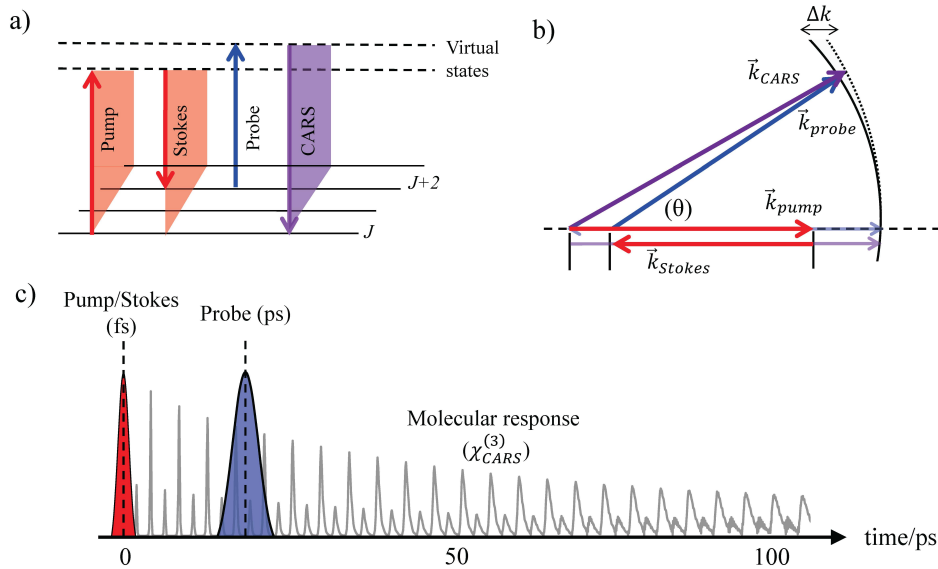
Figure 2.3: The three principles of two-beam pure-rotational CARS. a) energy conservation, b) momentum conservation (phase-matching) and c) intra-pulse combination in the time-domain.

During the coherent excitation, molecules undergo transitions within the discrete ro-vibrational energy levels designated by the vibrational and rotational quantum numbers (v, J). In the context of Raman spectroscopy, only specific transitions are allowed, depending on the structure and intrinsic symmetries of the molecule. Therefore, the following "selection rules" apply:

- Q-branch, for Δv =+1, ΔJ=0, corresponding to pure-vibrational transitions.
- O-branch, for ΔJ=−2, corresponding to either pure-rotational or ro-vibrational transitions.

- S-branch, for ΔJ=+2, corresponding to either pure-rotational or ro-vibrational transitions.

One of the most important aspects that needs to be considered in the CARS process is the phase matching condition. Since the resulting electromagnetic radiation is coherent in nature, it propagates in the direction dictated by the conservation of momentum, as described by its wave vector ($\vec{k}_{CARS}$):

$$\vec{k}_{CARS} = \vec{k}_{pump} - \vec{k}_{Stokes} + \vec{k}_{probe} \tag{2.10}$$

To fulfil this criterion, the incident beams should be arranged in a specific way such that the CARS signal generated at a certain point in the probe volume is in phase with the signal generated at subsequent points. This leads to a constructive build-up of the signal. From a diagnostics perspective, the phase matching condition is thus important as it has a direct effect on the generation efficiency of the signal and the longitudinal spatial resolution. While there are several configurations developed to satisfy the momentum conservation constraint, the two-beam phase-matching scheme is the most convenient for CARS imaging applications [104]. In this configuration, the combined pump/Stokes and the probe beams are crossed at an arbitrary angle and the generated signal propagates approximately along the direction of the probe. The reduction from three to two laser beams considerably simplifies the spatial and temporal overlap of the laser pulses and allows to expand the probe volume to multi-dimensional spatial configurations (1D, 2D). Besides that, the spatial resolution is significantly enhanced in this arrangement. It can be tuned by simply changing the crossing angle (θ) between the two beams. The non-perfect alignment of the probe beam with respect to the pump/Stokes one, however, introduces a phase mismatch (Δk) in the CARS signal, resulting in a shorter wave vector which may limit the spectral response of the measurement. The wave-vector mismatch can be calculated using the following expression

$$\Delta k = (k_P - k_{St}) + k_{Pr} - k_{CARS} \tag{2.11}$$

Where, the term $(k_P - k_{St})$ represents the Raman shift. In Figure 2.3 (b) the phase-matching diagram for two-beam CARS is displayed. Depending on the value of θ, the beams can be nearly phase-matched for a wide range of pure-rotational Raman transitions. For a given probe beam, Δk can be computed as a function of the crossing angle as

$$\Delta k = \Omega + k_{Pr} - \sqrt{(\Omega + k_{Pr} \cdot \cos\theta)^2 + (k_{Pr} \cdot \sin\theta)^2} \qquad (2.12)$$

Since Δk increases as a function of the Raman shift, this effect becomes relevant when probing molecules with large rotational Raman transitions such as hydrogen.

It is important to keep in mind that in this phase-matching configuration, there is a trade-off between longitudinal spatial resolution and the CARS intensity obtained. The larger the crossing angle, the interaction length (z) between the pump/Stokes and probe beams becomes shorter, thus improving spatial resolution. However, the intensity of the signal is negatively affected as it is proportional to the interaction length and the wave-vector mismatch (Δk) according to the traditional CARS equation obtained with three beams:

$$I_{CARS} \propto z^2 \, sinc^2 \left(\frac{\Delta k \, z}{2}\right) \qquad (2.13)$$

It should be noted that Eq. (2.13) is obtained by assuming that the amplitude of the pump, the Stokes, and the probe electric fields are constant along z (i.e. the slowly varying amplitude approximation). For two-beam CARS, when $0 < \theta \geq 90$, the assumption of field independence of the interaction length does not hold true at least for the pump/Stokes beam. Therefore, a more appropriate way to present the functional dependence of the CARS signal intensity for Δk and z is given in Eq. (2.14) [79]:

$$I_{CARS} \propto e^{-\left(\frac{\Delta k \, z}{4}\right)^2} \qquad (2.14)$$

In this case, the combined pump/Stokes beam is modelled as a double Gaussian function, which spatial profile is described by a function on the form $e^{-\alpha z'^2}$. Now that the requirements in terms of energy and momentum conservation have been explained, in the following section a description of the time domain response of the CARS process is detailed.

2.2.1 Time-domain modelling

In the CARS process, the electric field from the incoming pump/Stokes beam polarizes the gas medium by changing the electron distribution relative to the

molecule's nuclei. The induced polarization $\vec{P}$ corresponds to the electric dipoles created by the incident light wave field and can be described as a power expansion:

$$\vec{P} = \varepsilon_0(\chi\vec{E} + \chi^{(2)}\vec{E}^2 + \chi^{(3)}\vec{E}^3 + \cdots) \tag{2.15}$$

where $\vec{E}$ is the electric field applied, ε_0 is the permittivity of free space and χ represents the susceptibility of the medium to be polarized. Although the higher-order terms in Eq. (2.15) are considerably weaker than the linear one, they become significant when a high electric field is applied, especially from a fs-laser pulse. The induced polarization of an isotropic medium, such as gas, is restricted to terms with odd orders due to inversion symmetries. Additionally, polarizations above the third order are disregarded, focusing on four-wave-mixing. The CARS process is governed by the third-order non-linear susceptibility of the optical medium ($\chi^{(3)}$).

In fs/ps CARS, $\chi^{(3)}$ is modeled as a transient in the time domain under two main assumptions. The first one is the instantaneous dephasing of the electronic coherence induced in the medium by the far-detuned pump, Stokes, and probe fields. The second one is the impulsive excitation of the rotational Raman coherence: molecules oscillate collectively (in phase) after turning off the fs electromagnetic field. This condition is achieved if the pump/Stokes pulse duration is comparable to or shorter than the rotational period of the probed Raman-active mode.

The third-order non-linear susceptibility of the medium can be modeled then, using a phenomenological approach. It results in the sum of elementary sine waves at the frequencies of the molecular Raman transitions, weighted by their relative transition strength.

$$\chi^{(3)}(t) = \sum_k \sum_v \sum_{\Delta J=+2} W_{J\rightarrow J+2} \cdot \exp\left[(i\omega_{J\rightarrow J+2} - \Gamma_{J\rightarrow J+2})t\right] \tag{2.16}$$

The term, $\omega_{J\rightarrow J+2}$ denotes the angular frequency of the Raman transitions and $\Gamma_{J\rightarrow J+2}$ is the J-dependent dephasing coefficient. The second term in the exponent in Eq. (2.16) dictates the coherence decay caused by inelastic collisions with perturber molecules in the dielectric medium. The index $W_{J\rightarrow J+2}$ accounts for the Raman transition strength

$$W_{J\rightarrow J+2} = X_k Y_k^2 F_{J\rightarrow J+2}^k b_{J\rightarrow J+2} \left|N_{J+2}^k - N_J^k\right| \tag{2.17}$$

where X_k is the species (k) mole fraction and Υ_k^2 is the polarizability anisotropy. The Placzek-Teller ($b_{J \to J+2}$) coefficients introduce corrections to the anisotropic polarizability accounting for the coupling of the angular momenta and are calculated depending on the final state of the transition. Therefore, these are different for the S- and the O-branch spectrum according to the algebraic formula [105]

$$b_{J \to J+2} = \frac{3(J+1)(J+2)}{2(2J+3)(2J+1)} \tag{2.18}$$

$$b_{J \to J-2} = \frac{3(J-1)J}{2(2J-3)(2J+1)} \tag{2.19}$$

The Herman-Wallis ($F_{J \to J+2}^k$) factors account for the change in the polarizability due to centrifugal distortions of the molecule affected by the rotational-vibrational coupling. These coefficients are calculated according to Eq. (2.20) following the Tipping-Ogilvie formulation [106] presented by Bohlin *et al.* [107]

$$F_{J \to J+2}^k = \left(1 + k^2 \frac{(J^2 + 3J + 3)}{\eta} \right)^2 \tag{2.20}$$

where $k = B_e^k / \omega_e^k$ represents the ratio between the rotational and vibrational constants for the species, k, involved and $\eta = \beta_0 / r_e \beta_1$ is a correction term for the anisotropic polarizability at the equilibrium internuclear distance (r_e).

Finally, the Boltzmann population difference factor, $\left| N_{J+2}^k - N_J^k \right|$, is determined by the thermal Boltzmann population distribution presented in section 2.1.3. These can be expressed as

$$\left| N_{J+2}^k - N_J^k \right| = N \cdot g_n^k \cdot g_z \cdot \left| \rho_{J+2}^k - \rho_J^k \right| \tag{2.21}$$

Figure 2.4 displays the imaginary part of the molecular response function ($\chi^{(3)}$) for room temperature N_2, O_2 and H_2; the molecules of interest for the present study. The temporal evolution of the rotational wave packet created by the impulsive excitation of these species is characterized by sharp features that appear periodically, therefore referred to as recurrence peaks. These peaks are created by the beating between cosine-shaped oscillations of individual J-states whose phase relation is locked by the well-defined time of the short fs-impulsive excitation

employed. At each revival, the axis of the molecules aligns with the direction of the electric field vector of the laser beam. The revival period is inversely proportional to the rotational constant of the molecule $T_{rev} = \hbar/2B$. As it can be seen, N_2 and O_2 display a rotational revival period of 8.38 and 11.60 ps respectively. In the case of hydrogen, this revival is much shorter and less defined in part because, at this temperature, only a few rotational states contribute to the molecular response. For comparison, Fig2.4(c) presents the temporal envelope of a sub-10 ps Gaussian-shaped probe pulse (4.5 ps fwhm) which is offset in time with respect to the excitation pulse. As it can be seen, the molecular response can be probed within the first revival periods of the wave packet before it starts to decay.
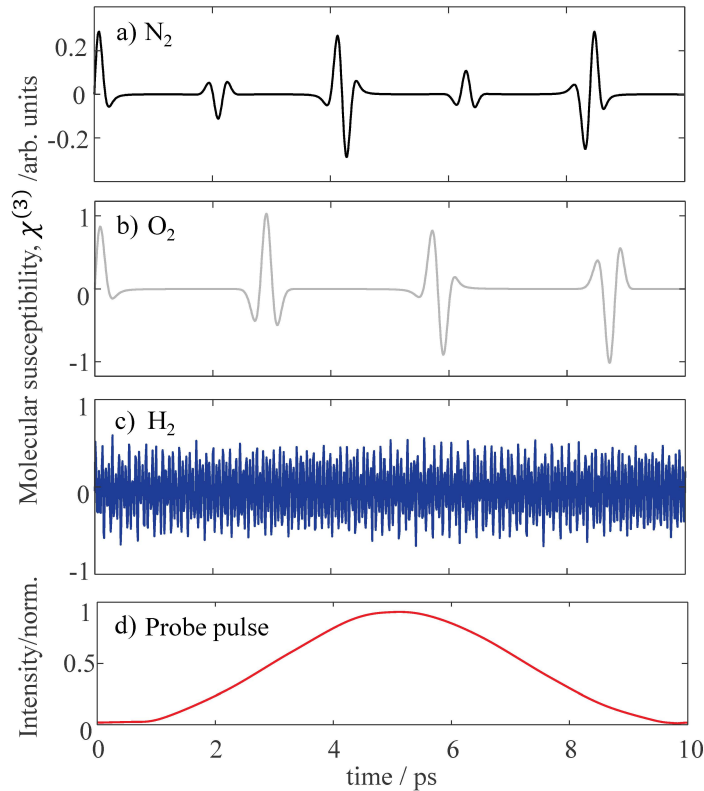
Figure 2.4: Time-domain traces of the transient non-linear Raman response in fs/ps CARS. Rotational revival structure simulated for the molecules of interest in the present study: N_2, O_2 and H_2. For comparison the temporal envelope of a simulated probe pulse of ~4 ps FWHM. The short duration of the probe pulse allows to generate the CARS signal during such a short window in time such that collisions with perturber molecules can be neglected.

In the general picture, the coherence decay of the time trace is due to collisions that occur between the active and the perturber molecules. Shortly after the fs-excitation pulse, however, other effects impact the decay, such as centrifugal

distortion and frequency spread dephasing [108]. At atmospheric pressure, however, the primary cause of dephasing is the rotational energy transfer (RET) during inelastic collisions. This is induced by quadrupole-quadrupole interactions within the ensemble if considering homonuclear molecules [109]. This effect is included in Eq. (2.16) via the *J*-dependent collisional dephasing coeficient, also discussed in the frequency domain as Raman linewidth coefficients ($\Gamma^k_{J \to J+2}$). In a molecular ensemble composed of various species, these coefficients are computed as a weighted sum according to

$$\Gamma^k_{J \to J+2} = \sum_p X_p \cdot \Gamma_{J \to J+2}(M_k - M_p) \tag{2.22}$$

where $\Gamma_{J \to J+2}(M_k - M_p)$ represent the dephasing coefficients of the radiator M_k, perturbed by the species M_p, and weighted by its mole fraction X_p. These coefficients also depend on the thermodynamic properties of the medium and are very sensitive to temperature.
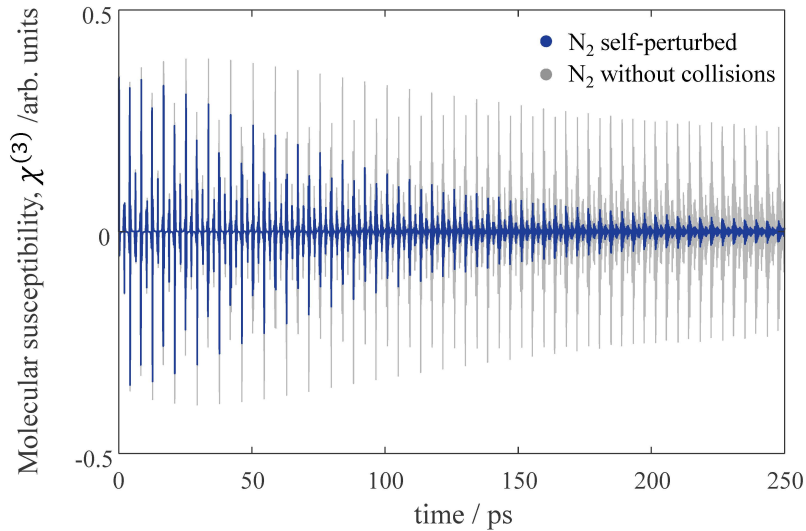
Figure 2.5: Collisional dephasing of the impulsively excited coherent Raman molecular response . The single exponential decay of the Raman coherence of nitrogen at 293 K, is here caused by self-perturbed N_2-N_2 inelastic collisions, simulated with coefficients obtained from Ref [117](blue line). After ~150 ps, the signal intensity has been reduced significantly. For comparison, the evolution of the Raman coherence when rotational energy transfer is neglected (grey line).

Figure 2.5 displays the imaginary part of the molecular response function of room temperature N_2 with and without including the self-perturbed Raman linewidths $\Gamma^{N_2}_{J \to J+2}$. Inelastic collisions impact the CARS signal in two ways. Firstly,

by dampening the signal intensity. Secondly, by changing the spectral shape because of the *J*-dependence of the dephasing coefficients. At atmospheric conditions, the effect of collisions can be neglected in the simulation of the CARS signal by probing the molecular response shortly after the impulsive excitation with the use of a short probe pulse delay. In this thesis, information about the dephasing rate of the pure-rotational N_2 CARS signal is still relevant as it has been used to deduce the concentration of water vapor in a hydrogen flame (see chapter 5).

There are a number of references available where these coefficients can be obtained. Because of its importance in N_2 CARS thermometry, studies have concentrated particularly on the effects of collisions between N_2 and other perturber species. A few examples are nitrogen (N_2-N_2) [110], carbon dioxide (N_2-CO_2) [111], water vapor (N_2-H_2O) [112], oxygen (N_2-O_2) [113], and hydrogen (N_2-H_2) [114]. In these cases, the Raman linewidths are obtained by the use of inverse Raman scattering or stimulated Raman scattering measurements in combination with dynamical scaling laws as a data fitting procedure. The most commonly employed scaling approaches used in the literature have been the energy-corrected sudden exponential law (ECS) and the modified exponential-gap law (MEG). In these models, the RET is calculated as a function of specific state-to-state transition rate constants. In the case of ECS, these constants are derived using the angular momentum coupling between two rotational energy states involved during the collision. On the other hand, the MEG model is based on the energy gap between the two states involved with the strong assumption that energy must be conserved.

Unfortunately, these models have been mostly developed for isotropic Q-branch transitions. To compute the linewidth coefficients for pure-rotational S- and O-branches, additional approximations are required. These coefficients can be retrieved by invoking the rotational wave approximation [115] as follows

$$\Gamma_{J \to J+2}^{k} = \frac{1}{2} \left(\Gamma_{J \to J}^{k} + \Gamma_{J+2 \to J+2}^{k} \right) \qquad (2.23)$$

A newer method to obtain the collisional dephasing coefficients for pure-rotational Raman transitions is by directly measuring the coherence decay of each individual transition using time-resolved CARS [116,117]. This is usually done by sequentially delaying the ps-probe pulse versus the fs-excitation pulse (combined pump/Stokes pulse) and recording the decay of the time-resolved CARS spectrum. Such measurements can be favourably performed in a binary gas mixture using a

heated optical cell. Assuming isolated spectral lines, the Raman linewidth can be obtained from the following relation

$$\Gamma_{J \to J+2}^{k} = \left(2\pi c \tau_{CARS, J \to J+2}\right)^{-1} \tag{2.24}$$

Where c is the speed of light in cm/s and $\tau_{CARS, J \to J+2}$ denotes the measured coherence decay coefficient.

2.2.2 Temperature and species concentration sensitivity

The pure-rotational CARS spectra are very sensitive to temperature and species concentration, and to extract the scalar information from an experiment, a non-linear interpolation spectral fitting routine is used. This routine compares a recorded experimental spectrum against a library of pre-calculated spectra for the prevalent experimental condition. The temperature is decided from the spectrum in the precalculated library which is in best agreement with the experimental spectrum.

The pure-rotational fs/ps CARS spectra are calculated with the Fourier transform of the time-dependent CARS electric field $E_{CARS}(t)$. For a given probe-pulse delay, τ, $E_{CARS}(t, \tau)$ is obtained as the product of the square root of the time-varying probe-pulse intensity I_{pr} (which is measured) and the molecular response function calculated as in Eq. (2.16). The expression is the following:

$$E_{CARS}(t - \tau) = \chi^{(3)}(t) \sqrt{I_{pr}(t - \tau)} \tag{2.25}$$

In Figure 2.6, the normalized N_2, O_2, and H_2 spectra simulated at 293 K, 1000 K, and 2200 K are displayed to show how sensitive the CARS signal is to temperature. To compute $E_{CARS}(t, \tau)$, a transform-limited probe pulse of 6 ps fwhm is used at a probe delay $\tau = 10$ ps. The S-branch spectrum of each of the three species is composed of equidistant spectral lines separated proportionally to the rotational constant of each molecule. The spacing between each of these spectral peaks is given by the quantized rotational energy calculated in Eq. 2.6 and the selection rules governing the rotational transitions.
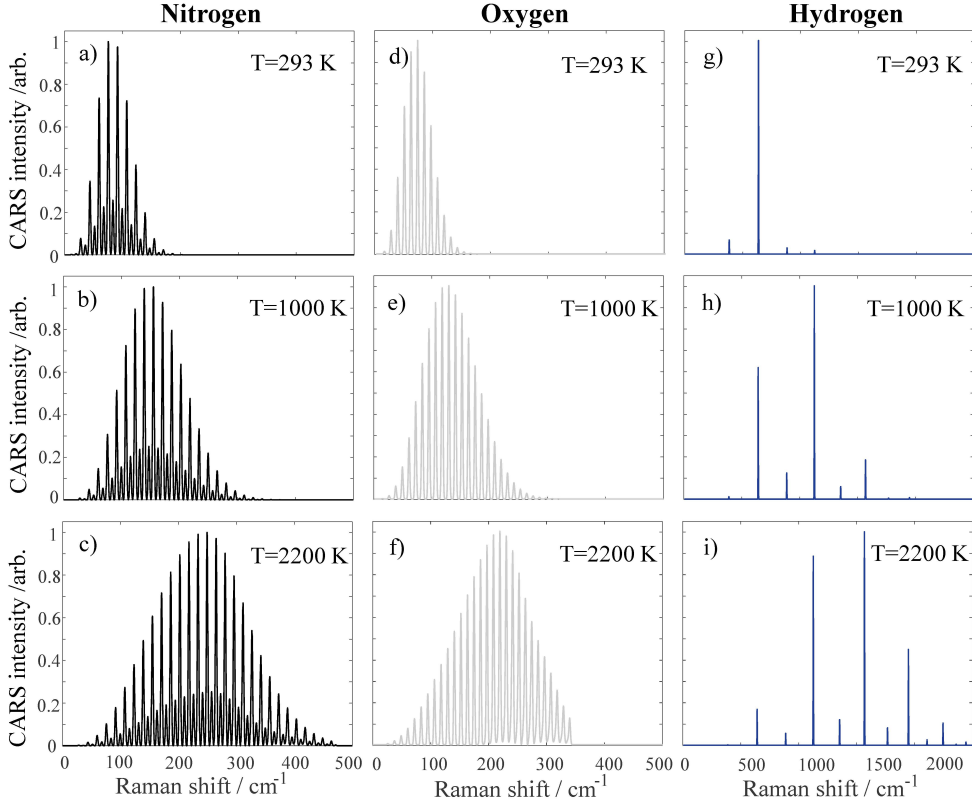
Figure 2.6: Sensitivity of pure-rotational CARS spectra to temperature. Spectra of N_2, O_2, and H_2 are generated at three distinct temperatures of 293 K, 1000 K, and 2200 K. It can be seen how the spectra gets positioned at higher Raman shifts and more dispersed as a function of temperature.

The energy difference between two adjacent rotational levels (ΔE) can be expressed as

$$\Delta E = E_{J+2} - E_J \tag{2.26}$$

$$\Delta E = (J + 2)(J + 3)B - J(J + 1)B \tag{2.27}$$

Thus, energy separation between adjacent rotational Raman transitions is consistently 4 times the rotational constant (4B). The varying intensity between even and odd transitions in Fig 2.6, is related to the nuclear spin statistical weight (g_n^k) included in the CARS model using Eq. 2.21. This factor is different for each of the molecules, depending on their nuclear spin (I) and if their total wavefunction is even or odd. Oxygen has an even number of protons and neutrons in its nucleus, resulting in a total nuclear spin of zero. Consequently, only transitions with ΔJ

being even are allowed, leading to the observed intensity ratio of 1 to 0 between each consecutive peak in the spectrum. On the other hand, nitrogen and hydrogen, with two identical nuclei (each with $I=1/2$), exhibit a nuclear spin of $I=1$. For N_2, $g_n^{N_2} = 6$ for even and $g_n^{N_2} = 3$ for odd J-number, so that the intensity ratio of even to odd Raman transition strengths is 2:1. Similarly, the degeneracy for even and odd transitions in the H_2 spectrum are $g_n^{H_2} = 1$, and $g_n^{H_2} = 3$, respectively.
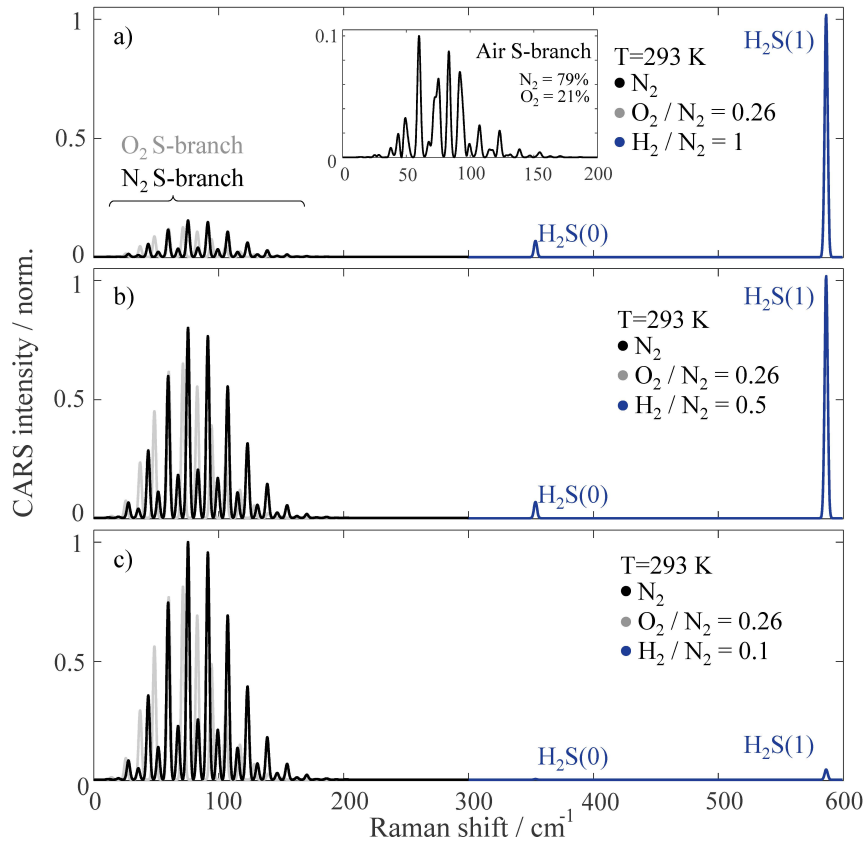
Figure 2.7: Sensitivity of the pure-rotational CARS spectra to species concentration. Species mole fraction is extracted based on the intensity of the spectrum relative to N_2. The sensitivity of various H_2 concentrations is displayed with respect to air. In the inset, it is shown how the shape of the N_2 spectrum is modified depending on the O_2 concentration. Since the spectral lines of the two species (i.e. N_2 and O_2) slightly overlap, the irregular contour is a result of signal beating which changes as a function of probe pulse delay.

Temperature significantly modifies the spectral shape by positioning the distribution towards a higher Raman shift and making the spectral envelope more dispersed. This change follows the thermal Boltzmann population distribution of the rotational quantum states manifold discussed in section 2.1.3. While N_2 and O_2 present a similar spectral distribution located within ~0-500 cm^{-1}, the H_2 CARS

spectra span a significantly wider range between ~350-2200 cm^{-1}. This makes the acquisition of the complete spectrum more challenging as the bandwidth of state-of-the-art fs-laser systems is limited to excite transitions up to ~600 cm^{-1}.

The sensitivity to species concentration (X_k), on the other hand, is obtained from the relative intensity between the CARS spectra of the molecules involved. Since the N_2 mole fraction in combustion conditions is nearly constant from reactants to products, concentrations are frequently assessed relative to this molecule. The relative intensity between the CARS spectra of Raman active molecules is given by the species-dependent polarizability anisotropy (γ_k) factors. In this thesis, the polarizability anisotropy values for N_2, O_2, and H_2 are obtained from Ref. [118] and included in the time-domain CARS model using Eq. 2.17. To illustrate the sensitivity of the CARS spectrum to concentration measurements of major species in H_2 flames, Figure 2.7: shows the simulated pure-rotational S-branch spectrum of room-temperature air (i.e. $X_{O_2}/X_{N_2} = 0.25$) in combination with various amounts of H_2 in the mixture such as $X_{N_2} + X_{O_2} + X_{H_2} = 1$. For this simulation, the CARS signal is generated for a gaussian probe pulse of ~6 ps-duration fwhm as this is the typical duration of a pulse generated using an SHBC. Similarly, only transitions within 0-600 cm^{-1} are considered. This corresponds to the approximate excitation bandwidth delivered in state-of-the-art fs lasers as the one employed in this thesis which typically produces pulses with a duration of around 35 fs. As can be seen from the figure, using this probe pulse duration, the N_2 (in black) and O_2 (in grey) spectral lines are not well resolved due to the proximity of the rotational Raman transitions of both molecules. This gives rise to an irregular spectral shape which changes as a function of probe delay due to beating between the two signals. Nevertheless, this fact does not affect the retrieval of temperature or relative concentration of these two species. Moreover, in Fig 2.7(a) it is possible to see that for an equal amount of N_2 and H_2 in the gas mixture (i.e. $X_{H_2}/X_{N_2} = 1$) the H_2 spectrum is significantly stronger than the N_2 one. This may be because in H_2 rotational energy is distributed over a smaller number of quantum states. As a result, it is expected that the relative concentration of these molecules can be measured for a wide range of conditions using only S(0) and S(1) H_2 transitions.

It should be noted that as the temperature increases, the population of the pure-rotational H_2 CARS spectrum is shifted toward higher energy states, and therefore relying solely on the S(0) and S(1) spectral lines for relative concentration measurements becomes increasingly challenging at temperatures exceeding approximately 1200 K. At such elevated temperatures, rotational energy is

distributed mostly over six energy states and transition S(3) dominates the rotational spectrum. Nonetheless, in most of the combustion applications where H_2 is used as a fuel, it gets rapidly consumed in the chemical reaction, and consequently, above this temperature its spectrum practically disappears. In this sense, one could argue that for such cases the use of these two transitions is sufficient to measure the entire evolution of H_2 in flames. On the other hand, in specific applications in which H_2 is present at higher temperatures, for instance, towards the product gases of highly rich premixed flames, fs pulses with a significantly larger excitation bandwidth are required to retrieve reliable information from the pure-rotational H_2 CARS spectrum. During the course of this thesis, I also contributed to the development of an ultrabroadband excitation for CARS with the use of fs-laser induced filamentation (Paper VI), used to excite up six rotational O-branch Raman transitions – from O(2) at 354 cm^{-1} to O(7) at 1447 cm^{-1} – using the same laser architecture described in chapter 3. However, this is not discussed in this framework.

Chapter 3

Development and validation of spatiotemporal CARS

The CARS instrument architecture is designed with the goal of creating a compact and sturdy system that can withstand disturbances and vibrations on the test platform. The core of the system is composed of two principal modules: signal generation and signal detection. The generation of the one-dimensional CARS signal is achieved through the utilization of a single regenerative amplifier, which concurrently produces both pump/Stokes and probe laser beams providing automatic pulse synchronization at the probe volume location. On the detection side, a wide-field polarization-sensitive coherent imaging spectrometer is developed, allowing the fast image acquisition of the CARS signal. This chapter elaborates on each of these components, granting the reader a better understanding of the system's capabilities for the investigation of H_2 flames as well as other applications in reactive flows. Moreover, the evaluation of the instrument's accuracy and precision is presented incorporating a benchmarking methodology designed specifically for spatiotemporal CARS. A more comprehensive overview of the system is outlined in paper I.

Part of the results discussed in this chapter haven been published in papers I and VI

3.1 Two-beam 1D-CARS using a single regenerative amplifier

The signal generation block is depicted in Fig. 3.1. It is primarily based on an ultrafast Ti:sapphire amplifier (Astrella, Coherent) which provides 7 mJ per pulse at a wavelength of 800 nm and operates at a repetition rate of 1 kHz.
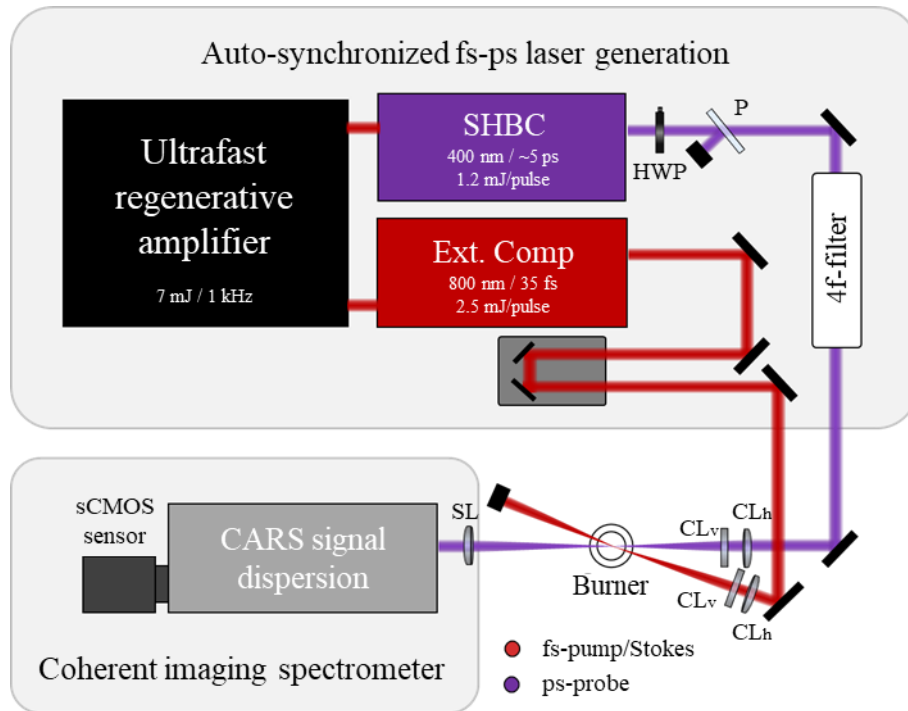

Figure 3.1: The ultrafast regenerative amplifier, SHBC and external compressor employed to generate synchronized femtosecond (fs) pump/Stokes and picosecond (ps) probe pulses for 1D-CARS diagnostics. The half wave plate (HWP) controls the polarization orientation of the beams. A custom built 4f-filter provides flexible control of the spectral and temporal shape of the probe pulse. Cylindrical lenses (CL) are used to focus the beams to form a one-dimensional line image. To enable quick image acquisition, a polarization sensitive coherent imaging spectrometer equipped with a sCMOS camera detector is used.

In the Astrella Ti:sapphire amplifier, a train of mode-locked fs pulses is amplified using chirp pulse amplification (CPA). In this scheme, the "seed" fs pulses are first stretched in time by introducing group velocity dispersion (also known as chirping) to the pulse. This allows for attenuation of the pulse's peak power below ~10 GW/cm^2 [119] whilst preserving the input beam's irradiance. Above this limit, the crystal would burn and can no longer act as a lasing medium. Additionally, non-linear effects such as Kerr lensing – intense coherent light would

modify the refractive index of a medium and consequently self-focuses in the material – could appear, further aggravating this situation. To amplify the seeding pulse, a pair of Pockels cells act as optical gates, confining the seeding pulse within a regenerative amplifier cavity until the desired gain is obtained after several round trips (~5-7). This cavity is pumped with an Nd:YLF ns-pulsed laser operating at a 1 kHz repetition rate. Upon amplification, the beam leaves the cavity and is split into two portions, with 65% (4.5 mJ/pulse) being internally compressed and directed towards the SHBC unit to form a narrowband picosecond beam. The remaining 35% (2.5 mJ/pulse) is routed into an external compressor unit to shape the broadband femtosecond beam. The motivation behind splitting the beam before the internal compressor in this particular Astrella unit is to forestall additional stretching caused by splitting optics before the SHBC, thus ensuring optimal compression efficiency. As a result, this laser architecture generates two repetition-synchronized beams: the first delivers narrowband pulses of ~ 4 ps duration (~1.2 mJ/pulse) centered at 400 nm, while the second produces near-IR broadband pulses of about 35 fs duration (~2.5 mJ/pulse) centered at 800 nm. These two beams provide the pump, Stokes, and probe photos required to generate the CARS signal.

In this CARS system, a two-beam phase matching configuration is adopted. This means that the pump and Stokes photons are supplied by a single broadband fs-laser beam, which intersects the narrowband ps-laser beam—serving as the probe—at an angle θ, as illustrated in Fig. 3.1. The path length difference between the two beams, is compensated with an optical delay line, and the relative arrival time is controlled by an automated translation stage which provides sub-10 fs resolution. A half-wave plate combined with the polarizer are used to control the energy of each of the two beams. However, an additional half-wave plate is also introduced in each of the beams to control the relative polarization of the pump/Stokes beam with respect to the probe beam.

On the opposite side of the signal generation block in Fig. 3.1, the detection system is depicted. It consists of a coherent imaging spectrometer designed to capture the laser-like CARS signal generated at the intersection of the two beams and to relay the 1D image from the probe volume to the camera detector plane. In the following sections, specific details about the experimental set-up will be given.

3.1.1 The pump/stokes excitation beam

The main challenge in generating the pump/Stokes beam is to maintain the temporal shape of the pulse while it propagates to the measurement location. Ultrashort

femtosecond laser pulses are composed by a coherent combination of quasi-monochromatic waves that add together forming the pulse. The propagation of a pulse through an optical medium incurs a modification of its spectral phase due to the differential velocities at which the constituent waves traverse the medium. In nearly all materials, shorter wavelengths propagate slower than longer wavelengths. This phenomenon is known as positive group delay dispersion (GDD) or positive chirp. This effect is detrimental to the CARS spectral response as the pulse is stretched in time and due to the time-frequency uncertainty relation, the instantaneous excitation bandwidth is reduced. For example, when a 10 fs laser pulse at a central wavelength of 800 nm passes through 4 mm of BK7 glass, it experiences a positive GDD getting stretched up to ~ 50 fs [120]. This represents a significant reduction of the available excitation bandwidth. This effect can be introduced by various optical components along the beam path and is especially pronounced when thick optical windows are used in enclosed combustors. Therefore, it is imperative to devise means of compensating for this effect in the design of the system.
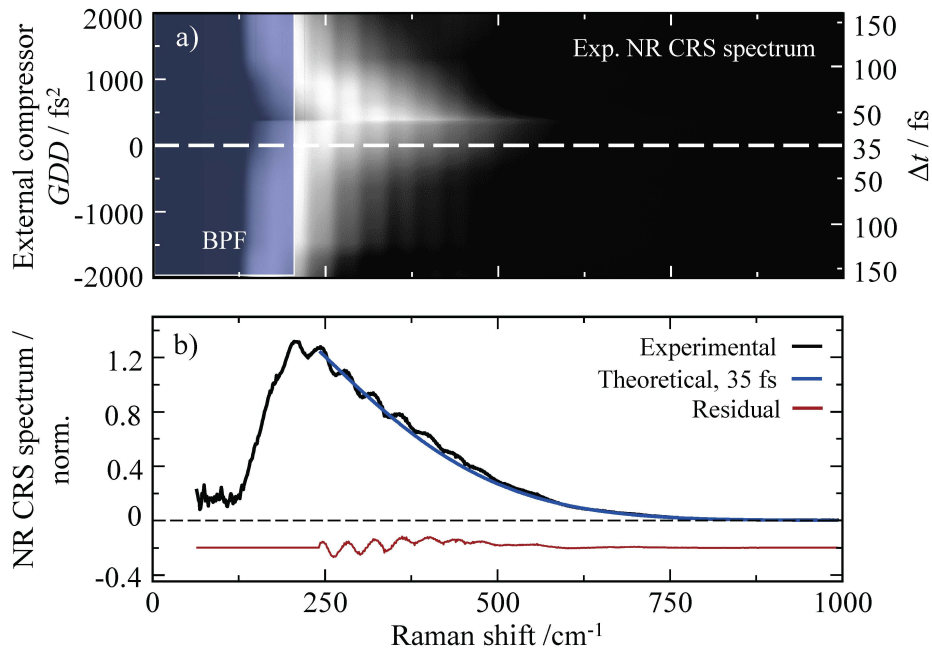
Figure 3.2: Effect of temporal chirp on the instantaneous excitation bandwidth. (a) Experimental autocorrelation of the fs pulse as measured by the non-resonant CARS signal of methane for various levels of chirp introduced using the external compressor unit. The region in blue denotes the spectral region impacted by the bandpass filter (BPF). The white dashed line identifies the condition of a near-transform-limited (TL) pulse. (b) Bandwidth of the optimized TL pump/Stokes excitation pulse represented by the non-resonant CARS spectrum of methane fitted to the time-domain CARS model.

The current setup compensates for the effect in question by deploying a folded grating external compressor. In this device, the temporal shape of the uncompressed amplifier output is tuned using a diffraction grating mounted in a tilt stage. By adjusting the stage motor, the relative orientation of the grating with respect to the beam trajectory is altered, allowing for an extended propagation distance of the low-frequency component (red-shifted) of the pulse, thereby imparting a negative chirp. This allows a flexible compensation of the chirp arising along the optical path even when thick optical combustor windows are in place. The amount of negative chirp required to deliver the shortest pump/Stokes pulse at the measurement location can be determined by simply optimizing the excitation bandwidth provided by the pump/Stokes beam using the spectral intensity of the non-resonant CARS signal.

A comprehensive evaluation of the external compressor performance when the pump/Stokes pulse is transported along thick optical materials is documented in paper IV. This study examines the impact of temporal chirp by performing autocorrelation measurements of the pump/Stokes pulse electric field. A numerical model is developed to simulate the non-resonant CARS signal which is utilized to quantify the instantaneous pulse duration as various levels of chirp are imparted, taking into consideration the quadratic phase terms of GDD. Figure 3.2, depicts the variations in the instantaneous bandwidth of the pulse as a function of the grating's position within the external compressor, along with the pulse duration calculated using the devised simulation model. Optimization of the pulse spectral phase results in a duration of 35 fs, as quantified through its full width at half-maximum. The negligible residual chirp attests to the transform-limited nature of the pulse, implying that its duration is optimized for the given laser spectral bandwidth. These results are also in line with the specifications provided by the laser manufacturer.

The duration of this pulse guarantees the impulsive excitation of the N_2 rotational manifold, the molecular species used for thermometry. The term "impulsive" is used when the duration of the pump/Stokes laser pulses is roughly one-tenth of the rotational period of the probed molecule. Laser pulses with a duration of 50 fs or less are thus required to impulsively excite N_2, which has a rotational period of approximately 500 fs. The O- and S-branch pure-rotational transitions ($\Delta J=\pm2$) are driven with equal efficiency by this mode of excitation, thereby preserving the thermodynamic properties of the medium. This also results in augmented signal intensity, as the phase-aligned oscillations of the probed molecules contribute to the instantaneous signal build-up upon the establishment of molecular coherence.

The broad spectral bandwidth of this pulse also represents a distinct advantage in probing rotational Raman transitions of various species of interest within high-temperature combustion environments. As illustrated in Figure 3.2(b), the pump/Stokes bandwidth expands up to approximately 600 cm^{-1}, enabling the coherent excitation of N_2, O_2, and even the first two pure-rotational transitions of H_2, located at 383 cm^{-1} and 587 cm^{-1}, respectively.

3.1.2 The probe beam

The probe beam is formed by compressing the bandwidth of one of the regenerative amplifier's outputs using a commercially available SHBC (Light conversion). In this unit, a sum-frequency generation (SFG) is created through the combination of phase-conjugate chirped portions of the initial femtosecond beam in a β-Barium Borate (BBO) crystal. In this process, a narrowband ps-pulse (~5 ps FWHM) is produced at a 400 nm wavelength with ~30 % conversion efficiency. The use of SHBC probe pulses for CARS imaging offers some advantages over traditional picosecond laser sources. Specifically, the short duration of the pulses (i.e. < 10 ps) enables to resolve the evolution of the rotational coherence even in pressurized environments in which collisional dephasing is pronounced [82]. Additionally, the utilization of a 400 nm wavelength instead of the 532 nm (2nd harmonic of nd:YAG laser) employed in most of the existing CARS systems enhances the signal quality, as evidenced by the improved spatial resolution and a more efficient scattering mechanism.

The increased spatial resolution is related to the superior focusing properties of the 400 nm wavelength of the beam. The smallest size that a laser beam may be focused on without losing coherence is known as the diffraction limit. This limit sets the upper bound on the achievable spatial resolution for a laser diagnostics technique which is defined by the size of the focused beam waist. The diffraction limit (d) is directly dependent on the laser wavelength (λ) as follows [46]:

$$d = \frac{2\lambda f}{D} \tag{3.1}$$

Where f represents the focal length of the lens which is used to focus the beam and D, the beam diameter incident on the lens, assuming a Gaussian amplitude distribution of the beam. Other factors such as optical aberrations and laser beam quality can affect the final focus spot size and consequently, the spatial resolution. The beam waist in the developed system is measured to be near the diffraction limit (<30 μm). Following the expression given in Eq. (3.1), this is about 25% smaller than the one that would be obtained with a 532 nm laser with the same optical configuration.
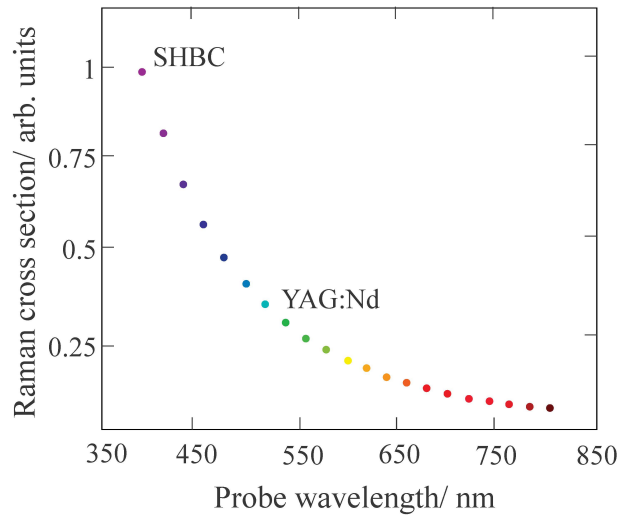

Figure 3.3: Variation in Raman cross-section as a function of probe pulse wavelength within the 400nm to 800nm range. The 400nm ps-duration pulse, produced by the SHBC, exhibits a notable increase in Raman cross-section compared to the commonly employed 532nm wavelength in CARS spectroscopy

The use of a 400 nm probe pulse, also provides an enhancement in the CARS signal strength. This occurs as a result of the Raman cross section's strong dependence on the wavelength of the probe electromagnetic field. The Raman cross-section defines the efficiency of probe pulse scattering by the molecular wave packet created in the gas mixture. It is proportional to the reciprocal of the second power of the wavelength, such that $\sigma_R \sim 1/\lambda^2$. Figure 3.3 illustrates the dependence of the Raman cross-section on different wavelengths of the visible electromagnetic spectrum. The signal intensity is found to be considerably higher for shorter carrier wavelengths. By utilizing an SHBC, it is expected that the signal strength obtained would be at least three times greater compared to that acquired from traditional Nd:YAG picosecond laser sources. This offers a significant advantage in performing CARS imaging in flames, particularly in this setup where a single

regenerative amplifier laser is used to generate both pump/Stokes and probe laser beams, requiring high signal generation efficiency.
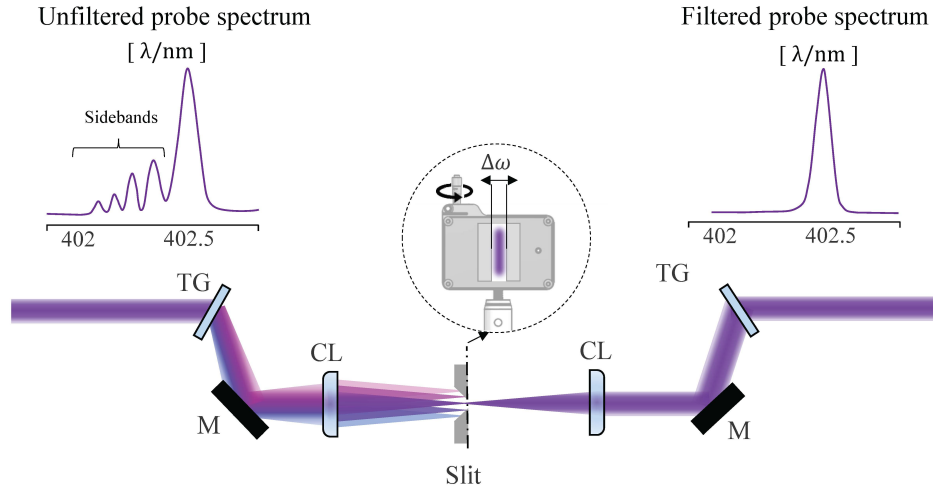

Figure 3.4: The 4-f pulse shaper used to filter the spectral sidebands in the probe pulse. The set-up is composed by a pair of transmission gratings oriented at Littrow angle, two cylindrical lenses (CL) and a slit which controls the pulse bandwidth.

Albeit its potential advantages, the utilization of an SHBC in CARS spectroscopy also entails several challenges that must be taken into account. One such challenge is related to the constraints on output pulse power. The SHBC unit can be pumped with a maximum of 4.5 mJ per pulse before reaching saturation of the SFG crystal. Given the SHBC conversion efficiency, the resulting maximum power attainable with the developed configuration is approximately 1.2 mJ/pulse. Another constraint is associated with the emergence of undesired spectral sidebands, which result from non-linear chirp induced within the SHBC stretcher. While the intensity of these sidebands is significantly weaker than the fundamental spectral peak of the pulse, it is equivalent to the strength of the CARS signal. If not suppressed, the sidebands interfere with the CARS spectra, precluding meaningful quantitative determination of scalars in flames. In this thesis, I faced this challenge by removing these undesired spectral peaks implementing an unfolded 4-f pulse shaper as depicted in Fig. 3.4.

A 4-f shaper is an optical device that manipulates the spectral and temporal properties of ultrashort laser pulses by employing a Fourier transform and a filtering element. In this custom-built device, a high-resolution grating in transmission (3040 grooves/mm) is used to spatially disperse the picosecond laser beam. The dispersed light is imaged at the Fourier plane by a cylindrical lens (f:300 mm) located 300

mm away, thus providing independent control over the spatial and spectral components of the beam. An adjustable mechanical slit mounted in a two-axis translational stage is then used to selectively filter the spatially-distributed sidebands, allowing only a narrow portion of the fundamental probe spectral peak (located at 402.3 nm) to pass through. As a consequence, the resulting pulse is stretched in time and its duration can be tuned accordingly by changing the width of the slit. Subsequently, a second cylindrical lens collimates the filtered probe pulse, and a second grating in transmission recombines the spectral components to generate the beam with the desired spectral and temporal characteristics.

The use of dispersion elements with high diffraction efficiency (>90 %) results in a filtering process with reduced losses. Probe pulses with a power output ranging between 300 and 400 µJ per pulse are thus produced, which prove to be adequate for CARS imaging in flames. It is worth noticing that the quality of the signal could be significantly improved by exploiting all the power available before the pulse is filtered at the *4-f* pulse shaper (i.e. ~1.2 mJ/pulse). However, in such case the effect of the spectral sidebands on the signal must be included in the time-domain CARS model to obtain reasonable agreement between the experimental and the simulated CARS spectra. The additional power output provided by the probe beam side bands would provide numerous benefits, such as improving the signal-to-noise ratio at flame temperatures (above 2000 K), where the CARS signal intensity is significantly damped or when multiprobe schemes are required to measure the signal in the time-domain. In chapter 4, I attempt to include the effect of sidebands in the CARS model by carrying out a comprehensive characterization of the spectral phase of the probe pulse.

3.1.3 The probe volume

Once the spectral and temporal characteristics of the degenerate pump/Stokes and the probe pulses have been tailored, both beams are crossed at the measurement location forming the probe volume (Fig. 3.4). The size of this volume defines the spatial resolution of the system which, for 1D-CARS, can be approximated to an elliptic cylinder of height L, width D_w, and length D_z. The height of the probe volume represents the image field of view (FOV) and is tuned accordingly to ensure a sufficient signal-to-noise ratio at flame temperatures. The height of the line is compressed to increase the signal strength by enhancing the irradiance of the beam. This is achieved using a pair of cylindrical lenses with their focusing axes oriented perpendicular to each other and separated at an arbitrary distance Δx_{CL}. The first lens focuses the beam along a vertical line while the second one compresses the

length of this line to increase the irradiance of the beam. Figure 3.4(b) shows the radial intensity distribution of the probe beam measured using a beam profiler camera (DataRay) positioned at the location where the beams cross. This distribution is then analyzed to characterize the height and width of the probe volume, yielding L~1.5 mm and D_w=22 μm as measured by $1/e^2$.
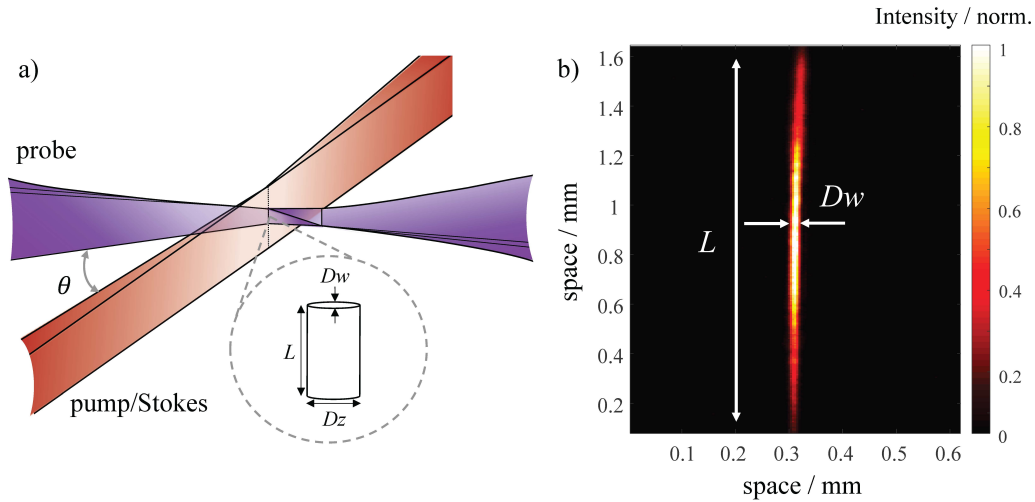

Figure 3.4: (a) Illustration of the probe volume shape created by the interaction of the probe and pump/Stokes laser beams (b) Probe beam cross section measured by a beam profiler camera placed at the beams crossing location. The false colour code displays the normalized intensity distribution used to calculate the width and height of the probe volume.

Furthermore, The longitudinal extent of the probe volume is approximated by calculating the interaction length (D_z) between the excitation and probe laser beams as

$$D_z = \frac{D_w}{\sin \theta} \tag{3.2}$$

Where θ is the crossing angle between the two beams and D_w=22 μm represents the waist of the pump/stokes beam along which the CARS signal is built. A crossing angle of 3 degrees is implemented for the majority of the experiments conducted in this thesis as it provides an optimal trade-off between phase mismatch, signal intensity, and spatial resolution. Consequently, the longitudinal extent of the probe volume is determined to be D_z~0.6 mm using Eq.(3.2). This probe volume dimension is the most sensitive to spatial averaging effects and thus needs to be optimized accordingly for the required application. While this requirement may be relaxed in laminar flames owing to the uniformity of the flow, a short interaction

length is necessary when turbulence is present due to the rapid fluctuations between burnt and unburnt reactants inside the probe volume.

3.2 Coherent imaging spectrometer

The 1D-CARS signal generated at the probe volume is detected in a custom-built slitless spectrometer depicted in Fig.3.5. This device is designed to detect the spatiotemporal CARS signal, with the sufficient spectral and imaging resolution required to resolve steep temperature gradients and species mole fractions typically found across laminar and turbulent flame fronts. The spectrometer is composed of a ~1:1 magnifying telescope built from two achromatic spherical lenses (f=400 mm) combined with a transmission grating (~3040 l/mm, Ibsen Photonics) which relay-image the dispersed CARS spectra onto the camera detector (Zyla 4.2, Andor). Since the spectral range of the pure-rotational CARS signal is in close vicinity of the probe beam wavelength, the probe beam needs to be rejected before the detector plane. This is performed by the angle-tuning of a bandpass filter (BP) from Semrock.

An important novelty in this spectrometer is the first implementation of an sCMOS (scientific-grade complementary metal-oxide-semiconductor) sensor without an intensifier to detect the 1 kHz imaging CARS signal. CARS spectrometers have traditionally been outfitted with CCD (charge-couple device) camera sensors, which enable a high quantum efficiency (>95%) while keeping a relatively low noise level. These sensors work by converting light into electrical charge, which is then transferred across the chip in a multi-step process including the sequential transfer of charge from one pixel to the next thus leading to relatively slow acquisition rates (~Hz). To achieve higher sampling rates (~ kHz) a reduced portion of the sensor can be exposed, however, limiting its use to point-wise spectra. In contrast, CMOS sensors include independent amplifiers and readout circuits for each pixel. Its independent pixel-level readout capability enables simultaneous and parallel processing of many pixels, leading to faster acquisition rates. Additionally, these sensors can be designed with a rolling shutter, which allows the readout of the sensor to occur continuously during exposure to light, thereby making it possible to acquire single-shot images at kHz rate. These capabilities have significant implications for both image and temporal resolution.
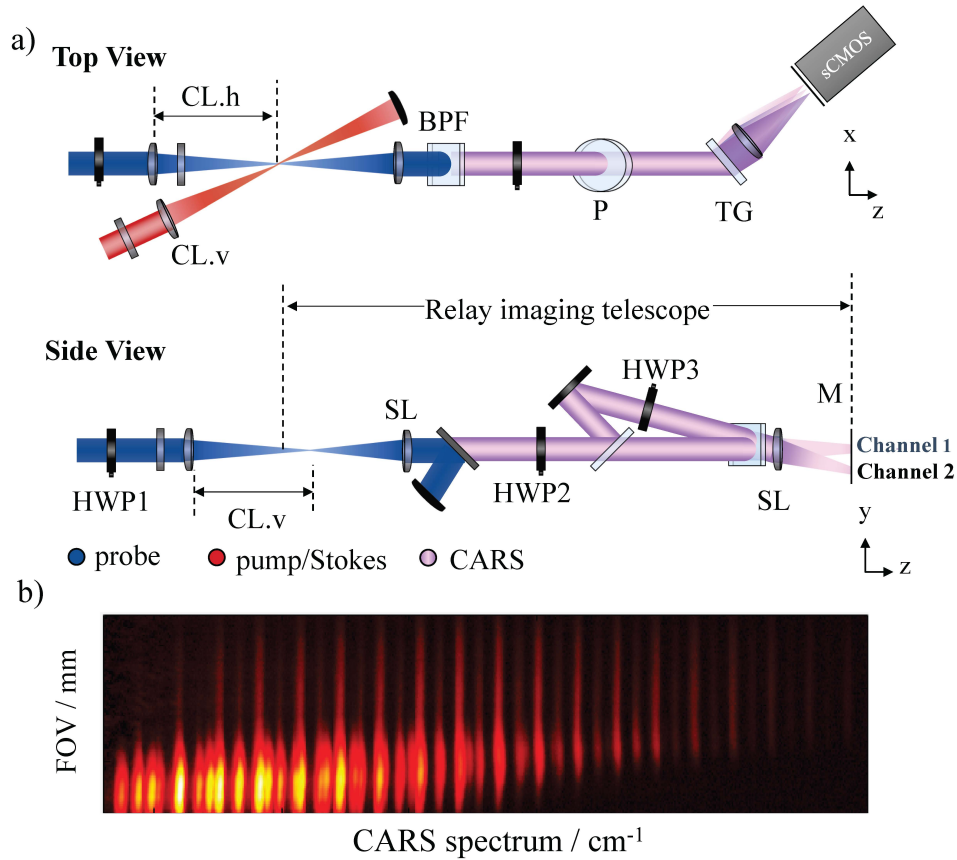
Figure 3.5: (a) The polarization-sensitive coherent imaging spectrometer designed to detect the one-dimensional CARS image at 1 kHz acquisition rate. Two distinct detection channels for P- and S- polarized light are relay-imaged from the signal generation to the sCMOS detector plane. (b) A single-shot CARS image recorded across a laminar CH_4/air flame front. CL - cylindrical lens, HWP – half-waveplate, BPF – bandpass filter, TG – transmission grating, SL – spherical lens.

In this spectrometer, a central portion of the sCMOS sensor, comprising 200 x 2048 pixels, is selected to detect the signal. This enables the synchronization of the camera with the femtosecond amplifier to acquire the 1D-CARS signal at a 1 kHz frame rate. As an example, Fig. 3.5(b) shows a single-shot CARS image acquired across the flame front of a laminar premixed CH_4/air flame. The dispersed CARS spectra are resolved along the horizontal dimension of the sensor with a resolution of 0.3 cm^{-1}/pixel for Raman transitions within the ~0-600 cm^{-1} range. The vertical dimension is binned every two pixels and serves as a spatial map, containing 100 spatially correlated spectra per single shot image. The maximum number of images that can be collected per dataset is determined by the internal memory capacity of the camera, with up to 1000 single-shot images obtainable for a 200 x 2048 pixels image.

Another unique feature of this spectrometer design is its polarization sensitivity. This spectrometer is composed of two independent detection channels with the capability to distinguish between S- and P-polarized signals. This is achieved using a combination of two 400 nm half-wave plates and a thin film polarizer (Eksma optics) as depicted in Fig. 3.5 a. A half-wave plate (HWP2) aligns the polarization of the cross-polarized signals to the transmission axis of the polarizer. The S-polarized signals are transmitted and directed to the camera detector, forming channel 1. Meanwhile, the P-polarized signals are reflected by the polarizer and redirected to the same camera detector using a mirror, thus creating channel 2. The second half-wave plate (HWP3), is mounted on the channel 2 to turn from P- to S-polarization, ensuring the maximum grating transmission efficiency.

3.2.1 Polarization sensitivity

The polarization sensitivity of the spectrometer played a crucial role in the development of this thesis. In CARS, the best signal efficiency is achieved when the polarization of the pump/Stokes and the probe beams are oriented parallel to each other. However, for certain applications, it is convenient to control the polarization state of the resonant and non-resonant components of the CARS spectrum. This can be achieved by arranging the relative polarization orientation of the input laser beams.

The theory of polarization control for rotational CARS relies on the model of the non-linear optical response of anisotropic media developed by Owyoung *et al*. [121] and was first implemented in rotational CARS by Vestin *et al*. [122]. A detailed description of the model employed in this thesis is discussed in the supplementary material of paper IV. In this model, the polarization angle of the resonant (β) and no-resonant (γ) components of the CARS signal with respect to the excitation beam is given by:

$$\tan \beta = (1 - 2\rho) \tan \alpha \qquad (3.3)$$

$$\tan \gamma = \frac{1}{3} \tan \alpha \qquad (3.4)$$

Where α denotes the relative orientation of the polarization of the probe beam with respect to the pump/Stokes, and ρ is the depolarization ratio of the Raman active molecules, which depends on the symmetry of the nuclei' molecular motions.

In this thesis, the polarization control of the CARS signal was a key to the development of the following publications:

1. Firstly, it is introduced in paper I, to generate an efficient stray light rejection for accurate 1D CARS thermometry. In the two-beam phase-matching scheme, the probe beam propagates in a direction similar to that of the CARS signal. Since the probe beam pulse is orders of magnitude stronger than the CARS signal, efficient suppression of the probe beam is essential to prevent scattered light from damaging the camera detector and contaminating the signal. This suppression is achieved by generating the resonant CARS signal with a polarization state oriented perpendicular to the probe beam, allowing to separate them before reaching the camera sensor. There is, however, a trade-off between the effective suppression of the probe beam and the efficiency of CARS signal generation. A relative polarization angle of 50° between the pump/Stokes and the probe beam results in 100% suppression of the probe beam in the spectrometer, but this comes at the cost of approximately 40% efficiency loss in the CARS signal. Conversely, rotating the polarization of the probe beam by 30° relative to the pump/Stokes results in a 30% suppression of the probe, with only a 20% efficiency loss in the CARS signal. Thus, different polarization ratios between the beams can be adjusted for each experiment depending on the required signal-to-noise ratio.

2. Secondly, the polarization-sensitivity of the spectrometer is employed in papers III and IV to provide *in-situ* referencing of the impulsive excitation efficiency in flames. In CARS thermometry, the non-resonant signal is a crucial reference to map the finite bandwidth of the excitation field and the transmission efficiency along the spectrometer optical path. The *in-situ* acquisition of the non-resonant signal as opposed to traditional ex-situ referencing protocols is particularly important to account for shot-to-shot pulse dispersion effects occurring when the ultrashort excitation pulse propagates through the flame. In these two papers, the concurrent detection of resonant and non-resonant CARS signals generated *in-situ* in the flame is demonstrated for the first time. This is achieved by controlling the relative polarization angle of the resonant and non-resonant signals allowing them to be detected simultaneously using a single spectrometer. By rotating the polarization of the probe beam 67.5° relative to the vertically polarized pump/Stokes beam, orthogonally polarized resonant and non-resonant CARS signals can be simultaneously detected in channel 1 and channel 2 of the spectrometer, respectively.

3. Finally, this feature is also discussed in papers V and VI to perform single-shot measurements of temperature and water vapor mole fraction in a turbulent H_2 diffusion flame. In this case, the spectrometer was employed to measure the dephasing of the N_2 CARS signal by simultaneously detecting the cross-polarized resonant CARS signals generated at two distinct probe delays.

3.2.2 Imaging resolution

The imaging resolution indicates the smallest image detail that the spectrometer optical system can form. A poor image resolution translates into systematic errors of the measured scalar as a consequence of spatial averaging effects along the field of view. It should be noted, however, that imaging and spatial resolution are related but distinct concepts in 1D-CARS. Spatial resolution refers to the smallest feature that can be measured by the system perpendicular to the measurement line. It is therefore defined by the width and length of the probe volume. Imaging resolution, on the other hand, refers to the quality of the signal retrieved by the detection system. It is a measure of how well the spectrometer can capture step gradients across the one-dimensional image generated in the probe volume. The imaging resolution thus depends directly on the magnification of the telescope, diffraction and aberration effects of the optical components employed, as well as the fidelity of the detector array which is given by the pixel size.

The image resolution of the coherent imaging spectrometer is estimated by the line spread function (LSF). This is a mathematical function that describes the response of an optical imaging system to a line-shaped object. To calculate it, a CARS signal is generated in room-temperature N_2. Then, a knife-edge is introduced at the probe volume location, creating a sharp straight discontinuity in the CARS image, as shown in Fig. 3.6(a). For this purpose, the intensity of both laser beams has to be significantly attenuated to avoid damaging the knife-edge target. This edge is then relay-imaged on the camera detector using the 1:1 imaging telescope on the spectrometer. Figure 3.6(b) shows the single-shot line intensity profile measured across the image FOV, which corresponds to the edge response function (ERF). As it can be seen, only ~3-4 pixels are required to rise from 10% to 90% of the maximum signal intensity. Finally, the LSF is obtained from the numerical derivative of the edge response curve (Fig. 3.6(c)). This yields an LSF of ~ 20 μm fwhm in the object space.
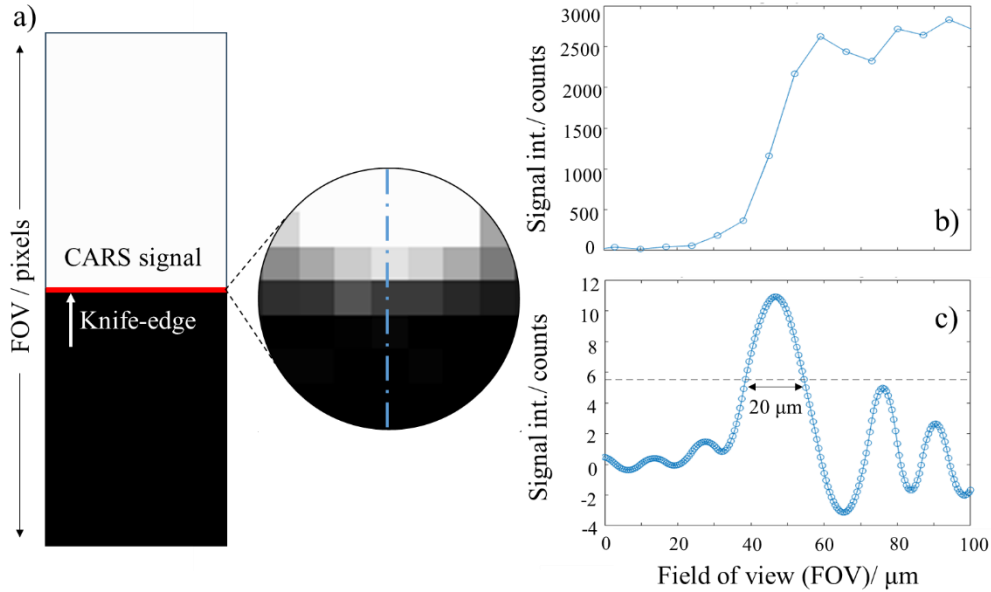
Figure 3.6: Experimental determination of 1D-CARS imaging resolution. (a) A knife-edge is introduced into the probe volume, positioned perpendicular to the vertical axis of the laser beam. (b) The edge response function is obtained by measuring the 1D-CARS intensity profile across the FOV after introducing the edge. (c) The line spread function, calculated from the numerical derivative of the edge response curve, reveals a spatial resolution of approximately 20 µm fwhm.

The study conducted in section 1.2.1 revealed that spatial averaging effects can considerably influence the retrieval of the flame-front contour when the imaging resolution is inadequate to resolve high temperature and species concentration profiles. A resolution of at least 20 µm is necessary to avoid systematic bias on the scalar retrieval in premixed laminar H_2/air flames. Given the resolution capabilities of the developed instrument, it is fair to say that it is capable of performing high-fidelity measurements in combustion environments with significantly sharp scalar gradients, including those involving both hydrocarbon and hydrogen flames.

3.2.3 Dynamic Range

The dynamic range of a coherent imaging system refers to the ability to capture and resolve a wide range of signal amplitudes simultaneously. In CARS spectroscopy, a high dynamic range is essential to detect the coherent Raman spectra generated in flames, as changes in temperature and molecular concentration cause significant variations in the signal intensity. The sCMOS detector employed in the developed spectrometer has a 16-bit digitalization depth which means that it can detect up to 65,536 distinct levels of brightness with a linearity of ~99%. For some applications, however, this may not be sufficient, and hence other strategies must be implemented to extend the spectrometer's dynamic range.

One of the main challenges in 1D-CARS thermometry is to measure both hot and cold temperatures simultaneously within the image field of view. This is a situation frequently encountered across flame fronts in laminar and turbulent reacting flows where temperature gradients are often steep. At short probe delays, the strength of the CARS signal at room temperature (292 k) is about 3-4 orders of magnitude higher than that in the flame (>2000 K). The dynamic range of the detection system is not sufficient to capture these gradients and low-temperature signals usually saturate the camera sensor. Some of the methods that have been employed to increase the dynamic range of the spectrometer include the development of dual-channel detection schemes in which two different camera sensors are deployed to detect the signal generated from hot and cold locations in the flame independently [123]. Other schemes, make use of cylindrical optics to spread point spectra vertically on the camera sensor, reducing the signal irradiance per pixel. For CARS imaging, however, the most suitable way to defeat the dynamic range limitation is to use a dephasing balance detection.

In the balance detection scheme, the *J*-dependence of the collisional decay of the Raman coherence is used to optimize the dynamic range of the temperature measured across the flame front. The intensity of pure-rotational CARS spectra generated at low temperatures decay at a faster rate as compared to that generated at high temperatures in the flame. By increasing the probe pulse delay low and high-temperature signals can be equalized and therefore acquired within the 16-bit dynamic range of the sensor. To achieve this, a probe delay of ~30-40 ps needs to be introduced in the configuration developed in this thesis.

In addition, the dynamic range is also critical for measuring the coherence decay of the CARS signal. In this thesis, I propose to use information about the dephasing rate of the N_2 CARS signal to deduce the concentration of water vapor. To achieve sufficient sensitivity, the CARS signal should be acquired along a significantly large range of probe delays of 0-300 ps, resulting in a dynamic range spanning six orders of magnitude in signal level. I extended the dynamic range of the signal detection using a detuned dual probe approach (see chapter 6). This approach enables to probe the molecular coherence simultaneously at ~20 and ~250 ps on the basis of a single-laser-shot, recording the resulting signals in two distinct detection channels of the spectrometer. By controlling the pulse power of each of the probe pulses independently the intensity of both signals can be equalized.

3.3 Correlated space-time resolution

The capabilities of the system to measure scalars with correlated space-time resolution were demonstrated by measuring simultaneously temperature and relative O_2/N_2 mole fraction across an unstable laminar premixed methane/air flame-front. To mitigate the impact of spatial averaging along the direction of the laser beam propagation, the flame was stabilized using a cylindrical bluff body placed above the burner rim, which generates a two-dimensional flame geometry. In this configuration, a nozzle feeds the combustible mixture (Φ=0.9) with a bulk velocity of ~1.3 m/s, ensuring the laminar regime. The resulting flame front has a relatively flat structure and comprises a narrow layer of ~500 μm in which the whole progression of the combustion reaction occurs. A dataset composed of 1000 single-shot 1D-CARS images was acquired across this region (~1.4 mm field-of-view) to resolve the progression of the combustion reaction. The corresponding temperature and O_2/N_2 mole fraction were obtained by fitting the experimental spectra to a two-dimensional library (temperature vs O_2/N_2 concentration) generated using the time-domain CARS model discussed in section 2.2.

The cinematographic evolution of temperature across the flame-front is displayed in Fig. 3.7. With the available spatial resolution, it was possible to capture instantaneously the temperature progression of the reaction, spanning from ~300 K in the reactants up to ~2200 K in the product gases. Additionally, the correlated space-time resolution obtained in this CARS scheme proved to be sufficient for tracking the position of the flame front at any moment in the course of the experiment. Harmonic oscillations of temperature are observed, corresponding to a frequency of ~13 Hz. These oscillations are caused by physical perturbations of the flame emerging from the interaction between hot combustion products and the air at ambient temperature surrounding the flame. In Fig. 3.8 the results obtained from the chemiluminescence study discussed in section 1.2.3 and performed on the same flame are presented again along with the temporal evolution of temperature and O_2/N_2 mol fraction at an arbitrary spatial position within the flame-front for a sampling period of 0.5 seconds. As can be seen, the temperature fluctuations measured by using 1D-CARS resemble the flickering motion of the flame-front observed by the chemiluminescence study. This is further confirmed by the O_2/N_2 mole fraction response which as expected presents a strong negative correlation to the temperature. These fluctuations might induce significant uncertainty in the evaluated temperature due to the steep gradients in the flame front.
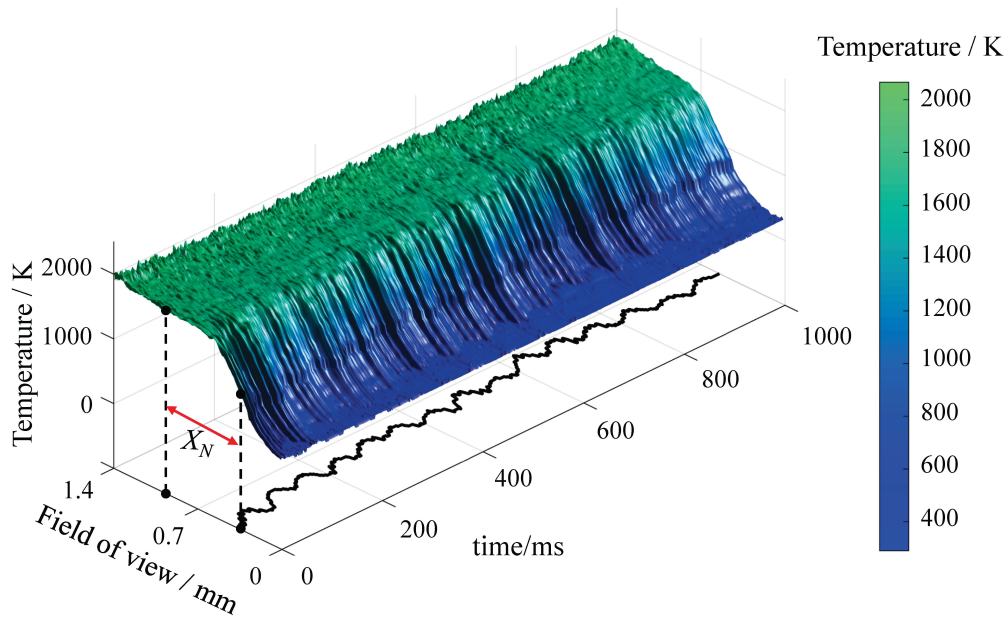
Figure 3.7: Spatiotemporal map of the temperature evolution across a laminar premixed CH$_4$/air flame. Temperature statistics are measured at a distance X_N conditional to the flame ignition point.
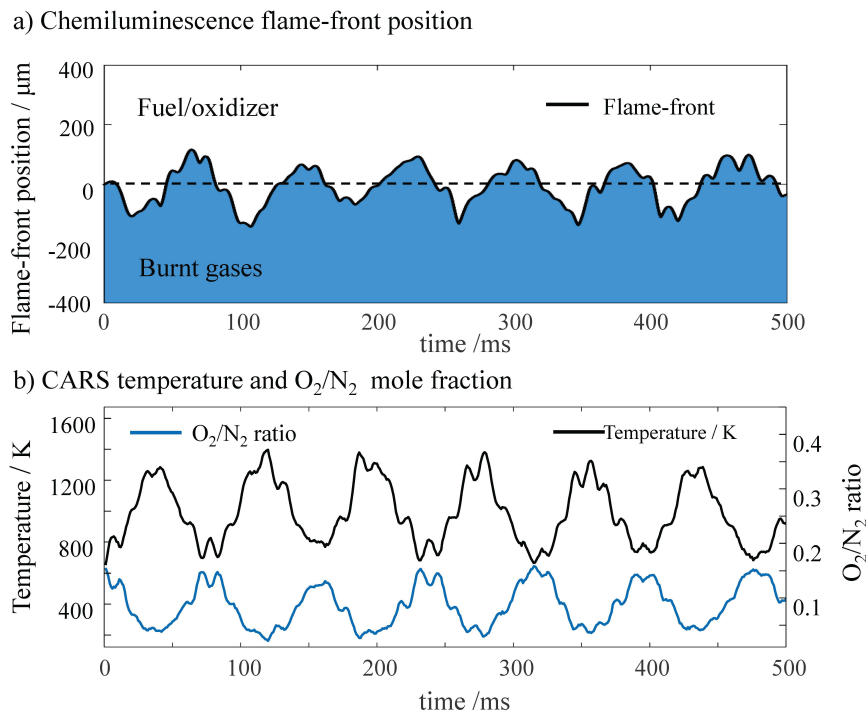
Figure 3.8: Harmonic oscillations of the flame front induced by unstable boundary conditions. (a) Spatial shift of the flame position measured using high speed chemiluminescence (b) Correlated temperature and O$_2$/N$_2$ concentration evolution obtained at an arbitrary fixed position on the reaction zone of the flame using spatiotemporal 1D-CARS.

When temperature statistics are evaluated at a fixed position above the burner rim (as in point-wise CARS) single-shot precision is significantly harmed. This happens, because in such cases, fluctuations in the flame-front position are not considered. To show this effect, Fig. 3.9(a) presents the assessment of the discrete probability density function (PDF) obtained at three arbitrary fixed positions within the flame front; the first one is located in the preheat zone at $\bar{T}$=400 K, the second one at the reaction zone ($\bar{T}$=1380 K) and the last one in the product gases ($\bar{T}$=1711 K). When the temperature is measured within the homogeneously distributed product gases, the influence of the flame flickering motion is minimal, and a relatively low standard deviation of ~2.5% is obtained. However, regions with steep temperature gradients (such as the reaction and preheat zones of the flame) yield a much wider spread in the probability density function (PDF) and thus a worst single-shot precision (12.5% and 16%, respectively). To improve the way single-shot precision of temperature measurements is obtained in such regions, it is necessary to use a more advanced methodology that takes into account physical fluctuations in the flame front position.

a) Point-wise CARS statistics (0-D)

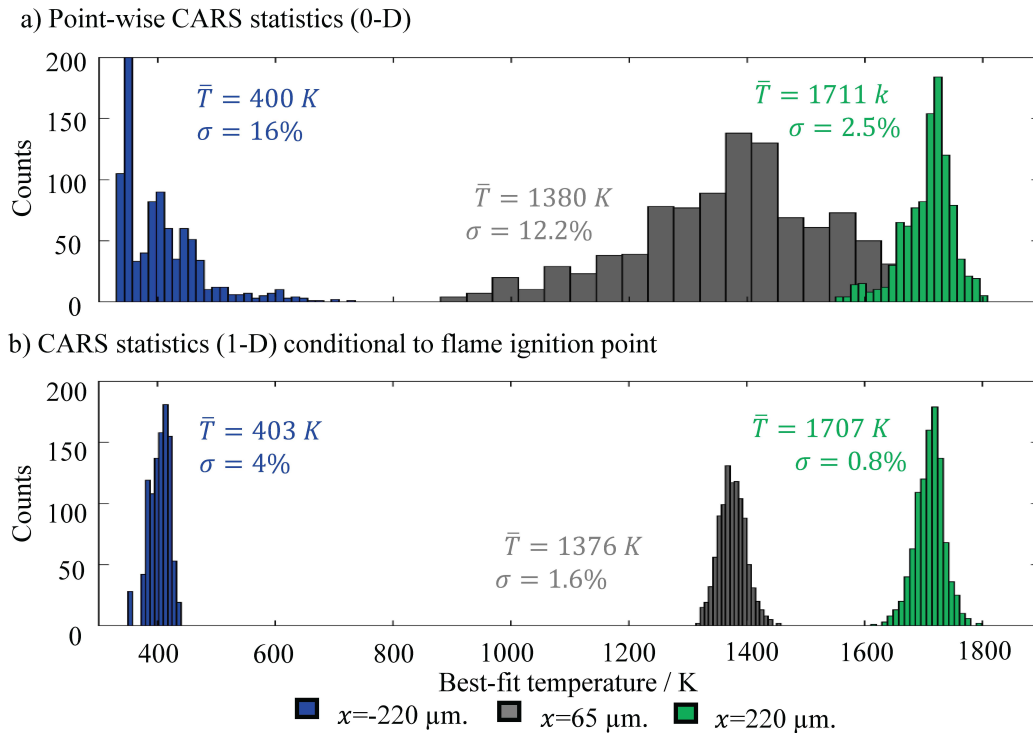b) CARS statistics (1-D) conditional to flame ignition point

Figure 3.9: Probability density functions of 1000 single-shot CARS images evaluated using (a) point-wise statistics at three fixed spatial positions within the field of view and (b) conditional to the flame ignition point.

In this thesis, the single-shot precision of temperature measurements is evaluated using a conditional statistical analysis that takes into account the harmonic oscillations of the flame. In this approach, temperature statistics are deduced relative to the flame ignition point defined, in the scope of this thesis, as the measurement point yielding the closest temperature to 1150 K. This value corresponds to the inflection point of the temperature profile across the reaction layer of the flame simulated using the CHEM1D numerical code. Figure 3.9(b) provides a discrete probability density distribution of 1000 samples for three different positions (x_1=-220 μm, x_2=65 μm, and x_3=220 μm), where the mean temperature is approximately the same as the three points previously discussed through point-wise statistics. The conditional statistical analysis leads to a significant improvement in the single-shot precision, particularly in the reaction zone, where the standard deviation reduces from 12.5% to approximately 1.6%. The remaining source of uncertainty in the single-shot precision analysis stems from shot-to-shot fluctuations on the instantaneous excitation bandwidth of the pump/Stokes pulse as well as from background noise detected at positions within the CARS image with low signal-to-background ratio, such as in the high-temperature product gases of the flame. In the central portion of the image, which exhibits the highest excitation efficiency and probe beam intensity, the precision of the current measurements is estimated to be approximately 0.7%.
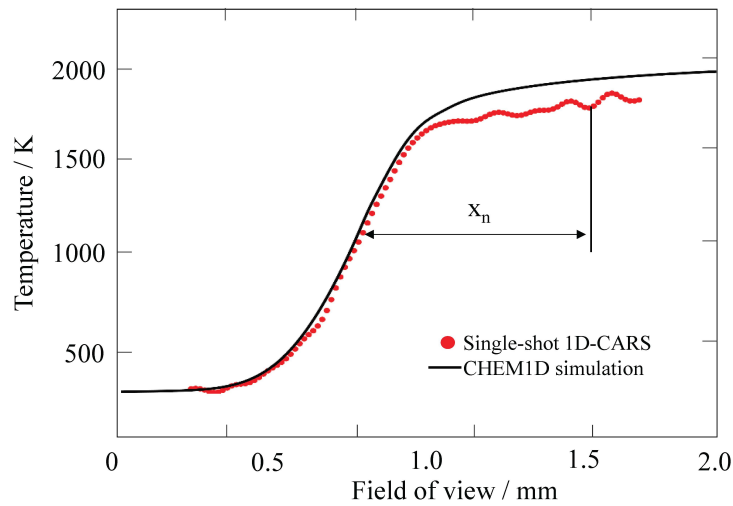
Figure 3.10: Conditional statistical analysis comparing the single-shot 1D-CARS temperature profile (depicted by red dots) against the CHEM1D model (depicted in black). The measurement uncertainty is assessed at a specific distance, denoted as x_n, relative to the flame's ignition point, corresponding to ~ 1150 K.

Similarly, the systematic error associated with CARS measurements is determined by evaluating the mean temperature ~220 μm conditional to the flame

ignition point. This value is then compared to the temperature expected for the specific flame conditions (equivalence ratio=0.9) calculated using CHEM1D (Fig. 3.10). As a result, the accuracy of the measurements is estimated to be ~2.5 %. The main contribution to this inaccuracy in this analysis arises from the uncertainty in the settings of the rotameter employed to control the fuel and oxidizer streams, resulting in slightly different conditions than those simulated by the numerical code.

Chapter 4

Spectral-phase characterization of SHBC picosecond pulses

The present chapter describes efforts to improve the performance of the fs/ps CARS system for flame diagnostics through a detailed spectral and phase characterization of the probe pulses. While the use of second-harmonic-bandwidth-compressors (SHBC) to generate narrow-band picosecond pulses offers significant advantages for efficient CARS generation, the reduction in pulse energy after filtering undesired spectral side-bands in the 4-f pulse shaper can introduce a systematic bias in flame thermometry. This bias arises from shot-to-shot noise fluctuations affecting spectra with low signal-to-background ratio. For instance, when the CARS signal is acquired in flames using a field of view larger than ~1.5 mm and when measuring the dephasing of the CARS signal at long probe delays. To address this issue, I developed a novel methodology to perform autocorrelation measurements of ps laser pulses using the non-resonant CARS signal. The measured spectrochronographic properties of the pulse are incorporated into the time-domain CARS model allowing operation without the 4-f pulse-shaper. The resulting synthetic CARS model accurately renders the additional modulation of the experimental spectra caused by the spectral sidebands, allowing for successful thermometry as shown by the experiments performed in a flow of N_2 and H_2 at room temperature.

4.1 The use of SHBC for CARS spectroscopy

In recent years, the use of SHBC to generate narrowband ps-pulses is taking hold in non-linear spectroscopy applications, owing to its simplicity, robustness, and relatively large conversion efficiency (~30%). Since the first proof-of-concept of this methodology [124] it has been extensively used in several laser diagnostics techniques including sum-frequency generation [125], stimulated Raman scattering [126] and in particular for hybrid fs/ps CARS.
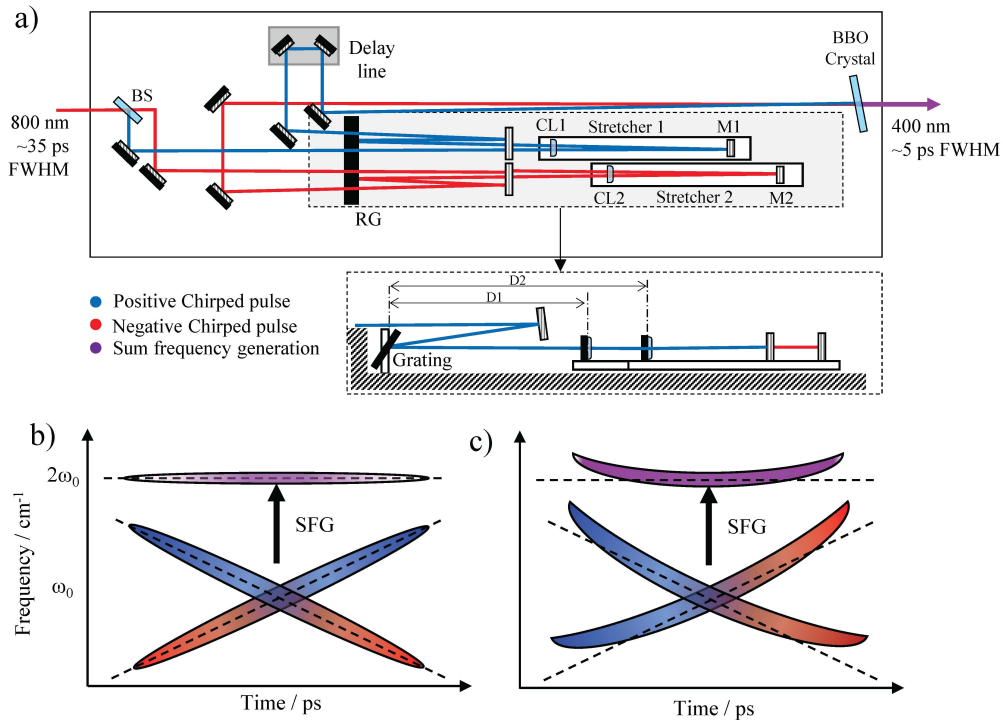
Figure 4.1: Schematic representation of the Second Harmonic Bandwidth Compression process. a) Optical setup: blue and red lines depict positively and negatively chirped beams generated by pulse stretchers 1 and 2, respectively. Index D1 and D2 represent the offset distance between the grating and the lens focal point which introduces the conjugated chirp between the beams. The pulses are synchronized in time using a delay line and then spatially overlapped at the Beta Barium Borate (BBO) crystal, producing the probe pulse. The optical components include Cylindrical lenses (CL1, CL2), Beam splitter (BS), Mirrors (M1, M2), and Reflection grating (RG). b) Sum frequency generation using oppositely chirped pulses: Ideal linearly chirped pulses on the left and pulses with non-linear chirp on the right.

In particular, this approach allows hybrid fs/ps CARS measurements to be performed with a single laser source, overcoming previous limitations of filtering shaping techniques that have generally resulted in prohibitively low probe energy. Kearney *et al*. [92] were the first to use an SHBC to produce ps-duration pulses for

flame diagnostics in pure-rotational hybrid CARS. Using a broadband 100 fs-duration input pulse, a 5.4 ps fwhm probe centered at 400 nm was produced with energies as high as 1.1 mJ/pulse. This allowed to have auto-synchronized pump, Stokes, and probe pulses generated at kHz repetition rate. Since then, several platforms have made use of this pulse shaping technique, especially for a flame [127] and plasma diagnostics [128] as well as in high-pressure (1-70 atm) gas-phase applications where sub-10 ps pulses are required due to the fast decay of the N_2 molecular coherence at these conditions [129]. One of the downsides of using SHBC, however, is the residual chirp that may remain in the compressed probe spectrum, preventing meaningful comparison between the experimental results and the simulated spectra.

In the SHBC unit employed in this thesis, sum-frequency generation is carried out by combining two femtosecond pulses with phase conjugate linear chirps in a non-linear Beta-Barium Borate (BBO) crystal. To generate the conjugated chirp pulses, the transform-limited femtosecond beam generated at the compressed output of the Astrella amplifier is split into two parts of equal energy. The maximum pulse energy of the input pulse should not be larger than ~4,5 mJ at 1 kHz repetition rate in order to avoid saturation and further damage of the BBO crystal. Each portion is directed to a folded 4-f pulse stretcher, composed of a single diffraction grating in reflection, a pair of cylindrical lenses, and two retro-reflector mirrors placed at the Fourier plane of each cylindrical lens. As shown in Fig. 4.1, positive (indicated in blue) and negative (indicated in red) chirp is imparted to the pulses by varying the distance ($D1$ and $D2$, respectively) between each lens with respect to the grating such as, $D1 < f_{CL1}$ and $D2 > f_{CL2}$ (f_{CL} is the focal length of the cylindrical lens). The second harmonic pulse is generated after overlapping the two pulses — in space and time— at the BBO crystal. As a result, a ps-pulse is generated at a frequency that is twice the input pulse, and the bandwidth is compressed by a factor of more than 30.

Unfortunately, numerous platforms have reported the appearance of sidebands in the compressed output spectrum stemming from high-order non-linearity on the chirp of the phase-conjugated pulses (Fig. 4.1(b)). Depending on the configuration of the SHBC set-up, the ensuing picosecond pulses may present high-order chirp in the time domain which causes a phase shift between the fundamental pulse and each of the sidebands. These sidebands can thus generate multiple CARS signals that beat in time and overlap with each other. Consequently, the modeling and temperature-fitting of these CARS signals become unachievable and overly complex. To address this issue, various types of optical filters can be deployed to

eliminate the sidebands created through the SHBC process to perform spectrally resolved CARS measurements. Examples of these filters include volume Bragg gratings (VBG) [130] and external *4-f* pulse shaper configurations [131,132]. An alternative approach is also to remove the non-linear components of the phase-conjugated pulses directly in the pulse stretcher of the SHBC unit before combining them on the non-linear crystal [133]. Nonetheless, in all of these filtering approaches, a significantly large portion of the available photons is wasted. In particular, in the *4-f* pulse shaper configuration employed in this thesis (see section 3.1.2), the filtering process led to a loss in probe intensity of ~70% limiting the probe energy to ~300-350 mJ/pulse. In high-temperature applications (>2000 K), this power reduction may impact the ability of the developed system to achieve a field of view larger than ~1.5 mm as reported in Paper I . Furthermore, this fact may also affect the strength of the CARS signal acquired at large probe delays (>300 ps) used to measure the concentration of water vapor adopting the methodology outlined in Paper II.

In this chapter, I propose to use the direct output of the SHBC —without filtering the probe spectral sidebands— in an effort to enhance the strength of the CARS signal which depends linearly on the probe pulse intensity. To achieve this objective, a detailed characterization of the spectral and phase properties of the probe pulse is performed. In this way, the effect of the sidebands on the signal can be simulated, enabling the fitting of both experimental and synthetic CARS spectra. This characterization is not trivial; to the best of the author's knowledge, there are not established methodologies that allow to measure the spectral-phase of ps-duration pulses. One of the main objectives of this chapter is to introduce a novel methodology that employs the non-resonant CARS signal to measure the relative phase between groups of frequencies in the SHBC probe pulse. Finally, this chapter also addresses the implications of this approach on the accuracy and precision of N_2 CARS thermometry.

4.2 Spectral and temporal shape of SHBC ps-probe pulses

Experimental information on the spectral and the temporal envelope of the probe pulse is required to model the time-domain CARS signal. As it was shown in Eq. 2.27, $E_{CARS}(t, \tau)$ is obtained as the product of the molecular response function and the square root of the time-dependent probe-pulse intensity I_{pr}. In this study, the probe spectrum is experimentally measured by directing a portion of the laser beam towards the coherent imaging spectrometer which is described in section 3.2. On the other hand, the temporal I_{pr} envelope is obtained by cross-correlation of the

probe pulse with the 35 fs-duration non-resonant CARS signal. Given that the non-resonant CARS only occurs when the pump/Stokes and probe pulses coincide in time, the time-dependent non-resonant signal strength is typically used to map the duration of the probe pulses.
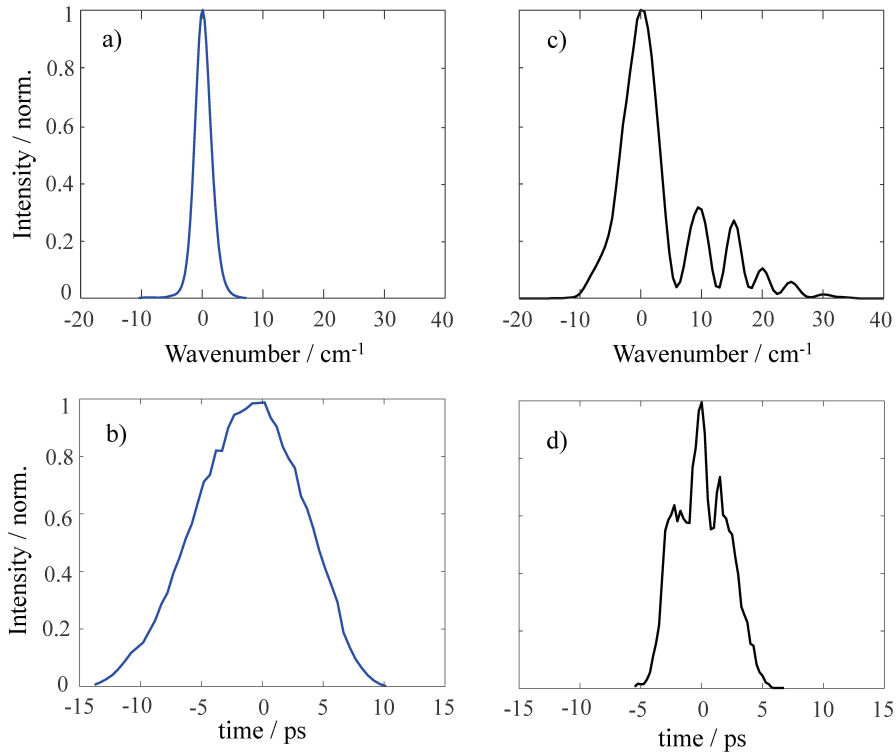
Figure 4.2: Spectral (black) and temporal (red) intensity of the SHBC-produced picosecond pulses. a) and b) The slit at the *4-f* pulse shaper is set to 150 μm resulting in a narrowband pulse of ~2.7 cm^{-1} fwhm and ~13 ps fwhm. In panels c) and d) the slit is opened and a set of five blue-shifted spectral peaks emerge, corresponding to a shorter pulse duration of ~6 ps fwhm.

Figure 4.2 presents a comparison between the spectral and temporal characteristics of the probe beam with and without filtering it with a tunable 4-*f* pulse shaper. To obtain a spectrally resolved pure-rotational N$_2$ CARS spectrum, the slit located at the Fourier plane is set to ~150 μm. This allows to filter out the blue-shifted sidebands generated by the probe pulse using the current SHBC configuration. This results in a narrowband pulse of ~2.7cm^{-1} fwhm bandwidth, centered at 402.3 nm.

In the time domain, the I_{pr} shows a good agreement with the anticipated time-bandwidth product calculated after de-convolving the measured spectrum from the instrument broadening function, resulting in a fwhm duration of ~13 ps.

Nonetheless, the presence of a hard edge introduced by the slit at the Fourier plane of the 4-*f* pulse shaper causes small ringing distortions in the probe temporal profile, which resembles the standard transform pair of a sinc function. These additional modulations need to be taken into account when selecting the probe delay to avoid interference with the non-resonant CARS signal. When the fs/ps CARS instrument is operated without using the 4-*f* pulse shaper (i.e. the slit is entirely open), a set of approximately five additional spectral peaks emerge in the spectrum, spanning roughly 30 cm^{-1}. As a result, the time-domain profile of the pulse can no be longer represented by the sinc^2 function. Instead, it presents an uneven envelope characterized by a multimodal profile. The asymmetry of this profile probably originates from the non-linear phase of the pulse imposed during the bandwidth compression process.

To accurately simulate the CARS signal generated when the slit is open (i.e. without operating the *4-f* pulse shaper), a precise characterization of the relative phase of these spectral side wings with respect to the fundamental peak of the probe pulse should be performed. The complex electric field of an optical pulse at a fixed position in space may be described as a sum of harmonic waves of frequency ω_n weighted by its amplitude A_n, as shown Eq. 4.1 [134].

$$E(t) = \sum_n A_n * e^{(\omega_n t + \phi_n)}$$

where ϕ_n represents the initial phase of the harmonic waves combined to create the pulse. Consequently, to adequately model the probe electric field, information about the intensity and the phase of the constituent frequencies forming the pulse must be measured.

Unfortunately, the procedure described above does not allow to quantify this information and more sophisticated methods had to be developed to establish the correlation between the frequency and temporal information encoded in the probe electric field, $E_{probe}(t)$. In this thesis, I developed a new methodology to characterize the spectral phase of the probe pulse which is otherwise difficult to obtain as there are not standard ways to measure it. This methodology involved two main steps. In the first one, the frequency content of the probe pulse was discretized into a fixed number (*n*) of equally spaced narrowband segments using the 4-*f* pulse shaper. The mechanical slit located at the Fourier plane, is used to sequentially scan segments of the pulse constituent frequencies, which are spatially distributed along the horizontal beam axis. Figure 4.3(a) presents a comparative analysis between the

spectral intensity of the probe pulse when the slit is open (dashed grey line) and the resulting frequency segments as measured with the coherent imaging spectrometer.
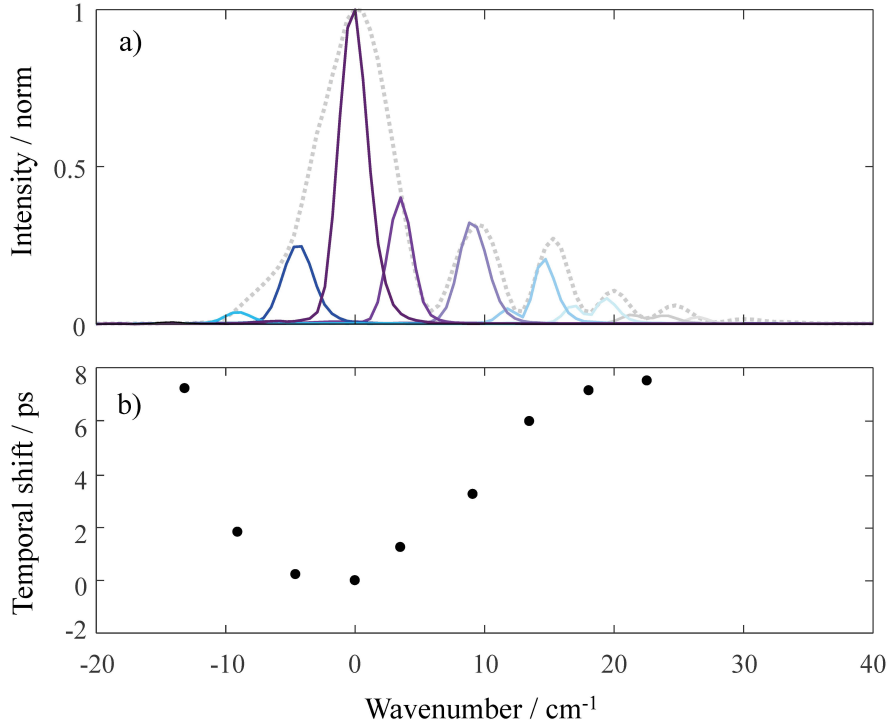

Figure 4.3: a) Comparison between the spectrum of the unfiltered probe pulse (Gray dashed line) and the corresponding frequency segments (indicated by colors) selected with the slit in the *4-f* pulse shaper. b) The relative arrival time of the resulting pulse created at each frequency segment with respect to the fundamental peak, obtained by mapping the corresponding non-resonant CSRS signal intensity in time.

The high dispersion (i.e. 3600 lines/mm) of the transmission grating employed on the pulse shaper allows discretizing the pulse into *n=9* independent segments of $\Delta\omega_n \sim 2$ cm^{-1} fwhm bandwidth. The selected number of segments guarantees a high spectral resolution while preventing contamination from the light scattered at the slit edges when the aperture is below ~40 µm

Once this is done, the temporal shift between each group of frequencies is characterized. This is achieved by measuring the arrival time $\tau_0(\omega_n)$ of each of the discretized pulses, with respect to the fundamental probe peak centered at 402.3 nm. The arrival time is obtained from the time-dependent intensity of each of the pulses which is mapped using the integrated non-resonant spectrum. In this set of experiments, the same set-up described in paper I of this thesis for pure-rotational spatiotemporal CARS was employed. However, in this particular investigation, the O-branch instead

of the S-branch signal was acquired (i.e. the coherent Stokes Raman scattering signal (CSRS)). As can be seen in Fig. 4.2(b) the spectral sidebands appear on the high frequency side of the fundamental probe peak. Consequently, these sidebands overlap with the low Raman-shifted transitions of the S-branch spectrum. The intensity of these sidebands is significantly stronger than the CARS signal itself, making it impossible to acquire the pure-rotational spectrum of molecules such as N_2 and O_2 without risking damaging the sCMOS sensor.

The non-resonant CSRS spectrum was generated across a one-dimensional field-of-view of ~1,4 mm in a thin BK7 glass plate. The advantage of using a solid sample in this experiment is that intensity fluctuations caused by beam-steering are significantly dampened as compared to more common methods in which the signal is generated in a flow of a non-resonant gas such as argon. In this way, uncertainties in the retrieval of the pulse temporal shape caused by fluctuations in the intensity of the non-resonant spectrum might be minimized. A probe delay scan was performed by acquiring a set of 500 non-resonant CSRS spectra in steps of 250 fs at each slit location. In Fig. 4.3(b) the resulting arrival time of each of the discretized frequency segments is presented. As can be seen, the proposed methodology provided sufficient sensitivity to resolve the temporal shift between the different groups of frequencies selected for this experiment. A strong non-linearity in the phase relationship between the generated pulses is observed, indicating that the direct pulse produced by the SHBC is significantly stretched in time and therefore cannot be described as a TL pulse.
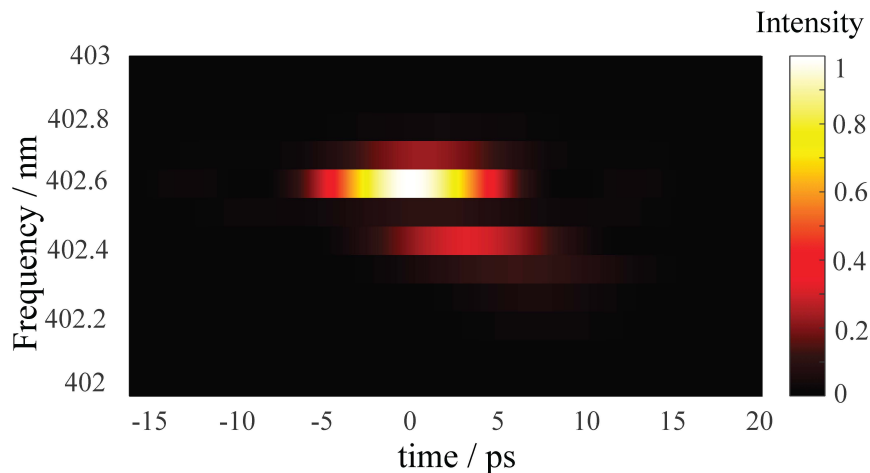

Figure 4.4: Picosecond probe pulse spectrogram reconstructed using the methodology developed in this thesis. The color-coded representation illustrates the intensity of the electric field at each frequency over time.

The resulting temporal dependence of the discretized pulse frequencies and their relative intensity measured in the aforementioned steps is further used to reconstruct the probe pulse electric field, following Eq. 4.1. The pulse is generated synthetically by first adding sinusoidal waves of equal intensity at the different frequencies ω_n contained in the bandwidth transmitted at each slit position and attributing the initial phase. This phase is nothing more than the relative arrival time of the pulses with respect to the fundamental peak. A set of nine pulses are consequently generated, corresponding to each frequency segment selected with the slit. Secondly, each of the resulting pulses is weighted by the relative amplitude $A_n = \sqrt{I_n}$, calculated as the square root of the measured spectral intensity. Finally, the electric fields of all frequency segments are linearly added, generating an interferogram that gives rise to the reconstructed probe pulse. Figure 4.4 presents a synthetic pulse spectrochronogram simulated using the spectral phase properties obtained using the aforementioned methodology.

4.3 Validation of the results

The accuracy of the results obtained in the characterization of the probe spectral phase is validated by generating the pure-rotational CSRS signal in a flow of room-temperature nitrogen as well as in an unreacted flow of hydrogen.
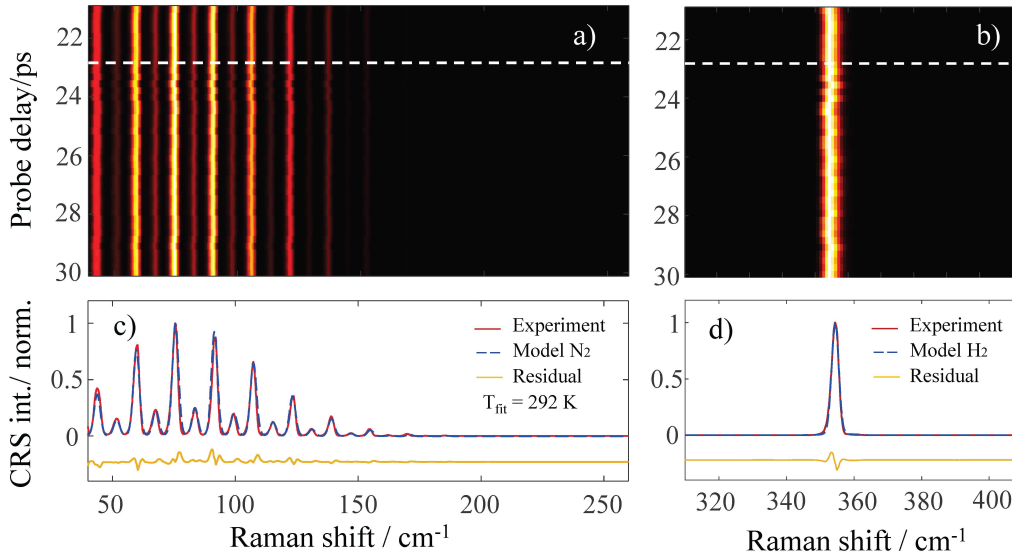

Figure 4.5 Spectrochronogram of the pure-rotational CSRS signal of a) N_2 and b) H_2 acquired experimentally after passing the probe pulse through the *4-f* tunable pulse shaper. c) and d) best-fit between the averaged experimental spectrum and the time-domain CSRS model for a probe delay of 23 ps.

These experimental spectra are then fitted to a theoretical library in which the synthetic probe electric field reconstructed in Fig. 4.4 is used to compute the CSRS electric field. For this purpose, two cases were investigated. In the first one, the *4-f* pulse shaper is used to filter out the probe pulse sidebands by selecting a narrow portion of the fundamental spectral peak. In this way, the probe pulse is near transform-limited, generating a CSRS spectrum with nearly isolated lines. In the second case, the slit is completely opened and therefore the CSRS signal is produced using the direct output of the SHBC without filtering. In both cases, a probe delay scan is performed acquiring 40 data sets of 1000 single-shot CSRS images every 250 fs in the range of 20-30 ps.

Figure 4.5 presents the experimental spectrochronogram map obtained from the N_2 spectra acquired in the range of ~40 to 250 cm^{-1} as well as for the O(2) H_2 transition located at 354 cm^{-1}. This dataset pertains to one specific location within the CSRS image where the probe spectral phase characterization was conducted. Additionally, Fig 4.5(c) and (d) present the fit between the experimental spectrum obtained at an arbitrary probe delay $\tau = 23$ ps and the theoretical spectra generated using the time-domain CSRS model. As it can be observed, upon filtering out the sidebands, it becomes evident that the O-branch transitions in the N_2 spectrum are nearly isolated. Consequently, the spectra exhibit minimal changes over time, which indicates that in this configuration, the probe pulse is close to transform limited and the CSRS model can accurately quantify the temperature of the gas flow. Similarly, the shape of the H_2 transition, which is isolated from other spectral lines, remains constant over time.

In contrast, a marked difference becomes apparent when the slit is open, especially in the N_2 resonant spectra. Figure 4.6(a) shows the spectrochronogram of the N_2 CSRS signal acquired for the same probe delay range as in the previous case. The N_2 CSRS signal produced by the SHBC's direct output exhibits a complex temporal interference pattern. This results from line mixing between even and odd rotational Raman transitions as well as the beating between the signals produced by the different spectral sidebands, which are generated at a different time with respect to the fundamental probe peak. As a consequence, minimal changes in the probe delay induce substantial variations in the spectral shape. The periodicity of this beating pattern corresponds to the characteristic revival period in the N_2 molecular response which is ~8.38 ps at ambient temperature. Overall, it can be seen that the reconstructed chirped probe pulse included in the time-domain CSRS model can successfully capture the influence of the probe sidebands on the shape of the N_2 spectra to a good extent. While the quality of the fit might be different depending

on the probe delay used to acquire the signal, it is sufficiently accurate to perform quantitative measurements with a high degree of confidence. This results in an accuracy better than ~1, with respect to the reference temperature value, defined as the temperature measured with the filtered probe pulse. On the other hand, the H_2 spectrum is characterized by the appearance of additional spectral peaks toward higher frequencies. These peaks correspond to blue-shifted H_2 CRSR signals generated at the different carrier frequencies of the probe sidebands. The shape of this peak closely mirrors the shape of the probe spectrum used in the experiment. As opposite to N_2, the H_2 spectrum does not beat in time, and the model is also able to accurately predict the shape as a function of probe delay.
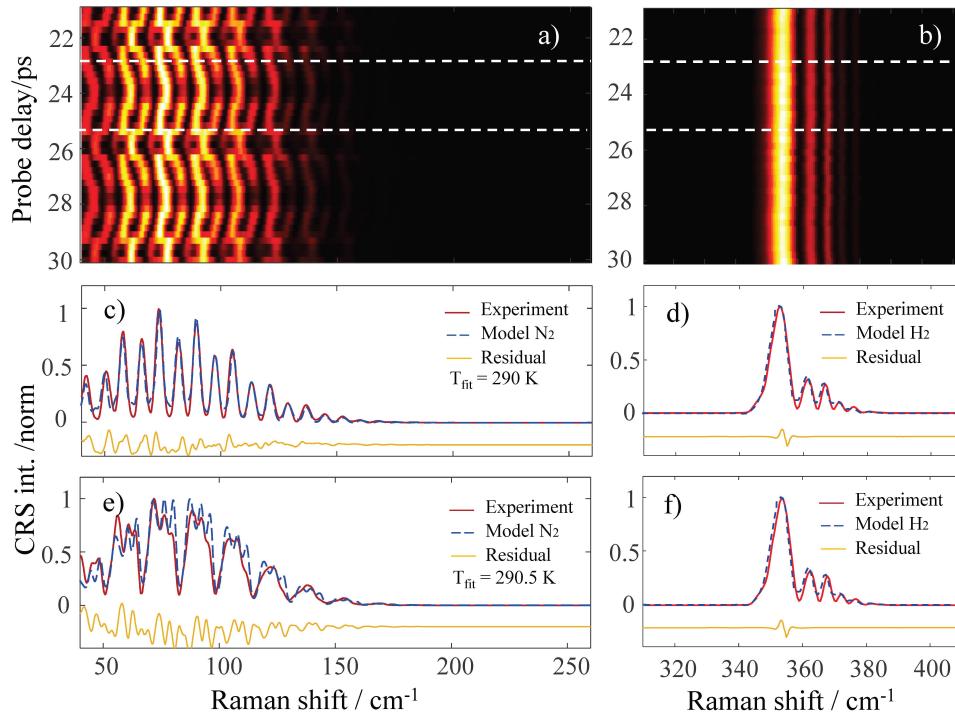
Figure 4.6: Spectrochronogram of the pure-rotational CSRS signal of a) N_2 and b) H_2 acquired experimentally using the direct SHBC's pulse output. The experimental fs/ps N_2 CSRS spectrum is affected by a severe beating of all the spectral lines, due to the unresolved transitions between the many rotational energy states populated at this temperature and the non-linear chirp of the pulse. In comparison, the O(2) pure rotational Raman transition of H_2 displays minimal temporal beating, and its spectral shape closely mirrors the probe pulse spectrum. Panels c) to f) depict the best-fit between the experimental spectrum and the time-domain CSRS model, with the reconstructed probe pulse included, at probe delays of 23 ps and 25.5 ps.

To quantify the effect of the additional probe's photon content on the signal strength, a comparative study of the signal-to-background ratio (SBR) of the acquired pure-rotational N_2 spectra was performed using both the filtered and the

unfiltered probe pulses. When the unfiltered probe is used to generate the signal – opening the slit in the *4-f* pulse shaper– the energy per pulse increases roughly by a factor of three from ~350 μJ/pulse to ~950 μJ/pulse. While, the strength of the coherent Raman signal, scales linearly with the probe pulse intensity, due to the extreme temporal beating of the N_2 spectra observed using the direct output of the SHBC, it is not straightforward to predict if this linear relationship still holds. Constructive and destructive interference may affect the signal strength depending on the probe delay and the molecule being probed. Figure 4.7(a) shows the normalized SBR of the peak with the highest intensity within the N_2 spectra as a function of time for the two evaluated cases. For the filtered probe case, this peak corresponds to the O-branch transition located at 71.5 cm^{-1}. In the unfiltered probe case, the peak with the highest intensity is not fixed and varies between different Raman shift locations depending on the probe delay. As expected, the signal generated using the unfiltered pulse presents a periodic fluctuation in intensity. The
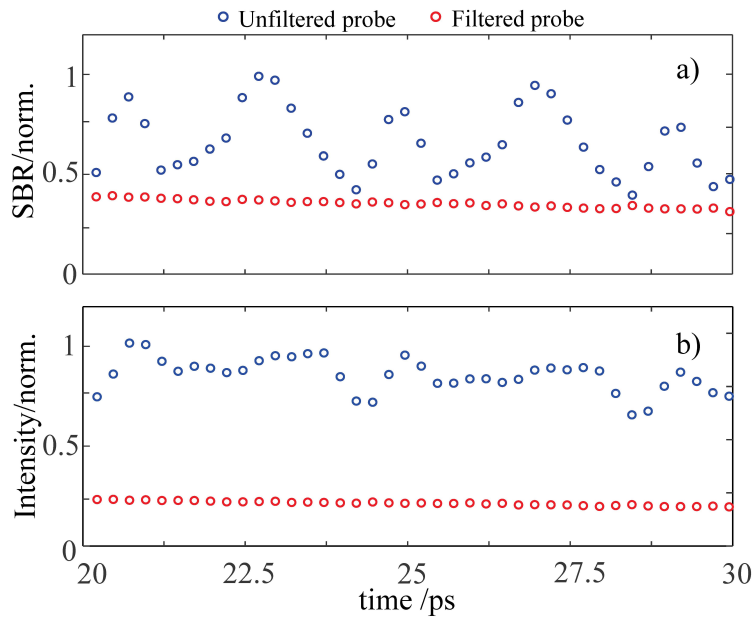
Figure 4.7: Comparison between the strength of the fs/ps CSRS signal obtained experimentally using the direct SHBC's pulse output (represented by blue open circles) and the pulse filtered using the *4-f* pulse shaper (represented by red open circles) as function of probe delay. a) Evaluation of the relative signal to background ratio (SBR) of a single peak within the pure-rotational N_2 spectra with the highest intensity. b) Relative intensity of the integrated spectrum at each probe delay for the two evaluated cases.

overall SBR varies according to the beating period of the signal and is between ~1.1 and ~2.5 times higher than the signal generated using the filtered probe pulse.

Furthermore, a comparative analysis of the strength of the integrated signal generated using both filtered and unfiltered probe beams was also performed. In time-resolved CARS, the integrated CARS signal is typically used to measure the dephasing rate of the molecular Raman coherence caused by collisions between the molecules present in the probe volume. As can be seen in Fig. 4.7(b), the integrated signal generated with the unfiltered probe pulse is ~4 times higher than the one generated when the sidebands are filtered. Therefore, the implementation of this methodology could present significant advantages for dephasing measurements which usually struggle to obtain sufficient signal strength at large probe delays, especially in high-temperature environments such as flames.

Chapter 5

Water vapor concentration measurements using time-resolved CARS

In this chapter, I introduce a new detection strategy to measure the concentration of water vapor in hydrogen flames via the time-resolved measurement of the collisional dephasing of the nitrogen CARS signal. The rotational Raman coherence of the N_2 molecules, induced by the interaction with the pump and Stokes laser fields, dephases on a timescale of hundreds of picoseconds (ps), mostly due to inelastic collisions with other molecules in atmospheric flames. The presence of water vapor in the flame results in faster dephasing of the N_2 coherence compared to other major combustion species. The dephasing rate of the N_2 coherence can thus be used to determine the concentration of water vapor. To demonstrate the applicability of this methodology, sequential measurements of the exponential decay of the N_2 CARS signal are performed up to 360 ps across the flame front of a laminar H_2/air diffusion flame. Temperature and the relative O_2/N_2 and H_2/N_2 concentrations are measured at a short probe delay, and the results are input into the time-domain model to extract the H_2O mole fraction. As water vapor is the only major product of combustion in hydrogen flames, its concentration is an essential scalar for characterizing the flame's structure. With the implementation of this methodology, all major scalar flow fields across the flame can be simultaneously measured providing valuable insight into the underlying physics of molecular mass transport processes occurring during the chemical reaction.

Part of the results discussed in this chapter haven been published in paper II

5.1 Water vapor diagnostics in combustion environments

A recognized challenge for absolute concentration measurements in combustion environments is to detect water vapor. This combustion species is typically probed using absorption spectroscopy [135] rather than Raman-based techniques, owing to its relatively low Raman cross-section [136]. However, an inherent drawback of absorption spectroscopy is the limitation to line-of-sight measurements. In this regard, non-linear optical diagnostics prevail because they can provide *in-situ* H_2O measurements with spatial resolution. O'Byrne *et al.* [137] employed CARS to measure the temperature and the mole fractions of nitrogen (N_2), oxygen (O_2), and hydrogen (H_2) in a supersonic combustor and estimated the H_2O concentration by assuming it to be the only other major species contributing to the non-resonant susceptibility of the gas-phase medium. Direct measurements of the ro-vibrational CARS spectrum of the H_2O *v1* symmetric stretch at ~3650 cm^{-1} were first attempted by Hall *et al.* [138] in 1979. Hall and Sherley [139], as well as Porter and Williams [140] performed ro-vibrational H_2O CARS thermometry at temperatures as high as 2000 K. Greenhalgh *et al.* [141] also investigated the H_2O *v1* CARS spectrum at high temperatures and elevated pressures. Despite the good agreement shown by the experimental data and the theoretical CARS models, further studies on this spectrum were scarce, probably owing to the isolated location of the H_2O *v1* spectrum beyond the vibrational fingerprint region, which hinders the simultaneous detection of multiple species. In a recent work conducted by Nishihara *et al.* [142], for the first time, the relative concentrations of H_2/N_2, O_2/H_2, and H_2O/H_2 were measured in a plasma-stabilized hydrogen diffusion flame using dual-pump ns-CARS. While successfully obtaining these measurements, the necessity for multiple combinations of laser dyes to generate the ro-vibrational CARS signal for each molecule led to separate sequences of measurements. In this sense, a more efficient strategy would be shifting towards the pure-rotational CARS spectrum of water vapor as multiple species could be acquired simultaneously on a single-shot basis, providing a more comprehensive understanding of combustion dynamics.

The use of the pure-rotational Raman spectra of water vapor for flame diagnostics, however, poses a number of theoretical and experimental difficulties. Some of them have been detailly addressed in the work of Avila *et al.* [143]. Even though the pure-rotational H_2O spectra can be detected within the same spectral region as N_2, the usual reference molecule, the integrated intensity of the spectrum at room temperature is approximately 4-5 orders of magnitude weaker. This is primarily due to the small anisotropy of its molecular polarizability as well as the larger number of rotational transitions that the molecule undergoes. Furthermore,

due to its asymmetric top structure and the three different rotational constants of H_2O, it is more difficult to simulate high-temperature spectra in flames. Nordström *et al.* [64] have recently examined the applicability of pure-rotational CARS for high-temperature diagnostics. Unfortunately, they concluded that H_2O is an unsuitable candidate for CARS concentration measurements in combustion. The extreme dimness of the pure-rotational H_2O CARS signal and the strong non-resonant contribution made it impossible to detect the signal even using considerably long integration periods.

In this thesis, I proposed the use of time-resolved CARS to measure the H_2O mole fraction in hydrogen flames through its impact on the pure-rotational N_2 spectrum. As Nordström *et al.* pointed out in the conclusion of their work, despite its CARS spectrum being negligible, water vapor has a significant collisional impact on the N_2 CARS spectrum. Rotational energy transfer in inelastic collisions between the coherently excited N_2 molecules and other molecules results in the temporal dephasing of the pure-rotational N_2 CARS signal on a time scale of picoseconds (ps) at ambient conditions. This dephasing can be measured by employing ultrashort laser pulses (fs/ps) to resolve the temporal evolution of the Raman coherence thus measuring the RET in the time domain.

5.2 Dephasing of the N₂ CARS signal

The evolution of the induced Raman coherence is determined by the interference of the Raman modes corresponding to transitions from different *J*-states as well as by the dephasing coefficients associated with the transition. Due to symmetry constraints, the natural decay lifetime of N_2 is on the order of seconds [144], so it can be neglected in this discussion. Similarly, the effect of pure dephasing due to elastic collisions ($\Delta J = 0$) can be neglected at ambient pressure [144]. The main contribution to dephasing thus stems from inelastic collisions ($\Delta J \neq 0$), responsible for the RET between the coherently excited N_2 molecules and the molecular perturbers in the flame. In this work, the dephasing of the N_2 CARS signal due to collisions takes into account the following perturbers: N_2-N_2 (i.e. self-perturbed) [117], N_2-O_2 [145], N_2-H_2 [146], and N_2-H_2O [112]. Figure 5.1 shows the corresponding state-dependent dephasing coefficients of N_2 perturbed by these molecules for $J = 0$-60. While the N_2-N_2 and N_2-O_2 coefficients show comparable *J*-dependence, owing to the similar rotational energy manifold, both N_2-H_2 and N_2-H_2O coefficients show peculiar trends over the different *J*-states and have an overall larger magnitude. The *J*-dependence of the N_2-H_2 coefficients is less pronounced than for the other collisional partners, due to the large spacing between the states in

the rotational energy manifold of H_2, resulting in a similarly reduced RET for all the J-states of the N_2 molecule. On the other hand, the overall large magnitude of these coefficients is explained by the larger thermal velocity of the lightweight H_2 molecule, allowing it to penetrate closer to the repulsive wall of the interaction potential with the N_2 molecule [146]. The N_2-H_2O dephasing coefficients are characterized by a strongly non-monotonic J-dependence, with a temperature-dependent local maximum (e.g. $J = 24$ at 1600 K), which is attributed to the complex structure of the rotational energy manifold of the H_2O molecule. This results in a strong dependence of the RET on the initial rotational state of the N_2 molecule [112].
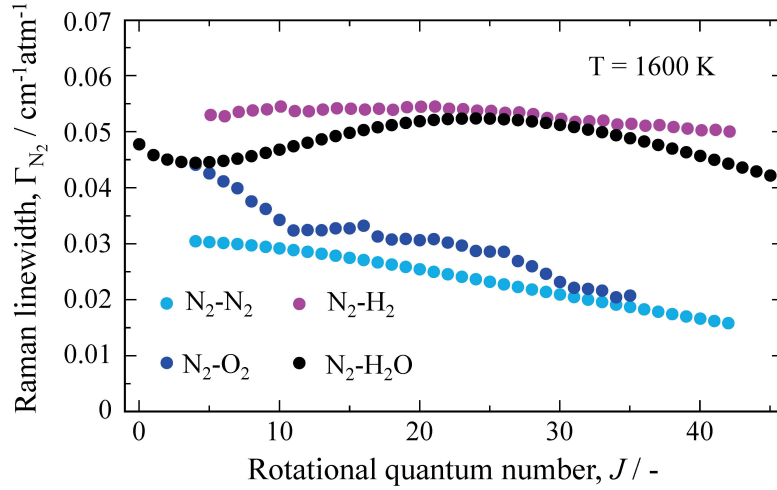
Figure 5.1: The J-dependence of the species specific N2 CARS dephasing coefficients for inelastic collisions with major combustion species in H_2/air flames, including N_2, O_2, H_2 and H_2O at a temperature of 1600 K.

In the flame, the total N_2 dephasing coefficients can be computed using Eq. (2.22) introduced in section 2.2.1:

$$\Gamma_{J \to J+2}^{k} = \sum_{p} X_p \cdot \Gamma_{J \to J+2}(M_k - M_p) \qquad (2.22)$$

where $\Gamma_{J \to J+2}$ are the dephasing coefficients due to collisions of N_2 with the kth perturbers, weighted by its mole fraction X_p. This equation introduces the dependence of the N_2 CARS signal on the presence of H_2O, which is employed to measure the H_2O concentration (X_{H2O}). In this context, the collisional environment can be interpreted as an equivalent binary system composed of H_2O on one hand,

and a weighted combination of all other perturber species whose concentration is directly measured in the frequency domain (i.e. X_{N_2}, X_{O_2} and X_{H_2}) on the other.

$$\Gamma^{N_2}_{J \to J+2} = \sum_{k'} X_{k'} \cdot \Gamma_{J \to J+2}(N_2 - M_{k'}) + X_{H_2O} \cdot \Gamma_{J \to J+2}(N_2 - H_2O) \qquad (5.1)$$

The proposed diagnostic approach can thus be employed to measure the X_{H_2O} in all combustion environments where the concentration of every other relevant collisional partner is accessible in the CARS spectrum.
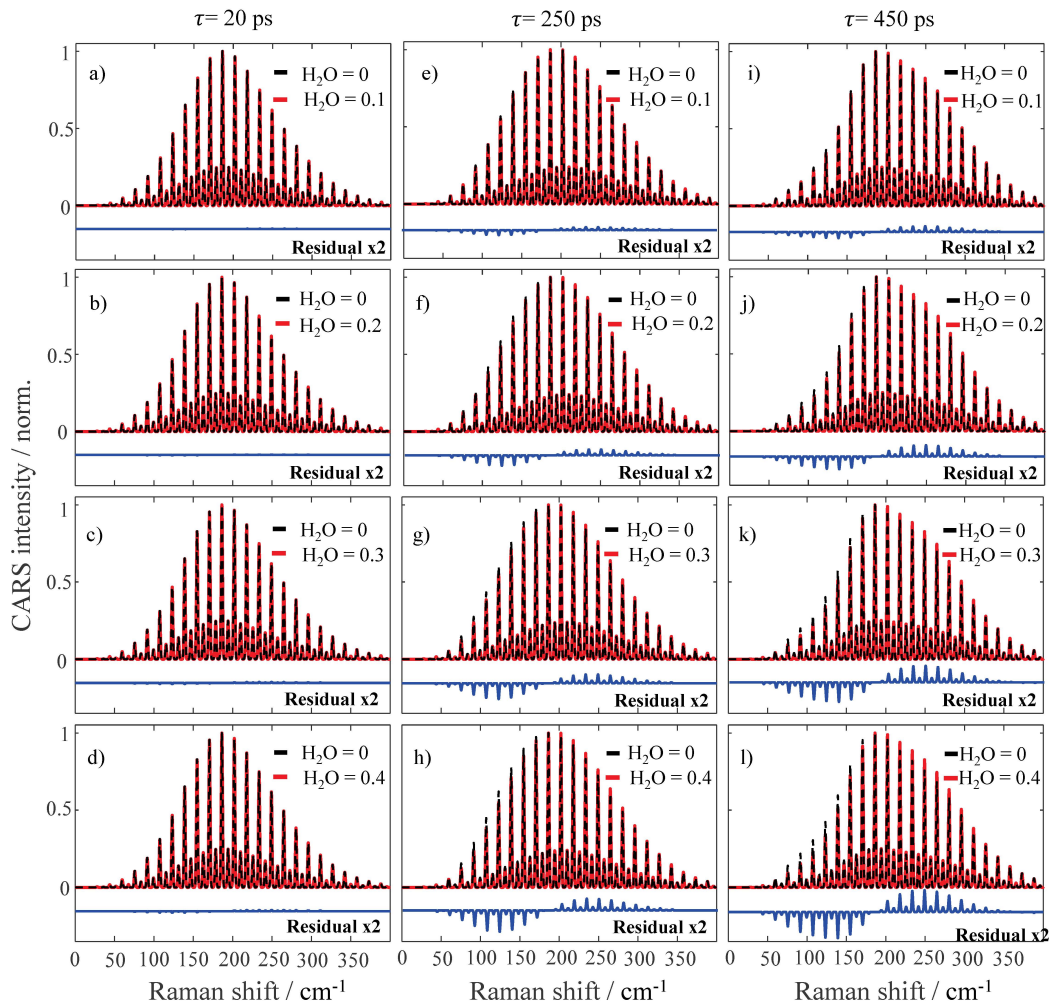
Figure 5.2: Dependence of the N_2 CARS spectrum to inelastic between N_2-N_2 and N_2-H_2O. Simulated pure-rotational spectrum of pure N_2 at flame temperature T=1600 K. Spectral heating is observed as both the concentration of water vapor and the probe delay are systematically increased.

The inelastic collisions between N_2 and H_2O can affect the pure-rotational N_2 CARS signal in two distinct ways. Firstly, the shape of the spectrum can be altered due to the J-dependence of the combined collisional dephasing coefficients N_2-N_2 and N_2-H_2O. As the probe delay increases, the intensity of low Raman transitions decays faster than higher transitions proportionally to the H_2O mole fraction in the gas mixture. Secondly, a change in the overall decay of the integrated signal intensity can occur, arising from the $\exp\left[\left(i\omega_{J\rightarrow J+2} - \Gamma_{J\rightarrow J+2}\right)t\right]$ factor in Eq (2.16). While either of these two dependence mechanisms may be utilized to estimate the concentration of water, it is not straightforward to determine which one is more suitable for flame studies.

To gain further insights into the influence of water vapor on the pure-rotational N_2 CARS spectrum, a synthetic analysis was conducted using the time-domain CARS code and taking into consideration the N_2-N_2 and N_2-H_2O dephasing coefficients. Figure 5.2 illustrates the dependence of the N_2 CARS spectral shape to the presence of water vapor for three distinct probe delays of $\tau = 20$, 250, and 450 ps at a temperature of T=1600 K. In each of these cases, X_{H_2O} is stepwise increased from 0 up to 0.4. In each of the insets, the residual represents the difference in the shape of the spectrum for a given condition as compared to pure nitrogen. As it can be seen, at the shortest probe delay (i.e. $\tau = 20$ ps) the spectrum is not significantly impacted by the presence of water in the gaseous mixture. Therefore, temperature measurements can be performed without concern for inelastic collisions influencing the results. However, at larger probe delays, an increased shifting in the relative intensity of the peaks within the N_2 CARS spectrum is observed when the water concentration increases, giving the impression that the spectrum originates from higher-temperature gases. This phenomenon, however, is solely attributable to the effects of inelastic collisions between N_2 and H_2O due to the J-number dependence of the dephasing coefficients of the molecules involved. The H_2O mole fraction can thus be obtained by measuring the temperature of the gas mixtures at a short probe delay and then fitting the spectra obtained at longer probe delays to a synthetic library of spectra generated for the measured temperature.

Furthermore, the sensitivity of the time-dependent N_2 CARS signal strength to the presence of water vapor concentration was also investigated. The exponential decay of the integrated signal intensity was obtained synthetically by integrating the N_2 CARS spectra generated at T=1600 K in a binary mixture of N_2 and various concentrations of water vapor. Figure 5.3 shows a comparison between the normalized dephasing curves obtained by integrating the intensity of the pure-

rotational spectrum of N_2 in the range of $20 < \tau < 370$ ps. As it can be seen, water induces an overall faster decay of the CARS signal due to the larger magnitude of the N_2-H_2O dephasing coefficients in comparison to N_2 self-perturbed ones. At the evaluated temperature, this decay scales roughly as $1/e^{x_{H2O}}$. An advantage of this approach is that it is significantly less sensitive to temperature fluctuations. In stable laminar flames, the dephasing can be measured by acquiring sequentially the CARS signal at various probe delays.
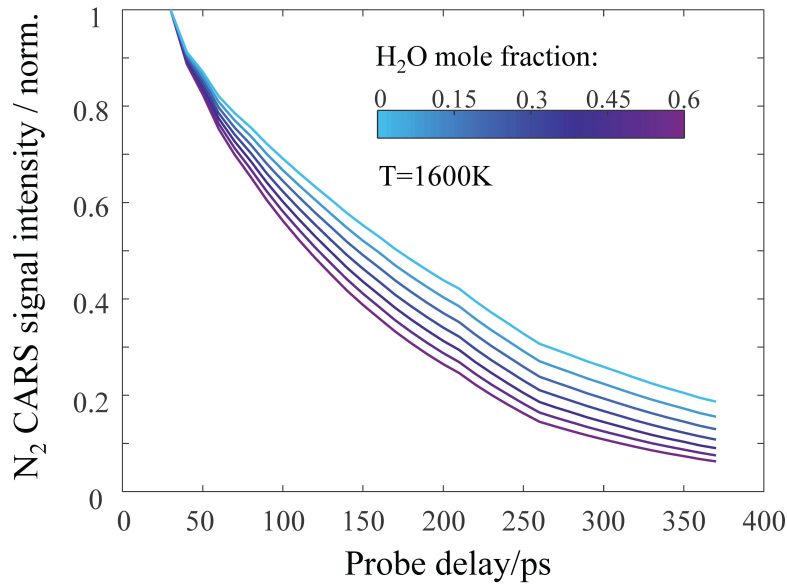
Figure 5.3: Simulated exponential decay of the integrated N_2 CARS spectrum calculated for a binary gas mixture of N_2 and H_2O at T= 1600 K, in the range of $20 < \tau < 400$ ps. In this simulation, the H_2O mole fraction progressively increases (from blue to purple) from $X_{H_2O} = 0$ up to $X_{H_2O} = 0.6$ in steps of 0.1. A faster decay of the N_2 CARS signal is observed as the concentration of water vapor increases. The impact of water vapor is more pronounced at lower concentrations, a evidenced by the distinct 'squeezing' of the decay curves at larger X_{H_2O}.

I applied this approach to measure the signal dephasing of the N_2 CARS signal at different locations across the flame front of a laminar H_2 diffusion flame. This served as a proof of concept for the feasibility of the technique. Nonetheless, it is noteworthy that in the case of more dynamic applications such as turbulent flames, scalars usually present shot-to-shot fluctuations and multi-probe schemes may be still required to obtain single-shot information about the dephasing of the N_2 CARS signal.

5.3 Water vapor concentration detection strategy

The proof-of-principle demonstration of H_2O concentration measurements was performed by measuring the dephasing rate of the N_2 CARS signal in a laminar H_2/air diffusion flame shown in Fig. 5.4(a). This flame serves as an ideal test scenario for the technique as the product gases are composed of a binary mixture of N_2 and H_2O at high temperatures. Furthermore, the composition of other major species, such as H_2 and O_2, along the flame can be quantified in the frequency domain by acquiring their pure-rotational spectra.
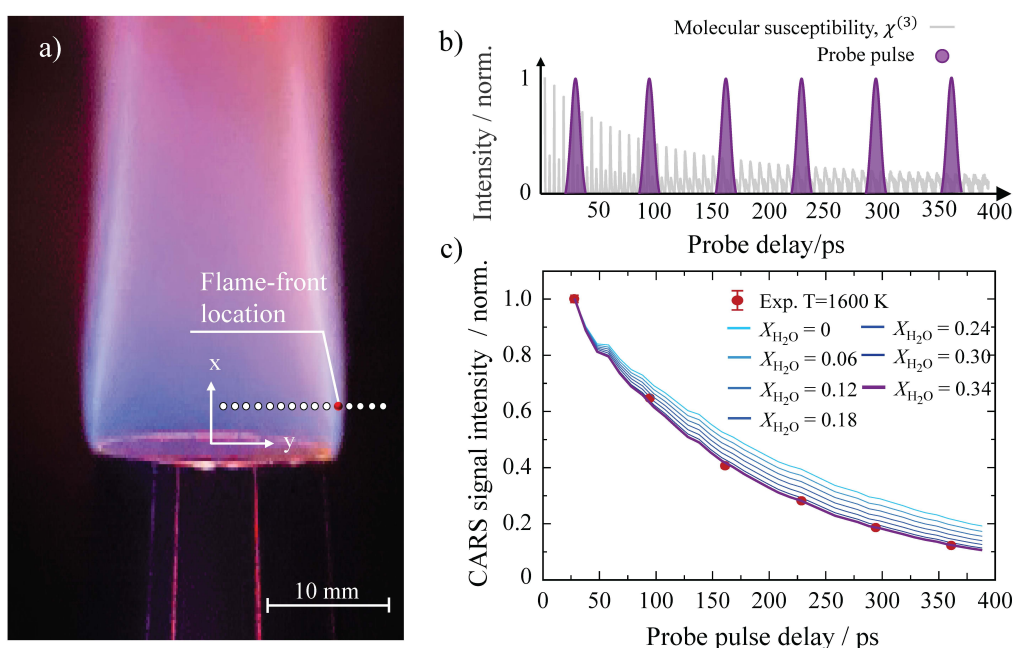
Figure 5.4: Proof of concept of the proposed methodology for water vapor concentration measurements. a) Picture of the laminar diffusion H_2/N_2/air flame stabilized in a Bunsen burner used to test this methodology. The white dotes represent the location of the measurements performed at x=1 mm above the burner rim from y=0 mm (fuel stream) to y=12 mm (oxidizer stream). b) Illustration of the evolution of the N_2 molecular susceptibility and the corresponding probe delay scan performed to measure the collisional decay rate. c) Fitting procedure of the collisional dephasing of the N_2 CARS signal measured experimentally at one location within the reaction zone of flame with the highest water vapor concentration. The experimental decay (red dots) is compared to a library of simulated dephasing curves generated for the temperature measured at short probe delay to extract the H_2O mole fraction.

The burner utilized in the experiment is a seamless, stainless steel pipe with ~19 mm inner diameter. A mixture of N_2 and H_2 in a 50% - 50% volume ratio is introduced with a bulk velocity of around 1 m/s, resulting in a Reynolds number of

less than 150. To stabilize the flame, a stainless steel mesh is positioned at a height-above-the-burner (HAB) of approximately 30 mm.

The two-beam fs/ps CARS system used in this study is described in greater detail in chapter 3 and only specific details for this experiment are outlined as follows. The probe pulse duration is set by adjusting the slit width at the 4-f filter. This corresponds to a ~12 ps FWHM with ~300 μJ/pulse. For the combined fs pump/Stokes pulse, an 800 nm half-wave plate and a thin film polarizer are used to attenuate the pulse energy to ~60 μJ/pulse to prevent fs laser-induced filamentation [147]. This was verified by performing a power scaling of the N_2 CARS signal at room temperature: at this fluence level, no change in the spectral envelope was observed. Spherical optics (f:=500 mm and 300 mm, respectively) focus the pump/Stokes and probe beams to the measurement location, and the crossing angle for the two-beam phase-matching configuration is estimated to be ~3°, resulting in the following probe volume dimensions: ~22 μm (height) x ~1.1 mm (length) x ~22 μm (width). The pump/Stokes and probe pulses are therefore automatically synchronized, and an automated delay stage (sub-10 fs resolution, Thorlabs) is employed to precisely control the relative probe pulse delay. A wedge prism is inserted in the pump/Stokes beam path after the probe volume, and the low-power reflection is imaged onto a beam profiler (WinCamD, Dataray) in the far field to monitor and maintain the alignment of the pump/Stokes beam when moving the delay stage.

Point-wise (0-D) CARS measurements were performed at a location ~1 mm HAB, with a radial scan conducted from the center of the burner (y = 0 mm) extending to the rim, and data points were acquired at intervals of 0.5 mm up to y = 12 mm. At each measurement location, 6 datasets of 1000 single-shot CARS spectra were acquired for a probe delay varying from 30 to 360 ps (Fig 5.4(b)). The spectra obtained at the lowest probe delay were employed to measure the temperature and the relative O_2/N_2 and H_2/N_2 concentrations. Neglecting the effect of collisions at the short probe delay timescale leads to an inaccuracy of less than ~0.8% in the estimated temperature: the CARS signal generated at this delay is thus assumed as nearly collisional independent. By integrating the N_2 CARS signal acquired at the longer probe delays, the collisional dephasing was measured and compared to the single-exponential decay model in Eqs. (2.22) and (5.1) to extract the H_2O mole fraction. Figure 5.4(c) shows the experimental dephasing measured at one location within the reaction zone compared to the theoretical dephasing curves predicted by the time-domain N_2 CARS. The red dots represent the signal dephasing at y=9.5 mm (at 1 mm above the burner rim), where the H_2O mole

fraction is measured to be 0.34 according to the best-fitting curve: a large sensitivity to the H_2O concentration is shown by the significant bias between the experimental data and the theoretical dephasing predicted for $X_{H_2O} = 0$.

5.4 Temperature and chemical composition fields

The methodology just explained allows to measure the whole temperature and chemical composition fields across the flame front. The resulting experimental profiles for the temperature and the mole fractions of O_2, H_2, and H_2O are presented in Fig 5.5.
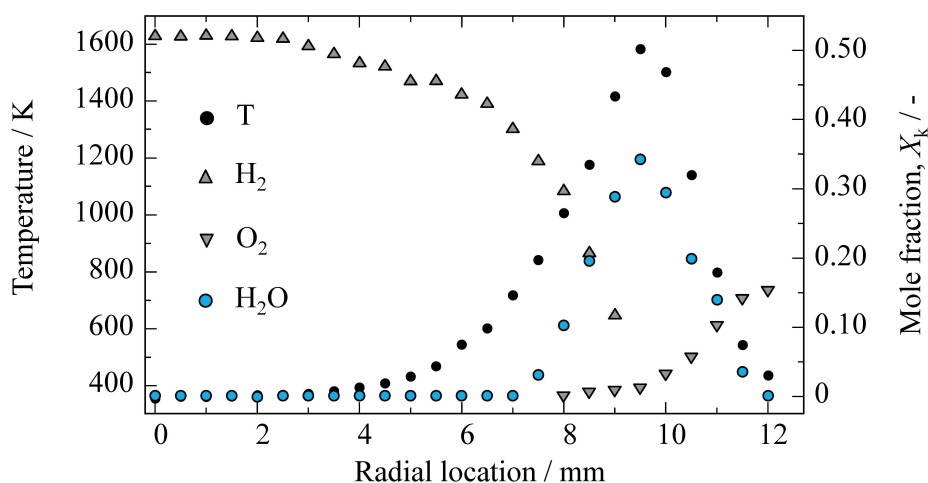
Figure 5.5: Experimental temperature and mole fraction profiles for the major combustion species obtained along the flame front of a laminar H_2/air diffusion flame. The H_2O mole fraction at x =1 mm is detected within the range X_{H_2O} = 0.03-0.34 in the reaction zone spanning y = 7.5-11.5 mm.

As it can be seen, the temperature smoothly increases from ∼360 K in the fuel stream at the center of the burner (y = 0 mm), peaking to 1620 K above the burner rim (y = 9.5 mm), and decreases more rapidly in the lean reaction zone, reaching ∼440 K in the oxidizer stream at y=12 mm. The good single-shot precision of the CARS thermometry, varying in the range of 0.8–3.7% in the high-temperature reaction zone, indicates a limited impact of the temperature fluctuations on the signal intensity, thus justifying the use of sequential measurements of the collisional dephasing. The H2 mole fraction decreases from ∼52% in the fuel stream at the center of the burner as the mixing and chemical reaction progress toward the burner rim. The simultaneous detection of the pure-rotational N2 CARS spectrum and of two rotational lines of the pure-rotational H2 CARS spectrum, namely S(0) at 354 cm-1 and S(1) at 587 cm-1, allows for measuring the relative H2/N2 concentration

at temperatures as high as 1450 K at location y = 9 mm. The O_2 mole fraction, on the other hand, smoothly grows from 0.01 measured at y = 8 mm up to 0.15 at the last measurement location in the oxidizer stream. The relative standard deviation of the measured mole fractions of H_2 and O_2 is, respectively, lesser than 2.5 and 8% at all measurement locations. H_2O is detected in the reaction zone, for y = 7.5–11.5 mm, with a maximum mole fraction of 0.34 at y = 9.5 mm.

The uncertainty in the measured H_2O concentrations is mostly due to shot-to-shot fluctuations in the temperature and flow composition. This was assessed by propagating the uncertainty in the measured temperature and relative O_2/N_2 and H_2/N_2 concentrations and fitting the experimental data to the corresponding limit curves for the theoretical dephasing. The relative uncertainty in the H_2O mole fraction is thus estimated to be < 8% at all measurement locations, with the sole exception of $y = 10.5$ mm, where the relative uncertainty is 15%, corresponding to a measured H_2O mole fraction in the range 0.18–0.21. The temperature and mole fraction profiles in Fig. 5.5 are in good qualitative and quantitative agreement with those reported by Toro *et al*. for a similar laminar H_2/air diffusion flame [148] and show the effect of preferential diffusion of H_2 in the fuel stream. In the region $y = 2.5$–6.5 mm, the H_2 mole fraction reduces from 0.52 to 0.42, while no water vapor is detected, and the temperature is only slightly increasing due to heat transfer from the reaction zone, yet remaining below the auto-ignition threshold. The simultaneous resolution of the local temperature and composition fields thus allows us to render the physics of mass transport in the laminar diffusion flame.

5.5 Water vapor concentration in an equivalent ternary collisional system N₂-N₂, N₂-H₂O, and N₂-CO₂

In the previous section, it was discussed that the collisional environment in a hydrogen/air flame can be interpreted as an equivalent binary system composed of N_2-H_2O on the one hand, and a weighted combination of all other perturber species whose concentration is directly measured in the frequency domain (i.e. N_2-N_2, N_2-O_2, and N_2-H_2) on the other.

This has led to a straightforward implementation of the methodology proposed in the previous section of this thesis to detect water vapor from the dephasing of the N_2 CARS signal in the time domain. However, it is not yet clear whether the same methodology can be extended to more complex collisional environments with the presence of a third collisional system (i.e. N_2-CO_2) in which the concentration of the perturber cannot be detected with pure-rotational fs/ps CARS. Such a collisional environment is often found in the product gases of a typical hydrocarbon flame, where CO_2 can reach up to ~10% mol fraction. Similar to water vapor, the concentration of CO_2 in flames is difficult to measure directly in the frequency domain using its pure-rotational Raman spectrum due to the low Raman cross-section of this molecule. The pure-rotational CO_2 spectrum can instead complicate temperature measurements obtained from the pure-rotational N_2 spectrum, especially for Raman shifts below 100 cm^{-1} [149]. When compared to N_2-N_2 and N_2-H_2O, the amplitude and J-dependence of the dephasing coefficients for N_2-CO_2 are significantly different. Consequently, the presence of CO_2 in the probe volume could potentially impact the accurate detection of water vapor in a hydrocarbon flame.
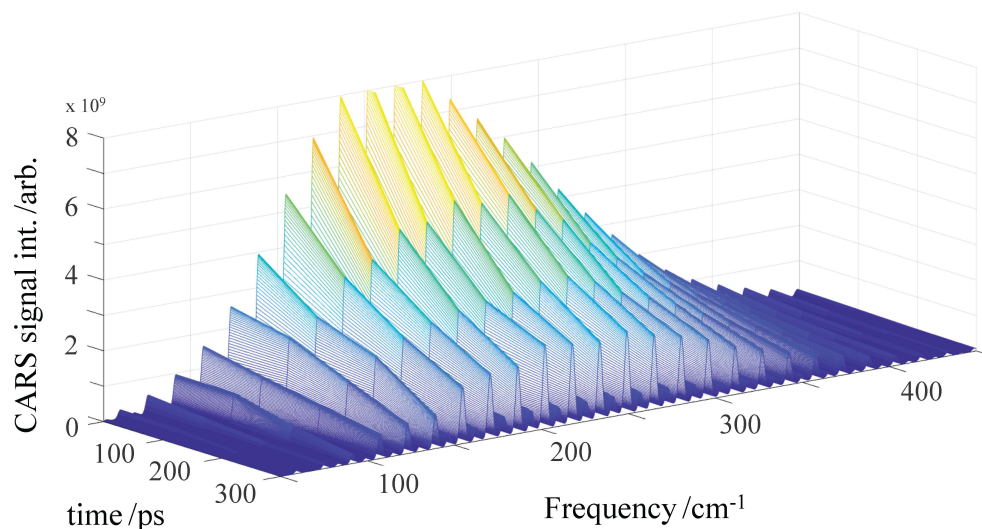
Figure 5.6: Evolution of the N_2 CARS spectra simulated under representative conditions for the product gases of a premixed a CH$_4$/air flame: T=2100 K, X_{H_2O}=20% and X_{CO_2} =10%.

To investigate this complex interaction, I performed a numerical investigation of the effects of N_2-CO_2 inelastic collisions on the determination of water vapor concentration in hydrocarbon flames. This was done by simulating the time-dependent N_2 CARS spectra at conditions typically found on the products of a

stoichiometric CH_4/air flame at atmospheric conditions (i.e. T=2100; X_{H_2O}=0.2). The time-domain CARS model introduced in section 2.2.1 was used to generate the pure-rotational CARS spectra of N_2 at the given conditions for multiple probe delays in the range of 20-470 ps.
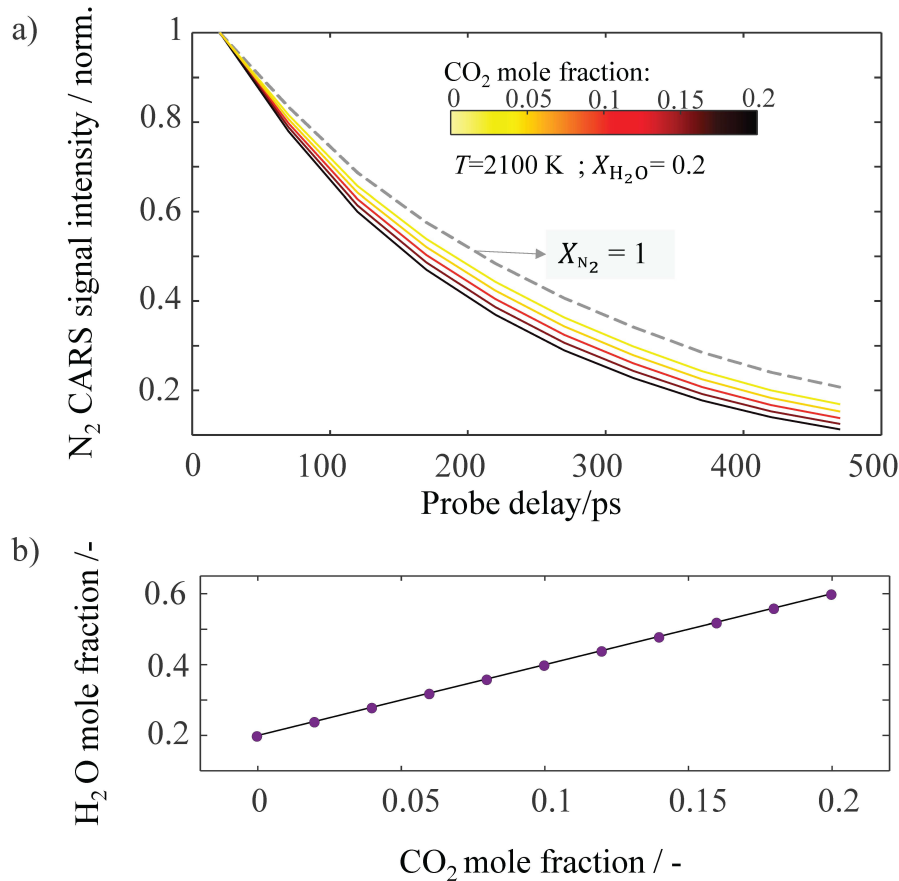
Figure 5.7: a) Simulated exponential decay of the integrated N_2 CARS spectrum in a ternary mixture of N_2, H_2O, and CO_2 at flame temperature T=2100 K and X_{H_2O}=0.2. In this figure, the CO_2 mole fraction progressively increases (from yellow to black) from X_{CO_2}= 0 up to X_{CO_2}= 0.2 in steps of 0.05. A faster decay of the N_2 CARS signal is observed as the concentration of CO_2 increases. For comparison, the grey dashed line represents the decay of pure nitrogen $X_{N_2} = 1$ b) Potential overestimation of the water vapour concentration predicted when the CO_2 mole fraction cannot be measured directly in the frequency-domain using fs/ps CARS.

To model the evolution of the N_2 molecular coherence in time, the dephasing coefficients of N_2-N_2 [117], N_2-H_2O [112] and N_2-CO_2 [150] were included in the model following Eq. 5.2.

$$\Gamma_{J \to J+2}^{N_2} = X_{N_2} \cdot \Gamma_{J \to J+2}(N_2 - N_2) + X_{H_2O} \cdot \Gamma_{J \to J+2}(N_2 - H_2O) \qquad (5.2)$$
$$+ X_{CO_2} \cdot \Gamma_{J \to J+2}(N_2 - CO_2)$$

A sensitivity analysis was then performed, generating each set of CARS signals with different amounts of CO_2 concentrations (X_{CO_2}) while keeping the temperature and water vapor mol fraction fixed. In this way, the effects of N_2-CO_2 collisions are isolated. Figure 5.6 shows an example of the N_2 CARS spectrochronogram generated for one of the evaluated cases corresponding to T=2100 K, X_{H_2O} =20% and X_{CO_2} =10%. The RET caused by inelastic collisions between the simulated species is manifested both in the decay of the intensity of each rotational transition as a function of time and in the shape of the spectrum due to the difference in the dephasing rate of each of the Raman transitions.

Following the methodology described in section 5.3, a first numerical experiment was performed exploring the sensitivity of the CARS signal intensity to inelastic collisions between the evaluated molecules. The signal simulated at each probe delay was spectrally integrated, thereby yielding the exponential decay of the signal in time. Figure 5.7(a), presents the decay of the spectrally integrated CARS signal in an equivalent ternary collisional system (i.e. N_2-N_2, N_2-H_2O, and N_2-CO_2) for T=2100 K, $X_{H_2O} = 0.2$ and X_{CO_2} varying in the range of 0-0.2. As it can be seen, the time-domain N_2 CARS signal is highly sensitive to the presence of CO_2 within the gaseous mixture, causing the Raman coherence to decay faster. Unfortunately, this dependence implies that if the concentration of CO_2 in the gas mixture is unknown, a significant bias of X_{H_2O} would occur. To quantify this bias, a library of theoretical dephasing curves was created using the time-domain CARS model for T= 2100 K, assuming $X_{CO_2}= 0$ and instead varying X_{H_2O} . Subsequently, each of the exponential curves depicted in Fig. 5.7(a) were fitted to this library using a simple sum-square residual routine. Figure 5.7(b) shows the resulting concentration of water vapor estimated as a function of CO_2 concentration in the mixture. It can be seen that as expected when X_{CO_2} increases, the model predicts a linear overestimation of X_{H_2O}. In the products of a hydrocarbon flame where CO_2 can be found to be X_{CO_2}~10% of the molecular composition of the mixture, X_{H_2O} might be overestimated up to twice their true value from X_{H_2O}=0.2 to X_{H_2O}=0.4.

Furthermore, a second numerical experiment was performed, this time using the *J*-dependence of the CARS spectra to inelastic collisions in the ternary mixture. To do that, the pure-rotational N_2 spectra were simulated for the same conditions as

in the previous case (i.e. T=2100 K and X_{H_2O}=0.2) replicating the temperature and composition of the product gases of a hydrocarbon flame. For this purpose, only the long probe delay τ =470 ps CARS signals were considered, assuming that at this delay the dephasing is significantly manifested in the change of the spectral shape.
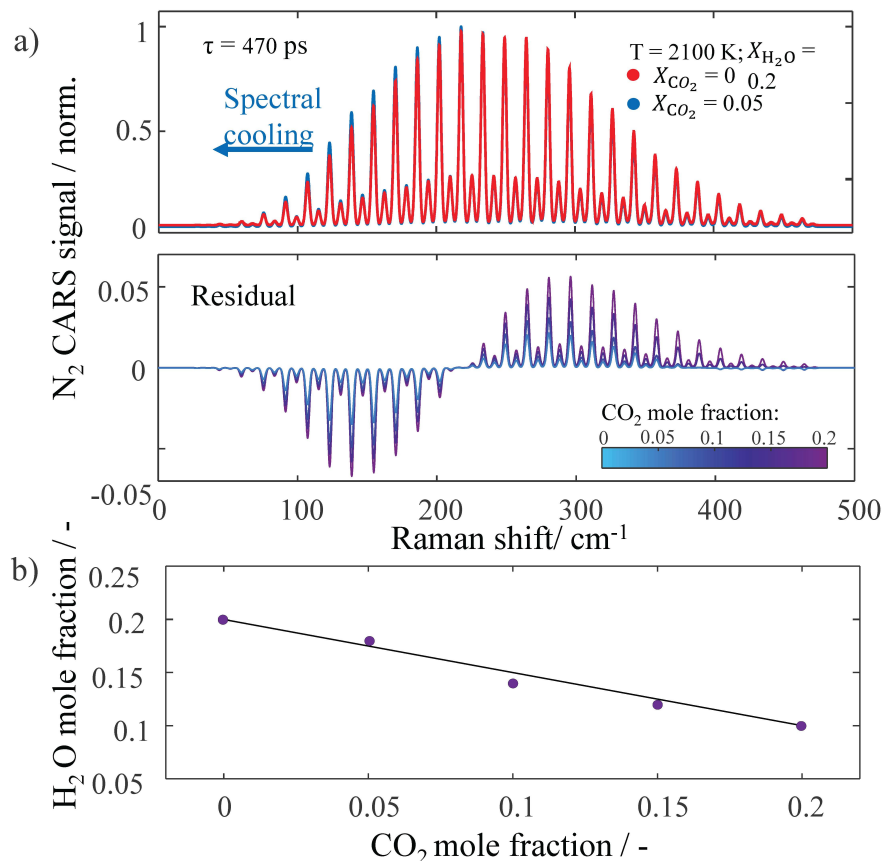
Figure 5.8: Sensitivity of the N_2 CARS spectrum to inelastic collisions with N_2 (i.e. self-perturbed), H_2O and CO_2. a) Simulated pure-rotational spectrum of N_2 for T=2100 K and X_{H_2O}=0.2 at a probe delay τ =470 ps. Two different CO_2 concentrations in the gas mixture are displayed (X_{CO_2}=0 and X_{CO_2}= 0.05). Spectral cooling is observed in N_2 spectrum with increasing CO_2 concentration as evidenced on residual plot which result from subtracting the spectrum computed for X_{CO_2}= 0 from the spectra where X_{CO_2}> 0. b) Potential underestimation of the water vapour concentration predicted when the CO_2 mole fraction cannot be measured directly in the frequency-domain using fs/ps CARS.

To illustrate this, Fig. 5.8 presents the change in the spectrum envelope for various levels of X_{CO_2} in the gas mixture. As it can be seen, when X_{CO_2} increases, the spectrum reassembles that of a colder temperature. Even if this difference may

not appear to be as severe as when the signal is spectrally integrated, this methodology may still bias the measurement of H_2O in the flame. To quantify this bias, each of the simulated spectra was fitted to a library of N_2 CARS spectra generated for the given temperature, assuming that there is no CO_2 in the mixture and therefore dephasing is caused solely by RET between N_2-N_2 and N_2-H_2O. These results are presented in Fig. 5.8(b). As it can be seen, when the concentration of CO_2 is unknown, water vapor is considerably underestimated. The concentration of water vapor estimated in a hydrocarbon flame can be up to 25% lower than the true value. This suggests that in order to make this technique work for hydrocarbon flames, it is imperative that X_{CO_2} can be measured simultaneously in the flame.
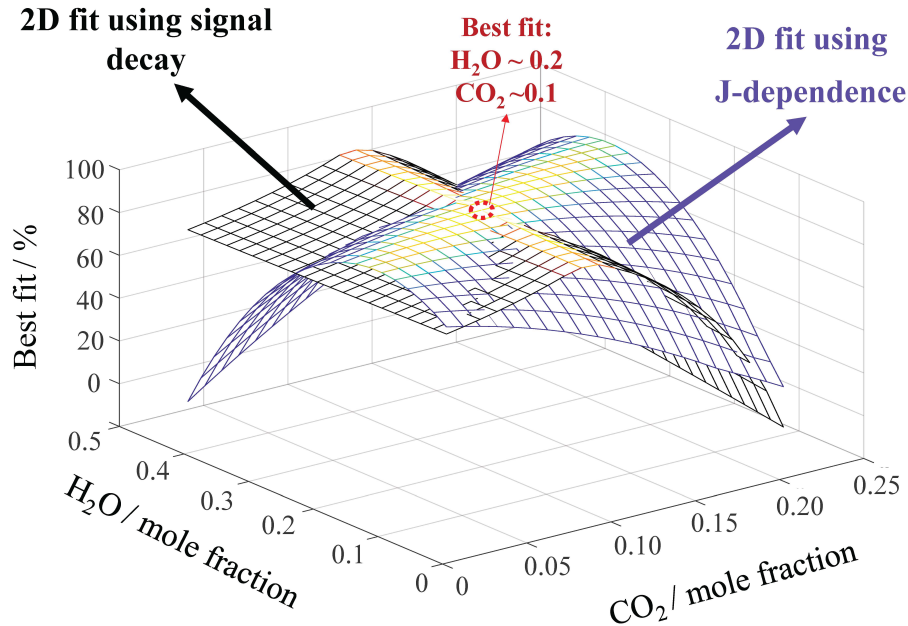
Figure 5.9: Two-dimensional fit of H_2O and CO_2 concentration obtained independently by using both the *J*-dependence (depicted in blue) and exponential decay (depicted in black) of the CARS signal for a synthetic spectrum of N_2 simulated at the conditions expected in a hydrocarbon flame (i.e. T=2100 K, X_{H_2O}= 0.2 and X_{CO_2}=0.1) in the range $20 < \tau < 470$ ps. By combining these two methodologies, a solution for the two unknown scalars can be obtained.

Nonetheless, the fact that N_2-CO_2 inelastic collisions have a large impact on the time-domain N_2 CARS signal can potentially be used to measure simultaneously X_{CO_2} and X_{H_2O} in a flame. This can be achieved by employing a two-dimensional fitting routine in which X_{CO_2} and X_{H_2O} are estimated from the combined sensitivity of the CARS signal to inelastic collisions both on the change of the spectral envelope at long probe delays (i.e. *J*-dependence) and on the exponential decay of

the spectrally integrated signal. To test this hypothesis, the procedure used in Case A and Case B was repeated, this time using a two-dimensional library generated for T=2100K, X_{CO_2} and X_{H_2O}. Figure 5.9 presents the best fit obtained independently using the J-dependence (blue curve) and exponential decay (black curve) for the evaluated case. As it can be seen, in both methods, various combinations of X_{CO_2} and X_{H_2O} are possible for the given dephasing rate of the signal. Therefore, it is virtually impossible to obtain a single solution to the problem using each of them independently. However, when both methods are applied the solutions converge and it might be possible to deduce X_{CO_2} and X_{H_2O} simultaneously.

A more detailed investigation should be performed in order to verify the feasibility of using the time-domain N_2 CARS signal for the determination of the concentration of two distinct species simultaneously. This methodology thus opens a new field for further research into the prospects of measuring the concentration of more species by leveraging the sensitivity of fs/ps CARS signal to RET between molecules in gas-phase reacting environments.

Chapter 6

Spatiotemporal 1D-CARS for multi-scalar measurements in turbulent hydrogen flames

This thesis chapter delves into the application of all the CARS advancements presented in this thesis to explore the potential of the system for quantifying molecular transport phenomena within turbulent hydrogen flames. Simultaneous single-shot imaging of temperature, H_2, and H_2O mole fractions are obtained along a one-dimensional field of view of 0.8 mm, at 1 kHz sampling rate in a replica of the TU Darmstadt/DLR Stuttgart H3 flame, which is a canonical turbulent non-premixed H_2 flame. Due to the constraints outlined in the methodology presented in chapter 5 regarding water vapor measurements exclusively being applicable to laminar flames, certain modifications to the experimental setup are introduced. This involves the development of a polarization separation approach to probe the molecular coherence simultaneously at ~7.5 ps and ~250 ps, and record the resulting signals in two distinct detection channels of the polarization-sensitive coherent imaging spectrometer. This approach enables the acquisition of single-shot measurements of water vapor even within dynamic environments, providing the possibility to measure directly the transport of relevant combustion species such as hydrogen in turbulent flames.

Part of the results discussed in this chapter haven been published in paper II

6.1 Introduction

The results presented in chapter 3, showcased the capability of the system to perform temperature measurements with correlated spatiotemporal resolution across a one-dimensional field of view in high-temperature combustion environments. This demonstrated a state-of-the-art resolution in which step scalar gradients can be resolved in space-time on the basis of a single laser shot, and to some extent, dynamics in transient environments can be resolved using kHz repetition rate. Furthermore, in chapter 5, I introduced a new methodology to measure the complete set of relevant scalars in an H_2 flame. Nitrogen thermometry and H_2 and O_2 species concentration were simultaneously obtained from the pure-rotational CARS signal in the frequency domain. On the other hand, water vapor was obtained using the species' sensitivity to inelastic collisions between N_2 and H_2O in the time domain. The decay of the CARS signal is directly measured by sequentially acquiring the pure-rotational N_2 spectra at different probe-pulse delays. In this sense, its applicability might be limited only to stable environments such as laminar flames. To overcome this limitation, the present chapter presents a new methodology that allows the application of all the advancements developed during this thesis to obtain multi-field CARS imaging in turbulent H_2 flames.

The goal of performing multifield diagnostics in turbulent hydrogen flames is to obtain direct insight into the flame structure, which is governed by flow turbulence and complex molecular mass transport processes. These flames differ from typical hydrocarbon flames mainly due to the fast diffusion of hydrogen. Numerical models often assume that all major species in flames have the same diffusivity, and thus, turbulent transport is dominant over molecular mixing [151]. Although this is a reasonable assumption for hydrocarbon flames, differential diffusion can cause serious distortions of the local flame structure and combustion dynamics when light-weight H_2 molecules are present. An inverse relationship exists between the diffusion rate of a molecule in the gas phase and the squared root of its molecular weight [152]. This means that, compared to oxygen, hydrogen molecules diffuse four times faster. In reacting flows where heat is produced, this causes the mass diffusivity of hydrogen to be much faster than its thermal diffusivity, a phenomenon known as preferential diffusion. This effect is quantified by the Lewis number *Le*, which defines the ratio of thermal conductivity (α) to mass diffusivity (D_m) in the flame. Currently, the investigation of hydrogen preferential diffusion remains a critical outstanding challenge for the development of systems

working under both premixed and non-premixed H_2 combustion as it has a direct impact not only on the flame structure (i.e. temperature, scalar flux, strain rate, flame orientation) [153,154], but also on the stability of combustion systems in close to real-world applications as it can lead to thermodiffusive instabilities [155]. Unfortunately, to date, comprehensive scalar measurements in turbulent H_2 flames are scarce and have yet to become available [156].

The first detailed measurements of the temperature and species distribution in turbulent hydrogen flames were performed in the nineteen eighties with the pioneering work of Dibble *et al*. [157] at Sandia National Laboratories and later by Meier *et al*. [158] at DLR Stuttgart. In the work of Meier *et al*. radial profiles of temperature, as well as N_2, O_2, H_2, and H_2O mole fractions were obtained from point-wise spontaneous Raman scattering measurements. These datasets were obtained in a series of turbulent non-premixed test flames cases, using a simplified unconfined jet burner developed at The Technical University of Darmstadt [159]. In particular, one of these flame cases, known as the H3 flame, became the standard benchmark case for the investigation of hydrogen non-premixed combustion [160] and was in this flame that for the first time, the effects of H_2 differential diffusion were observed. After that, very few detailed spectroscopy diagnostics studies have been performed in turbulent H_2 flames, and thus, the data obtained in Meier's measurement campaign is still used to test the numerical turbulent combustion models [161–164].

From a diagnostics perspective, recent developments in fs/ps CARS imaging spectroscopy as the ones presented in this thesis, could bring several advantages for the development of predictive engineering models that still rely on the experimental data obtained by Meier *et al*.. For instance, hydrogen preferential diffusion could be directly measured for the first time by correlating single-shot temperature profiles and the corresponding instantaneous species gradient in the flame. Additionally, the experimental data can be obtained with increased spatial and temporal resolution as compared to Ref. [158] where measurements were performed with a lateral spatial resolution of 0.65 mm at the $1/e^2$ at 5 Hz repetition rate. This chapter demonstrates the feasibility of performing spatiotemporal 1D-CARS in a turbulent hydrogen flame, mapping simultaneously the temperature and correlated composition of the H_2, O_2, and H_2O in the canonical H3 flame. Although, detailed multi-field 1D-CARS measurements have been successfully performed both in CH_4/air [165] and H_2/air [166] flames, in these works water vapor profiles across the flame-front had not been reported. Therefore, the methodology introduced in chapter 5 to detect water vapor has been adapted for single-shot

measurements. This is achieved by using a dual-probe CARS approach to simultaneously acquire the CARS spectra a short and long probe delay mapping the dephasing of the pure rotational CARS signal.

6.2 Experimental set-up

6.2.1 The H3 flame

A replica of the TU Darmstadt unconfined jet burner used in [158] was built to generate the H3 flame. The simplicity of this burner geometry allows to easily reproduce the results for experimental verification as well as for further simulation and is depicted in Fig. 6.1. The burner consists of a straight stainless-steel tube, with an 8 mm inner diameter and a tapered rim at the exit. A concentric contoured nozzle, with an inner diameter of 140 mm, provides a low-speed coflowing airstream helping to stabilize the flame as well as to shield it from local air currents in the ambient. As in the original model, a settling chamber composed of three sets of fine meshes is installed to straighten the air co-flow and provide a top-hat velocity profile.
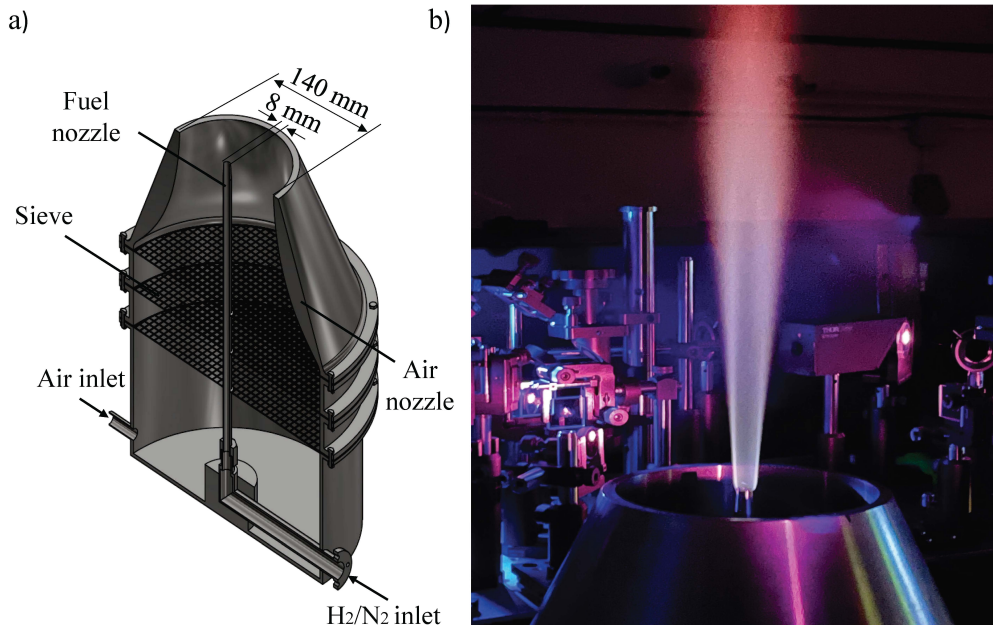
Figure 6.1: Turbulent diffusion H_2-N_2/air jet flame. a) Cross-sectional view of the burner. The central pipe (8 mm diameter) carries H_2 fuel diluted with N_2 in a 1:1 volumetric ratio. A series of three meshes straighten the air in the co-flow, which is subsequently accelerated thought the contoured nozzle, ensuring laminar velocity profile. Relevant dimensions and key components are highlighted. b) Picture of the turbulent H3 jet flame stabilized on the rim of the burner.

Digital mass flow controllers (Bronkhorst) are employed to regulate the volumetric flows of N_2 and H_2 constituting a 50%–50% (in volume) mixture. The reason why N_2 is included in the fuel stream is to reduce the heat losses induced by radiation, however, it also reduces the spatial resolution requirements of the diagnostics instrument as a "thicker" flame front is generated. The H_2/N_2 mixture is further streamed through the center pipe of the burner with an exit speed of 34.8 m/s resulting in a turbulent fuel flow with Re=10000. Finally, the burner is mounted on a set of 3-D mechanical translation stages to control its axial, and radial position.

Figure 6.1(b), presents a photograph of the H3 flame generated in the advanced laser and flames laboratory at TU Delft. While H_2 flames are presumed to be "invisible" to the human eye due to the absence of carbon radicals emitting light in the visible electromagnetic spectrum, surprisingly, this flame is characterized by a subtle yet entrancing interplay of pale blue and reddish chemiluminescence emission. The source of the red emission is traced back to the hot water vapor generated at the product gases of the flame. However, a recent study suggests that the embrittlement of metal particles in the pressurized hydrogen cylinders might be the main cause of the reddish color of the flame [167]. Conversely, discerning the origin of the blue emission proves to be a nontrivial pursuit. Fundamental studies in these hydrogen flames suggest that this emission comes from reactions between hydrogen atoms (H) and hydroxyl radicals (OH) [168,169]. Still, further investigation is needed to understand completely the origin of this emission.

6.2.2 Two-beam fs/ps CARS optical system

The measurements are performed using the fs/ps CARS imaging set-up already described in chapter 3. However, in this case, O-branch Raman transitions were measured instead of S-branch Raman transitions. The reason is that the coherent Raman signal is stronger on the Stokes side due to the higher efficiency of the spectrometer at wavelengths >400 nm. Following the methodology described in chapter 5, temperature is obtained from the pure-rotational Raman spectra of N_2. On the other hand, the concentration of O_2 and H_2 is obtained in the frequency domain from the relative intensity of the CARS spectra of these molecules with respect to N_2. Finally, water vapor concentration is deduced from the time-resolved measurement of the N_2 CARS signal dephasing rate. However, since the temperature and chemical composition of the flow are highly dynamic in turbulent flames, a dual-probe CARS scheme is implemented to achieve single-shot water vapor measurements. This is achieved by splitting the probe pulse into two separate beams and controlling the delay of each of them relative to the pump/Stokes pulse.

In this way, collisional-independent measurements at short probe delay and a time-resolved measurement of the RET at longer probe delays. The dual-probe approach was first demonstrated by Patterson *et al.* to perform single-shot measurements of the collisional dephasing of the S-branch N_2 CARS spectrum [170], and subsequently employed to perform CARS pressure measurements in point-wise and one-dimensional configurations [171–173].
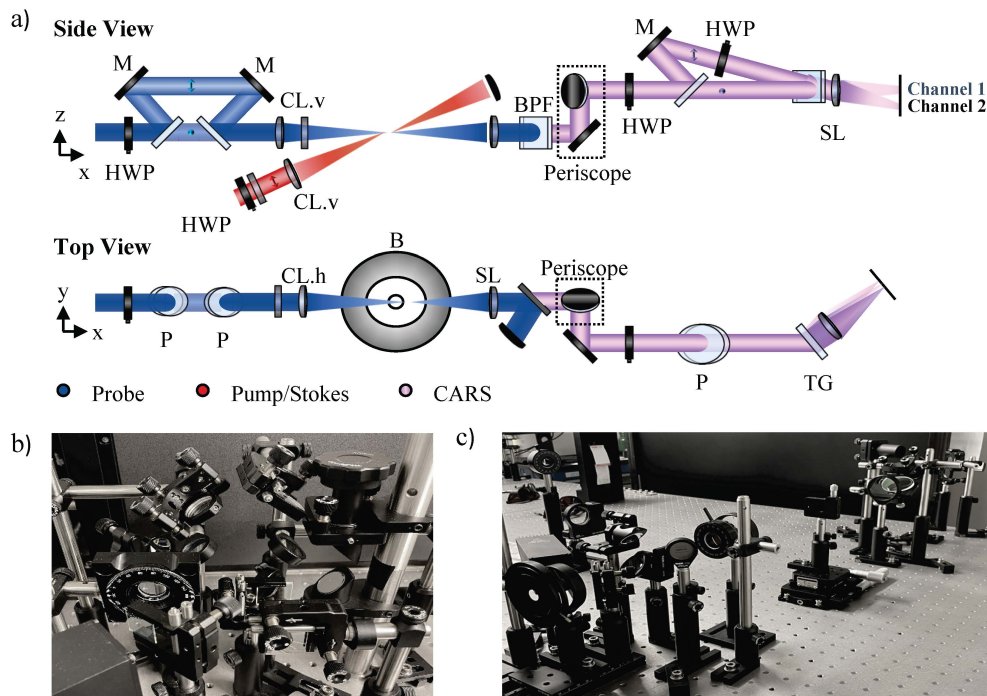
Figure 6.2: a) Schematic of the experimental setup employed for single-shot dual-probe CARS measurements in the H3 flame. A half wave plate (HWP) combined with a pair of thin-film polarizers (P) are employed to split the probe in two pulses with orthogonal polarization and recombine them with an intra-pulse delay of ~250 ps. The subscripts "v" (vertical) and "h" (horizontal) represent the alignment of the symmetry axes of the cylindrical lenses (CL). The cross-polarized CARS signals are simultaneously collected in two distinct detection channels in the polarization-sensitive coherent imaging spectrometer. M, mirrors; SL, spherical lens; BPF, band-pass filter; TG, transmission grating; B, burner. The insets b) and c) , show respectively a picture of the dual-probe optical arrangement and the polarization-sensitive coherent imaging spectrometer.

Two main modifications to the optical set-up were thus required. The first one is regarding the generation of the dual probe. After shaping the probe pulse in the *4-f* filter, a 400 nm half-wave plate combined with a thin-film polarizer is introduced in the beam path to split the probe laser beam into two orthogonally polarized components. The vertically polarized component of the beam is reflected

by the polarizer and directed to a retroreflector mounted on a linear translation stage that controls the relative delay of the two probe pulses. Both components are recombined using a second thin film polarizer at a buster angle. Furthermore, the two laser beams are directed towards the probe volume in a collinear fashion, resulting in an intra-pulse delay of 250 ps. The collinear dual-probe approach guarantees the automatic overlap of the two probe pulses at the measurement location and minimizes the uncertainty due to phase-mismatch between the degenerate pump/Stokes and probe beams, which can significantly impact the intensity of the second H_2 line at higher Raman shifts.

The polarization-sensitive coherent imaging spectrometer described in paper V is adapted for this study to perform simultaneous detection of short- and long-probe delay CARS signals in two distinct detection channels. A 400 nm half-wave plate tunes the polarization of the CRS signals to match the polarization axis of a thin film polarizer, which separates the orthogonally polarized signals in two different detection channels of the spectrometer. An additional half-wave plate mounted on channel #2 aligns the polarization of the signal to optimize the transmission efficiency of the high-resolution transmission grating (3600 l/mm). Finally, a spherical lens ($f:=400$ mm) is used to image the dispersed CRS signals onto the sCMOS sensor, allowing the acquisition of both signals simultaneously.

Measurements were initially conducted using a point-wise configuration to validate the technique, and upon successful demonstration of its feasibility, the methodology was subsequently extended to 1D imaging. In the first set of experiments, the pump/Stokes and the probe beams are focused on the measurement location using spherical lenses of 500 mm and 300 mm focal length respectively. Point-wise 0-D measurements are thus acquired in the H3 flame providing a first proof of concept of the applicability of the dual-probe approach in turbulent reactive flows. The crossing angle for the two-beam phase-matching configuration is estimated to be ~3°, which results in a probe volume of ~22 μm (height) x ~0.6 mm (length) x ~22 μm (width). In these measurements, the probe duration was set to ~12 ps FWHM, with ~300 μJ/pulse, corresponding to a FWHM bandwidth of ~2.7 cm^{-1}. On the other hand, the pump/Stokes energy was attenuated from ~2.5 mJ/pulse to ~60 μJ/pulse to avoid undesired effects such as semipermanent molecular alignment and laser-induced plasma generation.
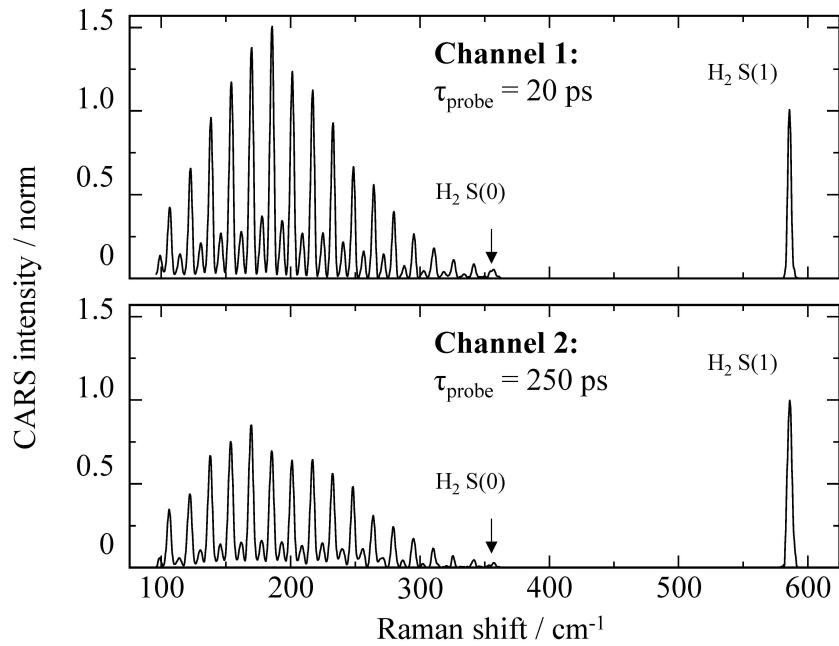
Figure 6.3: Point-wise single-shot CARS spectra simultaneously generated at 20 ps and 250 ps in the fuel stream of the H3 flame, and recorded in the two detection channels. Both spectra are normalized with respect to the S(1) rotational line of H_2, at 587 cm-1.
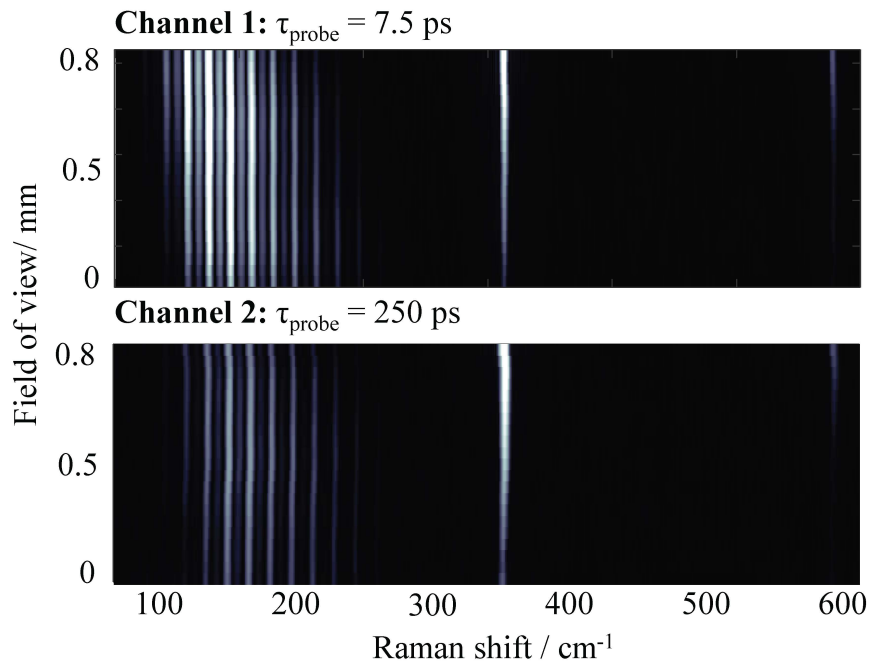
Figure 6.4: Raw single-shot 1D-CARS images acquired simultaneously at τ=7.5 ps and τ=250 ps in the fuel stream of the H3 flame. Top part of the image is positioned towards the fuel stream in the of the burner. The spatial shift in the population of the N_2 transitions, suggest a gradual change in temperature across the evaluated field of view. The diminishing intensity of the first two H_2 rotational transitions highlights the ongoing fuel consumption during the chemical reaction.

In the second experimental arrangement, the combined pump/Stokes and probe beams are focused using plano-convex cylindrical optics (CL.h=500 mm and 300 mm, respectively) to generate a horizontal 1-D FOV oriented horizontally perpendicular to the flame-front. The length of the light sheet at the probe volume of both the femtosecond and the picosecond beams is tuned to ~2 mm and ~0.8 mm respectively. This operation is perform by introducing an additional cylindrical lens in each of the beams (CL.v=1000 mm and 300 mm respectively) with the focusing axis perpendicular to the first lens (CL.h). The compression of the light sheet enhances the irradiance of the beams, consequently increasing the signal strength. Additionally, by reducing the length of the probe laser sheet, short and long probe delay CARS images can be acquired simultaneously on a 200x2048 pixels area around the center of the camera sensor, maintaining an imaging resolution of 20 μm. This enables the acquisition of single-shot dual-probe images at a repetition rate of 1 kHz. The resulting spatial resolution of the system is thus ~20 μm (height) x ~0.5 mm (length) x 0.8 mm (width). In this case, the width of the probe volume corresponds to the imaging field of view. While the probe energy was maintained at ~300 μJ/pulse, the energy of the pump/Stokes beam has to be set to 2 mJ/pulse to obtain sufficient SNR across the entire FOV.

For this particular set-up, a turning periscope composed of two flat silver mirrors is mounted at the entrance of the imaging spectrometer after collimating the CARS beam. In this way, the image is rotated 90° thus mapping the one-dimensional spatial coordinate of both CARS signals along the vertical axis of the sCMOS sensor, while storing the pure-rotational spectra along the horizontal axis. The imaging resolution of the coherent spectrometer obtained by inserting a razor blade at the probe volume and quantifying the corresponding LSF yielded ~22 μm for channel #1 and ~32 μm for channel #2. The slightly worse resolution obtained in channel #2 is due to defocusing aberration which affects the image sharpness and is caused by a difference in the beam path between the two channels after the last imaging lens.

Acquiring the CARS signals within the dynamic range of the sCMOS sensor was one of the key difficulties in both point-wise and line imaging experimental setups. This is due to the significant differences in signal strength induced by number density, coherence dephasing, and molecular susceptibility of the Raman active species involved. The balanced detection of the signal is thus performed by controlling the ratio of energy between the two cross-polarized probe pulses so as to avoid signal saturation at room-temperature in both channels. Additionally, signals below ~150 cm^{-1} were attenuated using the angle-tuned bandpass filter. To

account for the difference in pulse energy as well as for the polarization-dependent signal generation efficiency and the transmission efficiency of the two detection channels, the experimental spectra are corrected generating the signal in a room-temperature N_2 flow with the two probe pulses at the same relative delay. Figure 6.3 shows an example of the two single-shot spectra simultaneously generated at 20 and 250 ps in the fuel stream using point-wise measurements. The effect of molecular collisions after 250 ps is visible on the envelope of the pure-rotational N_2 CARS spectrum, as well as on the differential dephasing of the pure-rotational H_2 signal characterized by a much lesser RET rate. Similarly, Fig. 6.4 shows the simultaneous single-shot detection of short and long probe delay images, generated in the fuel stream of the H3 flame at 0.5 HAB. Remarkably, a gradient of temperature can be resolved within this FOV as demonstrated by the gradual shift in the population of N_2 rotational energy levels across the spatial axis of the image. Additionally, it is possible to see that the intensity of O(1) and O(2) hydrogen transitions changes significantly across the FOV thus suggesting a steep gradient in the concentration of H_2 at the evaluated flame location at this particular instant of time.

6.3 Results

6.3.1 Dual-probe point-wise CARS measurements

The developed approach for simultaneous single-shot detection of main combustion species in the turbulent H3 flame was first demonstrated by performing point-wise CARS measurements. Four samples of 300 single-shot CARS spectra were acquired at a radial location 6.75 mm from the centreline of the flame, at the highest temperature in the oxidizer stream. The scatter plot in Fig. 6.5 shows the measured H_2O mole fraction versus temperature at the chosen flame location, while the grayscale color of each data point represents the local O_2 mole fraction. The latter shows an inverse correlation to the local temperature, with the O_2 mole fraction increasing at lower temperatures. Similarly, the measured H_2O mole fraction has a clear correlation to the temperature in the reaction zone of the turbulent flame, with the concentration increasing with the local progress of the reaction in the probe volume. The clustering of the data points showing a high H_2O mole fraction at high temperatures is in good agreement with the original measurements performed by Meier *et al*. on the H3 flame. At lower temperatures, when a significant concentration of O_2 is present in the probe volume, the measured

H_2O mole fraction shows a more spurious correlation, which is probably due to the beating of the N_2 lines employed in the measurement with O2 lines.
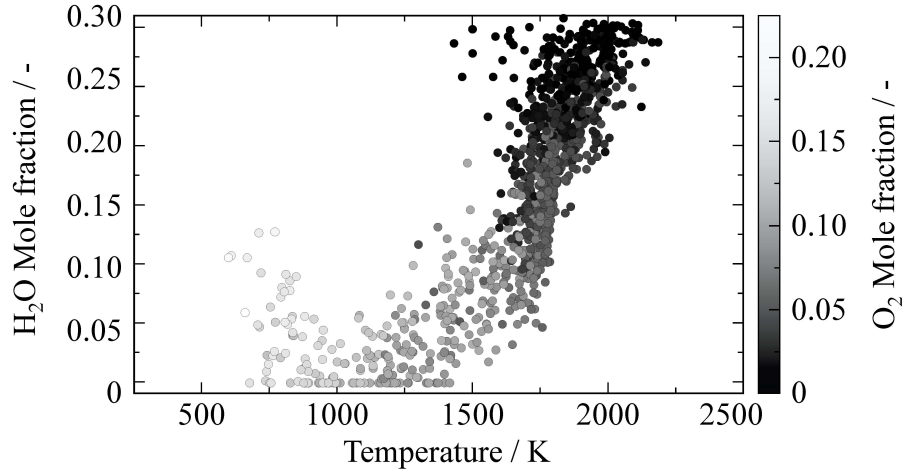
Figure 6.5: Scatter plot of the H_2O mole fraction versus temperature measured by the 1200 single-shot CARS spectra acquired at the location with the highest temperature in the turbulent H3 flame. The grayscale color represents the measured O_2 mole fraction.
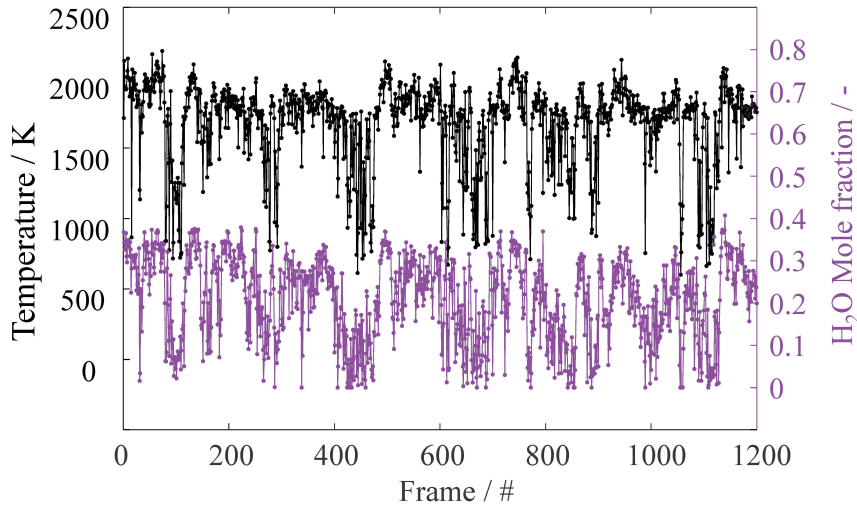
Figure 6.6: Temporal correlation of temperature and water vapor concentration for 1200 single-shots measured at y= 6.5 mm at 0.5 HAB. Turbulence-driven fluctuations in temperature exhibit a synchronous relationship with variations in water vapor concentration. At this spatial location, some dynamics can be resolved with the sampling rate employed.

From the point-wise data obtained at this location, it is also possible to correlate the different scalar fields measured at a fixed spatial location in the flame as a function of time. An example of this is presented in Fig. 6.6 which shows the fluctuations in temperature as well as the corresponding water vapor mole fraction

obtained for 1200 sequential single laser shots acquired at a repetition rate of 300 Hz. employed in the measurement with O_2 lines.

First of all, it is possible to see that low-frequency fluctuations in temperature can be captured at this location in the flame. During the course of the experiment, the temperature fluctuates between ~900 K and ~2200 K. Such fluctuations are most likely caused by Kelvin-Helmholtz vortices generated at the interface between the fuel and air flows at the burner exit. Moreover, by looking at the time evolution of the measured data, it is clear that there is a direct correlation between these two scalars. As expected, when the temperature increases, the concentration of water vapour rises varying between $X_{H_2O} = 0$ and $X_{H_2O} \sim 0.35$ in mole fraction at the highest temperature.

6.3.2 Multi-field spatiotemporal 1D-CARS measurements

Once the proof-of-concept of the dual-probe approach was achieved, measurements using the second experimental arrangement were performed. A dataset composed of 1000 single-shot 1D-CARS images was acquired simultaneously, both at short and long probe delays, at 1kHz repetition rate. The FOV was oriented perpendicular to the flow to measure the evolution of the reaction and between the fuel and oxidizer. The probe volume was located at 0.5 HAB, at an axial position $y = 4.0$ mm away from the centreline of the fuel nozzle.

Figure 6.7 shows the spatiotemporal temperature map obtained from the short probe CARS signal, measured at this location during the first 100 milliseconds of the experiment. Highly step temperature gradients can be resolved across the FOV where temperature rises from ~400 K and can reach ~1000 K increasing towards a larger axial distance from the center of the burner. Additionally, it is possible to observe that at this location, the temperature varies greatly from shot-to-shot. Such variations are most likely caused by physical fluctuations in the flame-front position induced by shear-driven instabilities at the interface of the jet fuel and the air stream in the co-flow. Small coherent vortices develop within the hot jet shear layer remaining coherent for short distances downstream until they coalesce [174]. The of 200-400 Hz are predicted for H_2/N_2 diffusion flames with similar burner geometry [175].
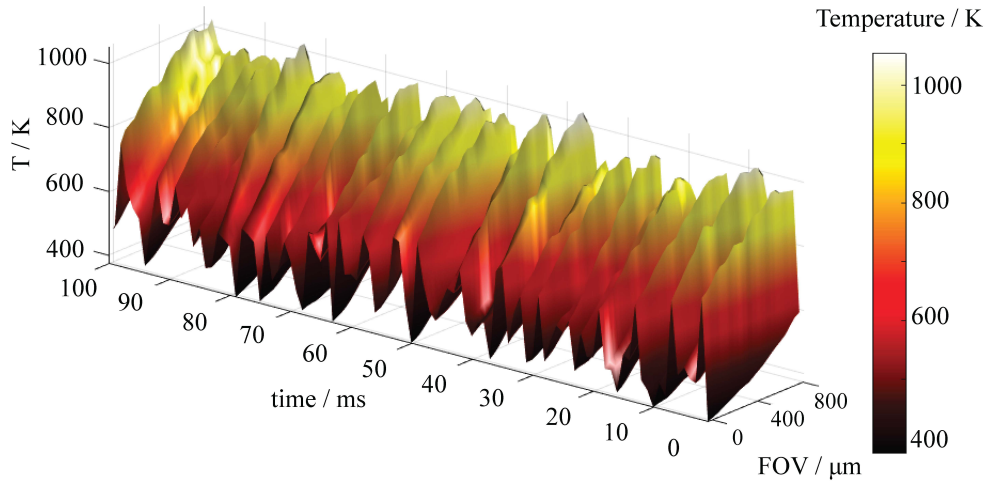
Figure 6.7: Spatiotemporal map of temperature evolution in the fuel stream of the H3 Flame at y=4 mm from the burner centre: Initial 100 single-shot images from a 1000-frames data set acquired at 1 kHz rate. The exceptional spatial resolution captures step scalar gradients, ranging from ~400 K to ~1000 K, occurring within approximately 0.8 mm, offering detailed insights into the dynamic temperature profile.

Moreover, in Fig. 6.8, correlated single-shot profiles of temperature, as well as H_2 and H_2O mole fractions measured at four different instants in time of the experiment are presented as an example of the type of thermochemical mapping achievable with this technique. Several observations can be made from these scalar profiles. As it can be seen in Fig. 6.8(a), when temperature rises from ~400K and ~700 K, the H_2 mole fraction is relatively stable, and minimal consumption is observed. At this instant of time, the concentration of water vapor hovers around zero, indicating that the reaction has not yet started. Furthermore, as shown in Fig. 6.7(b) when temperatures increase above ~700 K, H_2 starts to be consumed faster, exhibiting a proportional response to the temperature increase. However, in some frames captured at this flame location, the correlation between temperature and species mole fraction becomes less obvious. For instance, in Fig. 6.8(b), the H_2 profile shows a prominent peak in concentration of $X_{H_2} = 0.6$, followed by a sudden decrease to a minimum value of $X_{H_2} = 0.2$, all within a narrow spatial range of ~ 400 µm. Notably, the corresponding temperature profile at this location does not seem to increase proportionally to this trend. Likewise, the H_2 profile in Fig. 6.8(b) exhibits a pronounced non-uniformity, with local minimal found at different points within the field of view. This behaviour might be linked to unreacted pockets of H_2 transported due to the molecule's fast diffusivity. These observations are consistent

with measurements reported by Meier *et al.*, who identified H_2 preferential diffusion as a major factor determining the flame structure near the burner rim.
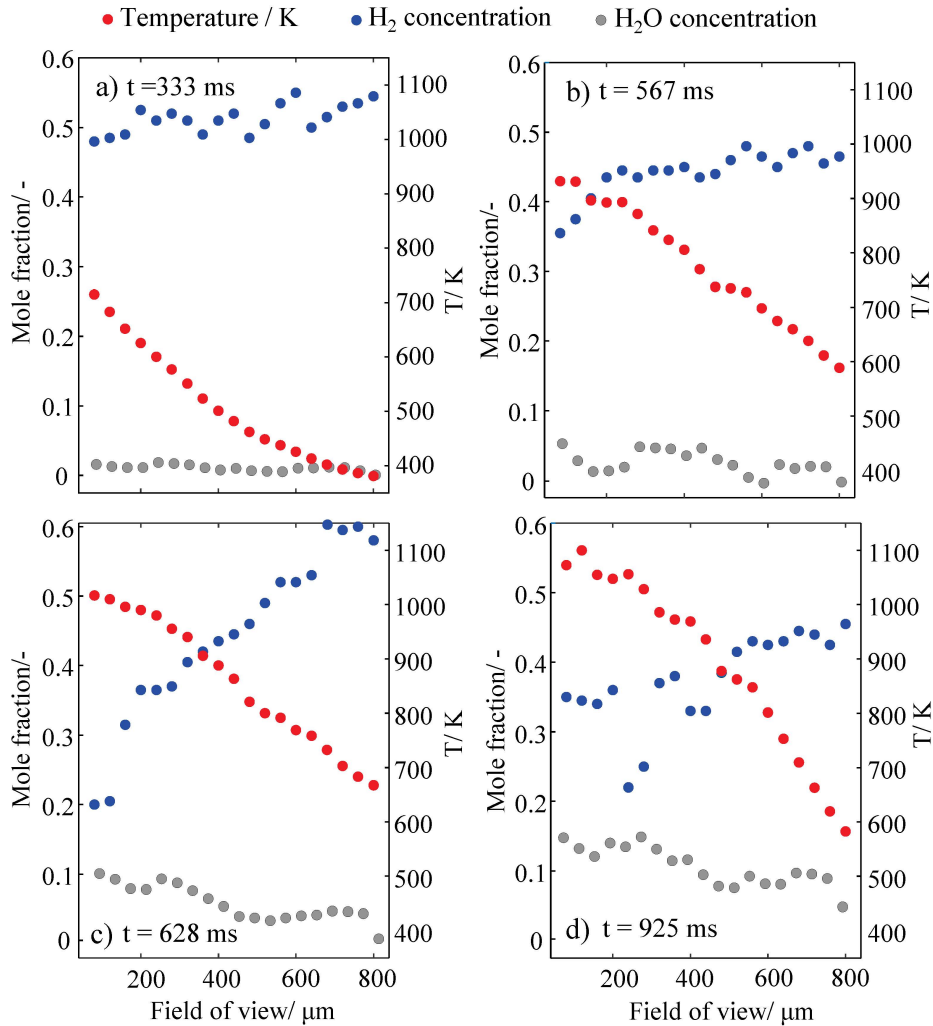
Figure 6.8: Comparison of single-shot 1D-CARS temperature, H_2, and H_2O mole fraction profiles at y=4 mm, 0.5 HAB, obtained at t=333 ms, 567 ms, 628 ms, and 925 ms. Panels a) and b) illustrate cases where the temperature profile gradually increases (towards the oxidizer stream), and hydrogen begins to decrease in response to the chemical reaction. In contrast, panels c) and d) reveal steeper gradients, particularly in hydrogen mole fraction, which do not correlate with the temperature profile. This discrepancy may be attributed to unreacted pockets of hydrogen, possibly caused by the fast diffusion of this molecule.

Overall, the novel CARS approach presented here has promising applications as an all-around laser diagnostic technique for multifield scalar imaging measurements in both laminar and turbulent hydrogen flames, allowing for the simultaneous mapping of the temperature and chemical composition of the flow.

Chapter 7

Conclusions and outlook

This doctoral thesis has focused on the development of an ultrafast fs/ps CARS instrument tailored to investigate the local structure of hydrogen flames. The pressing relevance of hydrogen in combustion applications underscores the paramount importance of this work, as it directly addresses the need for high-fidelity diagnostics to harness the full potential of hydrogen in clean and efficient energy systems. Throughout the course of this research, several pioneering advancements have been achieved particularly in terms of spatiotemporal resolution for multifield scalar measurements across step spatial gradients. These achievements translate into a marked improvement in the accuracy and precision of scalar measurements in dynamic environments. Additionally, a key contribution of this work was the evaluation of the feasibility of simultaneous measurements of the most relevant scalar fields in hydrogen flames which allows the direct observation of molecular transport processes that govern the propagation of laminar and turbulent hydrogen flames.

The first stage of the project involved the design and construction of the experimental platform, documented in paper I. For the first time, two-beam fs/ps CARS line imaging was achieved at a kilohertz repetition rate using a single regenerative amplifier system. The inherent broadband spectrum of the 35 fs-duration laser pulses employed, allowed to impulsively excite the entire pure-rotational energy manifold of N_2 and O_2 molecules, as well as the first two rotational Raman transitions of H_2 located at 354 and 587 cm^{-1} respectively. The use of second harmonic compression allowed to efficiently generate high-energy picosecond probe pulses, which are temporally locked to femtosecond pulses. As a result, CARS signal can be generated across a field of view of ~1.5 mm at 1 kHz repetition rate at flame temperatures.

To detect the CARS signal, a wide-field coherent imaging spectrometer had to be specially designed to capture the single-shot 1D-CARS images at 1 kHz acquisition rate with sufficient spectral resolution to resolve pure-rotational transitions of the N_2, O_2, and H_2 in the range of 0-600 cm^{-1}. In this respect, this work

provided the first demonstration of an sCMOS sensor without an intensifier for gas-phase CARS signal detection. The dynamic range of this sensor (16-bit) proved to be more than adequate for capturing the large temperature gradients observed in the flame front of a typical laminar premixed flame, providing a linearity better than 99%. The capability of acquiring high-temperature CARS signals with an sCMOS camera can be caused by the high Raman cross-section that this technique provides due to the use of a 400 nm probe pulse as compared to the convenient 532 nm wavelength (2nd harmonic of Nd:YAG laser) employed in most of the existing CARS systems. However, further investigation should be undertaken to evaluate the probe wavelength dependence on the Raman cross section in the context of fs/ps CARS spectroscopy.

Significant improvements have been achieved in spatial resolution when compared to state-of-the-art CARS instruments documented in the literature. Specifically, I reported an improvement from the previous 40 μm to the current 20 μm. Likewise, the imaging resolution has seen a similar enhancement, going from 50-60 μm [80,173] to approximately 20 μm. To provide context for the relevance of these advancements, it is important to consider a typical laminar premixed hydrogen/air flame under stoichiometric conditions, where both the preheat and reaction zones extend over approximately 500 μm with a steep temperature gradient ranging from 300 K to 2400 K. In Section 1.2.1, it was observed that avoiding systematic bias in temperature retrieval in such an environment, caused by spatial averaging effects, requires instruments with a spatial resolution of at least 20 μm. Consequently, the imaging capabilities of this CARS instrument enable the sampling of such a gradient with 25 independent measurement points.

To benchmark the system, cinematographic 1D-CARS thermometry at 1 kHz was demonstrated across an unstable premixed methane/air flame front. Even though the use of a single regenerative amplifier provides a limitation in the available probe and pump/Stokes pulse power, sufficient signal strength was achieved to image the temperature and O_2/N_2 mole fraction across the entire flame structure from reactants (~300 K) to fully burnt products (~2200 K) on the basis of a single laser shot. With the available spatiotemporal resolution, the system proves to be sufficiently robust against disturbances originating from the laboratory frame by tracking the position of the flame-front in every instant in time. For instance, periodic fluctuations in the flame-front position at frequencies of 13 Hz and 75 Hz and amplitudes of ~300 μm and 50 μm respectively were discerned. This correlated resolution thus provided a significant reduction in the uncertainty of the

measurements as compared to point-wise measurements yielding state-of-the-art single-shot precision <1% and inaccuracy <3% for flame-front studies.

One of the biggest challenges faced during the implementation of second harmonic bandwidth compression to generate the ps-duration probe pulses was dealing with the blue-shifted sidebands that appeared on the pulse spectrum spanning ~40 cm^{-1}. This complication rendered the acquisition of CARS signals at low Raman shift impractical, given the interference between the sidebands and the pure-rotational spectrum. In this doctoral dissertation, I presented two distinct approaches for using the SHBC-produced picosecond pulses in two-beam CARS diagnostics. The first one involved the implementation of a custom 4-f pulse shaper to filter out the sidebands, as detailed in paper I. This method was successfully applied for spatiotemporal 1D-CARS diagnostics allowing to resolve pure-rotational N_2 CARS transitions even at low Raman shifts. Unfortunately, using this methodology, a loss of ~70% of the available pulse energy was observed which might limit the applicability of the technique in more demanding applications.

Hence, in the second approach, I proposed to use the output of the SHBC directly, without filtering the spectral sidebands, and acquire the CSRS instead of the CARS spectrum, thus avoiding interference between the signal and the probe pulses at the sCMOS sensor. In this scenario, achieving a precise characterization of the probe spectral phase became crucial for modelling CSRS signals due to the non-linear chirp observed in the pulse. This characterization was successfully achieved in paper III through the development of a new methodology in which the inherently ultrashort duration of the CARS non-resonant signal (~35 fs) was employed to measure the relative phase of different spectral components of the probe pulse. The main advantage of this methodology is that the CRS process itself was used to realize autocorrelation measurement on the ps probe pulse without the need for additional equipment.

Furthermore, this thesis also delved into a well-known challenge for two-beam fs/ps CARS spectroscopy: the robust measurement of the H_2 pure-rotational Raman spectrum. At flame temperature, the H_2 spectrum spans more than 2000 cm^{-1} making it difficult to perform reliable multiplex measurements with commercially available fs laser sources. Nonetheless, with the available bandwidth of the transform-limited 35 fs-duration pulses provided by the Astrella amplifier, I was able to measure simultaneously the entire pure-rotational N_2 CARS spectrum and two rotational transitions of the pure-rotational H_2 CARS spectrum, namely S(0) at 354 cm^{-1} and S(1) at 587 cm^{-1}. This allowed me to accurately determine the relative concentration of H_2 in a laminar H_2/N_2 diffusion flame, in the range of ~0.1-0.5 mol

fraction. The lower detection limit was affected by the diminished population of S(0) and S(1) H_2 transitions when temperatures exceed ~1500 K. Nevertheless, above this temperature, it is expected that most of the hydrogen is consumed, thus the first two rotational transitions of hydrogen provide sufficient sensitivity to track the concentration of this scalar in most flames in which H_2 is present in the fuel stream. In all evaluated cases, the relative standard deviation of the measured mole fractions of H_2 remained below ~2.5%. From these results, however, it became evident that to enhance H_2 concentration sensitivity at higher temperatures in flames, more sophisticated excitation schemes are necessary to induce rotational coherence within the entire H_2 energy ensemble. This was successfully demonstrated in paper VI, where laser-induced filamentation was employed to simultaneously probe six rotational lines of H_2, ranging from O(2) at 354 cm^{-1} to O(7) at 1447 cm^{-1}, at elevated temperatures. For further details, interested readers can refer to the work of Mazza *et al.* [176]

In addition, one of the main novelties presented in this thesis was the development of a new strategy to deduce the concentration of water vapor from the pure-rotational N_2 CARS signal in the time domain. Due to the weak H_2O resonant Raman spectra, this molecule cannot be directly measured in the frequency domain. However, inelastic collisions between N_2 and H_2O for which a higher energy exchange rate is observed as compared to other major combustion species provide an additional degree of sensitivity that can be used to determine its mol fraction. To test this hypothesis, a laminar H_2/air diffusion flame was employed, and point-wise measurements of correlated temperature and the relative O_2/N_2 and H_2/N_2 concentrations were performed in the frequency domain. The local H_2O concentration, was thus deduced from the exponential decay of the N_2 CARS spectra acquired sequentially at probe delays up to 360 ps. Water vapor was detected in the reaction zone, with a maximum mole fraction of 0.34 at 1600 K and a minimum of 0.03 at 800 K. The uncertainty in the measured H_2O concentrations is mostly due to shot-to-shot fluctuation in the temperature and flow composition good single-shot precision of the CARS thermometry, varying in the range 0.8-3.7%. These were some of the most remarkable results obtained from this thesis, as the information simultaneously accessible with this new development has the potential to provide significant insights into the chemical and physical processes in hydrogen flames. This was demonstrated by the direct measurement of H_2 preferential diffusion in the tested flame.

To complement this study, a numerical investigation was carried-out to explore the possibility to extend the technique to measure water vapor in an equivalent

ternary collisional systems where the concentration of two perturber species is unknown. This is the case of measurements performed in the products of typical hydrocarbon flames where CO_2 –one of the major combustion species present in the products– cannot be directly measured in the frequency domain using fs/ps CARS. Unfortunately, in such cases, the water vapor concentration measurements are significantly affected by the presence of CO_2 even at small amounts of ~0.1 mol fraction. When the sensitivity of the integrated N_2 CARS spectrum is employed, I found that X_{H_2O} is overestimated by at least 100%. This overestimation increases lineally with X_{CO_2}. On the other hand, when the *J*-dependence of the spectral envelope is exploited, the estimated concentration of water vapor can be up to 25% lower than the true value. This issue could potentially be solved by using the sensitivity of the N_2 CARS signal from both the *J*-dependence and the decay of the integrated spectrum to estimate the concentration of the two unknown perturber species (i.e. H_2O and CO_2) simultaneously. However, this hypothesis should still be tested experimentally.

Finally, all the developments described in this thesis were employed to measure the main scalar fields in the turbulent TU Darmstadt/DLR Stuttgart canonical 'H3 flame. This flame has been vastly investigated both experimentally and numerically for the validation of turbulent combustion models, and it was in this flame that, for the first time, the effects of hydrogen preferential diffusion were observed. Therefore, I selected this flame as a test case to investigate the feasibility of measuring directly molecular transport processes affecting the flame structure using spatiotemporal 1D-CARS. The development of polarization separation technique to generate dual-probe CARS, combined with the implementation of the polarization sensitive coherent imaging spectrometer developed in paper V was instrumental to achieve this objective. The molecular N_2 coherence was successfully acquired simultaneously at short (i.e. ~7.5 ps) and long (i.e. ~250 ps) probe delays. This allowed me to obtain thermometry and H_2, O_2, and H_2O concentration measurements on the basis of a single-laser-shot. One of the caveats of the presented results is that the collisional dephasing of the N_2 CARS signal could only be measured at two probe delays. To increase the sensitivity and robustness of the single-shot CARS measurements of water vapor, the *J*-dependence of the collisional dephasing coefficients could be thus incorporated as an additional source of sensitivity to H_2O mole fractions. Additionally, by applying the methodology outlined in Paper III to be able to use the high-energy ps-probe pulse produced by the SHBC without filtering the sidebands, the strength of integrated CARS signals could be amplified by a factor of ~4. This enhancement

opens up possibilities to extend the field of view and conduct measurements at probe delays beyond those reported in this thesis.

Acknowledgements

The present dissertation represents the culmination of a journey that began almost five years ago in the Netherlands, where I embarked on the challenging yet fascinating world of non-linear optical spectroscopy and its application in reacting flows. The achievements I have reached during this time would not have been possible without the support, guidance, and encouragement of many people, including colleagues, family, and friends.

First and foremost, I would like to express my deepest gratitude to all those involved in the development of the advanced laser diagnostics and flames laboratory at TU Delft, especially my daily supervisor, Alexis Bohlin, my promotor, Piero Colonna, Dmitrii Kliukin and Francesco Mazza for their unwavering support.

Dear Alexis, thank you for the incredible opportunity to be part of this project. From day one, you personally trained me and introduced me to hands-on work with ultrafast lasers and molecular spectroscopy stimulating my passion for this field. I will always treasure our long meetings, which could last an entire day, discussing everything from philosophy and Northern culture to the physics and history of CARS.

To my colleague Francesco, I couldn't have asked for a better teammate. Together, we navigated some of the toughest challenges but also shared many of the happiest moments during this journey. Your professionalism and passion for physics and non-linear optics are truly inspiring. I must admit, keeping up with all the brilliant ideas that emerged during our long conversations was not always easy, but I hope that one day we will bring many of them to fruition.

Dear Dmitrii, your ideas were fundamental in making the CARS instrument a reality. I deeply appreciate your patience and the knowledge you shared with me, both in the laboratory and in life. Your critical thinking and your ability to challenge widely accepted concepts will always inspire me.

My life in the Netherlands would not have been the same without the support of many dear friends with whom I share countless happy memories, from my arrival in the country to the challenging times of the COVID-19 pandemic. Thank you, Ana, Juan David, Federico, Manuela, David, Billy, Nadine, and Lorena, for your

companionship. Your presence has made my journey in this country truly unforgettable. A special thanks to Thamara and Ramiro, who have become more than friends, a family.

Agradezco especialmente a mis padres, Martha y José, por su amor incondicional y por tenerme siempre en sus oraciones. A mi hermano Duván, por ser un gran ejemplo a seguir y por motivarme cada día, desde mi maestría en Brasil hasta mi doctorado en Holanda. A Valentina, a quien extraño inmensamente, por ser esa luz que me guía de vuelta a casa. Este logro es por ustedes

Por último, pero no menos importante, quiero agradecer a Laura, quien con su alegría logró poner color a los días más grises. Eres la persona más valiente que he conocido. Gracias por confiar en mí y embarcarte en esta aventura. Fuiste mi razón para nunca desistir. Lo logramos.

References

[1] Cecere D, Giacomazzi E, Ingenito A. A review on hydrogen industrial aerospace applications. Int J Hydrogen Energy 2014;39:10731–47. https://doi.org/10.1016/j.ijhydene.2014.04.126.

[2] Foust J. NASA'S Space Launch System Will Lift Off. IEEE Spectr 2022;59.

[3] Ha D, Roh TS, Huh H, Lee HJ. Development Trend of Liquid Hydrogen-Fueled Rocket Engines (Part 1: Performance and Operation). International Journal of Aeronautical and Space Sciences 2023;24:131–45. https://doi.org/10.1007/s42405-022-00519-7.

[4] Liu W, Zuo H, Wang J, Xue Q, Ren B, Yang F. The production and application of hydrogen in steel industry. Int J Hydrogen Energy 2021;46:10548–69. https://doi.org/10.1016/j.ijhydene.2020.12.123.

[5] Pei M, Petäjäniemi M, Regnell A, Wijk O. Toward a fossil free future with hybrit: Development of iron and steelmaking technology in Sweden and Finland. Metals (Basel) 2020;10:1–11. https://doi.org/10.3390/met10070972.

[6] Maria Hessels CJ. Reduction of combusted iron using hydrogen. Eindhoven University of Technology, 2023.

[7] Baigmohammadi M, Prasidha W, Stevens NC, Shoshyn YL, Spee T, de Goey P. Towards utilization of iron powders for heating and power. Applications in Energy and Combustion Science 2023;13. https://doi.org/10.1016/j.jaecs.2023.100116.

[8] Bergthorson JM, Goroshin S, Soo MJ, Julien P, Palecka J, Frost DL, et al. Direct combustion of recyclable metal fuels for zero-carbon heat and power. Appl Energy 2015;160:368–82. https://doi.org/10.1016/j.apenergy.2015.09.037.

[9]   Ghavam S, Vahdati M, Wilson IAG, Styring P. Sustainable Ammonia Production Processes. Front Energy Res 2021;9. https://doi.org/10.3389/fenrg.2021.580808.

[10]   Nose M, Kawakami T, Tanimura S. Hydrogen-fired Gas Turbine Targeting Realization of CO2-free Society. Mitsubishi Heavy Industries Technical Review n.d.;55.

[11]   Lantz A, Collin R, Alden M, Lindholm A, Larfeldt J, Lorstad D. Investigation of hydrogen enriched natural gas flames in a SGT-700/800 burner using oh PLIF and chemiluminescence imaging. J Eng Gas Turbine Power 2015;137. https://doi.org/10.1115/1.4028462.

[12]   Menon S, Bouten T, Withag J, Klein S, Gangoli Rao A. Numerical Investigation of 100% Premixed Hydrogen Combustor at Gas Turbines Conditions Using Detailed Chemistry. Volume 3: Ceramics; Coal, Biomass, Hydrogen, and Alternative Fuels, American Society of Mechanical Engineers; 2020. https://doi.org/10.1115/GT2020-16134.

[13]   Meloni R, Orsino S, Ansari N, Yadav R, Bessette D, Castellani S, et al. Partially Premixed Hydrogen-Methane Flame Simulations at Relevant Gas Turbine Conditions With a Thickened Flame Model Enhancement. Volume 3A: Combustion, Fuels, and Emissions, American Society of Mechanical Engineers; 2023. https://doi.org/10.1115/GT2023-102427.

[14]   Rao AG, Yin F, Van Buijtenen JP. A hybrid engine concept for multi-fuel blended wing body. Aircraft Engineering and Aerospace Technology 2014;86:483–93. https://doi.org/10.1108/AEAT-04-2014-0054.

[15]   Choubey G, D Y, Huang W, Yan L, Babazadeh H, Pandey KM. Hydrogen fuel in scramjet engines - A brief review. Int J Hydrogen Energy 2020;45:16799–815. https://doi.org/10.1016/j.ijhydene.2020.04.086.

[16]   Khandelwal B, Karakurt A, Sekaran PR, Sethi V, Singh R. Hydrogen powered aircraft: The future of air transport. Progress in Aerospace Sciences 2013;60:45–59. https://doi.org/10.1016/j.paerosci.2012.12.002.

[17]   Bradley MK, Droney CK. Subsonic Ultra Green Aircraft Research PhaseII: N+4 Advanced Concept Development. 2012.

[18]   Zheng X, Mukhopadhaya J, Johnson T, Gardner G, Searle S. Environmental limits on supersonic aircraft in 2035. 2022.

[19]   Energy Transition Comission. Making Net-Zero Aviation Possible. 2022.

[20]   Colorado A, McDonell V, Samuelsen S. Direct emissions of nitrous oxide from combustion of gaseous fuels. Int J Hydrogen Energy 2017;42:711–9. https://doi.org/10.1016/j.ijhydene.2016.09.202.

[21]   Matthes S, Lee DS, De Leon RR, Lim L, Owen B, Skowron A, et al. Review: The Effects of Supersonic Aviation on Ozone and Climate. Aerospace 2022;9. https://doi.org/10.3390/aerospace9010041.

[22]   Hochgreb S. How fast can we burn, 2.0. Proceedings of the Combustion Institute 2023;39:2077–105. https://doi.org/10.1016/j.proci.2022.06.029.

[23]   Boivin P, Le Boursicaud M, Millán-Merino A, Taileb S, Melguizo-Gavilanes J, Williams F. Hydrogen Ignition and Safety. Hydrogen for Future Thermal Engines, vol. 1. 1st ed., 2023, p. 161–236. https://doi.org/10.1007/978-3-031-28412-0_5.

[24]   Warnatz J, Maas U, Dibble RW. Combustion: Physical and Chemical Fundamentals, Modelling and Simulation, Experiments, Pollutant formation. 4th ed. Springer-Verlag Berlin Heidelberg.; 2006.

[25]   Barlow RS, Dunn MJ, Sweeney MS, Hochgreb S. Effects of preferential transport in turbulent bluff-body-stabilized lean premixed CH 4/air flames. Combust Flame 2012;159:2563–75. https://doi.org/10.1016/j.combustflame.2011.11.013.

[26]   Steinberg A, Roy S, editors. Optical Diagnostics for Reacting and Non-Reacting Flows: Theory and Practice. Reston, VA: American Institute of Aeronautics and Astronautics, Inc.; 2023. https://doi.org/10.2514/4.106330.

[27]   Mallard E, Le Chatelier H. Recherches experimentales et theoriques sur la combustion des melanges gaseux explosifs. Annales Des Mines 1883.

[28]   Lewis B, Von Elbe G. Theory of Flame Propagation. Proceedings of the Symposium on Combustion 1948;1:183–8. https://doi.org/https://doi.org/10.1016/S1062-2888(65)80027-2.

[29]   Farooq A, Alquaity ABS, Raza M, Nasir EF, Yao S, Ren W. Laser sensors for energy systems and process industries: Perspectives and directions. Prog Energy Combust Sci 2022;91. https://doi.org/10.1016/j.pecs.2022.100997.

[30]   Bohlin A, Kliewer CJ. Direct coherent Raman temperature imaging and wideband chemical detection in a hydrocarbon flat flame. Journal of Physical Chemistry Letters 2015;6:643–9. https://doi.org/10.1021/acs.jpclett.5b00014.

[31]   van Oijen JA, de Goey LPH. Modelling of premixed laminar flames using flamelet-generated manifolds. Combustion Science and Technology 2000;161:113–37. https://doi.org/10.1080/00102200008935814.

[32]   Correa SM. A review of NOx formation under gas-turbine combustion conditions. Combustion Science and Technology 1993;87:329–62. https://doi.org/10.1080/00102209208947221.

[33]   Trivedi S, Cant RS. Turbulence Intensity and Length Scale Effects on Premixed Turbulent Flame Propagation. Flow Turbul Combust 2022;109:101–23. https://doi.org/10.1007/s10494-021-00315-5.

[34]   Kostiuk LW, Cheng RK. The Coupling of Conical Wrinkled Laminar Flames with Gravity. Combust Flame 1995.

[35]   Kimura I. Stability of laminar-jet flames. The Combustion Institute; 1965.

[36]   Krikunova AI. M-shaped flame dynamics. Physics of Fluids 2019;31. https://doi.org/10.1063/1.5129250.

[37]   Guahk YT, Lee DK, Oh KC, Shin HD. Flame-intrinsic kelvin-helmholtz instability of flickering premixed flames. Energy and Fuels 2009;23:3875–84. https://doi.org/10.1021/ef900147x.

[38]   Searby G, Rochwerger D. A parametric acoustic instability in premixed flames. J Fluid Mech 1991;231:529–43. https://doi.org/10.1017/S002211209100349X.

[39]   Searby G. Acoustic Instability in Premixed Flames. Combustion Science and Technology 1992;81:221–31. https://doi.org/10.1080/00102209208951803.

[40]   Higgins JR. Sampling Theory in Fourier and Signal Analysis. Oxford
        Science Publications; 1996.

[41]   Lee S-R, Park S-S, Chung S-H. Flame Structure and Thermal NOx
        Formation in Hydrogen Diffusion Flames with Reduced Kinetic
        Mechanisms. KSME Journal 1995;9:377–84.

[42]   Richardson DR, Stauffer HU, Roy S, Gord JR. Comparison of chirped-
        probe-pulse and hybrid femtosecond/picosecond coherent anti-Stokes
        Raman scattering for combustion thermometry. Appl Opt 2017;56:E37.
        https://doi.org/10.1364/ao.56.000e37.

[43]   Kearney SP. Hybrid fs/ps rotational CARS temperature and oxygen
        measurements in the product gases of canonical flat flames. Combust Flame
        2014;162:1748–58. https://doi.org/10.1016/j.combustflame.2014.11.036.

[44]   Maker PD, Terhune RW. Study of Optical Effects Due to an Induced
        Polarization Third Order in the Electric Field Strength. Physical Review
        1965;137.

[45]   Begley RF, Harvey AB, Byer RL. Coherent anti-Stokes Raman
        spectroscopy.   Appl   Phys   Lett   1974;25:387–90.
        https://doi.org/10.1063/1.1655519.

[46]   Eckbreth AC. Laser diagnostics for combustions temperature and species.
        vol. 3. CRC press; 1996.

[47]   Reignier PR, Moya F, Taran JPE. Gas Concentration Measurement by
        Coherent Raman Anti-Stokes Scattering. AIAA Journal 1974;12:826–31.
        https://doi.org/10.2514/3.49358.

[48]   Moya F, Druet SAJ, Taran JPE. Gas Spectroscopy and Temperature
        Measurement by Coherent Raman Anti-Stokes Scattering. Optics
        Comunications 1975.

[49]   Greenhalgh D, Porter FM. The Application of Coherent Anti-Stokes Raman
        Scattering to Turbulent Combustion Thermometry. Combust Flame
        1983;49:171–81.

[50]   Eckbreth AC, Hall RJ. CARS Thermometry in a Sooting Flame. Combust
        Flame 1979;36:87–98.

[51] Roh WB, Schreiber PW, Taran JPE. Single-pulse coherent anti-Stokes Raman scattering. Appl Phys Lett 1976;29:174–6. https://doi.org/10.1063/1.89013.

[52] Eckbreth AC, Anderson TJ. Simultaneous rotational coherent anti-Stokes Raman spectroscopy and coherent Stokes Raman spectroscopy with arbitrary pump-Stokes spectral separation. Opt Lett 1986;11.

[53] Seeger T, Leipertz A. Experimental comparison of single-shot broadband vibrational and dual-broadband pure rotational coherent anti-Stokes Raman scattering in hot air. Appl Opt 1996;35.

[54] Alden M, Bengtsson P-E, Edner H. Rotational CARS generation through a multiple four-color interaction. Appl Opt 1986;25.

[55] Martinsson L, Bengtsson PE, Aldén M, Kröll S, Bonamy J. A test of different rotational Raman linewidth models: Accuracy of rotational coherent anti-Stokes Raman scattering thermometry in nitrogen from 295 to 1850 K. J Chem Phys 1993;99:2466–77. https://doi.org/10.1063/1.466197.

[56] Barrett JJ. Generation of coherent anti-Stokes rotational Raman radiation in hydrogen gas. Appl Phys Lett 1976;29:722–4. https://doi.org/10.1063/1.88916.

[57] Martinsson L, Bengtsson P-E, Alden M. Oxygen concentration and temperature measurements in N2-O2 mixtures using rotational coherent anti-Stokes Raman spectroscopy. Applied Physics B 1996;62:29–37.

[58] Leipertz A, Magens E, Seeger T, Spiegel H. Flame Diagnostics by Pure Rotational CARS. Aerothermodynamics in Combustors, 1992.

[59] Afzelius M, Brackmann C, Vestin F, Bengtsson E. Pure rotational coherent anti-Stokes Raman spectroscopy in mixtures of CO and N2. Appl Opt 2004;43.

[60] Bohlin A, Bengtsson PE. Rotational CARS thermometry in diffusion flames: On the influence of nitrogen spectral line-broadening by CH4 and H2. Proceedings of the Combustion Institute 2011;33:823–30. https://doi.org/10.1016/j.proci.2010.05.023.

[61]   Schenk M, Seeger T, Leipertz A. Time-resolved CO2 thermometry for pressures as great as 5 MPa by use of pure rotational coherent anti-Stokes Raman scattering. Appl Opt 2005;44.

[62]   Vestin F, Nilsson K, Bengtsson E. Validation of a rotational coherent anti-Stokes Raman spectroscopy model for carbon dioxide using high-resolution detection in the temperature range 294-1143 K. 2008.

[63]   Bohlin A, Kindeya A, Nordström E, Bengtsson PE. Validation of a rotational coherent anti-Stokes Raman scattering model for N2O at temperatures from 295 K to 796 K. Journal of Raman Spectroscopy, vol. 43, John Wiley and Sons Ltd; 2012, p. 604–10. https://doi.org/10.1002/jrs.3148.

[64]   Nordström E, Bohlin A, Bengtsson PE. Pure rotational Coherent anti-Stokes Raman spectroscopy of water vapor and its relevance for combustion diagnostics. Journal of Raman Spectroscopy, vol. 44, John Wiley and Sons Ltd; 2013, p. 1322–5. https://doi.org/10.1002/jrs.4275.

[65]   Buldyreva J, Bonamy J, Weikl MC, Beyrau F, Seeger T, Leipertz A, et al. Linewidth modelling of C2H2-N2 mixtures tested by rotational CARS measurements. Journal of Raman Spectroscopy, vol. 37, John Wiley and Sons Ltd; 2006, p. 647–54. https://doi.org/10.1002/jrs.1491.

[66]   Bengtsson P-E, Martinsson L, Alden M. Combined Vibrational and Rotational CARS for Simultaneous Measurements of Temperature and Concentrations of Fuel, Oxygen, and Nitrogen. 1995.

[67]   Hosseinnia A, Nordström E, Bood J, Bengtsson PE. Ethane thermometry using rotational coherent anti-Stokes Raman scattering (CARS). Proceedings of the Combustion Institute 2017;36:4461–8. https://doi.org/10.1016/j.proci.2016.06.011.

[68]   Hosseinnia A, Nordström E, Fatehi H, Bood J, Bengtsson PE. Rotational CARS thermometry and concentration measurements in ethane-nitrogen mixtures using Fourier analysis. Journal of Raman Spectroscopy 2018;49:1096–108. https://doi.org/10.1002/jrs.5339.

[69]   Bloembergen N, Chen K -H, Lü C -Z, Mazur E. Multiplex pure rotational coherent anti-stokes Raman spectroscopy in a molecular beam. Journal of

Raman   Spectroscopy   1990;21:819–25.
https://doi.org/10.1002/jrs.1250211210.

[70]   Hosseinnia A, Brackmann C, Bengtsson PE. Pure rotational coherent anti-
        Stokes Raman spectroscopy of ethylene, experiments and modelling. J Quant
        Spectrosc   Radiat   Transf   2019;234:24–31.
        https://doi.org/10.1016/j.jqsrt.2019.05.022.

[71]   Bohlin A, Nordström E, Carlsson H, Bai XS, Bengtsson PE. Pure rotational
        CARS measurements of temperature and relative O2 concentration in a low
        swirl turbulent premixed flame. Proceedings of the Combustion Institute
        2013;34:3629–36. https://doi.org/10.1016/j.proci.2012.05.016.

[72]   Alden M, Bengtsson P-E, Edner H, Kroll S, Nilsson D. Rotational CARS: a
        comparison of different techniques with emphasis on accuracy in
        temperature determination. Appl Opt 1989;28.

[73]   Lang T, Kompa K-L, Motzkus M. Femtosecond CARS on H2. Chem Phys
        Lett 1999.

[74]   Beaud P, Frey H-M, Lang T, Motzkus M. Flame thermometry by
        femtosecond CARS. Chem Phys Lett 2001;344:407–12.

[75]   Maine P, Strickland D, Bado P, Pessot M, Mourou DG. Generation of
        Ultrahigh Peak Power Pulses by Chirped Pulse Amplification. IEEE J
        Quantum Electron 1088;24.

[76]   Prince BD, Chakraborty A, Prince BM, Stauffer HU. Development of
        simultaneous frequency- And time-resolved coherent anti-Stokes Raman
        scattering for ultrafast detection of molecular Raman spectra. Journal of
        Chemical Physics 2006;125. https://doi.org/10.1063/1.2219439.

[77]   Pestov D, Murawski RK, Ariunbold GO, Wang X, Zhi M, Sokolov A V, et
        al. Optimizing the Laser-Pulse Configuration for Coherent Raman
        Spectroscopy. n.d.

[78]   Courtney TL, Mecker NT, Patterson BD, Linne M, Kliewer CJ. Hybrid
        femtosecond/picosecond pure rotational anti-Stokes Raman spectroscopy of
        nitrogen at high pressures (1-70 atm) and temperatures (300-1000 K). Appl
        Phys Lett 2019;114. https://doi.org/10.1063/1.5071438.

[79] Bohlin A, Patterson BD, Kliewer CJ. Communication: Simplified two-beam rotational CARS signal generation demonstrated in 1D. Journal of Chemical Physics 2013;138. https://doi.org/10.1063/1.4793556.

[80] Bohlin A, Mann M, Patterson BD, Dreizler A, Kliewer CJ. Development of two-beam femtosecond/picosecond one-dimensional rotational coherent anti-Stokes Raman spectroscopy: Time-resolved probing of flame wall interactions. Proceedings of the Combustion Institute 2015;35:3723–30. https://doi.org/10.1016/j.proci.2014.05.124.

[81] Bohlin A, Kliewer CJ. Communication: Two-dimensional gas-phase coherent anti-Stokes Raman spectroscopy (2D-CARS): Simultaneous planar imaging and multiplex spectroscopy in a single laser shot. Journal of Chemical Physics 2013;138. https://doi.org/10.1063/1.4810876.

[82] Bohlin A, Kliewer CJ. Diagnostic imaging in flames with instantaneous planar coherent Raman spectroscopy. Journal of Physical Chemistry Letters 2014;5:1243–8. https://doi.org/10.1021/jz500384y.

[83] Miller JD, Slipchenko MN, Mance JG, Roy S, Gord JR. 1-kHz two-dimensional coherent anti-Stokes Raman scattering (2D-CARS) for gas-phase thermometry. Opt Express 2016;24:24971. https://doi.org/10.1364/oe.24.024971.

[84] Barros J, Scherman M, Lin E, Fdida N, Santagata R, Attal-Tretout B, et al. 5 kHz single shot hybrid fs/ps-CARS thermometry in an atmospheric flame. Opt Express 2020;28:34656. https://doi.org/10.1364/oe.404380.

[85] Scherman M, Barros J, Santagata R, Lin E, Nicolas P, Faleni JP, et al. 1-kHz hybrid femtosecond/picosecond coherent anti-Stokes Raman scattering thermometry of turbulent combustion in a representative aeronautical test rig. Journal of Raman Spectroscopy 2021;52:1643–50. https://doi.org/10.1002/jrs.6106.

[86] Roy S, Hsu PS, Jiang N, Slipchenko MN, Gord JR. 100-kHz-rate gas-phase thermometry using 100-ps pulses from a burst-mode laser. Opt Lett 2015;40:5125. https://doi.org/10.1364/ol.40.005125.

[87]   Miller JD, Slipchenko MN, Meyer TR. Probe-pulse optimization for nonresonant suppression in hybrid fs/ps coherent anti-Stokes Raman scattering at high temperature. Opt Express 2011;19:13326.

[88]   Rahman KA, Braun EL, Slipchenko MN, Roy S, Meyer TR. Flexible chirp-free probe pulse amplification for kHz fs/ps rotational CARS. Opt Lett 2020;45:503. https://doi.org/10.1364/ol.382033.

[89]   Santagata R, Scherman M, Toubeix M, Nafa M, Tretout B, Bresson A. Ultrafast background-free ro-vibrational fs/ps-CARS thermometry using an Yb:YAG crystal-fiber amplified probe. Opt Express 2019;27:32924. https://doi.org/10.1364/oe.27.032924.

[90]   Thompson RJ, Dedic CE. Hybrid fs/ps CARS for quantifying CO and CO2. AIAA Science and Technology Forum and Exposition, AIAA SciTech Forum 2022, American Institute of Aeronautics and Astronautics Inc, AIAA; 2022. https://doi.org/10.2514/6.2022-0893.

[91]   Engel SR, Miller JD, Dedic CE, Seeger T, Leipertz A, Meyer TR. Hybrid femtosecond/picosecond coherent anti-Stokes Raman scattering for high-speed CH4/N2 measurements in binary gas mixtures. Journal of Raman Spectroscopy, vol. 44, John Wiley and Sons Ltd; 2013, p. 1336–43. https://doi.org/10.1002/jrs.4261.

[92]   Kearney SP, Scoglietti DJ. Hybrid femtosecond/picosecond rotational coherent anti-Stokes Raman scattering at flame temperatures using a second-harmonic bandwidth-compressed probe. 2013.

[93]   Kearney SP, Danehy PM. Pressure measurements using hybrid femtosecond/picosecond rotational coherent anti-Stokes Raman scattering. Opt Lett 2015;40:4082. https://doi.org/10.1364/ol.40.004082.

[94]   Kearney SP, Richardson DR, Retter J, Dedic C, Danehy PM. Simultaneous temperature/pressure monitoring in compressible flows using hybrid fs/ps pure-rotational cars. AIAA Scitech 2020 Forum 2020. https://doi.org/10.2514/6.2020-0770.

[95]   Escofet-Martin D, Ojo AO, Collins J, Mecker NT, Linne M, Peterson B. Dual-probe 1D hybrid fs/ps rotational CARS for simultaneous single-shot

temperature, pressure, and O2 /N2 measurements. Opt Lett 2020;45:4758. https://doi.org/10.1364/ol.400595.

[96] Retter JE, Elliott GS. On the possibility of simultaneous temperature, species, and electric field measurements by coupled hybrid fs/ps CARS and EFISHG. Appl Opt 2019;58:2557. https://doi.org/10.1364/ao.58.002557.

[97] Courtney TL, Bohlin A, Patterson BD, Kliewer CJ. Pure-rotational H2 thermometry by ultrabroadband coherent anti-stokes Raman spectroscopy. Journal of Chemical Physics 2017;146. https://doi.org/10.1063/1.4984083.

[98] Bohlin A, Kliewer CJ. Two-beam ultrabroadband coherent anti-Stokes Raman spectroscopy for high resolution gas-phase multiplex imaging. Appl Phys Lett 2014;104. https://doi.org/10.1063/1.4862980.

[99] Bohlin A, Kliewer CJ. Single-shot hyperspectral coherent Raman planar imaging in the range 0-4200 cm-1. Appl Phys Lett 2014;105. https://doi.org/10.1063/1.4900477.

[100] Brown JM, Carrington A. Rotational Spectroscopy of Diatomic Molecules. Cambridge University Press; 2003.

[101] McQuarrie DA, Simon JD. Physical chemistry: a molecular approach. vol. 1. Sausalito, CA: University science books; 1997.

[102] Herzberg G. Spectra of diatomic molecules. Florida: Robert E. Krieger Publishing Company; 1989.

[103] Long DA. Raman spectroscopy. vol. 1. New York: 1977.

[104] Steinmetz SA, Kliewer CJ. Phase matching in two-dimensional coherent Raman imaging. Opt Express 2020;28:34586. https://doi.org/10.1364/oe.405517.

[105] Long DA. Classical Theory of Rayleigh and Raman Scattering. John Wiley & Sons: 2002.

[106] Tipping RH, Ogilvie JF. Herman-wallis factors for Raman transitions of $1\sum$-state diatomic molecules. Journal of Raman Spectroscopy 1984;15:38–40. https://doi.org/10.1002/jrs.1250150109.

[107] Bohlin A. Development and application of pure rotational CARS for reactive flows. Lund University, 2012.

[108] Lucht RP, Roy S, Meyer TR, Gord JR. Femtosecond coherent anti-Stokes Raman scattering measurement of gas temperatures from frequency-spread dephasing of the Raman coherence. Appl Phys Lett 2006;89. https://doi.org/10.1063/1.2410237.

[109] Sitz GO, Farrow RL. Preparation and decay of alignment in N2 (v=1). J Chem Phys 1994;101:4682–7. https://doi.org/10.1063/1.467457.

[110] Lavorel B, Millot G, Saint-Loup R, Wenger C, Berger H, Sala JP, et al. Rotational Collisional Line Broadening At High Temperatures In The N2 Fundamental Q-Branch Studied With Stimulated Raman Spectroscopy. Journal de Physique Paris 1986;47:417–25. https://doi.org/10.1051/jphys:01986004703041700.

[111] Gonze ML, Saint-Loup R, Santos J, Lavorel B, Chaux R, Millot G, et al. Collisional line broadening and line shifting in N2-CO2 mixture studied by inverse Raman spectroscopy. vol. 148. 1990.

[112] Bonamy J, Robert D, Hartmann JM, Gonze ML, Saint-Loup R, Berger H. Line broadening, line shifting, and line coupling effects on N2-H2O stimulated Raman spectra. J Chem Phys 1989;91:5916–25. https://doi.org/10.1063/1.457461.

[113] Millot G, Saint-Loup R, Santos J, Chaux R, Berger H, Bonamy J. Collisional effects in the stimulated Raman Q branch of O2 and O2-N2. J Chem Phys 1992;96:961–71. https://doi.org/10.1063/1.462116.

[114] Joubert P, Bonamy J, Gomez L, Bermejo D. N2-H2 isotropic Raman Q-branch linewidths: An Energy-Corrected Sudden scaling law. Journal of Raman Spectroscopy, vol. 39, John Wiley and Sons Ltd; 2008, p. 707–10. https://doi.org/10.1002/jrs.1975.

[115] DePristo AE, Augustin SD, Ramaswamy R, Rabitz H. Quantum number and energy scaling for nonreactive collisions. J Chem Phys 1979;71:850–65. https://doi.org/10.1063/1.438376.

[116] Miller JD, Roy S, Gord JR, Meyer TR. Communication: Time-domain measurement of high-pressure N2 and O2 self-broadened linewidths using hybrid femtosecondpicosecond coherent anti-Stokes Raman scattering. Journal of Chemical Physics 2011;135. https://doi.org/10.1063/1.3665932.

[117] Kliewer CJ, Bohlin A, Nordström E, Patterson BD, Bengtsson PE, Settersten TB. Time-domain measurements of S-branch N 2-N 2 Raman linewidths using picosecond pure rotational coherent anti-Stokes Raman spectroscopy. Appl Phys B 2012;108:419–26. https://doi.org/10.1007/s00340-012-5037-2.

[118] Asawaroengchai C, Rosenblatt GM. Rotational Raman intensities and the measured change with internuclear distance of the polarizability anisotropy of H2, D2, N2, O2, and CO. J Chem Phys 1980;72:2664–9. https://doi.org/10.1063/1.439412.

[119] Salin F, Piche M. Mode locking of Ti:Al2O3 lasers and self-focusing: a Gaussian approximation. Opt Lett 1991;16.

[120] Zheltikov A, L'Huillier A, Krausz F. Nonlinear Optics. In: Trager F, editor. Springer Handbook of Lasers and Optics, Kassel: Springer; 2007.

[121] Owyoung A. The Origins of Nonlinear Refractive Indices of Liquids and Gases. California Institute of Technology, 1971.

[122] Vestin F, Afzelius M, Bengtsson PE. Development of rotational CARS for combustion diagnostics using a polarization approach. Proceedings of the Combustion Institute 2007;31 I:833–40. https://doi.org/10.1016/j.proci.2006.07.066.

[123] Dennis CN, Satija A, Lucht RP. High dynamic range thermometry at 5 kHz in hydrogen-air diffusion flame using chirped-probe-pulse femtosecond coherent anti-stokes Raman scattering. Journal of Raman Spectroscopy 2016;47:177–88. https://doi.org/10.1002/jrs.4773.

[124] Raoult F, Boscheron ACL, Husson D, Sauteret C, Modena A, Malka V, et al. Efficient generation of narrow-bandwidth picosecond pulses by frequency doubling of femtosecond chirped pulses. Opt Lett 1998;23:1117.

[125] Heiner Z, Wang L, Petrov V, Mero M. Broadband vibrational sum-frequency generation spectrometer at 100 kHz in the 950-1750 cm -1 spectral range

utilizing a LiGaS2 optical parametric amplifier. Opt Express 2019;27:15289. https://doi.org/10.1364/oe.27.015289.

[126] Laimgruber S, Schachenmayr H, Schmidt B, Zinth W, Gilch P. A femtosecond stimulated raman spectrograph for the near ultraviolet. Appl Phys B 2006;85:557–64. https://doi.org/10.1007/s00340-006-2386-8.

[127] Yang C, Escofet-Martin D, Dunn-Rankin D, Chien YC, Yu X, Mukamel S. Hybrid femtosecond/picosecond pure-rotational coherent anti-Stokes Raman scattering with chirped probe pulses. Journal of Raman Spectroscopy 2017;48:1881–6. https://doi.org/10.1002/jrs.5262.

[128] Dedic CE. Hybrid fs/ps coherent anti-Stokes Raman scattering for multiparameter measurements of combustion and nonequilibrium. Iowa State University, 2017.

[129] Torge Mecker N, Courtney TL, Patterson BD, Escofet-Martin D, Peterson B, Kliewer CJ, et al. Optimizing hybrid rotational femtosecond/picosecond coherent anti-Stokes Raman spectroscopy in nitrogen at high pressures and temperatures. Journal of the Optical Society of America B 2020;37:1035. https://doi.org/10.1364/josab.383575.

[130] Richardson DR, Kearney SP, Beresh SJ. Femtosecond Coherent Anti-Stokes Raman Spectroscopy in a Cold-Flow Hypersonic Wind Tunnel for Simultaneous Pressure and Temperature Measurements. AIAA SciTech Forum 2022 2022.

[131] Courtney TL, Mecker NT, Patterson BD, Linne M, Kliewer CJ. Generation of narrowband pulses from chirped broadband pulse frequency mixing. Opt Lett 2019;44:835. https://doi.org/10.1364/ol.44.000835.

[132] Castellanos L, Mazza F, Kliukin D, Bohlin A. Pure-rotational 1D-CARS spatiotemporal thermometry with a single regenerative amplifier system. Opt Lett 2020;45:4662. https://doi.org/10.1364/ol.398982.

[133] Zhao H, Tian Z, Wu T, Li Y, Wei H. Dynamic and sensitive hybrid fs/ps vibrational CARS thermometry using a quasi-common-path second-harmonic bandwidth-compressed probe. Appl Phys Lett 2021;118. https://doi.org/10.1063/5.0036303.

[134] Wollenhaupt Matthias, Assion Andreas, Baumert Thomas. Femtosecond Laser Pulses: Linear Properties, manipulation, Generation and Measurement. In: Trager F, editor. Springer Handbook of Lasers and Optics, 2007, p. 937–79.

[135] Arroyo MP, Hanson RK. Absorption measurements of water-vapor concentration, temperature, and line-shape parameters using a tunable InGaAsP diode laser. Appl Opt 1993;32:6104. https://doi.org/10.1364/ao.32.006104.

[136] Murphy WF. The Rayleigh depolarization ratio and rotational Raman spectrum of water vapor and the polarizability components for the water molecule. J Chem Phys 1977;67:5877–82. https://doi.org/10.1063/1.434794.

[137] O'Byrne S, Danehy PM, Tedder SA, Cutler AD. Dual-pump coherent anti-Stokes Raman scattering measurements in a supersonic combustor. AIAA Journal 2007;45:922–33. https://doi.org/10.2514/1.26768.

[138] Hall RJ, Shirley JA, Eckbreth AC. Coherent anti-Stokes Raman spectroscopy: spectra of water vapor in flames. Opt Lett 1979;4.

[139] Hall RJ, Shirley JA. Coherent Anti-Stokes Raman Spectroscopy of Water Vapor for Combustion diagnostics. Appl Spectrosc 1982;37:196–202.

[140] Porter FM, Williams DR. Quantitative CARS Spectroscopy of the Band of Water Vapour. vol. 54. 1992.

[141] Greenhalght DA, Porter FM, England WA. Application of the Rotational Diffusion Model to-the CARS Spectra of High-Temperature, High-pressure Water Vapour. Journal of Raman Spectroscopy 1984;15.

[142] Nishihara M, Freund JB, Glumac NG, Elliott GS. Dual-pump CARS measurements in a hydrogen diffusion flame in cross-flow with AC dielectric barrier discharge. Plasma Sources Sci Technol 2018;27. https://doi.org/10.1088/1361-6595/aab323.

[143] Avila G, Tejeda G, Fernández JM, Montero S. The rotational Raman spectra and cross sections of H2O, D2O, and HDO. J Mol Spectrosc 2003;220:259–75. https://doi.org/10.1016/S0022-2852(03)00123-1.

[144] Patnaik AK, Roy S, Gord JR. Saturation of vibrational coherent anti-Stokes Raman scattering mediated by saturation of the rotational Raman transition. Phys Rev A 2013;87. https://doi.org/10.1103/PhysRevA.87.043801.

[145] Meißner C, Hölzer JI, Seeger T. Determination of N 2 –N 2 and N 2 –O 2 S-branch Raman linewidths using time-resolved picosecond pure rotational coherent anti-Stokes Raman scattering . Appl Opt 2019;58:C47. https://doi.org/10.1364/ao.58.000c47.

[146] Bohlin A, Nordström E, Patterson BD, Bengtsson PE, Kliewer CJ. Direct measurement of S-branch N 2-H 2 Raman linewidths using time-resolved pure rotational coherent anti-Stokes Raman spectroscopy. Journal of Chemical Physics 2012;137. https://doi.org/10.1063/1.4742915.

[147] Mazza F, Griffioen N, Castellanos L, Kliukin D, Bohlin A. High-temperature rotational-vibrational O2-CO2 coherent Raman spectroscopy with ultrabroadband femtosecond laser excitation generated in-situ. Combust Flame 2022;237. https://doi.org/10.1016/j.combustflame.2021.111738.

[148] Toro V V., Mokhov A V., Levinsky HB, Smooke MD. Combined experimental and computational study of laminar, axisymmetric hydrogen-air diffusion flames. Proceedings of the Combustion Institute 2005;30:485–92. https://doi.org/10.1016/j.proci.2004.08.221.

[149] Schenk M, Seeger T, Leipertz A. Simultaneous and time-resolved temperature and relative CO2-N2 and O2-CO2-N2 concentration measurements with pure rotational coherent anti-Stokes Raman scattering for pressures as great as 5 MPa. Appl Opt 2005.

[150] Gonze ML, Saint-Loup R, Santos J, Lavorel B, Chaux R, Millot G, et al. Collisional line broadening and line shifting in N2-CO2 mixture studied by inverse Raman spectroscopy. Chem Phys 1990;148:417–28.

[151] Barlow RS, Frank JH. Effects of Turbulence on Species Mass Fractions in Methane/Air Jet Flames. Symposium (International) on Combustion 1998:1087–95.

[152] Jiang J, Jiang X, Zhu M. A computational study of preferential diffusion and scalar transport in nonpremixed hydrogen-air flames. Int J Hydrogen Energy 2015;40:15709–22. https://doi.org/10.1016/j.ijhydene.2015.08.112.

[153] Ranga Dinesh KKJ, Jiang X, Van Oijen JA, Bastiaans RJM, De Goey LPH. Hydrogen-enriched nonpremixed jet flames: Effects of preferential diffusion. Int J Hydrogen Energy 2013;38:4848–63. https://doi.org/10.1016/j.ijhydene.2013.01.171.

[154] Mukundakumar N, Efimov D, Beishuizen N, van Oijen J. A new preferential diffusion model applied to FGM simulations of hydrogen flames. Combustion Theory and Modelling 2021;25:1245–67. https://doi.org/10.1080/13647830.2021.1970232.

[155] Chu H, Berger L, Grenga T, Wu Z, Pitsch H. Effects of differential diffusion on hydrogen flame kernel development under engine conditions. Proceedings of the Combustion Institute 2023;39:2129–38. https://doi.org/10.1016/j.proci.2022.07.042.

[156] Masri AR, Cleary MJ, Dunn MJ. Turbulent Flames of Hydrogen. In: Tingas E-A, editor. Hydrogen for Future Thermal Engines, 2023, p. 141–60. https://doi.org/10.1007/978-3-031-28412-0_4.

[157] Dibble RW, Hartmann V, Sehefer RW, Kollmann W. Experiments in Fluids Conditional sampling of velocity and scalars in turbulent flames using simultaneous LDV-Raman scattering*. vol. 5. 1987.

[158] Meier W, Prucker S, Cao MH, Stricker W. Characterization of turbulent H2/N2/air jet diffusion flames by single-Pulse spontaneous raman scattering. Combustion Science and Technology 1996;118:293–312. https://doi.org/10.1080/00102209608951983.

[159] Neuber AA, Hassel EP, Janicka J. Comparison of turbulent diffusion flame CARS temperature measurements and Reynolds stress model prediction. International Journal of Energetic Materials and Chemical Propulsion 1994;3:432–40. https://doi.org/10.1615/IntJEnergeticMaterialsChemProp.v3.i1-6.450.

[160] Barlow RS. Proceedings of the International Workshop on Measurement and Computation of Turbulent Nonpremixed Flames. https://tnfworkshop.org/; 1996.

[161] Pitsch H, Chen M, Peters N. Unsteady Flamelet Modeling of Turbulent Hydrogen-Air Diffusion Flames. 1998.

[162] Skottene M, Rian KE. A study of NOx formation in hydrogen flames. Int J Hydrogen Energy 2007;32:3572–85. https://doi.org/10.1016/j.ijhydene.2007.02.038.

[163] D'Ausilio A, Stankovic I, Merci B. Numerical study on the importance of the turbulent inlet boundary condition and differential diffusion in a turbulent H2/N2/air jet diffusion flame. Combustion Science and Technology 2019;191:109–25. https://doi.org/10.1080/00102202.2018.1452402.

[164] Sun H, Yan P, Xu Y. Numerical simulation on hydrogen combustion and flow characteristics of a jet-stabilized combustor. Int J Hydrogen Energy 2020;45:12604–15. https://doi.org/10.1016/j.ijhydene.2020.02.151.

[165] Bohlin A, Jainski C, Patterson BD, Dreizler A, Kliewer CJ. Multiparameter spatio-thermochemical probing of flame-wall interactions advanced with coherent Raman imaging. Proceedings of the Combustion Institute 2017;36:4557–64. https://doi.org/10.1016/j.proci.2016.07.062.

[166] Retter JE, Elliott GS, Kearney SP. Dielectric-barrier-discharge plasma-assisted hydrogen diffusion flame. Part 1: Temperature, oxygen, and fuel measurements by one-dimensional fs/ps rotational CARS imaging. Combust Flame 2018;191:527–40. https://doi.org/10.1016/j.combustflame.2018.01.031.

[167] Zhao Y, Soto Leytan KN, McDonell V, Samuelsen S. Investigation of visible light emission from hydrogen-air research flames. Int J Hydrogen Energy 2019;44:22347–54. https://doi.org/10.1016/j.ijhydene.2019.06.105.

[168] Padley PJ. The origin of the blue continuum in the hydrogen flame. Transactions of the Faraday Society 1960;56:449–54.

[169] Schefer RW, Kulatilaka WD, Patterson BD, Settersten TB. Visible emission of hydrogen flames. Combust Flame 2009;156:1234–41. https://doi.org/10.1016/j.combustflame.2009.01.011.

[170] Patterson BD, Gao Y, Seeger T, Kliewer CJ. Split-probe hybrid femtosecond/picosecond rotational CARS for time-domain measurement of S-branch Raman linewidths within a single laser shot. Opt Lett 2013;38:4566. https://doi.org/10.1364/ol.38.004566.

[171] Dedic CE, Cutler AD, Danehy PM. Characterization of supersonic flows using hybrid fs/ps cars. AIAA Scitech 2019 Forum, American Institute of Aeronautics and Astronautics Inc, AIAA; 2019. https://doi.org/10.2514/6.2019-1085.

[172] Escofet-Martin D, Ojo AO, Collins J, Mecker NT, Linne M, Peterson B. Dual-probe 1D hybrid fs/ps rotational CARS for simultaneous single-shot temperature, pressure, and O 2 /N 2 measurements . Opt Lett 2020;45:4758. https://doi.org/10.1364/ol.400595.

[173] Retter JE, Koll M, Dedic CE, Danehy PM, Richardson DR, Kearney SP. Hybrid time–frequency domain dual-probe coherent anti-Stokes Raman scattering for simultaneous temperature and pressure measurements in compressible flows via spectral fitting. Appl Opt 2023;62:50. https://doi.org/10.1364/ao.472831.

[174] Roquemore WM, Chen L-D, Goss LP, Lynn WF. The Structure of Jet Diffusion Flames. In: Borghi R, Murthy SNB, editors. Turbulent Reacting Flows, 1989, p. 49–63. https://doi.org/10.1007/978-1-4613-9631-4_4.

[175] Katta VR, Goss LP, Roquemore WM. Numerical investigations of transitional H2/N2 jet diffusion flames. AIAA Journal 1994;32:84–94. https://doi.org/10.2514/3.11954.

[176] Mazza F. Ultrabroadband coherent Raman spectroscopy for reacting flows. Delft University of Technology, 2023. https://doi.org/10.4233/uuid:f51b273d-eac8-495b-b692-919eb54b9974.

Optics Letters

Pure-rotational 1D-CARS spatiotemporal thermometry with a single regenerative amplifier system

Leonardo Castellanos, Francesco Mazza, Dmitrii Kliukin, ^{ID} and Alexis Bohlin* ^{ID}

Faculty of Aerospace Engineering, Delft University of Technology, Kluyverweg 1, 2629 HS Delft, The Netherlands
*Corresponding author: G.A.Bohlin@tudelft.nl

We report spatiotemporal pure-rotational coherent anti-Stokes Raman spectroscopy (CARS) in a one-dimensional imaging arrangement obtained with a single ultrafast regenerative amplifier system. The femtosecond pump/Stokes photon pairs, used for impulsive excitation, are delivered by an external compressor operating on a ~35% beam split of the uncompressed amplifier output (2.5 mJ/pulse). The picosecond 1.2 mJ probe pulse is produced via the second-harmonic bandwidth compression (SHBC) of the ~65% remainder of the amplifier output (4.5 mJ/pulse), which originates from the internal compressor. The two pump/Stokes and probe pulses are spatially, temporally, and repetition-wise correlated at the measurement, and the signal generation plane is relayed by a wide-field coherent imaging spectrometer onto the detector plane, which is refreshed at the same repetition rate as the ultrafast regenerative amplifier system. We demonstrate 1 kHz cinematographic 1D-CARS gas-phase thermometry across an unstable premixed methane/air flame-front, achieved with a single-shot precision <1% and accuracy <3%, 1.4 mm field of view, and an excellent <20 μm line-spread function. © 2020 Optical Society of America

https://doi.org/10.1364/OL.398982

Coherent anti-Stokes Raman spectroscopy (CARS) has been used to provide gas-phase quantitative scalar information (e.g., temperature and species concentration) in turbulent flows and flames for more than five decades. The technique belongs to the family of four-wave mixing, where the CARS signal is generated via the nonlinear optical interaction of three photons—denoted pump, Stokes, and probe—coupled to the internal energy states of the probed molecules. In dual-broadband pure-rotational CARS [1–3], transitions ($\Delta v = 0$, $\Delta J = \pm 2$) are induced within the entire rotational energy states manifold, and temperature is extracted from the relative intensity of the CARS spectral lines, following the Boltzmann population distribution. In hybrid femtosecond (fs)/picosecond (ps) pure-rotational CARS thermometry [4], the pump and Stokes photons are provided by broadband near-transform-limited femtosecond laser pulses, and the probe photon is provided by a narrowband picosecond laser pulse. The intra-pulse combination follows

the description of simultaneous time- and frequency-resolved probing [5,6], and the excitation is termed impulsive if the duration of the femtosecond laser pulses is about one-tenth of the molecular rotational period [7] (a ~50 fs laser pulse is required to impulsively excite N_2 with a ~500 fs rotational period). The impulsive excitation drives the pure-rotational O- and S-branch transitions ($\Delta J = \pm 2$) with equal efficiency, which is important to maintain the thermodynamic condition of the sample. The spectral resolution of this scheme is limited by the probe pulse linewidth and, if considering the energy separation of the pure-rotational N_2 CARS spectral lines ($\Delta E_J \sim 4B = 8 \text{ cm}^{-1}$), a ~10 ps duration probe pulse would result in isolated spectral lines, dispersed at the detector. The picosecond CARS probe pulse can be efficiently produced from the broadband source using second-harmonic bandwidth compression (SHBC) [8], and is automatically repetition-wise synchronized with the pump and Stokes pulses at the measurement. The repetition rate of ultrafast regenerative amplifier laser systems is conventionally in the kHz range, and the fast sequence of pulses can be utilized for spatiotemporal CARS thermometry [9]. In addition, the high peak power of short laser pulses allows for instantaneous one- and two-dimensional pure-rotational CARS signal generation [10,11]. Single-shot CARS imaging is very powerful in the study of flame-fronts, whose propagation depends highly on spatial effects such as diffusion, mixing, and energy transfer.

In this work, we combine many of these recent advancements for pure-rotational CARS thermometry and build a new diagnostics capability with simultaneous resolution obtained in space–time, here demonstrated across an unstable premixed methane/air flame-front. In Fig. 1, the optical layout, which is based primarily on a single ultrafast regenerative amplifier system (7.5 mJ, 1 kHz, Astrella Coherent), is displayed. The laser system outputs two repetition-wise synchronized beams: the first beam is the main compressed output (~65%, 4.5 mJ/pulse), and the second beam is an uncompressed output, which is split off before the internal compressor (~35%, 2.5 mJ/pulse). The first beam is directed to a SHBC unit (light conversion) to produce a narrowband ~4 ps duration probe pulse, obtained with a ~30% conversion efficiency (1.2 mJ/pulse). The second beam is sent to an external compressor (coherent) to produce a near-transform-limited

~35 fs duration combined pump/Stokes pulse. The external compressor allows for flexible compensation (pre-chirping) of dispersion terms along the optical path, ensuring the delivery of impulsive excitation at the measurement. The path length difference between the pump/Stokes beam and the probe beam is compensated for with an optical delay line, and the relative arrival time is controlled by an automated translation stage (Thorlabs, sub-10 fs resolution). A spatial $4f$-filter, consisting of two transmission gratings (~3040 l/mm, Ibsen Photonics), two cylindrical lenses ($f := 300$ mm), and a mechanical slit, is mounted in the probe beam path to tune the probe pulse linewidth. A set of half-wave plates (Eksma Optics) is inserted to: 1) satisfy the transmission axis of the gratings ($> 90\%$ diffraction efficiency at 400 nm, s-pol) for the probe beam (400 nm), 2) control the relative polarization of the pump/Stokes beam (800 nm) with respect to the probe beam, and 3) turn the polarization of the CARS beam (400 nm) to satisfy the transmission axis of the polarization beam splitter and the grating of the spectrometer. Since the spectral range of the pure-rotational N_2 CARS signal is in close vicinity of the probe beam wavelength, the probe beam needs to be rejected before the detector plane. In this work, the rejection is performed by the angle-tuning of a bandpass filter (Semrock) and is reinforced with various degrees of polarization gating [12]. The 1D-CARS signal is generated with two-beam phase matching [10], and the one-dimensional measurement geometry is formed by crossing the pump/Stokes and the probe beams, both shaped into thin sheets. The field of view (FOV) is optimized with convergent sheet-forming optics, where the irradiance of the beams is enhanced simply by compressing the laser-sheet height by shortening the CLh cylindrical lens ($f := 300$ mm at 400 nm, and $f := 1000$ mm at 800 nm) distance, relative to the CLv cylindrical lens ($f := 300$ mm at 400 nm, and $f := 500$ mm at 800 nm). The notations h-horizontal and v-vertical indicate the alignment symmetry axes of the cylindrical lenses, respectively. The FOV is limited by the ~1.4 mm height of the probe beam sheet, and the height of the pump/Stokes beam sheet is ~4 mm (fluence level ~18 TW/cm^2), as measured with a beam profiling camera (DataRay) placed at the beam crossing. The beam waists of the pump/Stokes and the probe beams are verified to be close to diffraction limited (< 60 μm and < 22 μm, respectively) with $M^2 = 1.2$, and the focal length of the cylindrical lenses is selected to minimize spatial averaging while retrieving the steep temperature gradient in the flame-front. The two-beam crossing angle of ~3° employed here results in a measured interaction length of ~0.6 mm; however, the requirement of spatial sectioning in the beam's longitudinal direction is relaxed at the current flame geometry. The 1D-CARS signal generation plane is relayed to the detector plane by a ~1:1 magnifying telescope composed of two achromatic plano-convex lenses ("spherical" SL, $f := 400$ mm). The telescope, combined with a transmission grating (~3040 l/mm, Ibsen Photonics), acts as a wide-field "slit-less" coherent imaging spectrometer. The high-dispersion grating allows for isolated spectral analysis of the pure-rotational N_2 CARS transitions, and the detection (over the range ~0 − 525 cm^{-1}, 0.25 cm^{-1}/pixel, 2048 pixels) is obtained with an instrumental broadening function (fitted with a Voigt lineshape consisting of a ~0.1 cm^{-1} FWHM Lorentzian and a ~1.8 cm^{-1} FWHM Gaussian contribution). The spatial information is retrieved with a < 20 μm FWHM line-spread function using collimating and imaging lenses with
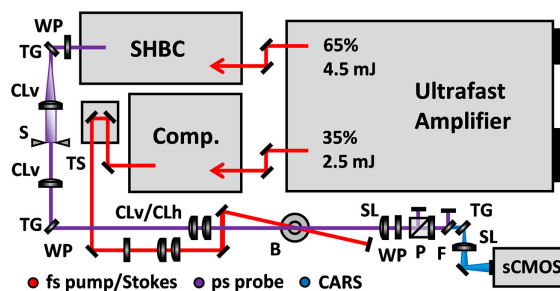

Fig. 1. Ultrafast amplifier system, combined with SHBC and an external compressor, produces auto-synchronized fs pump/Stokes and ps probe pulses for space–time 1D-CARS diagnostics. A wide-field coherent imaging spectrometer equipped with a sCMOS camera is used for fast image acquisition. TG, transmission grating; S, slit; TS, translation stage; CL, cylindrical lens with horizontal (h) and vertical (v) alignment symmetry axes; WP, half-wave plate; B, burner; P, polarizer; F, bandpass filter; SL, spherical lens.

$f := 400$ mm focal distance and 10.6 mm beam size. This was quantified by the spread of an edge response, by inserting a razor blade in the probe beam, at the CARS signal generation plane. The data rows are binned within the line-spread function ($2 \times$ rows $= 2 \times 6.5 = 13$ μm), resulting in a digital resolution still finer than the spatial resolution. A sCMOS camera (Zyla 4.2, Andor) with manufacturer specified linearity of 99.8% and 40% quantum efficiency at 400 nm is mounted at the spectrometer image plane, allowing for repetition-wise synchronized detection, with 200×2048 pixel image acquisition obtained at a 1 kHz frame rate.

The SHBC technique consists of the sum-frequency generation (SFG) of phase-conjugate linearly chirped femtosecond pulses, combined in a χ_2 nonlinear crystal. A spectral filtering of the SHBC-produced probe pulse is required, because it contains both the fundamental SFG component and spectral side-bands. The spectral side-bands are due to imperfections in the conversion of the pump beams [13] and, despite being several orders of magnitude weaker than at the peak of the probe beam, their intensity is comparable to the CARS signal strength. Therefore, if not modeled correctly, the interference of these side-bands with the CARS spectral lines can obstruct the evaluation of temperature and species concentrations in the flame. We solve this by implementing a tunable pulse shaper ($4f$-filter in transmission), which effectively removes the residual side-bands originating from the SFG process. As a narrow portion of the input probe pulse spectrum is transmitted through the slit of the pulse shaper, the residual temporal chirp is minimized, and the resulting pulse is near-transform-limited. The filtering occurs with minimal losses in pulse energy due to the employment of high-end transmission gratings with $> 90\%$ diffraction efficiency. In Figs. 2(a) and 2(b), the temporal (13, 8, and 5 ps FWHM) and spectral (~2.7, 3.1, and 5.0 cm^{-1} FWHM) profiles of the CARS probe pulse are displayed, as resulting from different discriminating slit-widths in the pulse shaper: 70, 100, and 150 μm, respectively. Accordingly, by adjusting the opening of the mechanical slit, the probe pulse duration can easily be tuned in a wide range of 4–13 ps, with corresponding pulse energies of 1.2–0.3 mJ, respectively. The temporal profile of the probe pulse is measured through a probe-delay scan performed in argon. Argon is a noble gas, with no resonant CARS transitions. The instantaneous four-wave-mixing signal is instead a
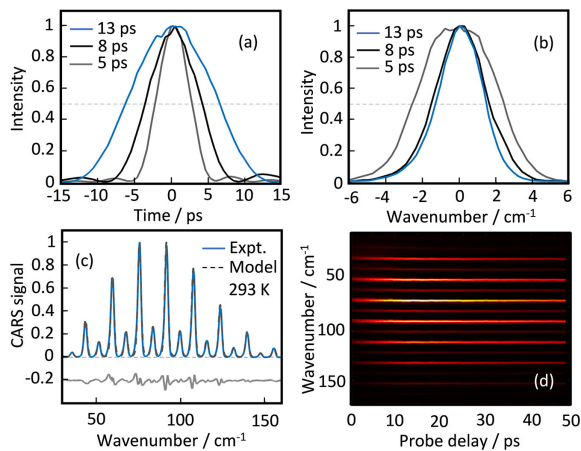
Fig. 2. Time- and frequency-domain characteristics of the SHBC-produced probe after passing through a tunable pulse shaper. (a) Temporal profile resulting in a probe pulse with a 13, 8, and 5 ps FWHM duration, respectively. (b) Corresponding bandwidths of the probe pulse are ∼2.7, 3.1, and 5 cm^{-1} FWHM. (c) Single-shot pure-rotational N_2 CARS spectrum with the best-fit of a time-domain CARS model and residuals. (d) Pure-rotational N_2 CARS spectra at variable probe delays.

non-resonant CARS signal, which is generated as a consequence of time-coinciding fs pump/Stokes and ps probe beams. Thus, a sequential delay of the beams' overlap in time (probe-delay scan), while recording the non-resonant CARS signal, maps the temporal shape of the probe pulse. The spectral profile of the probe pulse is measured with the imaging spectrometer, and after de-convolving the measured spectrum from the instrument broadening function, the results presented in Figs. 2(a) and 2(b) are in good agreement with the expected time-bandwidth product. One should be aware of the fact that the current pulse shaping, which consists of the introduction of a hard edge in the probe spectral domain, also results in slight ringing artifacts in the probe temporal profile, which is described in close analogy with the standard transform pair of a sinc function [14]. As such, the complete temporal shape of the SHBC-produced probe beam, after passing through the tunable pulse shaper, needs to be considered in the modeling of the CARS spectra. A single-shot pure-rotational N_2 CARS spectrum recorded at room temperature, with the best-fit of a time-domain CARS model (see, for instance, Refs. [4,8]) and residuals, is displayed in Fig. 2(c). Here, a ∼13 ps duration probe pulse is employed, with a ∼40 ps probe delay: the well-isolated spectral lines dispersed at the detector can be observed.

In recent works that also concern the shaping of a narrow-band picosecond probe pulse for use in fs/ps CARS (e.g., with SHBC [13,15] and volume Bragg gratings [16,17]), temporal chirp (group velocity dispersion) has been discussed as a possible artifact. Although the temporal chirp in the probe pulse can be adequately modeled for point-CARS thermometry [15], the use of a sub-10 ps probe pulse in 1D-CARS imaging becomes slightly more critical, and it is of great importance to minimize effects due to temporal chirp in the probe pulse. The presence of temporal chirp in the probe pulse has a direct impact on the CARS signal, by shifting it according to the instant central frequency of the probe pulse. This is due to the fact that the peaks in the molecular interferogram, in response

to the impulsive excitation, act as a "temporal gate" on the probe pulse. Other complications, which may arise due to temporal chirp in the probe pulse, are an "uncontrolled" beating of the $O_2/N_2 J$-specific spectral lines and a considerable uncertainty in the spectrometer calibration. In Fig. 2(d), pure-rotational N_2 CARS spectra at variable probe delays are shown. Since the CARS signal remains at its spectral position, the absence of temporal chirp in the probe pulse with the current settings is clearly demonstrated. A spatial chirp of ∼2 cm^{-1}/mm is compensated for by floating the calibration shift of each row at the image in the spectral fitting routine.

The benchmarking of the spatiotemporal pure-rotational 1D-CARS thermometry is performed across an unstable laminar flame-front. A snap-shot photograph in Fig. 3(a) shows the used V-shaped flame, which is anchored at a steel rod (3 mm diameter) positioned ∼10 mm above a nozzle (10 mm tube diameter). The nozzle feeds the combustible mixture (premixed methane/air at $\Phi = 0.9$) with a bulk velocity of ∼1.3 m/s, controlled with rotameters (Omega) supplying the fuel- and oxidizer streams. The V-shaped laminar flame-front has a relatively flat structure and consists of a "thin" layer (∼400 μm, global thickness), where most of the exothermic reactions take place. This results in a steep temperature gradient, where almost the complete combustion history, from the unburnt mixture to the post-flame region, is covered within the ∼1.5 mm FOV.

A dataset of 1000 single-shot 1D-CARS images, each containing 200 spatially correlated spectra, was acquired at a 1 kHz frame rate. A typical single-shot 1D-CARS image is shown in Fig. 3(c). The spatial information, along the y axis, is oriented perpendicularly across the flame-front, and the x axis displays the dispersed CARS spectrum for a unique spatial position in the flame. It can be seen in Fig. 3(c) that the image is dominated by the pure-rotational N_2 CARS spectral lines (S-branch transitions), with the central weight of the spectral envelope corresponding to the local flame temperature. In addition, distinct pure-rotational O_2 CARS spectral lines can be distinguished up to the middle of the image, where most of the oxygen gets consumed in the combustion process. The CARS signal at room temperature is two orders of magnitude stronger than at flame temperature, as the signal strength scales with the square of the number density of the gas. In Fig. 3(c), the logarithm of the CARS intensity is shown, to stretch the global contrast in the image. Usually, the signal-to-background ratio rapidly degrades in the products zone, making it challenging to capture the entire temperature profile without camera saturation in the preheating zone. A balanced detection technique is employed by introducing a longer probe delay (∼40 ps), which takes advantage of the significantly higher collisional dephasing of the signal in the low temperature region of the flame. Figures 3(d) and 3(e) show single-shot CARS spectra at locations post- and pre-flame-front, respectively, which have been extracted from the CARS image in Fig. 3(c). Both spectra are background-subtracted and the spectral referencing, which accounts for the finite width of the excitation bandwidth, is performed by dividing the resonant CARS spectra with a non-resonant CARS spectrum recorded in argon. A satisfactory best-fit is obtained with a time-domain CARS model (similar to Refs. [4,8]), and is confirmed along the entire FOV. The precision and accuracy of the current CARS thermometry are evaluated in the product gases at a distance of ∼190 μm conditional to the flame-front (inferred at the 1000 K isotherm). In Fig. 3(b), the discrete probability density

Fig. 4. Spatiotemporal evolution map of (a) temperature and (b) relative species concentration (oxygen/nitrogen) across the reaction layer of an unstable premixed flame as measured with space–time CARS resolution.
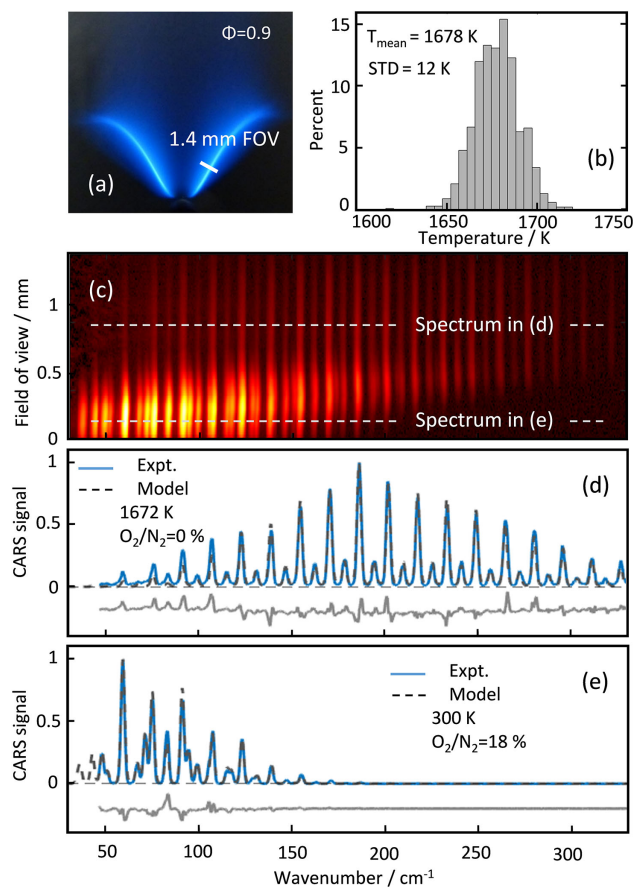
Fig. 3. (a) Snap-shot photograph of the premixed methane/air V-shaped flame-front intersected with the 1D-CARS measurement field of view. (b) Discrete probability density function from a recording in the product gases of the flame ($\Phi = 0.9$). (c) Single-shot 1D-CARS image recorded across the flame-front at 1 kHz frame rate. CARS spectrum (d) post- and (e) pre-flame-front displayed with the best-fit model and residuals.

In conclusion, we have demonstrated two-beam fs/ps pure-rotational CARS line imaging at kilohertz refresh rate. This was achieved with a single regenerative amplifier system, combined with suitable compressor units, producing both the fs pump/Stokes and the ps probe beams, auto-synchronized with the detector. The current space–time CARS resolution (1.4 mm FOV and 1 kHz acquisition) allows for mapping temperature and relative species concentrations (oxygen/nitrogen) in dynamical scenes, such as those found, for instance, in moderate turbulent flames.

Disclosures. The authors declare no conflicts of interest.

function (PDF) obtained is reported. The CARS evaluated mean temperature $T_{mean} = 1678$ K, can be compared with an expected temperature of ∼1720 K for the current flame condition as computed with the CHEM1D code [18]. A systematic deviation of ∼2.5% thus results from the comparison with the numerical simulation. The main contribution to inaccuracy is ascribed to the uncertainty in the employed settings of the rotameters for controlling the oxidizer and the fuel streams. Nonetheless, the precision of the current CARS technique is ∼0.7% in the central portion of the image, which has the highest excitation efficiency and probe beam intensity.

The spatiotemporal evolution of temperature and relative O_2/N_2 concentrations across the flame-front is displayed in Fig. 4. With the available space–time CARS resolution, an out-of-phase oscillating pattern with two frequencies at 13 and 75 Hz is clearly identified. We speculate that the lower frequency oscillation pattern might be caused by an unstable local equivalence ratio, induced by the volumetric flow controllers and/or buoyancy effects that provoke the formation of a Kelvin–Helmholtz-type vortex in the boundary of the flame [19]. The 75 Hz signal is most likely to be associated with internal acoustic modes of the burner.
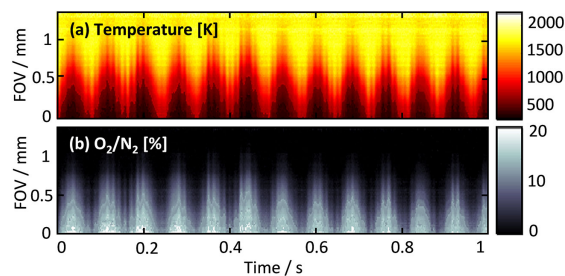
REFERENCES

1. A. C. Eckbreth and T. J. Anderson, Opt. Lett. **11**, 496 (1986).
2. M. Aldén, P. E. Bengtsson, and H. Edner, Appl. Opt. **25**, 4493 (1986).
3. T. Seeger and A. Leipertz, Appl. Opt. **35**, 2665 (1996).
4. J. D. Miller, M. N. Slipchenko, T. R. Meyer, H. U. Stauffer, and J. R. Gord, Opt. Lett. **35**, 2430 (2010).
5. B. D. Prince, A. Chakraborty, B. M. Prince, and H. U. Stauffer, J. Chem. Phys. **125**, 044502 (2006).
6. D. Pestov, R. K. Murawski, G. O. Ariunbold, X. Wang, M. C. Zhi, A. V. Sokolov, V. A. Sautenkov, Y. V. Rostovtsev, A. Dogariu, Y. Huang, and M. O. Scully, Science **316**, 265 (2007).
7. N. Owschimikow, B. Schmidt, and N. Schwentner, Phys. Chem. Chem. Phys. **13**, 8671 (2011).
8. S. P. Kearney and D. J. Scoglietti, Opt. Lett. **38**, 833 (2013).
9. S. Roy, W. D. Kulatilaka, D. R. Richardson, R. P. Lucht, and J. R. Gord, Opt. Lett. **34**, 3857 (2009).
10. A. Bohlin, B. D. Patterson, and C. J. Kliewer, J. Chem. Phys. **138**, 081102 (2013).
11. A. Bohlin and C. J. Kliewer, J. Chem. Phys. **138**, 221101 (2013).
12. F. Vestin, M. Afzelius, and P.-E. Bengtsson, Proc. Combust. Inst. **31**, 833 (2007).
13. T. L. Courtney, N. T. Mecker, B. D. Patterson, M. Linne, and C. J. Kliewer, Opt. Lett. **44**, 835 (2019).
14. M. Marrocco, Opt. Lett. **39**, 4831 (2014).
15. C. Yang, D. Escofet-Martin, D. Dunn-Rankin, Y. C. Chien, X. Yu, and S. Mukamel, J. Raman Spectrosc. **48**, 1881 (2017).
16. R. Santagata, M. Scherman, M. Toubeix, M. Nafa, B. Tretout, and A. Bresson, Opt. Express **27**, 32924 (2019).
17. K. Arafat Rahman, E. L. Braun, M. N. Slipchenko, S. Roy, and T. R. Meyer, Opt. Lett. **45**, 503 (2020).
18. J. A. van Oijen and P. de Goey, Combust. Sci. Technol. **161**, 113 (2000).
19. A. I. Krikunova, Phys. Fluids **31**, 123607 (2019).

Water vapor in hydrogen flames measured by time-resolved collisional dephasing of the pure-rotational N_2 CARS signal

Leonardo Castellanos [a], Francesco Mazza [a], Alexis Bohlin [a,b,*]

[a] *Ultrafast Laser Diagnostics and Flames Laboratory, Faculty of Aerospace Engineering, Delft University of Technology, Kluyverweg 1, Delft 2629 HS, the Netherlands*
[b] *Space Propulsion Laboratory, Department of Computer Science, Electrical and Space Engineering, Luleå University of Technology, Bengt Hultqvists väg 1, Kiruna 98128, Sweden*

Abstract

We present a novel diagnostic technique to probe water vapor (H_2O) concentration in hydrogen (H_2) combustion environments via the time-resolved measurement of the collisional dephasing of the pure-rotational coherent anti-Stokes Raman scattering (CARS) signal of nitrogen (N_2). The rotational Raman coherence of the N_2 molecules, induced by the interaction with the pump and Stokes laser fields, dephases on a timescale of hundreds of picoseconds (ps), mostly due to inelastic collisions with other molecules in atmospheric flames. In the spatial region of H_2 flames where H_2O is present in appreciable amount, it introduces a faster dephasing of the N_2 coherence than the other major combustion species do: we use time-resolved femtosecond/picosecond (fs/ps) CARS to deduce the H_2O mole fraction from the dephasing effect of its inelastic collisions with N_2. The proof-of-principle is demonstrated in a laminar H_2/air diffusion flame, performing sequential measurements of the collisional dephasing of the N_2 CARS signal up to 360 ps. We measure the temperature and the relative O_2/N_2 and H_2/N_2 concentrations at a short probe delay, and input the results in the time-domain model to extract the H_2O mole fraction from the signal decay, thus measuring the whole scalar flow fields across the flame front. We furthermore present single-shot simultaneous thermometry and absolute concentration measurements in the turbulent TU Darmstadt/DLR Stuttgart canonical 'H3 flame' performed by dual-probe CARS measurements obtained with a polarization separation approach. This allows us to probe the molecular coherence simultaneously at ∼20 and ∼250 ps on the basis of a single-laser-shot, and record the resulting signals in two distinct detection channels of our unique polarization-sensitive coherent imaging spectrometer. The proposed technique allows for measuring the absolute concentrations of all the major species of H_2 flames, thus providing a full characterization of the flow composition, as well as of the temperature field.

© 2022 The Author(s). Published by Elsevier Inc. on behalf of The Combustion Institute.

---

* Corresponding author at: Space Propulsion Laboratory, Department of Computer Science, Electrical and Space Engineering, Luleå University of Technology, Bengt Hultqvists väg 1, Kiruna 98128, Sweden.

E-mail address: alexis.bohlin@ltu.se (A. Bohlin).

1. Introduction

Coherent anti-Stokes Raman spectroscopy (CARS) is a laser diagnostic technique that has found vast application to the experimental investigation of combustion processes, owing to the possibility of performing *in-situ*, non-perturbative measurements, with excellent spatial and temporal resolution [1]. CARS is currently the gold-standard for high-fidelity thermometry in gas-phase reacting flows [2], and is employed in many measurement scenarios of practical interest, such as internal combustion engines [3,4] gas-turbine engines [5,6], rocket combustors [7] and detonation processes [8]. In addition to thermometry, CARS has been extensively applied to the detection of major combustion species [9,10], performing relative concentration measurements on both ro-vibrational [11] and pure rotational [12] Raman spectra, and even absolute concentration measurements have been demonstrated [13].

A recognized challenge for absolute concentration measurements in combustion environments is to detect water vapor (H_2O): this is typically achieved through absorption spectroscopy [14] rather than Raman-based techniques, owing to its relatively low Raman cross section [15]. An inherent drawback of absorption spectroscopy is the limitation to line-of-sight measurements: the development of non-linear optical diagnostics could thus provide *in-situ* H_2O measurements with spatial resolution. In the context of hydrogen combustion, H_2O plays a key role as it is the only major product: quantitative measurements of the H_2O concentration and local temperature thus allow for mapping the progress of the chemical reaction. In this respect, the H_2O mass fraction typically plays a key role in the definition of the progress variable employed in numerical codes, e.g. based on flamelet-generated manifolds [43]. O'Byrne et al. [16] employed CARS to measure the temperature and the mole fractions of nitrogen (N_2), oxygen (O_2), and hydrogen (H_2) in a supersonic combustor, and estimated the H_2O concentration by assuming it to be the only other major species contributing to the non-resonant susceptibility of the gas-phase medium. Direct measurements of the ro-vibrational CARS spectrum of the H_2O v_1 symmetric stretch at ~3650 cm^{-1} have been first attempted by Hall et al. [17] in 1979. Hall and Sherley [18], as well as Porter and Williams [19], performed ro-vibrational H_2O CARS thermometry at

temperatures as high as 2000 K. Greenhalgh et al. also investigated the H_2O v_1 CARS spectrum at high temperatures and elevated pressures [20]. Despite the good agreement shown by the experimental data and the theoretical CARS models, further studies on this spectrum were scarce, probably owing to the isolated location of the H_2O v_1 spectrum beyond the vibrational fingerprint region, which hinders the simultaneous detection of multiple species. In this sense, the application of CARS spectroscopy to the pure-rotational spectrum of gas-phase H_2O is more appealing for combustion diagnostics. This was attempted for the first and only time by Nordström et al. [21]: unfortunately, they concluded that H_2O is an unsuitable candidate for CARS concentration measurements in combustion, due to the signal intensity being more than five orders of magnitude smaller than that of N_2. The extreme dimness of the pure-rotational H_2O CARS signal was attributed to both its low Raman cross section and to the large number of rotational transitions of this asymmetric top molecule, characterized by three distinct principal moments of inertia [22].

In the present work, we demonstrate the use of time-resolved CARS to measure the H_2O mole fraction in laboratory flames, through its impact on the pure-rotational N_2 spectrum. Nordström et al. pointed out in the conclusion of their work that, despite its CARS spectrum being negligible, water vapor has a significant collisional impact on the N_2 CARS spectrum, as demonstrated experimentally in [21]. Rotational energy transfer (RET) in inelastic collisions between the coherently excited N_2 molecules and other molecules results in the temporal dephasing of the pure-rotational N_2 CARS signal on a time-scale of picoseconds (ps) at ambient conditions. The development, in recent years, of CARS techniques employing ultrashort laser pulses to resolve the temporal evolution of the Raman coherence [23] opened to the possibility of measuring the collisional RET in the time domain [24]. Here we employ hybrid femtoseconds/picosecond (fs/ps) CARS [25] to measure the dephasing of the pure-rotational N_2 CARS signal due to inelastic collisions with the H_2O molecules in H_2/air flames. The proof-of-principle measurements are performed across a laminar H_2/air diffusion flame, provided on a Bunsen burner. The applicability of the proposed technique to single-shot measurements in turbulent flames is further demonstrated by using single-shot

dual-probe CARS [26] in the canonical H3 flame [27].

2. Theoretical considerations

Hybrid fs/ps CARS employs ultrashort laser pulses to perform simultaneously time- and frequency-resolved ro-vibrational spectroscopy on the Raman-active molecules. Broadband fs pulses provide the pump and Stokes photons, whose frequency difference coherently excite the molecules to higher rotational energy states according to the selection rule: $\Delta v = 0$ and $\Delta J = +2$ (for the pure-rotational S-branch spectrum), where v is the vibrational quantum number, and J is the total angular momentum quantum number. The use of fs pulses further allows for a great simplification of the experimental setup, as a single combined pump/Stokes pulse can be employed to simultaneously deliver the constructive pump/Stokes photon-pairs, which are found across its broad bandwidth [28]. In addition, by using fs pulses with duration lesser than about one tenth of the molecular rotational period (i.e. $\sim$500 fs for N_2), we can maximize the rotational Raman coherence in the medium, through its impulsive excitation [29]. In our setup, we employ a $\sim$35 fs transform-limited (TL) pump/Stokes pulse to excite the rotational Raman coherence of the N_2 molecules, described on a macroscopic scale by the third-order non-linear optical susceptibility of the medium (χ_{CARS}). A relatively narrowband $\sim$12 ps probe pulse is then coherently scattered by the medium resulting in the generation of the CARS signal. The probe pulse is delayed with respect to the pump/Stokes pulse both to time-gate the generation of the non-resonant background and, for the purpose of this work, to measure the collisional dephasing of the Raman signal. The time-domain third-order susceptibility is then the interferogram resulting from the harmonics corresponding to the different Raman frequencies, as:

$$\chi_{CARS} = \sum_v \sum_J W_{v,J \to v,J+2} \cdot$$
$$\exp\left[(i\omega_{v,J \to v,J+2} - \Gamma_{v,J \to v,J+2})t/(2\pi c)\right] \quad (1)$$

where $W_{v,J \to v,J+2}$, $\omega_{v,J \to v,J+2}$, and $\Gamma_{v,J \to v,J+2}$ are respectively the overall probability, the Raman frequency and the temporal dephasing coefficient associated to each pure-rotational S-branch transition (i.e. $J \to J+2$). The temporal evolution of χ_{CARS} is thus determined by the interference of the Raman modes corresponding to transitions from different J states, as well as by the dephasing coefficients associated to the transitions. These account for the spontaneous emission from the coherent molecules and for the effect of decoherence due to molecular collisions. The natural decay life-
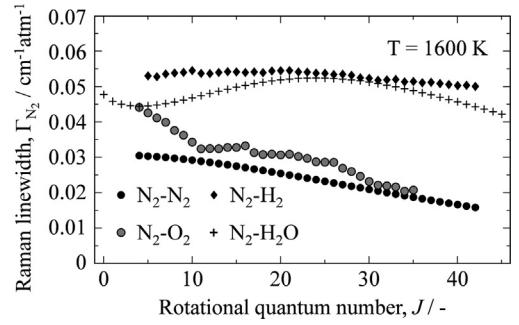

Fig. 1. The J-dependence of the species-specific N_2 CARS dephasing coefficients, for inelastic collisions with the major combustion species in H_2/air flames (i.e. N_2, O_2, H_2, and H_2O) at $T = 1600$ K.

time of N_2 is on the order of seconds due to symmetry constrains [30], so that it can be neglected in our discussion. As for the collisional dephasing, the effect of pure dephasing due to elastic collisions ($\Delta J = 0$) can be neglected at ambient pressure [30], so that the main contribution stems from inelastic collisions ($\Delta J \neq 0$), responsible for the RET between the coherently excited N_2 molecules and the molecular colliders in the flame. The collisional RET is both state-dependent and species-specific, owing to the spacing of the J states in the ro-vibrational energy manifold of the colliding molecules. In the present work, we account for the dephasing of the N_2 CARS signal due to collisions with the following perturbers in H_2/air flames: N_2-N_2 (i.e. self-perturbed) [31], N_2-O_2 [32], N_2-H_2 [33], and N_2-H_2O [34]. Figure 1 shows the corresponding state-dependent dephasing coefficients for $J = 0$-60: while the N_2-N_2 and N_2-O_2 coefficients show a comparable J-dependence, owing to the similar rotational energy manifold, both N_2-H_2 and N_2-H_2O coefficients show peculiar trends over the different J states and have an overall larger magnitude. The J-dependence of the N_2-H_2 coefficients is less pronounced than for the other collisional partners, due to the large spacing between the states in the rotational energy manifold of H_2, resulting in a similarly reduced RET for all the J states of the N_2 molecule. On the other hand, the overall large magnitude of these coefficients is explained by the larger thermal velocity of the lightweight H_2 molecule, allowing it to penetrate closer to the repulsive wall of the interaction potential with the N_2 molecule [33]. The N_2-H_2O dephasing coefficients are characterized by a strongly non-monotonic J-dependence, with a temperature-dependent local maximum (e.g. $J = 24$ at 1600 K), which is attributed to the complex structure of the rotational energy manifold of the H_2O molecule, resulting in a strong dependence of the RET on the initial rotational state of the N_2 molecule [34].

The total N_2 dephasing coefficients are then computed as:

$$\Gamma_{J \to J+2}^{N_2} = \sum_k X_k \cdot \Gamma_{J \to J+2}(N_2 - M_k) \qquad (2)$$

where $\Gamma_{J \to J+2}$ are the dephasing coefficients due to collisions of N_2 with the kth perturber, weighted by its mole fraction. Eq. (2) then introduces the dependence of the N_2 CARS signal on the H_2O mole fraction, which is employed in the present work to measure the H_2O concentration in H_2/air flames. In this context, the collisional environment can be interpreted as an equivalent binary system composed of H_2O on one hand, and a weighted combination of all other perturber species whose concentration is directly measured in the frequency domain (i.e. N_2, O_2 and H_2) on the other:

$$\Gamma_{J \to J+2}^{N_2} = \sum_{k'} X_{k'} \cdot \Gamma_{J \to J+2}(N_2 - M_{k'})$$
$$+ X_{H_2O} \cdot \Gamma_{J \to J+2}(N_2 - H_2O) \qquad (3)$$

The proposed diagnostic approach can thus be employed to measure the H_2O concentration in all combustion environments where the concentration of every other relevant collisional partner is accessible in the CARS spectrum.

3. Experimental methodology

3.1. Laminar flame experiment

The proof-of-principle demonstration of H_2O concentration measurements through the dephasing of the N_2 CARS signal is performed in a laminar H_2/air diffusion flame. The two-beam fs/ps CARS system is described in details in [35]: only a brief summary is presented here. A single regenerative laser amplifier system (Astrella, Coherent) provides ~35 fs (full-width-at-half-maximum, FWHM) pulses at 800 nm, with a total pulse energy of ~7.5 mJ, at 1 kHz repetition rate. The narrowband ps probe pulse is generated at ~403 nm by a second-harmonic bandwidth compressor (SHBC, Light Conversion) fed by a 65% portion slip off the fs laser output. A 4f-filter in transmission is placed in the probe beam path to tune the duration of the pulse: in the present work we set a probe duration of ~12 ps FWHM, with ~300 μJ/pulse, which corresponds to a FWHM bandwidth of ~2.7 cm^{-1}. The resulting spectral resolution is nearly two orders of magnitude larger than the N_2-H_2O Raman linewidths at the flame temperature, as shown in Fig. 1, and it prevents the direct measurement of the H_2O concentration in the frequency domain, by its broadening effect on N_2 lines in the CARS spectrum. The combined fs pump/Stokes pulse originates from the remainder 35% portion of the amplifier output, corresponding to 2.5 mJ/pulse; an external compressor unit is employed to compensate

for the optical dispersion terms arising along the beam path, ensuring a TL pulse at the measurement location. The pump/Stokes and probe pulses are therefore automatically synchronized, and an automated delay stage (sub-10 fs resolution, Thorlabs) is employed to control the relative probe pulse delay. Spherical optics (f : = 500 mm and 300 mm, respectively) focus the pump/Stokes and probe beams to the measurement location, and the crossing angle for the two-beam phase matching configuration is estimated to be ~3°, resulting in the following probe volume dimensions: ~22 μm (height) x ~1.1 mm (length) x ~22 μm (width). Half-wave plates for 400 and 800 mm are used to control the relative polarization of the two laser pulses and, in combination with a thin-film polarizer, to attenuate the pump/Stokes energy to ~60 μJ/pulse and avoid fs laser-induced filamentation [36]. This was verified by performing a power scaling of N_2 CARS signal at room temperature: at this fluence level no change in the spectral envelope was observed. A wedge prism is inserted in the pump/Stokes beam path after the probe volume, and the low-power reflection is imaged onto a beam profiler (WinCamD, Dataray) in the far-field to monitor and maintain the alignment of the pump/Stokes beam when moving the delay stage. The CARS signal is collected in a coherent imaging spectrometer constituted by a relay-imaging telescope (f : = 400 mm) combined with a high-dispersion transmission grating (3039 l/mm, Ibsen Photonics), allowing the detection of the CARS signal over the range ~50–600 cm^{-1}, with 0.25 cm^{-1}/pixel, by the sCMOS detector (Zyla, Andor). The pure-rotational CARS spectra of N_2 and O_2 are thus recorded along with the first two rotational lines of the pure-rotational H_2 CARS spectrum, enabling the measurement of the relative O_2/N_2 and H_2/N_2 concentrations.

The proof-of-principle demonstration of H_2O concentration measurements via time-domain N_2 CARS is performed in a laminar N_2-diluted H_2/air diffusion flame, provided on a Bunsen burner. The burner is made of a seamless, stainless steel pipe with ~19 mm inner diameter; a N_2-H_2 mixture (50%–50% in volume) is inlet with a bulk velocity of ~1 m/s, resulting in a Reynolds number < 150. A stainless steel mesh is placed over the burner at a height-above-the-burner (HAB) of ~30 mm, to stabilize the flame. The CARS measurements were performed at ~1 mm HAB, performing a radial scan from the center of the burner ($y = 0$ mm) and past the rim, with data-points acquired every 0.5 mm up to $y = 12$ mm. At each measurement location 6 datasets of 1000 single-shot CARS spectra were acquired for a probe delaying varying from 30 to 360 ps. The spectra acquired at the lowest probe delay were employed to measure the temperature and the relative O_2/N_2 and H_2/N_2 concentrations. Neglecting the effect of collisions at the short probe delay timescale leads to an inaccuracy of less than
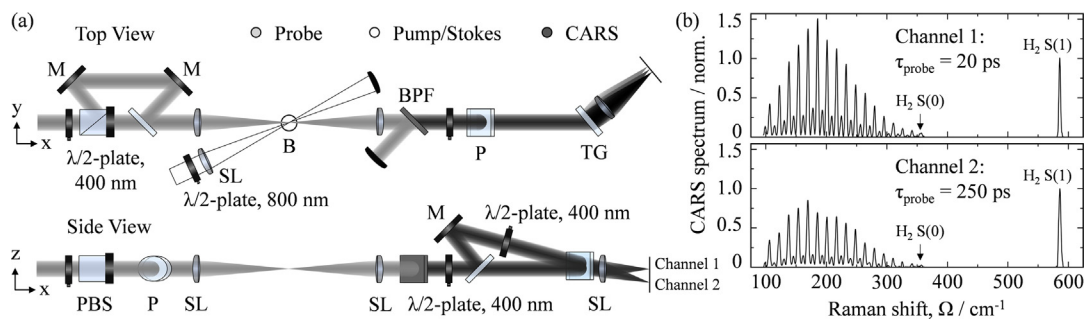
Fig. 2. (a) Schematic of the experimental setup employed for single-shot dual-probe CARS measurements in the H3 flame. A polarization beam splitter (PBS) and a thin-film polarizer (P) are employed to split the probe in two pulses with orthogonal polarization and an recombine them with an intra-pulse delay of 230 ps. The cross-polarized CARS signals are simultaneously collected in two distinct detection channels in the polarization-sensitive coherent imaging spectrometer. $\lambda/2$-plate, half-wave plates; M, mirrors; SL, spherical lenses; BPF, band-pass filter; TG, transmission grating; B, burner. (b) Single-shot CARS spectra simultaneously generated at 20 and 250 ps in the fuel stream of the laminar H_2/air diffusion flame, and recorded in the two detection channels. Both spectra are normalized with respect to the S(1) rotational line of H_2, at 587 cm^{-1}.

$\sim$0.8% in the estimated temperature: the CARS signal generated at this delay is thus assumed as nearly collisional independent. By integrating the N_2 CARS signal acquired at the longer probe delays the collisional dephasing was measured and compared to the single-exponential decay model in Eqs. (1) and (2) to extract the H_2O mole fraction (see Fig. 3).

3.2. Turbulent flame experiment

The methodology described in the previous section requires sequential measurements of the N_2 CARS signal at increasing probe delays and is thus not suitable to measurements in turbulent flames, where the temperature and chemical composition of the flow are highly dynamic. This limitation can be overcome by employing dual-probe CARS, i.e. by splitting the probe pulse and controlling the delay relative to the pump/Stokes pulse, so as to simultaneously perform a collisional-independent measurement at short probe delay and a time-resolved measurement of the RET at longer probe delays. This approach was first demonstrated by Patterson et al. to perform single-shot measurements of the collisional dephasing of the S-branch N_2 CARS spectrum [26], and subsequently employed to perform CARS pressure measurements in 0-D and 1-D configurations [37–40]. In the present work we demonstrate for the first time the use of a polarization separation approach to achieve dual-probe CARS measurements. The experimental setup described in the previous section is slightly modified as depicted in Fig. 2(a). A Glan-Taylor polarization beam splitter (PBS) is mounted on the probe beam path after the 4f-filter with horizontal transmission axis and a 400 nm half-wave plate tunes the ratio of the polarization splitting. The vertically-polarized component of the probe beam is reflected by the PBS and directed to a retroreflector mounted on a linear translation stage to control the relative delay of the two probe pulses: in the present work an intra-pulse delay of $\sim$230 ps was employed. A thin-film polarizer mounted at Brewster's angle is then used to recombine the two cross-polarized probe pulses on the same beam path. The polarization-sensitive coherent imaging spectrometer described in [41] is employed to simultaneously detect the cross-polarized signals in two distinct detection channels. Figure 2(b) present an example of the two single-shot spectra simultaneously generated at 20 and 250 ps in the fuel stream of the laminar H_2/air diffusion flame. The effect of molecular collisions after 250 ps is visible on the envelope of the pure-rotational N_2 CARS spectrum, as well as on the differential dephasing of the pure-rotational H_2 signal characterized by a much lesser RET rate. The balanced detection of the dual-probe CARS setup is performed by changing the pump/Stokes beam path-length to generate the signal (in a room-temperature N_2 flow) with the two probe pulses at the same relative delay, accounting both for the polarization-dependent signal generation efficiency and for the transmission efficiency of the two detection channels. This approach guarantees the automatic overlap of the two probe pulses at the measurement location and minimizes the uncertainty due to phase-mismatch of the degenerate pump/Stokes and probe beams, which can significantly impact the intensity of the second H_2 line at higher Raman shifts.

We demonstrate single-shot H_2O concentration measurements in the TU Darmstadt/DLR Stuttgart H3 flame, which is a canonical turbulent non-premixed H_2/air flame [27]. The burner consists of a straight stainless-steel tube, with 8 mm inner diameter (D) and a tapered rim at the exit, and a concentric contoured nozzle, with an inner
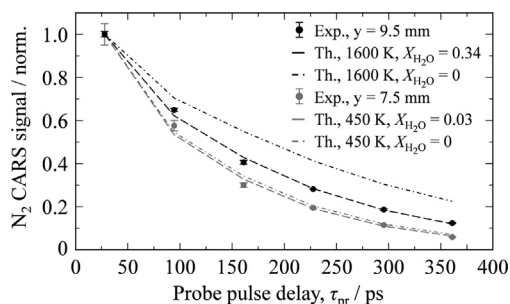
Fig. 3. Experimental measurement of the N_2 CARS signal collisional dephasing at two locations in the reaction zone of the laminar H_2/air flame. The experimental decay is compared to the time-domain CARS model to extract the H_2O mole fraction, resulting in $X_{H2O} = 0.03$ at $y = 7.5$ mm (grey), and $X_{H2O} = 0.34$ at $y = 9.5$ mm (black).
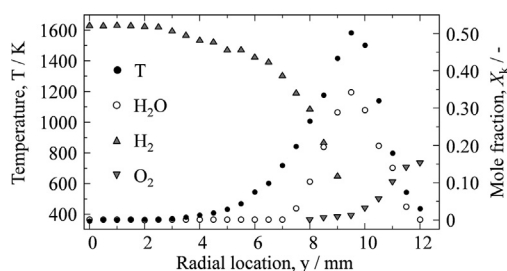

Fig. 4. Experimental profiles of the temperature and mole fractions of the major combustion species across the flame front of the laminar H_2/air diffusion flame. The measured H_2O mole fraction at 1 mm HAB varies in the range $X_{H2O} = 0.03$–0.34 in the reaction zone y = 7.5–11.5 mm.

diameter of 140 mm, providing a coflow of dry air. Digital flow controllers (Bronkhorst) are employed to regulate the volumetric flows of N_2 and H_2, constituting a 50%–50% (in volume) mixture provided through the center pipe of the burner with an exit speed of 34.8 m/s, resulting in a turbulent flow with Re = 10000, as well as the air coflow. The burner is mounted on translation stages to control its axial and radial position, and measurements are performed at a HAB of 20 mm (z/D = 2.5).

4. Results and discussion

4.1. Laminar flame measurements

At each radial location across the laminar H_2/air flame front we performed N_2 CARS thermometry and relative O_2/N_2 and H_2/N_2 concentration measurements on the spectra acquired at the shortest probe delay (i.e. 30 ps). At such early temporal delay the effect of inelastic collisions can be taken to be negligible, at atmospheric pressure. Once the temperature and the relative O_2/N_2 and H_2/N_2 concentrations are known, their experimental values are employed to generate a library of synthetic CARS spectra for varying relative H_2O/N_2 concentrations. The experimental N_2 CARS spectra are integrated in the spectral range ~120–230 cm^{-1}, corresponding to the N_2 lines $J = 14$–28, to avoid interference with the O_2 lines, and compared to the theoretical dephasing to measure the H_2O mole fraction. Figure 3 shows the experimental dephasing measured at two locations in the reaction zone and compared to the theoretical dephasing curves predicted by the time-domain N_2 CARS code for $X_{H2O} = 0$ and for the best-fit value. The black curves represent the signal dephasing at y = 9.5 mm (at 1 mm above the burner rim), where the H_2O mole fraction is measured to be 0.34 according to the best-fitting curve: a large sensitivity to the H_2O

concentration is shown by the significant bias between the experimental data and the theoretical dephasing predicted for $X_{H2O} = 0$. At y = 7.5 mm (grey curves) the H_2O mole fraction is reduced to 0.03, which represents the H_2O detection limit in the present work as a minimal deviation between the best-fit and the $X_{H2O} = 0$ theoretical curves is observed.

The methodology just explained is employed to measure the whole temperature and chemical composition fields across the flame front. Figure 4 shows the resulting experimental profiles for the temperature and the mole fractions of O_2, H_2 and H_2O. The temperature smoothly increases from ~360 K in the fuel stream at the center of the burner ($y = 0$ mm), peaking to 1620 K above the burner rim ($y = 9.5$ mm), and decreases more rapidly in the lean reaction zone reaching ~440 K in the oxidizer stream at $y = 12$ mm. The good single-shot precision of the CARS thermometry, varying in the range 0.8–3.7% in the high-temperature reaction zone, indicates a limited impact of the temperature fluctuations on the signal intensity, thus justifying the use of sequential measurements of the collisional dephasing for the laminar flame case. The H_2 mole fraction decreases from ~52% in the fuel stream at the center of the burner as the mixing and chemical reaction progress toward the burner rim. The simultaneous detection of the pure-rotational N_2 CARS spectrum and of two rotational lines of the pure-rotational H_2 CARS spectrum, namely S(0) at 354 cm^{-1} and S(1) at 587 cm^{-1}, allows for measuring the relative H_2/N_2 concentration at temperatures as high as 1450 K at location $y = 9$ mm. The O_2 mole fraction, on the other hand, smoothly grows from 0.01 measured at y = 8 mm up to 0.15 at the last measurement location in the oxidizer stream. The relative standard deviation of the measured mole fractions of H_2 and O_2 is, respectively, lesser than 2.5 and 8% at all measurement locations. H_2O is detected in the reaction zone, for $y = 7.5$–11.5 mm, with a maximum mole fraction of 0.34 at
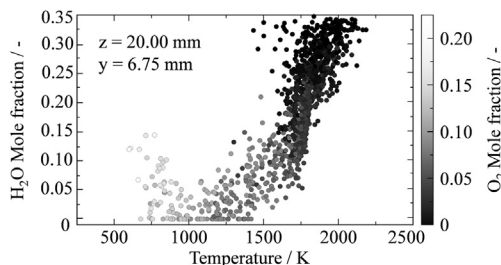
Fig. 5. Scatter plot of the H_2O mole fraction *versus* temperature measured by the 1200 single-shot CARS spectra acquired at the location with the highest temperature in the turbulent H3 flame. The grayscale color represents the measured O_2 mole fraction.

$y = 9.5$ mm. The uncertainty in the measured H_2O concentrations is mostly due to shot-to-shot fluctuation in the temperature and flow composition. This was assessed by propagating the uncertainty in the measured temperature and relative O_2/N_2 and H_2/N_2 concentrations and fitting the experimental data to the corresponding limit curves for the theoretical dephasing. The relative uncertainty in the H_2O mole fraction is thus estimated to be <8% at all measurement locations, with the sole exception of $y = 10.5$ mm, where the relative uncertainty is 15%, corresponding to a measured H_2O mole fraction in the range 0.18–0.21.

The temperature and mole fraction profiles in Fig. 4 are in good qualitative and quantitative agreement with those reported by Toro et al. for a similar laminar H_2/air diffusion flame [42], and moreover show the effect of preferential diffusion of H_2 in the fuel stream. In the region $y = 2.5$–6.5 mm, the H_2 mole fraction reduces from 0.52 to 0.42, while no water vapor is detected, and the temperature is only slightly increasing due to heat transfer from the reaction zone, yet remaining below the auto-ignition threshold. The simultaneous resolution of the local temperature and composition fields thus allows us to render the physics of mass transport in the laminar diffusion flame.

4.2. Turbulent flame measurements

Single-shot detection of water vapor concentration is demonstrated in the turbulent H3 flame, as described in Section 3.2. Four samples of 300 single-shot CARS spectra were acquired at a radial location 6.75 mm from the centerline of the flame, at the highest temperature in the oxidizer stream.

The scatter plot in Fig. 5 shows the measured H_2O mole fraction *versus* temperature at the chosen flame location, while the grayscale color of each data-point represents the local O_2 mole fraction. The latter shows an inverse correlation to the local temperature, with the O_2 mole fraction increasing at lower temperatures. Similarly, the measured H_2O

mole fraction has a clear correlation to the temperature in the reaction zone of the turbulent flame, with the concentration increasing with the local progress of the reaction in the probe volume. The clustering of the data-points showing high H_2O mole fraction at high temperatures is in good agreement with the original measurements performed by Meier et al. on the H3 flame [27]. At lower temperature, when a significant concentration of O_2 is present in the probe volume, the measured H_2O mole fraction shows a more spurious correlation, which is probably due to the beating of the N_2 lines employed in the measurement with O_2 lines. One additional caveat in the single-shot CARS measurements of the H_2O concentration is that the collisional dephasing of the N_2 CARS signal could only be measured at two probe delays. Further research effort should be spent on the investigation of the *J*-dependence of the collisional dephasing coefficients as an additional source of sensitivity to H_2O mole fractions, also to enhance the robustness of the measurements.

5. Conclusions

We have successfully demonstrated a novel time-resolved CARS diagnostic technique to quantify water vapor concentrations in hydrogen combustion environments. The technique relies on the use of relatively short ps probe pulses, following impulsive excitation, to realize measurements of the evolution and decay of the Raman coherence over a timescale of hundreds of ps. The dephasing of the pure-rotational N_2 CARS signal due to inelastic collisions with the H_2O molecules introduces a strong sensitivity to water vapor concentration. Coherent Raman-based detection of H_2O is otherwise very challenging, given the overall low Raman cross section of H_2O.

Proof-of-principle measurements of the H_2O concentrations were performed across the flame front of a laminar H_2/air diffusion flame. We recorded the pure-rotational N_2 CARS signals at six different probe delays relative to the pump/Stokes pulse, from 30 to 360 ps, and analyzed the corresponding collisional dephasing of the signal. The fs/ps CARS spectrum spans up to $\sim$600 cm^{-1} allowing the simultaneous measurement of the temperature and of the relative O_2/N_2 and H_2/N_2 concentrations. The successful measurement of the H_2O concentration thus allowed to map the chemical composition of the flow across the H_2/air flame front, by measuring the absolute concentrations of the major combustion species.

Single-shot measurements in the turbulent H3 flame are presented by dual-probe fs/ps CARS, obtained with polarization control over the signal generation. The probe pulse is split in two pulses with an intra-pulse delay of $\sim$230 ps and linear polarization set to be parallel and orthogonal to

the polarization of the pump/Stokes pulse. The N_2 CARS signal is thus simultaneously generated at ~20 and ~250 ps on the principle of a single-laser-shot; the cross-polarized signals are recorded in two distinct detection channels with our polarization-sensitive coherent imaging spectrometer. A total of 1200 single-shot CARS spectra were recorded at the highest temperature location in the oxidizer stream, at a HAB of 20 mm. The simultaneous measurement of the H_2O, O_2, H_2, and N_2 mole fractions, as well as temperature, was realized at this flame location. The statistical correlation of the measured quantities is in good agreement with experimental data available for this canonical flame, thus proving the applicability of the proposed technique to turbulent flames.

The novel CARS approach presented here has promising applications as an all-round laser diagnostic technique for scalar measurements in hydrogen flames, allowing for the simultaneous mapping of the temperature and chemical composition of the flow. Furthermore, its extension to more complex combustion environments, where a larger number of collisional partner is present, some of which might not be directly detected in the CARS spectrum, is an active research topic in our group.

Declaration of Competing Interest

The authors declare that they have no known competing financial interests or personal relationships that could have appeared to influence the work reported in this paper.

Acknowledgments

References

[1] A.C. Eckbreth, Laser Diagnostics for Combustion Temperature and Species, 2nd ed., Gordon and Breach Publishers, 1996.

[2] S. Roy, J.R. Gord, A.K. Patnaik, Recent advances in coherent anti-Stokes Raman scattering spectroscopy: fundamental developments and applications in reacting flows, Prog. Energy Combust. Sci. 36 (2010) 280–306.

[3] C. Brackmann, J. Bood, M. Afzelius, P.-E. Bengtsson, Thermometry in internal combustion engines via dual-broadband rotational coherent anti-Stokes Raman spectroscopy, Meas. Sci. Technol. 15 (2004) 13–15.

[4] D. Escofet-Martin, A.O. Ojo, N.T. Mecker, M.A. Linne, B. Peterson, Simultaneous 1D hybrid fs/ps rotational CARS, phosphor thermometry, and CH* imaging to study transient near-wall heat transfer processes, Proc. Combust. Inst. 38 (2021) 1579–1587.

[5] T.R. Meyer, S. Roy, R.P. Lucht, J.R. Gord, Dual-pump dual-broadband CARS for exhaust-gas temperature and CO_2–O_2–N_2 mole-fraction measurements in model gas-turbine combustors, Combust. Flame 142 (2005) 52–61.

[6] M. Scherman, R. Santagata, E. Lin, P. Nicolas, J.P. Faleni, A. Vincent-Randonnier, P. Cherubini, F. Guichard, A. Mohamed, D. Gaffie, B. Attal-Tretout, A. Bresson, 1-kHz hybrid femtosecond/picosecond coherent anti-Stokes Raman scattering thermometry of turbulent combustion in a representative aeronautical test rig, J. Raman Spectrosc. 52 (2021) 1643–1650.

[7] F. Grisch, P. Bouchardy, W. Clauss, CARS thermometry in high pressure rocket combustors, Aerosp. Sci. Technol 7 (2003) 317–330.

[8] D.R. Richardson, S.P. Kearney, D.R. Guildenbecher, Post-detonation fireball thermometry via femtosecond-picosecond coherent anti-Stokes Raman Scattering (CARS), Proc. Combust. Inst. 38 (2021) 1657–1664.

[9] H. Zhao, Z. Tian, Y. Li, H. Wei, Hybrid fs/ps vibrational coherent anti-Stokes Raman scattering for simultaneous gas-phase, Opt. Lett. 46 (7) (2021) 1688–1691.

[10] Y. Ran, A. Boden, F. Küster, F. An, A. Richter, S. Guhl, S. Nolte, R. Ackermann, *In situ* investigation of carbon gasification using ultrabroadband coherent anti-Stokes Raman scattering, Appl. Phys. Lett. 119 (2021) 243905.

[11] Y. Ran, M. Junghanns, A. Boden, S. Nolte, A. Tünnermann, R. Ackermann, Temperature and gas concentration measurements with vibrational ultra-broadband two-beam femtosecond/picosecond coherent anti-Stokes Raman scattering and spontaneous Raman scattering, J. Raman Spectrosc. 50 (2019) 1268–1275.

[12] S.P. Kearney, Hybrid fs/ps rotational CARS temperature and oxygen measurements in the product gases of canonical flat flames, Combust. Flame 162 (2015) 1748–1758.

[13] S.A. Tedder, J.L. Wheeler, A.D. Cutler, P.M. Danehy, Width-increased dual-pump enhanced coherent anti-Stokes Raman spectroscopy, Appl. Opt. 49 (8) (2010) 1305–1313.

[14] M.P. Arroyo, R.K. Hanson, Absorption measurements of water-vapor concentration, temperature, and line-shape parameters using a tunable InGaAsP diode laser, Appl. Opt. 32 (30) (1993) 6104–6116.

[15] W.F. Murphy, The Rayleigh depolarization ratio and rotational Raman spectrum of water vapor and the polarizability components for the water molecule, J. Chem. Phys. 67 (12) (1977) 5877–5882.

[16] S. O'Byrne, P.M. Danehy, A.D. Cutler, S.A. Tedder, Dual-pump coherent anti-Stokes Raman scattering measurements in a supersonic combustor, AIAA J. 45 (2007) 922–933.

[17] R.J. Hall, J.A. Shirley, A.C. Eckbreth, Coherent anti-Stokes Raman spectroscopy: spectra of water vapor in flames, Opt. Lett. 4 (3) (1979) 87–89.

[18] R.J. Hall, J.A. Shirley, Coherent anti-Stokes Raman

spectroscopy of water vapor for combustion diagnostics, Appl. Opt. 37 (2) (1983) 196–202.

[19] F.M. Porter, D.R. Williams, Quantitative CARS spectroscopy of the v_1 of water vapour, Appl. Phys. B 54 (1992) 103–108.

[20] D.A. Greenhalght, R.J. Hall, F.M. Porter, W.A. England, Application of the rotational diffusion model to the CARS spectra of high-temperature, high-pressure water vapour, J. Raman Spectrosc. 15 (2) (1984) 71–79.

[21] E. Nordström, A. Bohlin, P.E. Bengtsson, Pure rotational Coherent anti-Stokes Raman spectroscopy of water vapor and its relevance for combustion diagnostics, J. Raman Spectrosc. 44 (10) (2013) 1322–1325.

[22] D.A. Long, The Raman effect: A Unified Treatment of the Theory of Raman Scattering by Molecules, 1st ed., John Wiley & Sons Ltd., 2002.

[23] M. Schmitt, G. Knopp, A. Materny, W. Kiefer, The application of femtosecond time-resolved coherent anti-stokes raman scattering for the investigation of ground and excited state molecular dynamics of molecules in the gas phase, J. Phys. Chem. A 102 (1998) 4059–4065.

[24] H. Skenderović, T. Buckup, W. Wohlleben, M. Motzkus, Determination of collisional line broadening coefficients with femtosecond time-resolved CARS, J. Raman Spectrosc. 33 (2002) 866–871.

[25] B.D. Prince, A. Chakraborty, B.M. Prince, H.U. Stauffer, Development of simultaneous frequency- and time-resolved coherent anti-Stokes Raman scattering for ultrafast detection of molecular Raman spectra, J. Chem. Phys. 125 (2006) 044502.

[26] B.D. Patterson, Y. Gao, T. Seeger, C.J. Kliewer, Split-probe hybrid femtosecond/picosecond rotational CARS for time-domain measurement of S-branch Raman linewidths within a single laser shot, Opt. Lett. 38 (22) (2013) 4566–4569.

[27] W. Meier, S. Prucker, M.-H. Cao, W. Stricker, Characterization of turbulent H_2/N_2/air jet diffusion flames by single-pulse spontaneous raman scattering, Combust. Sci. Technol. 118 (1996) 293–312.

[28] A. Bohlin, B.D. Patterson, C.J. Kliewer, Communication: simplified two-beam rotational CARS signal generation demonstrated in 1D, J. Chem. Phys. 138 (2013) 081102.

[29] N. Owschimikow, F. Königsmann, J. Maurer, P. Giese, A. Ott, B. Schmidt, N. Schwentner, Cross sections for rotational decoherence of perturbed nitrogen measured via decay of laser-induced alignment, J. Chem. Phys. 133 (4) (2010) 044311.

[30] A.K. Patnaik, S. Roy, J.R. Gord, Saturation of vibrational coherent anti-Stokes Raman scattering mediated by saturation of the rotational Raman transition, Phys. Rev. A 87 (2013) 043801.

[31] C.J. Kliewer, A. Bohlin, E. Nordström, B.D. Patterson, P.-E. Bengtsson, T.B. Settersten, Time-domain measurements of S-branch N2-N2 Raman

linewidths using picosecond pure rotational coherent anti-Stokes Raman spectroscopy, Appl. Phys. B 108 (2012) 419–426.

[32] C. Meißner, J.I. Hölzer, T. Seeger, Determination of N_2–N_2 and N_2–O_2 S-branch Raman linewidths using time-resolved picosecond pure rotational coherent anti-Stokes Raman scattering, Appl. Opt. 58 (10) (2019) 47–54.

[33] A. Bohlin, E. Nordström, B.D. Patterson, P.E. Bengtsson, C.J. Kliewer, Direct measurement of S-branch N_2-H_2 Raman linewidths using time-resolved pure rotational coherent anti-Stokes Raman spectroscopy, J. Chem. Phys. 137 (2012) 074302.

[34] J. Bonamy, D. Robert, J.M. Hartmann, M.L. Gonze, R. Saint-Loup, H. Berger, Line broadening, line shifting, and line coupling effects on N_2-H_2O stimulated Raman spectra, J. Chem. Phys. 91 (1989) 5916.

[35] L. Castellanos, F. Mazza, D. Kliukin, A. Bohlin, Pure-rotational 1D-CARS spatiotemporal thermometry with a single regenerative amplifier system, Opt. Lett. 45 (17) (2020) 4662–4665.

[36] F. Mazza, N. Griffioen, L. Castellanos, D. Kliukin, A. Bohlin, High-temperature rotational-vibrational O_2-CO_2 coherent Raman spectroscopy with ultra-broadband femtosecond laser excitation generated in-situ, Combust. Flame 44 (10) (2022) 1322–1325.

[37] S.P. Kearney, P.M. Danehy, Pressure measurements using hybrid femtosecond/picosecond rotational coherent anti-Stokes Raman scattering, Opt. Lett. 40 (17) (2015) 4082–4085.

[38] C.E. Dedic, A.D. Cutler, P.M. Danehy, Characterization of supersonic flows using hybrid fs/ps CARS, AIAA SciTech Forum (2019) 1–13.

[39] S.P. Kearney, D.R. Richardson, J.E. Retter, C.E. Dedic, P.M. Danehy, Simultaneous temperature/pressure monitoring in compressible flows using hybrid fs/ps pure-rotational CARS, AIAA SciTech Forum (2020) 1–8.

[40] D. Escofet-Martin, A.O. Ojo, J. Collins, N.T. Mecker, M.A. Linne, B. Peterson, Dual-probe 1-d hybrid fs/ps rotational CARS for simultaneous single-shot temperature, pressure and O_2/N_2 measurements, Opt. Lett. 45 (17) (2020) 4758–4761.

[41] F. Mazza, L. Castellanos, D. Kliukin, A. Bohlin, Coherent Raman imaging thermometry with *in-situ* referencing of the impulsive excitation efficiency, Proc. Combust. Inst. 38 (2021) 1895–1904.

[42] V.V Toro, A.V. Mokhov, H.B. Levinsky, M.D. Smooke, Combined experimental and computational study of laminar, axisymmetric hydrogen–air diffusion flames, Proc. Combust. Inst. 30 (2005) 485–492.

[43] J. A. Van Oijen, L. P. De Goey, Modelling of premixed laminar flames using flamelet-generated manifolds, Combust. Sci. Technol. 161 (1) (2000) 113–137.

Coherent Raman imaging thermometry with *in-situ* referencing of the impulsive excitation efficiency

Francesco Mazza, Leonardo Castellanos, Dmitrii Kliukin, Alexis Bohlin*

Faculty of Aerospace Engineering, Delft University of Technology, Kluyverweg 1, 2629 HS Delft, the Netherlands

Abstract

Simultaneous detection of resonant and non-resonant femtosecond/picosecond coherent anti-Stokes Raman spectroscopy (CARS) signals has been developed as a viable technique to provide *in-situ* referencing of the impulsive excitation efficiency for temperature assessments in flames. In the framework of CARS thermometry, the occurrence of both a resonant and a non-resonant contribution to the third-order susceptibility is well known. While the resonant part conceives the useful spectral information for deriving temperature and species concentrations in the probed volume, the non-resonant part is often disregarded. It nonetheless serves the CARS technique as an essential reference to map the finite bandwidth of the laser excitation fields and the transmission characteristics of the signal along the detection path. Hence, the standard protocols for CARS flame measurements include the time-averaged recording of the non-resonant signal, to be performed sequentially to the experiment. In the present work we present the successful single-shot recordings of both the resonant and non-resonant CARS signals, split on the same detector frame, realizing the *in-situ* referencing of the impulsive excitation efficiency. We demonstrate the use of this technique on one-dimensional CARS imaging spectra, acquired across the flame front of a laminar premixed methane/air flame. The effect of pulse dispersion on the laser excitation fields, while propagating in the participating medium, is proved to result, if not accounted for, in an ∼1.3% systematic bias of the CARS-evaluated temperature in the oxidation region of the flame.

© 2020 The Combustion Institute. Published by Elsevier Inc. All rights reserved.

Keywords: Gas-phase thermometry; CARS; Femtosecond laser excitation; Non-linear optical spectroscopy; Combustion diagnostics

1. Introduction

Laser diagnostics is an important tool in the effort to develop clean combustion technologies, which is on the agenda for the propulsion and power industry, in-line with the current energy transition. These optical techniques have the ability to realize non-intrusive measurements *in-situ,* and to provide scalar information (e.g. temperature and species) with excellent spatial and temporal resolution. Laser diagnostics has been successfully employed over the years in multiple energy and combustion science applications where high-fidelity data are needed [1,2], e.g. by providing direct obser-

---

* Corresponding author.
E-mail address: g.a.bohlin@tudelft.nl (A. Bohlin).

vations and validating results from predictive engineering combustion models.

Coherent anti-Stokes Raman spectroscopy (CARS) is a versatile technique for assessing temperature and species concentrations in flames. It is unparalleled in the level of accuracy and precision it can provide, and the strong "laser-like" signal, which can be remotely detected, makes it well-suited for the application in extremely harsh and luminous environments such as combustion flows [3–5]. The conventional setup for CARS is based on nanosecond pulses; however, many variants exist, in which the inaccuracy and precision are technique-specific and need to be quantified respective to the measurement environment (e.g. nanosecond CARS thermometry has an approximate inaccuracy of $\sim$2–3%, and a single-shot imprecision of $\sim$4–5% [6,7]). In air-fed flames, the temperature sensitivity arises from the relative strength of the N_2 spectral lines. The spectrum uncovers the Boltzmann distribution (in principle) over the entire manifold of molecular rotational-vibrational states in the thermal ensemble. The retrieval of the quantitative temperature information from a CARS experiment is enabled by the combination of unobstructed detection of the spectrum and adequate spectroscopic modelling: the recorded data is evaluated using a goodness-of-fit routine [8].

The uncertainty in the CARS-evaluated temperature is related to critical parameters leading to either systematic (inaccuracy) or stochastic (imprecision) deviation from the true temperature. Much effort has been spent in quantifying the overall accuracy of the technique and limiting the impact of uncertainties originating e.g. from pressure broadening (Raman linewidths) [9], from the vibrational-rotational matrix-elements (Herman–Wallis factor) [10], and from the mode-amplitude and phase-mode fluctuations on the broadband laser emission profiles [11,12]. The influence of the uncertainty originating from the non-resonant susceptibility has also been investigated [13], although most of the effort in dealing with this parameter in CARS thermometry has been spent on the spectral fitting routine. This is partly because the total non-resonant susceptibility depends not only on the active molecule (e.g. N_2), but also on contributions from the background species [14,15]. A perfectly validated theoretical value of the non-resonant susceptibility, to be included in the spectral fitting routine, would then require the complete experimental retrieval of the chemical composition of the sample. The relative strength of the resonant and non-resonant CARS susceptibility is not only relevant for thermometry, but has been commonly employed for extracting species concentrations as well. This technique is particularly interesting for detecting water vapour [16,17], which is a recognized challenge for CARS diagnostics because of the relatively low Raman cross-section of the H_2O molecule [18].

The implementation of time-resolved CARS allows for reducing the impact of many of the aforementioned sources of uncertainty [19–21]. With "time-resolved CARS probing" we refer not only to the freezing of the energy-containing scale in the combustion flow, but also to the fact that the probing time is well within the characteristic molecular response time (dephasing). This temporal window for probing combustion-relevant species is usually on a picosecond timescale, the relatively long dephasing time of hydrogen being an exception [22]. On this short timescale the impact on the CARS spectrum of the Raman linewidths is small. Also the mode-amplitude and phase-mode fluctuations, affecting the emission profile of the broadband laser, are significantly reduced by using a near transform-limited femtosecond laser pulse, as compared to the broadband output from a nanosecond pumped dye-laser. In addition, with a time-resolved CARS technique, it is possible to suppress the non-resonant four-wave mixing signal by simply delaying the probe pulse relative to the pump and Stokes pulses [23,24]. Recent investigations aimed at the benchmarking of time-resolved CARS thermometry [25–27] have shown a considerably reduced relative standard deviation with respect to nanosecond CARS thermometry, reaching the unprecedented single-shot precision of $\sim$1% in room air and $\sim$1-3% in flames. When operating in flames, it is nonetheless difficult to make perfect statements about the statistical uncertainty inherent to the CARS technique. Indeed, the measured temperature might be affected by fluctuations in the experimental boundary conditions e.g. originating from factors related to the flow controllers and vibrations of the platform. In order to determine the overall accuracy of CARS-evaluated temperature, a similarity test with other experimental techniques and comparison to numerical simulations is thus important [28].

In the present work, we develop a technique aimed at minimizing the influence of the CARS thermometric uncertainty resulting from the effective bandwidth of the laser excitation fields. In turbulent flames and flows, the temperature and species gradients (and, accordingly, the number density of the gas mixture) change constantly with respect to the alignment of the laser excitation fields [29]. Therefore, shot-to-shot fluctuations may occur *in-situ*, affecting the delivery of a uniform bandwidth and the phase-matching condition necessary to coherently drive the temperature-sensitive Raman transitions. However, even in more still, stationary measurement conditions (e.g. in a laminar flame), which allow statistics to be obtained from signal averaging, the CARS spectrum depends on the effective bandwidth of the laser excitation fields as imposed by the measurement condition. In this

framework, the simultaneous referencing of the excitation efficiency has been developed to improve the CARS thermometric measurements obtained on the principle of a single-laser-shot [16,30]. Here, we use the non-resonant CARS susceptibility, measured *in-situ*, to extract information on the effective impulsive efficiency, as mapped directly by the spectrum of the non-resonant four-wave mixing signal. Concurrent resonant and non-resonant CARS signals are generated in the flame, and simultaneous, spatially divided detection of both signals is achieved through a novel polarization-sensitive wide-field coherent imaging spectrometer. We demonstrate the use of this spectrometer on spatially-correlated data, generated through single-shot hybrid femtosecond/picosecond 1D-CARS. We analyze the potential of the simultaneous, *in-situ* referencing in reducing the thermometric uncertainty, as compared to a standard protocol, where the spectral referencing is provided by a recording sequential to the experiment.

2. Theoretical considerations

In dual-broadband pure-rotational CARS [31,32], two-photon constructive pairs, available across the bandwidth of the laser excitation fields, coherently drive specific Raman shifts in the spectral range $\sim$0–500 cm^{-1}. This corresponds to N_2 pure-rotational S-branch transitions from quantum numbers J's = 0–60, zwith line separation $\Delta \varepsilon_{J,\ J+2} = 4B\ (J+3/2)$, and $4B \sim 8$ cm^{-1} for N_2. In hybrid femtosecond/picosecond CARS [26,33–39], the excitation efficiency across a specific Raman-active window is dictated by the finite bandwidth of the transform-limited fs-duration driving pulse. When considering pure-rotational CARS transitions (Δv=0, ΔJ=+/−2, ΔM_J=0), the laser excitation of the molecules results in a non-adiabatic interaction (here termed "impulsive") if the laser pulse duration is about one tenth of the molecular rotational period [40]. The impulsive excitation of N_2, for which the rotational periods are in the order of $\sim$500 fs, would thus require a $\sim$50 fs duration laser pulse. The high excitation efficiency provided by the impulsive drive of the rotational Raman transitions, is a prerequisite for generating non-resonant four-wave mixing at appreciable signal levels, for the instantaneous detection in high-temperature gaseous environments. In general, the strength of the CARS signal scales to the number density squared, and the number density is inversely proportional to the temperature in the sample.

The polarization dependence on the resonant and non-resonant CARS signals [41] is described with angles $\tan \beta = -\sin \phi\ /\ 2 \cos \phi$ for the resonant CARS signal, and $\tan \delta = \sin \phi\ /\ 3 \cos \phi$ for the non-resonant CARS signal, determined as a function of the relative polarization angle, ϕ, between the probe beam and the pump/Stokes beams, respectively. A probe angle of 67.5°, relative to the vertically polarized pump/Stokes beam, results in orthogonally polarized resonant and non-resonant CARS signals.

3. Experimental

The experimental setup was developed according to the two-beam femtosecond/picosecond phase-matching scheme for 1D-CARS imaging [42], here implemented with a single regenerative amplifier laser system [43]. The laser pulses originate as the $\sim$35 fs output of a high-power femtosecond regenerative amplifier, with a pulse energy of $\sim$7.5 mJ provided at a 1 kHz repetition-rate (Astrella, Coherent). A narrowband $\sim$7 ps-duration full-width-at-half-maximum (FWHM) probe pulse centered at $\sim$402 nm, is efficiently produced by means of the second-harmonic bandwidth compression [44,45] (Light Conversion) of a $\sim$65% portion of the fs laser output. This results in the ps probe pulse being both repetition-wise synchronized with the fs pump/Stokes pulse and automatically phase-locked at the CARS measurement, with an arbitrary arrival time. The near transform-limited fs pump/Stokes pulse is produced by an external compressor operating on a $\sim$35% portion of the uncompressed output from the amplifier. This design allows for flexible compensation (pre-chirping) of dispersion terms possibly arising along the optical path, thus providing impulsive excitation in the CARS measurement. The alignment of the laser beams and the polarization-sensitive detection of the single-shot hybrid femtosecond/picosecond 1D-CARS signals is depicted in Fig. 1.

The $\sim$2.3 mJ impulsive excitation beam (femtosecond laser pulse) and the $\sim$0.4 mJ probe beam (picosecond laser pulse) are intersected in a crossed-plane geometry, forming a one-dimensional spatial coordinate. The two beams are synchronized by an optical delay-line made of a high-finesse translation stage, ensuring sub-picosecond temporal resolution. The leveling and relative polarization of the laser beams are controlled with turning periscopes and a half-wave plate (Eksma optics) mounted in the pump/Stokes beam path; the shaping of the laser beams is performed with low-dispersion, sheet-forming optics. The irradiance of the probe beam ($\sim$1 J/cm^2) is significantly enhanced at the measurement location by means of astigmatic convergence [46], here realized by two cylindrical lenses with focal lengths f:=300 mm (v,h) -the indexes v (vertically) and h (horizontally) express the alignment symmetry axis. In efforts to match the phase-matching condition homogeneously across the line-image, a combination of focal lengths f:=500 mm (v) and f:=1000 mm (h) is employed in the pump/Stokes
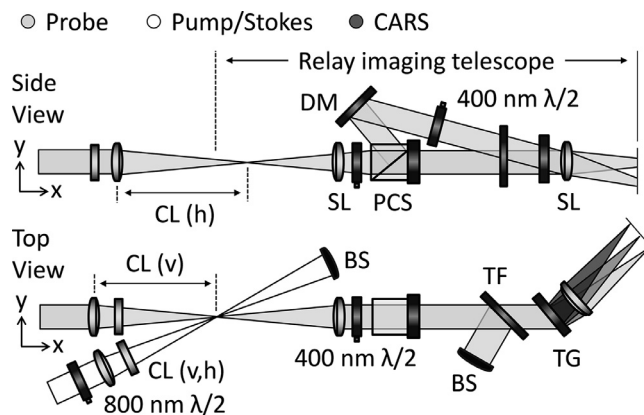
Fig. 1. The polarization-sensitive wide-field coherent imaging spectrometer used for spatially divided detection of resonant - and non-resonant hybrid femtosecond/picosecond one-dimensional (1D) coherent anti-Stokes Raman spectroscopy (CARS) signals. The indexes v (vertically) and h (horizontally) express the alignment symmetry axis of the cylindrical lenses cylindrical lenses (CL). Two separate detection channels for P- and S-polarized light, with orientation determined with respect to the transmission grating (TG), are relay-imaged with ∼1:1 magnification from the signal generation plane to the position of the detector. DM-dichroic mirror, PCS-polarization cube splitter, BS-beam stop, TF-tunable filter, and SL-spherical lens.

beam path. However, the phase-matching condition is relaxed for driving pure-rotational N_2 CARS transitions with the current beam configuration. The excitation beam is dumped before the first collection lens in the wide-field, one-to-one plane, coherent imaging spectrometer, while the probe beam is separated from the pure-rotational CARS signal through the angle-tuning of a spectral bandpass filter (Semrock). The resonant and non-resonant CARS signals are separated in two polarization-dependent detection channels, composed by two 400 nm half-wave plates and a polarization cube splitter (Eksma optics). Both channels are directed through a transmission grating (3040 lines/mm, Ibsen Photonics) and relay-imaged onto the same detector plane (Zyla 4.2, Andor). The first half-wave plate rotates the cross-polarized resonant and non-resonant CARS signals to fit the orthogonal S- and P-polarization transmission axes of the analyser. The second half-wave plate is mounted after the analyser to turn the polarization of the non-resonant CARS signal from P- to S-polarization and achieve the maximum grating transmission efficiency of >90% at 400 nm.

The measurement was performed across the flame front of a laminar premixed methane/air flame (Φ=0.95), provided on a Bunsen burner. The fuel (methane) and oxidizer (air) are delivered from separate containers, and variable-area flow meters (rotameters) provide independent control over each of the flows. Upon exiting the rotameters the flow lines are connected to a junction, after which the gases are mixed and the mixture is provided with a total bulk flow velocity of ∼1 m/s. The combustible mixture is then channeled through a seamless stainless burner pipe, designed with a length-

to-diameter ratio (∼1:100) sufficient to dampen coherent flow structures and provide a laminar flow at the exit (Reynolds number < 2000). The 10 mm inner diameter nozzle is tapered to minimize heat losses at the burner rim. The probe volume was positioned in proximity of the chemical reaction layer, and oriented so as to provide measurements along a line orthogonal to the flame front.

The crossing angle (θ) of the pump/Stokes and probe beams was measured to 3°, providing a probe volume of ∼0.03 mm (width) x ∼0.6 mm (length) x ∼1.3 mm (height), estimated from the assumption of a near diffraction-limited beam waist (e_0) of 30 μm FWHM (width), yielding an interaction length of $e_0/\sin(\theta) = 0.6$ mm. The total field-of-view (FOV) was measured to ∼1.3 mm (height) and the image quality was retrieved with a ∼40 μm line-spread function (LSF). These parameters were measured as the translation and steepness of an edge response in the signal, by inserting a razor blade at the plane of the two-beam crossing. A ∼3 ps relative temporal delay between the excitation beam and the probe beam was employed in the experiment, to generate the resonant and non-resonant CARS signals simultaneously. The "time equal zero" and the probe pulse duration were calibrated by performing a probe-delay measurement scan in argon, a monoatomic gas with no rotational degree of freedom. Consequently, the only signal component is the instantaneous four-wave mixing signal, which maps the temporal profile of the ps probe beam, synchronized with the fs pump/Stokes beam. The time-averaged argon spectrum also quantifies the constructive two-photon pairs available for the ex-
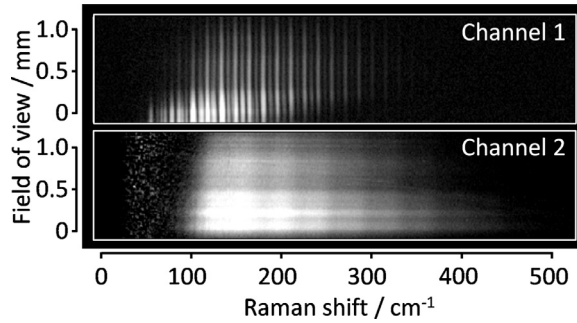
Fig. 2. Single-shot detection of concurrent resonant and non-resonant pure-rotational femtosecond/picosecond 1D-CARS signals acquired *in-situ* across the flame-front of a laminar premixed methane/air flame ($\Phi=0.95$). The label "Channel 1" indicates the portion of the detector frame employed for the acquisition of the resonant CARS signal, which is dominated by the characteristic spectral signature of N_2. "Channel 2" indicates the detection channel for the broadband non-resonant CARS signal (due to four-wave-mixing), which is scattered from all the species present in the probed volume.

citation of a specific Raman shift and is thus employed for the spectral referencing in standard protocols.

A sample of 900 single-shot, resonant and non-resonant CARS spectra was recorded simultaneously in the flame and analyzed to assess the thermometric accuracy and precision. The procedure was compared to a standard protocol, where the single-shot resonant CARS spectra are instead referenced by a time-averaged spectrum recorded in argon sequentially to the experiment.

4. Results and discussion

Figure 2 shows the simultaneous, single-shot detection of resonant and non-resonant 1D-CARS signals, generated across the flame front of a laminar premixed methane/air flame, and acquired on two distinct portions of the same detector frame. The labels "Channel 1" and "Channel 2" identify the portions of the detector where the resonant and non-resonant CARS signals are relayed, respectively.

As it can be seen in Fig. 2, the resonant CARS signal is dominated by the spectral lines of the nitrogen molecules, spanning Raman shifts from ~ 60 cm^{-1} to ~ 300 cm^{-1}, which result from the high-rotational energy levels being populated by the elevated temperature in the flame. The non-resonant CARS signal is instead continuous in nature, resulting from the four-wave-mixing from all the molecular species present in the sample. The highest signal intensity is detected in both channels around 180 cm^{-1}, while at frequencies lower than ~ 150 cm^{-1} the signals are attenuated by the angle-tuning of a spectral band-pass filter, to avoid spurious stray-light and residual probe beam reaching the detector.

Figure 3 shows a single-shot resonant spectrum acquired in the first detection channel, which is ref-

erenced by the non-resonant spectrum measured *in-situ* and detected simultaneously in the second channel.

The spectral resolution of the resonant CARS signal is dictated by the linewidth of the probe beam, measured to 2.1 cm^{-1} (FWHM), as well as by the instrumental broadening resulting from the wide-field coherent imaging spectrometer. In addition, the stray light covering the leftmost portion of the detector currently limits the spectral range available. This is nevertheless considered to have an insignificant impact on the N_2 thermometry, since, in correspondence of the elevated temperature in the product gases of the flame, the energy levels above 160 cm^{-1} are the most populated. The resonant CARS signal strength at room-temperature is several orders of magnitude stronger than the flame-temperature signal: the signal to background ratio (SNB) rapidly degrades as a function of temperature. The estimation of the temperature from the experimental CARS spectra was performed through a non-linear least-square contour fitting routine, comparing the acquired resonant spectra to a library of theoretical spectra pre-calculated for different input temperatures. These synthetic Raman spectra were computed by means of a time-domain CARS model, similar to previously-reported ones [34,26]. The broadening of the spectral linewidths due to the imaging system was accounted for by convolving the synthetic spectra with a Voigt instrument-response-function with a 1.6 cm^{-1}-wide Gaussian component (FWHM) and a 0.5 cm^{-1}-wide Lorentzian component (FWHM). The acquired resonant spectra were background-subtracted, introducing an area-averaged factor, thus accounting for possible shot-to-shot fluctuation in the magnitude of the background. Subsequently, the spectral referencing of the impulsive excitation efficiency was performed by dividing the resonant spectrum with the non-resonant spectrum (NR) obtained through two independent meth-
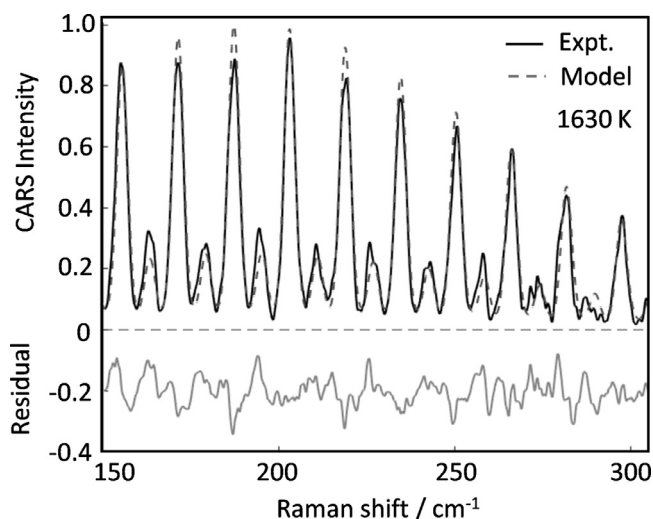
Fig. 3. Single-shot hybrid femtosecond/picosecond CARS spectrum, generated at short pump-probe pulse delay (∼3 ps) in the flame. The resulting temperature in the measurement location was estimated to 1630 K. The performance of the spectral fitting can be evaluated by the residuals of the theoretical and experimental spectra, which are presented in the figure, with an offset of −0.2 for clarity purposes.

ods: 1. non-resonant spectrum acquired in room-temperature argon (*ex-situ*); 2. non-resonant spectrum acquired in the flame (*in-situ*).

In Fig. 4, the comparison of the non-resonant CARS signal, as provided by the two techniques, is presented. The measurements were performed with spatially and temporally overlapped probe and pump/Stokes fields, at a ∼3 ps relative delay, for concurrent generation of the non-resonant CARS signal.

The signal quality from each of the single-shot recordings is sufficient to perform the spectral referencing: the signal counts of the single-shot spectra for the most critical condition (i.e. non-resonant signal from the flame) was ∼700 counts above the detector baseline. The non-resonant spectra show a clear decay for increasing values of the Raman shift: in this respect, the non-resonant signal provides an effective mapping of the laser bandwidth available for the excitation of the Raman-active molecules in the ensemble. If this pronounced slope were not taken into account in the spectral fitting routine (by spectral referencing), its effect would resemble a strong *J*-dependence similar to any other critical uncertainty factor, and result in a systematic bias (inaccuracy) in the CARS evaluated temperature. The comparison of the non-resonant spectra acquired *ex-situ* and *in-situ* clearly shows that the effective bandwidth available for the excitation of the temperature-sensitive Raman transitions in the combustion products is broader than the one mapped by the non-resonant spectrum acquired in room-temperature argon. This is explained by the strong dependence of the refractive index of the participating medium (i.e. the gaseous mix-

ture in the probe volume) on its temperature. Indeed, the group-velocity dispersion (GVD) of the fs pump/Stokes pulse induces a temporal broadening of the pulse itself as it propagates through the medium, resulting in a reduction of the effective bandwidth [47]. As the GVD for most gases at atmospheric pressure scales linearly with the density, the high temperature of the product gases in the flame determines a significant reduction of the GVD of the pump/Stokes pulse and the increase in the effective bandwidth shown in Fig. 4.

Furthermore, if a time-average NR spectrum, acquired *ex-situ*, is employed for the spectral referencing, possible variations in the excitation bandwidth available shot-to-shot would be neglected. This behavior is expected e.g. in turbulent flames, where the temperature field, as well as the chemical composition of the gas mixture in the probe volume, is highly dynamic in nature. Seemingly, this shot-to-shot variability in the slope of the NR spectra measured in the flame (*in-situ*) is neglected in the *ex-situ* measurement of the NR spectrum: this would lead to a stochastic uncertainty in the measurement. The bottom panel in Fig. 4 shows the relative standard deviation (RSTD) of the NR spectra acquired *in-situ* and *ex-situ*, as a function of the Raman shift: the trend of these curves thus represents the *J*-dependence of the shot-to-shot fluctuations in the NR spectrum, i.e. in the impulsive excitation efficiency. The RSTD of the *in-situ* NR spectrum is one order of magnitude higher across the whole spectral range compared to the *ex-situ* one: this is due to the reduced SNB available in the *in-situ* measurement, as compared to the *ex-situ*, because of the decreased number density of
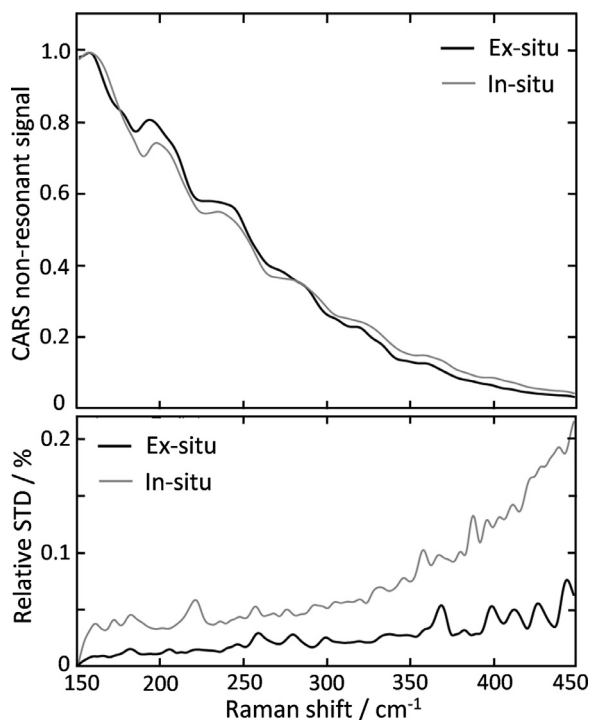
Fig. 4. (Top) Comparison of the average non-resonant spectra acquired in room-temperature argon (*ex-situ*) and at ∼390 µm from the flame-front in the oxidation region of the flame. (Bottom) The relative standard deviation as obtained from the 900 single-shot recordings.

the participating medium at high temperature. The difference in the RSTD values is more significant at the high-rotational energy levels populated at elevated temperatures: the variance of the available effective bandwidth in the fs pulse is shown to be higher in the *in-situ* measurements.

The use of the *in-situ* referencing of the impulsive excitation was demonstrated in CARS imaging thermometry, performed across the flame front of a laminar premixed methane/air flame ($\Phi=0.95$). In the scope of the present work, the location of the flame front is defined as the measurement point yielding the closest temperature to 1192 K; this value corresponding to the inflection point of the temperature profile across the reaction layer of the measured flame, as computed by the CHEM1D code [48]. The comparison of the temperature evaluations, obtained by applying the two referencing methods on 900 single-shot CARS spectra acquired in the flame, is discussed in the following.

In Fig. 5, the probability density functions (PDFs) of the temperature measurements are provided as a mean of comparison for the *ex-situ* and *in-situ* referencing techniques. The same resonant spectra, acquired in a 900 frames sample, were thus referenced by: 1. the time-averaged non-resonant spectrum acquired in room-temperature argon (*ex-*

situ), and 2. the single-shot non-resonant spectra acquired in the second detection channel, simultaneously to the resonant one (*in-situ*).

In the temperature measurements at ∼390 µm from the flame front, the *ex-situ* and *in-situ* referencing of the resonant spectra yielded, respectively: 1. an average temperature of 1696 K, with standard deviation 11 K (∼0.7%); 2. an average temperature of 1674 K with standard deviation 18 K (∼1.1%). The *ex-situ* referencing of the resonant CARS spectra results in a consistent bias towards higher temperatures, as compared to the results of the *in-situ* referencing: the systematic bias being quantified in 22 K (∼1.3%) at this flame location. This behavior is in good agreement with the aforementioned discrepancy in the available excitation bandwidth as mapped by NR spectra acquired *in-situ* and *ex-situ*: the lower density of the hot product gases is expected to have a lesser GVD on the laser excitation fields, thus resulting in a broader effective bandwidth. The effect of the temperature of the gaseous medium on the GVD of the fs pump/Stokes pulse, is even more evident when comparing the CARS measurements provided by *ex-situ* and *in-situ* referencing at lower temperatures. Indeed, at the flame front the two referencing techniques yielded the following results: 1. an average temperature of 1210 K (*ex-situ*) and
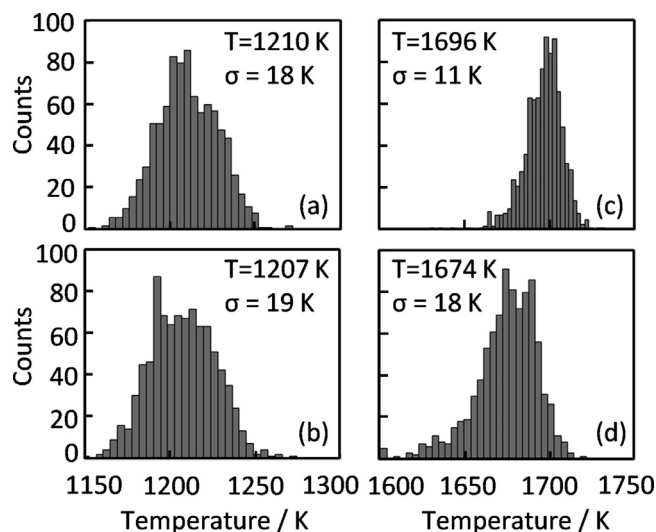
Fig. 5. Probability density functions of the 900 single-shot CARS-evaluated temperatures in the oxidation region of a laminar premixed methane/air flame. (a,b) Comparison for the measurements performed at the flame front. The *ex-situ* CARS measurement resulted in an average temperature of 1210 K, with standard deviation of 18 K (~1.5%); the *in-situ* referencing provided an average temperature of 1207 K, with standard deviation of 19 K (~1.6%). (c,d) Comparison of the temperature assessment provided by *ex-situ* and *in-situ* referencing of the resonant CARS spectra acquired at ~390 μm from the flame front. The *ex-situ* referencing resulted in an average temperature of 1696 K, with standard deviation 11 K (~0.7%); the *in-situ* provided an average temperature of 1674 K with standard deviation 18 K (~1.1%).

2. an average temperature of 1207 K (*in-situ*). The evident decrease in the systematic bias of the *ex-situ*-referenced CARS thermometry is well understood as a lesser impact the GVD on the fs pump/Stokes pulse.

It is nonetheless important to note that the CARS-evaluated temperatures seem to be significantly lower than as predicted by the numerical model in this spatial region of the flame: the expected temperature is indeed ~1870 K. This higher temperature value was moreover confirmed by performing CARS measurements at longer probe pulse delay (~27 ps), i.e. where the probe pulse is not temporally overlapped to the pump/Stokes pulse, and the self-referencing technique can thus not be employed. As a matter of fact, these measurement provide an average temperature of ~1840 K (inacurracy: ~1.6%). The reported discrepancy between the temperature measurements performed at long and short (i.e. within the temporal overlap of the pump/Stokes and probe pulses) pump-probe delays was consistently observed in different measurement locations within the flame front and for different values of the delay itself. This behavior seems to indicate the presence of a source of uncertainty in the evaluation of the temperature through the resonant CARS spectra generated at short pump-probe delays, which our theoretical model fails to take into account. Nevertheless, this uncertainty is not inherent to the *in-situ* referencing of the impulsive excitation, as it was also clearly observed in the temperature

measurements provided by the standard protocol, with *ex-situ* referencing by room-temperature argon.

As far as the relative standard deviation of the temperature measurements is concerned, the self-referencing shows a slightly worse precision as compared to the *ex-situ* referencing. This is attributed to the reduced SNB ratio available in the single-shot detection of the non-resonant signal in the self-referencing approach. Seemingly, this effect was more pronounced than any shot-to-shot variation in the effective excitation bandwidth, that the *in-situ* referencing could have accounted for. Nonetheless, the use of the self-referencing technique here described is foreseen to provide a substantial improvement in the precision of the CARS thermometric measurements in a number of applications of practical interest. We anticipate, for example, that the inherent compensation of the shot-to-shot fluctuations of the laser excitation fields can improve the thermometry in turbulent flows and flames. Future work in our laboratory will moreover quantify the impact of this technique on the performance of CARS systems employing laser sources which are more unstable in nature, such as supercontinuum generation.

5. Conclusions

In the present work, we have presented the application of a novel, *in-situ* referencing tech-

nique for CARS imaging thermometry. The simultaneous, *in-situ* referencing of the resonant Raman spectra was achieved by the concurrent, spatially divided detection of the resonant and non-resonant CARS signals in two distinct portions of the same detector frame. The non-resonant CARS signal detected in Channel 2 was thus employed as a spectral reference to the resonant CARS signal detected in Channel 1. Furthermore, we successfully demonstrated the application of this technique to the spatially correlated data provided by a single-shot one-dimensional CARS imaging system. Moreover, we have investigated the impact of the spectral referencing on CARS flame thermometry. A consistent bias of the *ex-situ* referencing towards higher temperatures was reported. This is understood in terms of the effect of the GVD change in the less dense product gases, as compared to the room-temperature argon employed to measure the *ex-situ* non-resonant spectrum. Nonetheless, the mean temperatures provided by both referencing methods were lower than predicted by the numerical evaluation of the measured flame front. This temperature bias was furthermore confirmed by additional CARS measurements performed at longer pump-probe delays, where no *in-situ* referencing is possible. In terms of relative standard deviation, the CARS-evaluated temperature obtained by applying the *in-situ* referencing was slightly worse than the *ex-situ* case. Nevertheless, the self-referencing technique here proposed is foreseen to improve the thermometric precision in more challenging measurement conditions.

Declaration of Competing Interest

The authors declare that they have no known competing financial interests or personal relationships that could have appeared to influence the work reported in this paper.

Acknowledgments

References

[1] K. Kohse-Höinghaus, R.S. Barlow, M. Aldén, E. Wolfrum, *Proc. Combust. Inst.* 30 (2005) 89–123.
[2] A.C. Eckbreth, *Laser Diagnostics for Combustion Temperature and Species*, 2nd ed., Gordon and Breach, Amsterdam, 1996.
[3] S. Druet, J.P. Taran, *Prog. Quant. Electr.* 7 (1981) 1–72.
[4] D.I. Greenhalgh, *Adv. Spectrosc.* 15 (1988) 193–251.
[5] S. Roy, J.R. Gord, A.K. Patnaik, *Prog. Energy Combust.* 36 (2010) 280.
[6] T. Seeger, A. Leipertz, *Appl. Opt.* 35 (1996) 2665–2671.
[7] A. Bohlin, E. Nordström, H. Carlsson, X.-S. Bai, P.-E. Bengtsson, *Proc. Combust. Inst.* 34 (2013) 3629.
[8] R.E. Palmer, *Sandia CARSFT Code*, Sandia National Laboratories, Livermore, CA, USA, 1989 Report No. SAND89-8206.
[9] L. Martinsson, P.-E. Bengtsson, M. Aldén, S. Kröll, J. Bonamy, *J. Chem. Phys.* 99 (4) (1993) 2466.
[10] M. Marrocco, *Proc. Combust. Inst.* 32 (2009) 863–870.
[11] S. Kröll, M. Aldén, T. Berglind, R.J. Hall, *Appl. Opt.* 26 (1987) 1068–1073.
[12] J.P. Kuehner, M.A. Woodmansee, R.P. Lucht, J.C. Dutton, *Appl. Opt.* 42 (2003) 6757–6767.
[13] M. Woyde, W. Stricker, *Appl. Phys. B* 50 (1990) 519–525.
[14] T. Lundeen, S.Y. Hou, J.W. Nibler, *J. Chem. Phys.* 79 (1983) 6301–6305.
[15] R.L. Farrow, R.P. Lucht, L.A. Rahn, *J. Opt. Soc. Am. B* 4 (1987) 1241–1246.
[16] F. Grisch, P. Bouchardy, W. Clauss, *Aerosp. Sci. Technol.* 7 (2003) 317–330.
[17] S.A. Tedder, J.L. Wheeler, A.D. Cutler, P.M. Danehy, *Appl. Opt.* 49 (2010) 1305–1313.
[18] W.F. Murphy, *J. Chem. Phys.* 67 (1977) 5877–5882.
[19] C.C. Hayden, D.W. Chandler, *J. Chem. Phys.* 103 (1995) 10465–10472.
[20] T. Lang, M. Motzkus, *J. Opt. Soc. Am. B* 19 (2002) 340.
[21] R.P. Lucht, S. Roy, T.R. Meyer, J.R. Gord, *Appl. Phys. Lett.* 89 (2006) 251112.
[22] W.D. Kulatilaka, P.S. Hsu, H.U. Stauffer, J.R. Gord, S. Roy, *Appl. Phys. Lett.* 97 (2010) 081112.
[23] D. Pestov, R.K. Murawski, G.O. Ariunbold, et al., *Science* 316 (2007) 265–268.
[24] T. Seeger, J. Kiefer, A. Leipertz, B.D. Patterson, C.J. Kliewer, T.B. Settersten, *Opt. Lett.* 34 (2009) 3755–3757.
[25] D.R. Richardson, H.U. Stauffer, S. Roy, J.R. Gord, *Appl. Opt.* 56 (2017) 37–49.
[26] S.P. Kearney, *Combust. Flame* 162 (2015) 1748–1758.
[27] A. Bohlin, C.J. Kliewer, *J. Phys. Chem. Lett.* 6 (2015) 643–649.
[28] R.S. Barlow, *Proc. Combust. Inst.* 31 (2007) 49–75.
[29] G. Magnotti, A.D. Cutler, P.M. Danehy, *Appl. Opt.* 51 (2012) 4730–4741.
[30] E.H. van Veen, D. Roekaerts, *Appl. Opt.* 44 (2005) 6995–7004.
[31] A.C. Eckbreth, T.J. Anderson, *Opt. Lett.* 11 (1986) 496–498.
[32] M. Aldén, P.-E. Bengtsson, H. Edner, *Appl. Opt.* 25 (1986) 4493–4500.
[33] B.D. Prince, A. Chakraborty, B.M. Prince, H.U. Stauffer, *J. Chem. Phys.* 125 (2006) 044502.
[34] J.D. Miller, S. Roy, M.N. Slipchenko, J.R. Gord, T.R. Meyer, *Opt. Express* 19 (2011) 15627–15640.
[35] A. Bohlin, M. Mann, B.D. Patterson, A. Dreizler, C.J. Kliewer, *Proc. Combust. Inst.* 35 (2015) 3723–3730.
[36] M. Scherman, M. Nafa, T. Schmid, et al., *Opt. Lett.* 41 (2016) 488–491.
[37] C.B. Yang, D. Escofet-Martin, D. Dunn-Rankin, Y.C. Chien, X. Yu, S. Mukamel, *J. Raman Spectrosc.* 48 (2017) 1881.

[38] Y. Ran, M. Junghanns, A. Boden, S. Nolte, A. Tün-nermann, R. Ackermann, *J. Raman Spectrosc.* 50 (9) (2019) 1268.

[39] J.E. Retter, G.S. Elliott, *Appl. Opt.* 58 (2019) 2557–2566.

[40] N. Owschimikow, B. Schmidt, N. Schwentner, *Phys. Chem. Chem. Phys.* 13 (2011) 8671–8680.

[41] F. Vestin, M. Afzelius, P.-E. Bengtsson, *Proc. Combust. Inst.* 31 (2007) 833–840.

[42] A. Bohlin, B.D. Patterson, C.J. Kliewer, *J. Chem. Phys.* 138 (2013) 081102.

[43] L. Castellanos, F. Mazza, D. Kliukin, A. Bohlin, *Opt. Lett.* 45 (2020) 4662–4665.

[44] S.P. Kearney, D.J. Scoglietti, *Opt. Lett.* 38 (2013) 833–835.

[45] F. Raoult, A.C.L. Boscheron, D. Husson, C. Sauteret, A. Modena, V. Malka, F. Dorchies, A. Migus, *Opt. Lett.* 23 (1998) 1117–1119.

[46] A. Bohlin, C.J. Kliewer, *Appl. Phys. Lett.* 105 (2014) 161111.

[47] P.J. Wrzesinski, D. Pestov, V.V. Lozovoy, J.R. Gord, R.J. Sukesh, *Opt. Express* 19 (2011) 5163–5171.

[48] J.A. van Oijen, L.P.H. de Goey, *Combust. Sci. Technol.* 161 (2000) 113–137.

Coherent Raman spectroscopy on hydrogen with *in-situ* generation, *in-situ* use, and *in-situ* referencing of the ultrabroadband excitation

FRANCESCO MAZZA,[1] **AERT STUTVOET,**[1] **LEONARDO CASTELLANOS,**[1] **DMITRII KLIUKIN,**[1,2] **AND ALEXIS BOHLIN**[1,3,*] 🔾

[1]*Faculty of Aerospace Engineering, Delft University of Technology, Kluyverweg 1, 2629 HS Delft, The Netherlands*

[2]*LaserLaB, Department of Physics and Astronomy, Vrije Universiteit Amsterdam, De Boelelaan 1081, 1081 HV Amsterdam, The Netherlands*

[3]*Space Propulsion Laboratory, Department of Computer Science, Electrical and Space Engineering, Luleå University of Technology, 98128 Kiruna, Sweden*

[*]alexis.bohlin@ltu.se

Abstract: Time-resolved spectroscopy can provide valuable insights in hydrogen chemistry, with applications ranging from fundamental physics to the use of hydrogen as a commercial fuel. This work represents the first-ever demonstration of *in-situ* femtosecond laser-induced filamentation to generate a compressed supercontinuum behind a thick optical window, and its *in-situ* use to perform femtosecond/picosecond coherent Raman spectroscopy (CRS) on molecular hydrogen (H_2). The ultrabroadband coherent excitation of Raman active molecules in measurement scenarios within an enclosed space has been hindered thus far by the window material imparting temporal stretch to the pulse. We overcome this challenge and present the simultaneous single-shot detection of the rotational H_2 and the non-resonant CRS spectra in a laminar H_2/air diffusion flame. Implementing an *in-situ* referencing protocol, the non-resonant spectrum measures the spectral phase of the supercontinuum pulse and maps the efficiency of the ultrabroadband coherent excitation achieved behind the window. This approach provides a straightforward path for the implementation of ultrabroadband H_2 CRS in enclosed environment such as next-generation hydrogen combustors and reforming reactors.

1. Introduction

Molecular hydrogen (H_2) is the object of an ever-increasing scientific interest, in view of its prospect use as the main energy carrier in the current energy transition [1], and a significant research effort is being spent on the development of technologies enabling H_2-based carbon-neutral combustion. The experimental investigation of H_2 chemistry [2,3], which plays a significant role in its storage and utilization, requires the availability of time-resolved spectroscopic techniques, providing information on the molecular dynamics on picosecond (ps) and femtosecond (fs) timescales [4]. The current state-of-the-art technique for gas-phase molecular spectroscopy is coherent Raman scattering (CRS) spectroscopy [5], which has found vast application to high fidelity *in-situ* measurements of the temperature field and chemical flow composition in combustion environments [6,7], and in non-equilibrium thermodynamic systems [8,9]. Since the first observation of rotational coherent Raman scattering in gas-phase media [10], CRS has been successfully demonstrated in gaseous H_2, both as a test-bench for fundamental physics (e.g. dynamic Stark effect [11]) and for enabling the development of novel photonic technologies [12]. Despite the research effort spent over the years, the application of CRS techniques to perform direct broadband multiplex spectroscopy on H_2 still presents a significant challenge due to sparse ro-vibrational energy manifold of the H_2 molecule [13]. Vibrational H_2 CRS

spectroscopy has been applied in combustion environments [14], as well as in plasmas [15], by employing broadband nanosecond dye lasers. Further development of H_2 CRS has been more recently promoted by the availability of ultrafast regenerative laser amplifiers, producing pulses a few tens of fs long, which have sprung the development of time-resolved spectroscopic techniques to investigate chemical reactions in real time [16]. Lang *et al.* were the first to employ fs pulses to perform coherent anti-Stokes Raman spectroscopy (CARS) on H_2, resolving the temporal dynamics of its ro-vibrational wave packet with sub-ps resolution [17]. Tran *et al.* used fs-CRS to study the H_2-N_2 collisional system and the speed-memory effects due to the high motility of the H_2 molecules [18]. Magnitskiĭ and Tunkin investigated the Dicke narrowing of the H_2 Q-branch, using ps-CRS to measure its coherence lifetime with high temporal and spectral resolution [19]; similar ps-CRS measurements of the H_2 Q-branch coherence lifetime were performed by Kulatilaka *et al.* [20]. The idea of combining broadband fs pulses to generate maximal quantum coherence of the Raman-active molecules [21] and relatively-narrowband ps pulses to perform simultaneously temporally- and spectrally-resolved measurements [22] has led to the development of hybrid fs/ps CRS [23]. The introduction of ultrabroadband fs laser sources greatly enhanced the spectral interrogation window of fs/ps CRS [24], allowing for the detection of virtually all the rotationally Raman-active species in the probed volume and for the investigation of their chemistry. Bohlin and Kliewer [25] demonstrated the use of a ~7 fs compressed supercontinuum, generated in an argon-filled hollow-core fiber, to simultaneously excite both the pure-rotational H_2 S-branch and the vibrational H_2 Q-branch transitions, in the range 0-4200 cm^{-1}. Despite the huge versatility of ultrabroadband fs/ps CRS, its application to perform measurements behind thick optical windows is limited by the significant chirp that these impart to broadband [26] and ultrabroadband fs pulses.

In the present work, we employ fs laser-induced filamentation [27] to generate a compressed supercontinuum pulse *in-situ*, where it is employed as a single pump/Stokes excitation pulse [28] to drive the pure-rotational Raman coherence up to ~1500 cm^{-1}. This approach is combined
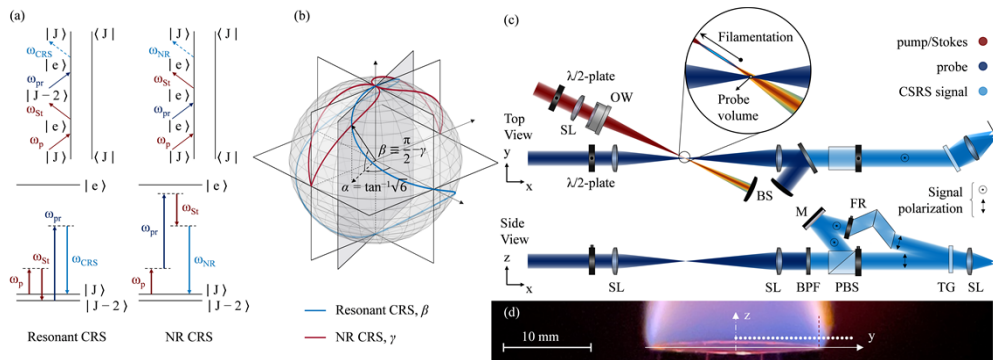

Fig. 1. (a) Energy and Feynman diagrams of a resonant (left) and a non-resonant (right) CRS pathways. (b) Polarization angles of the resonant (blue line) and non-resonant (red line) CRS signals, β and γ, represented as the elevation angle on the unit sphere as a function of the relative polarization angle (azimuthal angle) of the pump/Stokes and probe fields, α. (c) Schematic of the polarization-sensitive coherent imaging spectrometer. OW, optical window; SL, spherical lenses; M, mirror; BPF, band-pass filter; PBS, polarization beam splitter; FR, Fresnel rhomb; BS, beam stop. Inset: probe volume. The probe crosses the ultrabroadband pump/Stokes beam ~2mm after the end of the filament. The increment of input energy results in the elongation of the filament towards the focusing optics (arrow direction) (d) Measurements points across the H_2/air flame front, the dashed red line identifies the location of the burner rim at y = 9.5 mm.

with the simultaneous shot-to-shot measurement of the non-resonant (NR) CRS signal, due to the instantaneous electronic optical response of the medium (Fig. 1(a)), to map the spectral efficiency of the coherent excitation, which can significantly impact the accuracy and precision of the H_2 spectroscopy [29]. We use a polarization approach to simultaneously generate and detect the resonant and NR CRS signals with orthogonal polarization [30], as shown in Fig. 1(b). This *in-situ* spectral referencing allows us to monitor the spectrochronographic properties of the compressed supercontinuum and the bandwidth of the coherent Raman excitation. We demonstrate the application of fs/ps H_2 CRS with *in-situ* generation, use and referencing of the ultrabroadband coherent excitation to perform thermometric measurements in a laminar H_2/air diffusion flame as shown in Fig. 1(d), and to experimentally demonstrate preferential diffusion of H_2 [31].

2. Theory and methods

2.1. Analytical framework

The excitation efficiency of the H_2 Raman active modes depends on the spectrochronographic characteristics of the broadband pump/Stokes pulse, and is effectively controlled by its spectral phase [32,33], as shown in the application of coherent control theory to CRS [34,35]. We measure the excitation bandwidth provided by the combined pump/Stokes pulse using the intensity spectrum of the NR CRS signal. The NR CRS signal is here modelled in the time domain under the assumptions of instantaneous dephasing of the electronic coherence induced by the non-resonant two-photon excitation pathways in Fig. 1(a) and temporal overlap of the probe field E_3 with the pump/Stokes field E_{12} [24]:

$$P_{NR}^{(3)}(t) = \left(\frac{i}{\hbar}\right)^3 \chi_{NR}^{(3)} \cdot E_3(t) \cdot E_{12}^*(t) \cdot E_{12}(t) \tag{1}$$

The pump/Stokes pulse is assumed to have a Gaussian envelope in the time domain with duration Δt_{12} (FWHM):

$$E_{12}(t) \propto \exp[-2\ln 2(t - t_{12})^2 / \Delta t_{12}^2] \cdot \exp(i\omega_{12}t) + c.c. \tag{2}$$

with t_{12} being the arrival time of the combined pump/Stokes pulse, and ω_{12} the carrier (angular) frequency of the pulse ($\omega_{12} = 2.34$ rad/fs for 806.7 nm). The spectrum of the NR CRS field, resulting from the pump/Stokes photon-pairs found across the instantaneous bandwidth of the pulse, is then computed via the Fourier transform of Eq. (1), and is thus proportional to the spectral autocorrelation of the pump/Stokes laser field [36]:

$$P_{NR}^{(3)}(\omega) \propto \chi_{NR}^{(3)} E_3(\omega) * [E_{12}(\omega) \star E_{12}(\omega)] \tag{3}$$

$$I_{NR}(\omega) \propto |\chi_{NR}^{(3)} E_3(\omega) * [E_{12}(\omega) \star E_{12}(\omega)]|^2 \tag{4}$$

where $\star$ and $*$ represent the cross-correlation and convolution operators, respectively. Hence, the intensity spectrum in Eq. (4) is used to measure the spectral autocorrelation of the fs pump/Stokes pulse and deduce information on its spectral phase. Equation (2) and Eq. (4) are employed to generate a library of synthetic NR CRS spectra for varying pulse duration, and fit the experimental NR CRS spectra acquired in a non-resonant gas (e.g. methane or argon) flow. The spectral phase of the pump/Stokes pulse is introduced in the model through the Taylor expansion:

$$\varphi(\omega) = \sum_n L \cdot k_{(n)}(\omega_{12}) \cdot \frac{(\omega - \omega_{12})^n}{n!} \tag{5}$$

with L being the thickness of the optical window, and $k_{(n)}$ the nth-order derivative of the wave vector $k(\omega)$ in the dispersive medium ($k_{(2)}$ thus representing the group velocity dispersion of the

fs pulse). The chirped pump/Stokes pulse is thus represented in the frequency domain as:

$$E_{12}(\omega) \propto \exp\left[-2\ln 2(\omega - \omega_{12})^2/\Delta\omega_{12}^2\right] \cdot \exp\left[-i\sum_n \varphi_{(n)} \cdot \frac{(\omega - \omega_{12})^n}{n!}\right] \quad (6)$$

Substituting Eq. (6) into Eq. (3), the spectral autocorrelation of the pump/Stokes pulse is computed according to the integral:

$$(E_{12} \star E_{12})(\Omega) = \int_{-\infty}^{\infty} d\omega E_{12}^*(\omega)E_{12}(\omega + \Omega) \propto$$

$$\exp\left[-\left(\frac{\ln 2}{\Delta\omega_{12}^2} + i\frac{\varphi_2}{2}\right)\Omega^2\right] \cdot \int_{-\infty}^{\infty} d\omega \exp\left\{\frac{4\ln 2}{\Delta\omega_{12}^2}\left[\Omega + \frac{(\omega - \omega_{12})}{2}\right]^2 - i\varphi_2\Omega\frac{(\omega - \omega_{12})}{2}\right\}$$

$$(7)$$

where only the quadratic phase term (φ_2) has been included. Note that including the third-order dispersion (TOD, φ_3) would only contribute to the real part of the argument of the exponential integrand, as the imaginary part factors out in the product with the complex-conjugated field: this is true for all the odd terms in the spectral phase expansion of Eq. (5). A closed-form solution to the integral in Eq. (7) is given in the form:

$$(E_{12} \star E_{12})(\Omega) \propto \sqrt{\pi(4\log 2 + i\varphi_2\Delta\omega_{12}^2)}\exp\left[\left(-\frac{4\ln 2}{\Delta\omega_{12}^2} + i\varphi_2\right)\Omega^2\right] \quad (8)$$

which represents a Gaussian envelope modulated by non-linear harmonic oscillations, having the form of the derivative of Fresnel sine integral function, with local frequency proportional to the quadratic phase term. Equation (4) and Eq. (8) are employed to generate a library of synthetic NR CRS spectra for varying pulse duration, and fit the experimental NR CRS spectra, as shown in Fig. 2.

2.2. Experimental setup

The laser system employed for ultrabroadband fs/ps CRS spectroscopy is detailed in Ref. [37]. A single ultrafast regenerative amplifier system (Astrella, Coherent) combined with a second-harmonic bandwidth compressor unit (Light Conversion), provides the combined pump/Stokes (35 fs, 1650 µJ/pulse at 806.7 nm) and the probe (12.6 ps, 117 µJ/pulse at 403.4 nm) fields which are auto-synchronized at 1 kHz repetition rate and focused to the measurement location using spherical lenses (f: 500 and 300 mm, respectively). We demonstrate its applicability to measurements behind thick optical windows by transmitting the fs beam through a ~22 mm thick BK7 glass window. This glass has larger group velocity dispersion at 800 nm (~45 fs^2/mm) than other optical window materials (e.g. fused silica ~36 fs^2/mm), which demonstrates the application of this methodology to the more extreme conditions. The window is placed ~200 mm after the focusing lens to prevent white light generation inside the glass. The energy of the fs beam after the transmission thought the optical window is ~1500 µJ/pulse. We control the temporal chirp of the fs pulse prior the *in-situ* filamentation using an external pulse-compressor. Thin-film polarizers ensure the linear polarization of the pump/Stokes and the probe beams, and half-wave plates control their polarization angles. Ensuring the linearity of the polarization of the fs beam before it undergoes filamentation is critical to control the polarization state of the compressed supercontinuum, since electronic Kerr nonlinearity, electron plasma, and molecular alignment in the filament result in the rotation of the polarization ellipse [38]. Linearly polarized pulses maintain their polarization state in fs laser-induced filamentation and in the post-filamentation propagation [39]. Adopting a two-beam nearly phase-matched configuration
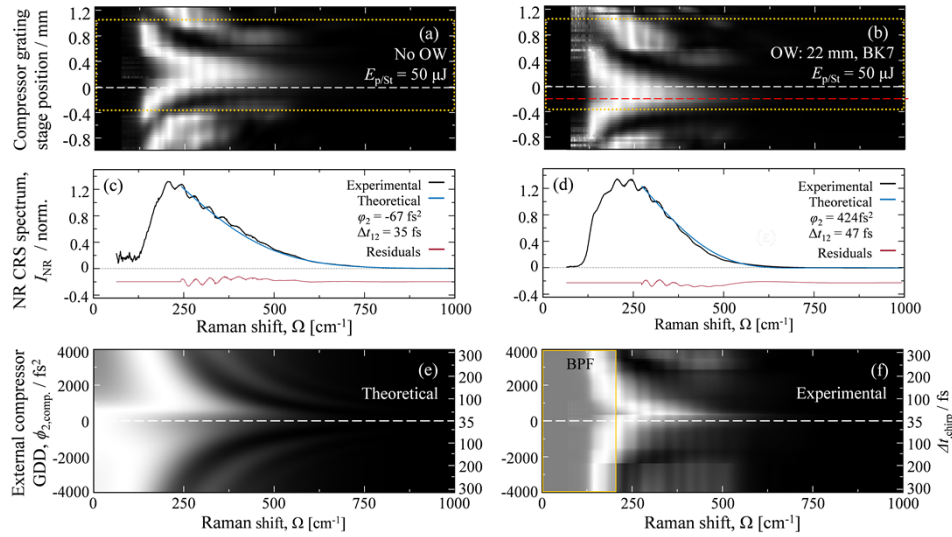
Fig. 2. (a) 1000-shot-averaged NR CRS spectra recorded, by varying the position of the compressor grating, in a flow of CH_4 without the optical window (No OW). The white dashed line identifies the condition of a near transform-limited (TL) pulse. (b) Corresponding NR CRS spectra after the introduction of a BK7 optical window (OW) in the pump/Stokes beam path. The red dashed line identifies the condition of a TL pulse obtained after transmission through the window. The dotted boxes represent the region of interest (ROI) analyzed in the present work. (c) NR CRS spectrum for a near TL pump/Stokes pulse as compared to the time-domain NR CRS model (No OW). (d) NR CRS spectrum for TL pump/Stokes pulse transmitted through the optical window (OW). (e) NR CRS signal for varying linear chirp in the input fs pump/Stokes pulse, as predicted by the time-domain model. For values of the pulse GDD larger than ~1000 fs^2 the spectral autocorrelation of the pulse results in the formation of sidebands in the CRS spectrum and in the narrowing of the excitation window. (f) Experimental autocorrelation of the fs pulse as measured by the NR CRS signal of room temperature CH_4 in the ROI. The opaque box represents the spectral region affected by the edge of the band pass filter (BPF).

[28], the pump/Stokes beam is crossed by the probe beam ~2 mm after the end of the filament to avoid ionization inside the probe volume. The ending point of the filamentation generated both across the flame and in non-resonant gases (i.e. argon and methane) is always fixed regardless of the input pulse energy and the local thermodynamic properties of the gas [37]. The resulting dimensions of the probe volume are thus estimated geometrically to be 20 μm (width, FWHM) x 2.5 mm (length, FWHM) x 20 μm (height, FWHM). The coherent imaging spectrometer developed for the simultaneous acquisition of the resonant and NR CRS signals in Ref. [30] is here adapted for the *in-situ* referencing of the ultrabroadband excitation generated in the flame. A Fresnel Rhomb rotates the polarization of the NR signal to maximize the efficiency of a high-resolution transmission diffraction grating (>90% diffraction efficiency for S-polarization, Ibsen Photonics). The signals are imaged onto the sCMOS detector (Zyla, Andor) through a fast-focusing lens (f: 100 mm), resulting in a detection bandwidth of 1900 cm^{-1}, with a dispersion of 0.93 cm^{-1}/pixel. The resolution of the H_2 CRS spectra is limited by the linewidth of the ps probe pulse which is measured to be ~2.7 cm^{-1}, and by the instrumental broadening of the spectrometer, which is fitted to a Voigt profile with a ~0.1 cm^{-1} FWHM Lorentzian and a ~1.7 cm^{-1} FWHM Gaussian contribution. For high-resolution spectroscopy in the pure-rotational region (~50-600 cm^{-1}) the spectrometer is adapted by changing the imaging lens to a slower

focus (f: 400 mm), resulting in a dispersion of ~0.27 cm^{-1}. H$_2$ CRS measurements were performed across the flame front of a laminar H$_2$/air diffusion flame, provided on a Bunsen burner: the probe volume was moved from the center of the burner towards its rim, in steps of 0.5 mm as shown in Fig. 1(d). A steel mesh was placed ~15 mm above the burner to stabilize the flame and the measurements were performed ~0.5 mm (H$_2$ CRS thermometry) and ~1 mm (preferential diffusion) above its nozzle. The H$_2$ flow was diluted in a 50% mixture with nitrogen (N$_2$) to perform conventional N$_2$ CRS thermometry for validation purposes. The *ex-situ* spectral referencing protocol is performed by measuring the NR CRS signal from the compressed supercontinuum generated in a flow of room temperature argon (which has no rotational degree of freedom).

3. Results

3.1. Autocorrelation measurements of the fs pump/Stokes pulse

The effect of temporal chirp in the pump/Stokes pulse on the spectral excitation efficiency is illustrated in Fig. 2. 1000-shot-averaged NR CRS spectra were recorded as a function of the pulse dispersion, controlled by the external compressor unit in Fig. 2 (a) and introduced by the optical window in Fig. 2 (b), in a non-resonant gas flow (methane, CH$_4$). The input pump/Stokes pulse energy was 50 μJ, i.e. lower than the filamentation onset. The amount of chirp in the input pulse is controlled by varying the angle of the diffraction grating in the external compressor unit (details in Supplement 1). A strong periodic modulation of the NR CRS spectra in Fig. 2(a) results from the introduction of quadratic phase to the pump/Stokes pulse, in accordance with the theoretical result of Eq. (8). The pulse transmission through the thick optical material only introduces linear chirp, as proven by the translation of the spectrochronogram from Fig. 2(a) to Fig. 2(b). The dependence of the NR CRS spectrum on the spectral phase of the pump/Stokes pulse can be exploited to measure its spectrochronographic properties: we do this by fitting the experimental spectra to our time-domain NR CRS model. We quantify the quadratic phase introduced by the external compressor, resulting in a stretching of the 35 fs near transform-limited (TL) pump/Stokes pulse in Fig. 2(c) to ~150 fs by either negative or positive dispersion. The same input chirp is combined with transmission through the window in Fig. 2(d), allowing for a direct evaluation of the positive group delay dispersion (GDD) arising due to the optical material: this is measured to be 424 fs^2, resulting in a stretching of the pulse duration to 47 fs. When the combined GDD is larger (in magnitude) than ~1000 fs^2, the autocorrelation of the pump/Stokes pulse results in the shift of the local maximum of the spectral excitation in the range ~300-1000 cm^{-1}, evident in the raw data of Fig. 2(a-b). For large pulse GDD, the NR CRS spectrum departs from the usual monotonic trend with the Raman shift, presenting multiple local maxima at locations which depend on the GDD itself. This behavior is similar to what has been shown by applying spectral focusing [40] and pulse shaping [41] techniques, but is here realized without any intra-pulse delay as our CRS system employs a single combined pump/Stokes pulse. Figure 2(e-f) shows the comparison of the experimental and the theoretical spectral autocorrelation of the fs pump/Stokes pulse as measured by the NR CRS signal. The time-domain CRS model illustrated by Fig. 2(e) predicts the parallel formation of spectral sidebands: this prediction is experimentally verified in Fig. 2(f). This behavior is analogous to the spectral focusing technique first demonstrated by T. Hellerer *et al.* [42] for CARS microscopy: introducing the same amount of GDD in their broadband fs pump and Stokes pulses, they demonstrated the coherent excitation of a narrow spectral region with spectral selectivity enabled by the tuning of the intrapulse delay. The experimental NR CRS spectra in Fig. 2(f) thus map the effect of the linear chirp in the input fs pulse, which results in the narrowing of the spectral excitation, and in its shift to values of the Raman shift $|\Omega| > 0$, even with a null intrapulse delay for our combined pump/Stokes pulse.

3.2. Generation of ultrabroadband coherent excitation behind the optical window

The use of ultrabroadband CRS techniques at measurement scenarios with an enclosed space (e.g. high-pressure combustors, optical cells, etc.) requires the experimentalist to maintain control of the spectral phase while the compressed supercontinuum pulse is transported through the optical windows, which is impractical, perhaps even impossible. In the present work we demonstrate that fs laser-induced filamentation [43,44] can be used to generate a compressed supercontinuum pulse *in-situ* behind an optical window, thus maximizing the rotational Raman coherence in gaseous H_2. The time-domain NR CSR model is extended to the ultrabroadband NR signal generated by the compressed supercontinuum acting as the pump/Stokes pulse. We let the duration of the fs pulse vary and used it as an additional fitting parameter, thus accounting for the increment of the pulse bandwidth due to its self-phase modulation in the filamentation process. The temporal compression of the resulting spectrally-broadened pulse, due to its non-linear propagation in the plasma medium, is again modelled by the GDD of the medium. The most stringent assumption introduced here is that of a symmetric broadening of the pulse spectrum, preserving its original Gaussian shape. The validity of this assumption could be limited when the pulse is compressed in air under tight focusing conditions: if the contribution of the non-linear refractive index of the dense plasma medium to self-phase modulation is greater than the one due to Kerr effect, an asymmetric broadening of the pulse spectrum would result to higher frequencies. Within the scope of the present work we nonetheless find the assumption reasonable, given the limited energy of the input fs pulse and the much-reduced density of the plasma generated in the hot environment of the flame. The pulse compression achieved via fs laser-induced filamentation can also be experimentally investigated as a function of the linear chirp in the input fs pulse, as shown in Fig. 3. The generation of the compressed supercontinuum in the filament depends on the complex interplay between multiple non-linear optical processes, whose relative magnitude is determined by the non-linear susceptibility of the gaseous medium where the filament is generated. While for non-resonant molecules (e.g. argon) the third-order non-linear susceptibility is entirely electronic in nature, the generation of rotational nuclear wave packets in Raman-active molecules (e.g. N_2 and O_2) can play a role in the pulse compression through self-phase modulation and non-linear light propagation. This explain the different output of the filamentation process, in terms of pulse compression and corresponding ultra-broad excitation bandwidth, in CH_4 and in air.

Figure 3(b) shows the ultrabroadband NR CRS spectra acquired in a room-temperature flow of CH_4, as a function of the linear chirp in the input pulse. The pulse compression –here quantified by the contour line at half maximum of the NR CRS spectrum in the region 200-1600 cm^{-1} (i.e. HWHM)– shows only a slight dependence on the input chirp pulse in the range between -500 fs^2 and 500 fs^2, and it decreases dramatically for larger (absolute) values of the pulse GDD. When realized in air, on the other hand, fs laser-induced filamentation has a more complex dependence on the input chirp, and the HWHM bandwidth contour shown in Fig. 3(a) remarkably presents a local minimum close to the condition of a TL pulse. Introducing a small amount of GDD in the input pulse enhances the pulse compression resulting in two local maxima of the excitation bandwidth for $\varphi_2 = 397$ fs^2 and $\varphi_2 = -492$ fs^2; the latter was found to optimize the pulse compression for ultrabroadband H_2 CRS spectroscopy in the flame. Furthermore, comparing the bandwidth of the compressed supercontinuum generated in CH_4 and in air, the higher electronic third-order susceptibility of CH_4, being almost thrice as large as that of N_2 and O_2 (see Table S1 in Supplement 1), results in a larger pulse compression via fs laser-induced filamentation. We operated the external compressor so as to optimize the pulse compression via filamentation in the flame environment, introducing a GDD of -492 fs^2 to the input pulse, which is thus stretched to ∼52 fs, as measured by the NR CRS signal in Fig. 3(c), recorded in flow of a non-resonant gas (argon) at low pulse energy (i.e. without filamentation).

Figure 3(d) shows the application of the NR CRS model to estimate the duration and the residual chirp of the compressed supercontinuum generated via fs laser-induced filamentation
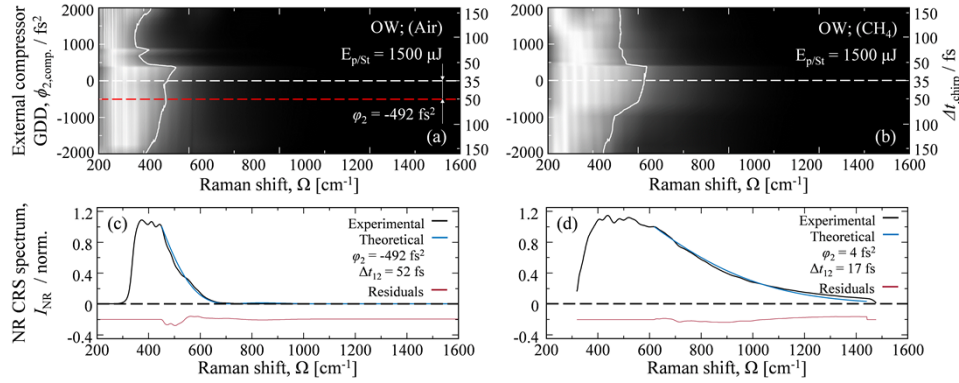
Fig. 3. Pulse compression by fs laser-induced filamentation behind the optical window. The ultrabroadband NR CRS signal is generated in room-temperature (a) air and (b) CH_4, for varying linear chirp in the input fs pump/Stokes pulse. 1000-shot-averaged spectra are shown. The white contour line identifies the HWHM excitation bandwidth. For moderate input chirp (i.e. $|\varphi_2| < 500$ fs^2) the bandwidth of the compressed supercontinuum generated in CH_4 is almost unaffected by the input chirp. In air, a local minimum in the bandwidth of the supercontinuum pulse is obtained for a TL input pulse, while two local maxima are achieved for slightly chirped pulses. The setting $\varphi_2 = $ -492 fs^2 (dashed red line) of the external compressor was employed to optimize the pulse compression in the flame experiments. (c) 1000-shot-averaged NR CRS spectrum of the chirped input fs pulse optimized for pulse compression via filamentation in the flame environment (d) 1000-shot-averaged ultrabroadband NR CRS spectrum recorded in a flow of argon. The spectrum clearly displays the success of generating a compressed supercontinuum behind the optical window, which can be used for ultrabroadband CRS in enclosed spaces.

in argon (*ex-situ*): this is measured to be a near-TL pulse with a duration of 17 fs. Finally, we can estimate the impact that the optical window would have on the transmission of this supercontinuum pulse generated *ex-situ*, when employed as the pump/Stokes pulse for H_2 CRS behind the window itself. The ~424 fs^2 GDD introduced by 22 mm of BK7 glass would result in a significant stretch of the compressed supercontinuum generated *ex-situ*, to ~68 fs requiring additional phase control techniques to guarantee a sufficient excitation bandwidth and perform ultrabroadband CRS on H_2.

3.3. *In-situ referencing of the compressed supercontinuum generated in the flame*

The experimental protocol for the *in-situ* referencing [30] of the fs laser excitation of the Raman-active modes relies on the simultaneous generation of the resonant and NR CRS signals with orthogonal polarization. The theory of polarization control over the generation of the resonant and NR CRS signals is detailed in Supplement 1. We assume the polarization of our combined pump/Stokes pulse as a reference, and define the relative polarization angles of the probe, and the resonant and the NR components of the CRS signal respectively as α, β, and γ. The polarization angles of the resonant and NR CRS signals, as a function of the relative probe polarization angle, are:

$$\tan \beta = (1 - 2\rho) \tan \alpha$$
$$\tan \gamma = \tfrac{1}{3} \tan \alpha$$

(9)

where ρ is the depolarization ratio of the Raman-active molecules. The functional relations in Eq. (9) are represented on the unit sphere in Fig. 1(b). Coupling Eq. (9) with the condition for simultaneous generation of cross-polarized resonant and NR CRS signals, i.e. $|\beta - \gamma| = \pi/2$, we

determine the required relative probe polarization angle:

$$\alpha = \tan^{-1}\left(\pm\frac{\sqrt{3}}{\sqrt{2\rho - 1}}\right) \tag{10}$$

Equation (10) has real solutions only for $\rho > 1/2$: the applicability of the *in-situ* referencing protocol is thus limited to weakly-polarized or depolarized Raman transitions. In the present work we are interested in applying the *in-situ* referencing protocol to the pure-rotational CRS spectrum of H_2, whose Raman-activity is entirely due to their anisotropic polarizability: the pure-rotational H_2 Raman spectrum is thus entirely depolarized and $\rho = 3/4$. Equation (10) then gives the relative probe polarization angle that results in cross-polarized resonant H_2 and NR CRS signals: $\alpha = \tan^{-1}\sqrt{6}$.

Figure 4(a) shows the average NR CRS spectra acquired *in-situ* at each measurement location across the flame front (see Fig. 1(d)) and is compared to the average NR CRS spectrum generated *ex-situ* in room-temperature argon (same as Fig. 3 (d)). The ultrabroadband CRS signal spans over 1600 cm^{-1}, and the band-pass filter is tuned to transmit the spectral region ~300-1500 cm^{-1}. The comparison between the fs laser excitation efficiency, as mapped by the NR signal generated *in-situ versus ex-situ*, illustrates the significant impact of the boundary conditions to the supercontinuum generation via *in-situ* filamentation in the flame. The instantaneous bandwidth of the compressed supercontinuum is here defined as half-width-at-half-maximum (HWHM) of the signal over the measured spectral range ~300-1500 cm^{-1}, and it is measured to be 394 cm^{-1} for the compressed supercontinuum generated *ex-situ* in argon. For comparison the excitation bandwidth provided by a 35 fs TL pump/Stokes pulse over the spectral range ~300-1500 cm^{-1} is 126 cm^{-1}. In the flame, the bandwidth of the supercontinuum varies from 206 cm^{-1} at y = 0 mm to 136 cm^{-1} at y = 8 mm, corresponding to a pulse duration of respectively 26 fs (GDD = 100 fs^2) and 30 fs (GDD = 100 fs^2). This reduction in the pulse compression is due to the lower effective refractive index of the optical medium along the filament propagation across the flame front. This has a comparable effect on the two non-linear optical effects underlying fs laser-induced filamentation, i.e. optical Kerr effect and multi-photon ionization. The lesser effective refractive index of the optical medium at higher temperatures determines a reduction of the self-phase modulation of the fs pulse and of the plasma density in the filament, resulting in a lesser pulse compression. This effect is of course highly dependent on the spatio-temporal boundary conditions to the filamentation process, requiring the *in-situ* referencing protocol to faithfully map the excitation efficiency of the different Raman transitions. The locality of the supercontinuum generation is moreover evident looking at the progressive reduction in the excitation bandwidth from the center of the burner to its rim, due to the three-dimensional curvature of the conical flame.

3.4. Pure-rotational H_2 CSR spectroscopy

Figure 4(b) presents the single-shot resonant H_2 CRS spectra acquired across the flame front. Six rotational lines of H_2 –from O(2) at 354 cm^{-1} to O(7) at 1447 cm^{-1}– were detected simultaneously, at high temperature, in the detection bandwidth of the spectrometer and within the dynamic range of the sCMOS detector. The rotational lines in the resonant spectra show the characteristic alternating intensity of even and odd lines, in accordance with the degeneracy of the single and triplet spin states [29]. The progression along the transverse axis clearly shows the shift in the rotational Boltzmann population of the H_2 molecules with the increasing temperature across the flame front. At y = 0 the relatively low temperature of the molecular ensemble results in the lower rotational states, in particular J = 1←3, being the most populated. Moving towards the rim of the burner, the increment in temperature results in the shift of the rotational population toward higher energy states: for y > 4.5 mm the transition J = 3←5 dominates the rotational spectrum.
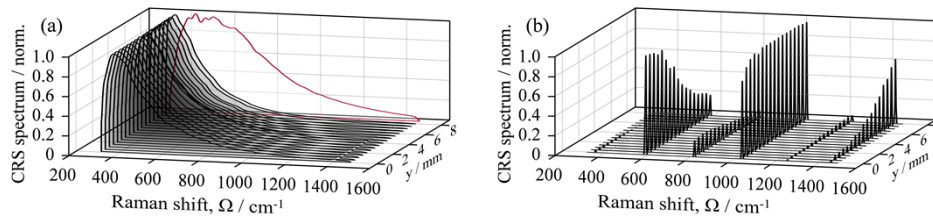
Fig. 4. (a) Ultrabroadband NR CRS spectra acquired *ex-situ* in room temperature argon (red curve) and *in-situ* at the different measurement locations across the flame front (black curves). Each curve represents the average of 1200 single-shot spectra. (b) Single-shot pure-rotational H_2 CRS spectra acquired across the flame front of a laminar H_2/air diffusion flame. Up to six rotational lines are detected simultaneously within the dynamic range of the sCMOS detector.

The single-shot H_2 spectra are fitted to a time-domain model similar to that presented in Ref. [29] (details in Supplement 1) to extract the local temperature across the flame front. An example of the spectral fit is shown in Fig. 5(a) and Fig. 5(b), where the comparison between the conventional *ex-situ* and the *in-situ* referencing protocol is presented. The larger bandwidth of the NR CRS signal generated *ex-situ* in room-temperature argon (Fig. 5(a)) overestimates the effective excitation efficiency of the higher Raman transitions, resulting in spectral cooling. This behavior severely skews the envelope of the Raman spectrum so that, even for the best-fitting temperature, the *ex-situ*-referenced spectrum does not follow Boltzmann distribution, as illustrated by the large misfit of most rotational lines. The use of the correct spectral reference, provided by the NR signal generated *in-situ* (Fig. 5(b)), is thus critical to perform quantitative spectroscopy on the pure-rotational H_2 spectrum. The temperature profile across the flame front, as measured by H_2 CRS thermometry, is shown in Fig. 5(c), along with the validation measurements performed by conventional N_2 CRS thermometry. As N_2-dilution of the H_2 flow is employed, conventional N_2 CRS measurements are possible on both sides of the flame front, allowing for a complete reconstruction of the temperature profile. H_2 on the other hand is rapidly consumed in the chemical reaction, so that the H_2 CRS signal rapidly decreases moving towards the burner rim, for the combined effect of the increasing temperature and the reduced H_2 concentration: ultrabroadband H_2 CRS measurements were performed up to y = 8 mm. The temperatures measured by N_2 CRS and H_2 CRS are well in agreement when the *in-situ* NR signal is employed for the spectral referencing of the ultrabroadband H_2 CRS spectra: the accuracy of the H_2 thermometry is below 1% for most measurement locations across the flame front. H_2 CRS thermometry employing *ex-situ* referencing, on the other hand, results in a significant bias (up to 80%) towards lower temperatures at all the measurement locations, as shown in Fig. 5(d).

The precision of ultrabroadband H_2 CRS thermometry was estimated as the standard deviation of the measured temperature over a sample of 1200 single-shot spectra. This is comparable to that of conventional N_2 CRS, varying in the range ∼1-3%, for y ≤ 6.5 mm, while it is negatively impacted by the H_2 consumption in the reaction zone of the flame, with a significant reduction of the signal intensity. At the last three measurement locations, this abatement of the signal impaired the detection of the O(2) line (see Fig. 4(b)), and the signal-to-background ratio (SBR) of the O(6) line was reduced to ∼2. At the last measurement point, the O(5) line was barely detectable (SBR∼1.3) and the spectral fit only relied on four lines, reducing the precision to ∼9%. These temperature measurements are in good agreement with the values reported by Toro *et al* for a similar laminar H_2/air diffusion flame [45].

Ultrabroadband CRS further provides new insights in the molecular transport processes taking place in the measurement environment presented here. Figure 6(a) shows the experimental temperature and relative H_2/N_2 concentration profiles, measured by ultrabroadband CRS across
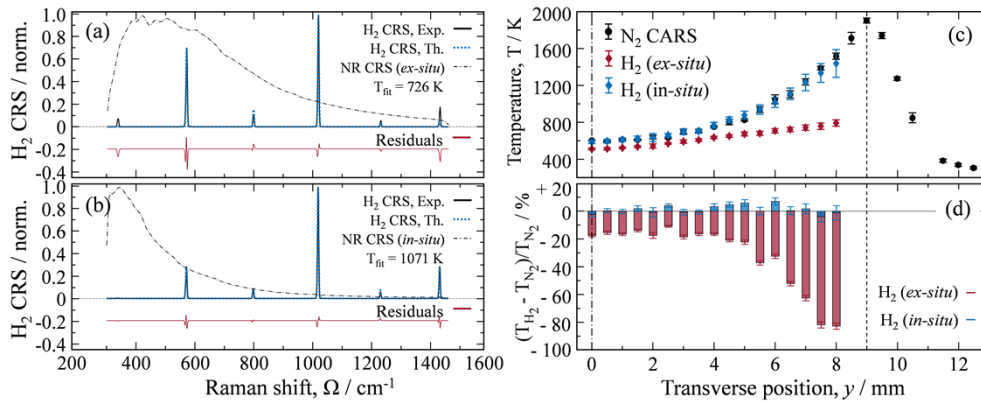
Fig. 5. (a) Single-shot experimental H_2 CRS spectrum (solid line) acquired in the flame at y = 6 mm, referenced by the NR CRS (dot-dashed line) spectrum acquired *ex-situ* in argon, and comparison to the time-domain H_2 CRS model (dotted line) to fit the Boltzmann distribution. (b) The same experimental spectrum is referenced by the NR CRS spectrum simultaneously acquired *in-situ*, and fitted to the time-domain H_2 CRS model. (c) Temperature profile measured by conventional pure-rotational N_2 CRS and ultrabroadband H_2 CRS spectroscopy. (d) Comparison of the measurement accuracy of H_2 CRS thermometry for the *ex-situ* and *in-situ* referencing protocols: the standard (*ex-situ*) protocol results in a consistent underestimation of the H_2 temperature.

the flame front: moving from the center of the burner to the chemical reaction zone, the H_2 concentration significantly reduces, from 50% to 40%, while the temperature presents only a minor increment up to y = 3.5 mm as shown in Fig. 6(b). This small change in temperature (~57 K) is attributed to heat transfer from the high-temperature reaction zone, rather than to the onset of the chemical reaction itself: H_2 is not consumed in this region, but it is rapidly transported towards the reaction zone, owing to its large mass diffusivity [31]. To the best of our knowledge, this represents the first direct observation of molecular preferential diffusion in a H_2/air flame.
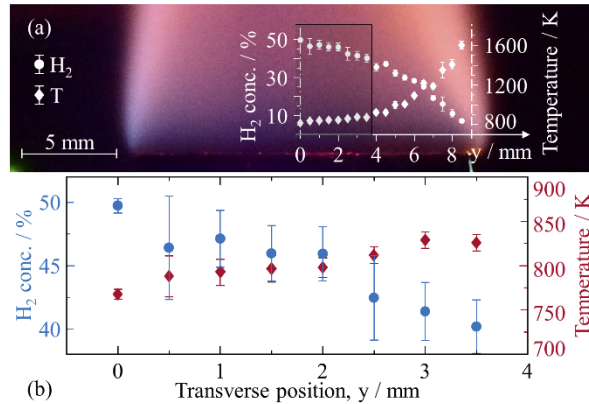

Fig. 6. (a) Simultaneous CRS measurement of the temperature and relative H_2/N_2 concentration across the flame front (1 mm above the nozzle). The black box represents the area of interest for H_2 preferential diffusion. (a) A significant reduction of the H_2 concentration, from 50% at y = 0 mm to 40% at y = 3.5 mm, is measured in the face of an almost constant temperature profile and is thus attributed to preferential diffusion.

4. Conclusions

A novel approach to ultrabroadband CRS is proposed as a straightforward pathway to rotational H_2 spectroscopy in closed environments, such as high-pressure combustors or chemical reactors. The investigation of H_2 chemistry by time-resolved coherent Raman techniques requires a compressed supercontinuum to generate coherence between the widely spaced states in the rotational energy manifold [29], but is hindered by the introduction of non-linear contributions to its spectral phase. To date ultrabroadband fs/ps H_2 CRS has not been applied in closed measurement scenarios.

The technique here proposed is based on the *in-situ* generation, use and referencing of the coherent excitation provided by supercontinuum compression in fs laser-induced filamentation. The 35 fs output of a regenerative fs laser amplifier was negatively chirped before its transmission through a 22 mm BK7 glass window, resulting in a residual negative chirp of ~490 fs^2: this value is experimentally demonstrated to optimize the multiphoton ionization and the optical Kerr effects that underpin the pulse compression in the filamentation process. We have shown that the NR CRS signal, which has often been considered detrimental to CRS, with much effort dedicated to its suppression [24,46], not only maps the efficiency of the coherent excitation delivered by the pump/Stokes pulse, but can be effectively used to perform spectral autocorrelation measurements of the pump/Stokes pulse and to characterize its transmission through optical media. This result is particularly powerful when combined to the last piece of the present diagnostic puzzle: the *in-situ* referencing protocol to monitor the ultrabroadband spectral excitation delivered by the compressed supercontinuum. This novel experimental protocol utilizes polarization control over the input laser fields to generate the resonant and NR signals with relative orthogonal polarization, and realizes their simultaneous separated detection in a polarization-sensitive coherent imaging spectrometer. Altogether *in-situ* generation, *in-situ* use, and *in-situ* referencing of the ultrabroadband coherent Raman excitation define a new diagnostics to investigate the rotational energy distribution in gaseous H_2.

Ultrabroadband H_2 CRS measurements were demonstrated over a wide range of temperature and H_2 concentration across a canonical H_2/air diffusion flame (Fig. 5), and validated against conventional N_2 CRS thermometry. The potential of our technique is further exemplified by what, to the best of our knowledge, is the first direct observation of H_2 preferential diffusion in H_2/air flames. The effect of the mass transport mechanism for the lightweight H_2 molecules is uncovered by the spatial mismatch of the temperature and relative H_2/N_2 concentration, as measured by pure-rotational CRS (Fig. 6). Although this configuration is designed for rather large-scale combustor test rigs (approximately 0.5 m in width), it can be extended to smaller-scale housings as in Ref. [26], provided that the numerical aperture and therefore the filament properties are maintained. For instance, the input beam diameter can be modified accordingly to reduce the field irradiance inside the window when short focal-length optics are required. We prospect the far ranging application of this diagnostics in all the research fields where H_2 chemistry plays a key role, from novel sustainable combustion technologies to methane reforming for H_2 production. To name one, liquid oxygen/gaseous H_2 rocket combustion is a thriving research field with application to low-Earth commercialization and sustainable space exploration [47]. Our technique has clear advantages in such high-pressure environments, where both the fs pulse compression and the coherent Raman excitations are enhanced, while time-resolved measurements can be realized probing the Raman coherences below the collisional time-scale.

Disclosures. The authors declare no conflicts of interest.

Data availability. Data underlying the results presented in this paper are not publicly available at this time, but may be obtained from the authors upon reasonable request.

Supplemental document. See Supplement 1 for supporting content.

References

1. "Hydrogen on the rise," Nat. Energy 1, 16127 (2016).
2. Y. Shagam, A. Klein, W. Skomorowski, R. Yun, V. Averbukh, C. P. Koch, and E. Narevicius, "Molecular hydrogen interacts more strongly when rotationally excited at low temperatures leading to faster reactions," Nat. Chem. **7**(11), 921–926 (2015).
3. S. A. Lahankar, J. Zhang, K. G. McKendrick, and T. K. Minton, "Product-state-resolved dynamics of the elementary reaction of atomic oxygen with molecular hydrogen, $O(^3P) + D2 \rightarrow OD(X\,^2\Pi) + D$," Nat. Chem. **5**(4), 315–319 (2013).
4. N. G. Kling, S. Díaz-Tendero, R. Obaid, M. R. Disla, H. Xiong, M. Sundberg, S. D. Khosravi, M. Davino, P. Drach, A. M. Carroll, T. Osipov, F. Martín, and N. Berrah, "Time-resolved molecular dynamics of single and double hydrogen migration in ethanol," Nat. Commun. **10**(1), 2813 (2019).
5. R. P. Lucht, "Femtosecond lasers for molecular measurements," Science **316**(5822), 207–208 (2007).
6. D. A. Greenhalgh, "Raman: An eye for combustion studies," Nature **291**(5816), 535–536 (1981).
7. S. Roy, J. R. Gord, and A. K. Patnaik, "Recent advances in coherent anti-Stokes Raman scattering spectroscopy: Fundamental developments and applications in reacting flows," Prog. Energy Combust. Sci. **36**(2), 280–306 (2010).
8. C. E. Dedic, T. R. Meyer, and J. B. Michael, "Single-shot ultrafast coherent anti-Stokes Raman scattering of vibrational/rotational nonequilibrium," Optica **4**(5), 563–570 (2017).
9. T. Chen, B. Goldberg, B. Patterson, E. Kolemen, C. Kliewer, K. Olemen, J. Yiguang, and C. H. J. K. Liewer, "1-D imaging of rotation-vibration non-equilibrium from pure rotational ultrafast coherent anti-Stokes Raman scattering," Opt. Lett. **45**(15), 4252–4255 (2020).
10. I. R. Beattie, T. R. Gilson, and D. A. Greenhalgh, "Low frequency coherent anti-Stokes Raman spectroscopy of air," Nature **276**(5686), 378–379 (1978).
11. R. L. Farrow and L. A. Rahn, "Optical Stark Splitting of Rotational Raman Transitions," Phys. Rev. Lett. **48**(6), 395–398 (1982).
12. F. Benabid, F. Couny, J. C. Knight, T. A. Birks, and P. S. J. Russell, "Compact, stable and efficient all-fibre gas cells using hollow-core photonic crystal fibres," Nature **434**(7032), 488–491 (2005).
13. R. L. Farrow and L. a Rahn, "Measurement of the self-broadening of the H_2 Q(0-5) Raman transitions from 295 to 1000 K," Phys. Rev. A **43**(11), 6075–6088 (1991).
14. V. Bergmann and W. Stricker, "H_2 CARS thermometry in a fuel-rich, premixed, laminar CH_4/air flame in the pressure range between 5 and 40 bar," Appl. Phys. B **61**(1), 49–57 (1995).
15. V. A. Shakhatov, O. De Pascale, M. Capitelli, K. Hassouni, G. Lombardi, and A. Gicquel, "Measurement of vibrational, gas, and rotational temperatures of H_2 $(X\,^1\Sigma_g{}^+)$ in radio frequency inductive discharge plasma by multiplex coherent anti-Stokes Raman scattering spectroscopy technique," Phys. Plasmas **12**(2), 023504 (2005).
16. A. H. Zewail, "Laser Femtochemistry," Science **242**(4886), 1645–1653 (1988).
17. T. Lang, K. Kompa, and M. Motzkus, "Femtosecond CARS on H_2," Chem. Phys. Lett. **310**(1-2), 65–72 (1999).
18. H. Tran, P. Joubert, L. Bonamy, B. Lavorel, V. Renard, F. Chaussard, O. Faucher, and B. Sinardet, "Femtosecond time resolved coherent anti-Stokes Raman spectroscopy: Experiment and modelization of speed memory effects on H_2-N_2 mixtures in the collision regime," J. Chem. Phys. **122**(19), 194317 (2005).
19. S. A. Magnitskiĭ and V. G. Tunkin, "Determination of the Dicke Narrowing in Gaseous Hydrogen By Direct Measurement of the Dephasing Time," Sov. J. quantum Electron. **11**(9), 1218–1220 (1981).
20. W. D. Kulatilaka, P. S. Hsu, H. U. Stauffer, J. R. Gord, and S. Roy, "Direct measurement of rotationally resolved H_2 Q-branch Raman coherence lifetimes using time-resolved picosecond coherent anti-Stokes Raman scattering," Appl. Phys. Lett. **97**(8), 081112 (2010).
21. M. O. Scully, G. W. Kattawar, R. P. Lucht, T. Opatrný, H. Pilloff, A. Rebane, A. V. Sokolov, and M. S. Zubairy, "FAST CARS: Engineering a laser spectroscopic technique for rapid identification of bacterial spores," Proc. Natl. Acad. Sci. U. S. A. **99**(17), 10994–11001 (2002).
22. D. Pestov, R. K. Murawski, G. O. Ariunbold, X. Wang, M. Zhi, A. V. Sokolov, V. A. Sautenkov, Y. V. Rostovtsev, A. Dogariu, Y. Huang, and M. O. Scully, "Optimizing the laser-pulse configuration for coherent Raman spectroscopy," Science **316**(5822), 265–268 (2007).
23. B. D. Prince, A. Chakraborty, B. M. Prince, and H. U. Stauffer, "Development of simultaneous frequency- and time-resolved coherent anti-Stokes Raman scattering for ultrafast detection of molecular Raman spectra," J. Chem. Phys. **125**(4), 044502 (2006).
24. N. Dudovich, D. Oron, and Y. Silberberg, "Single-pulse coherently controlled nonlinear Raman spectroscopy and microscopy," Nature **418**(6897), 512–514 (2002).
25. A. Bohlin and C. J. Kliewer, "Single-shot hyperspectral coherent Raman planar imaging in the range 0-4200 cm^{-1}," Appl. Phys. Lett. **105**(16), 161111 (2014).
26. D. R. Richardson, S. P. Kearney, and D. R. Guildenbecher, "Post-detonation fireball thermometry via femtosecond-picosecond coherent anti-Stokes Raman Scattering (CARS)," Proc. Combust. Inst. **38**(1), 1657–1664 (2021).

27. J. H. Odhner, D. A. Romanov, and R. J. Levis, "Rovibrational Wave-Packet Dispersion during Femtosecond Laser Filamentation in Air," Phys. Rev. Lett. **103**(7), 075005 (2009).

28. A. Bohlin, B. D. Patterson, and C. J. Kliewer, "Communication: Simplified two-beam rotational CARS signal generation demonstrated in 1D," J. Chem. Phys. **138**(8), 081102 (2013).

29. T. L. Courtney, A. Bohlin, B. D. Patterson, and C. J. Kliewer, "Pure-rotational H_2 thermometry by ultrabroadband coherent anti-stokes Raman spectroscopy," J. Chem. Phys. **146**(22), 224202 (2017).

30. F. Mazza, L. Castellanos, D. Kliukin, and A. Bohlin, "Coherent Raman imaging thermometry with in-situ referencing of the impulsive excitation efficiency," Proc. Combust. Inst. **38**(1), 1895–1904 (2021).

31. R. S. Barlow, M. J. Dunn, M. S. Sweeney, and S. Hochgreb, "Effects of preferential transport in turbulent bluff-body-stabilized lean premixed CH_4/air flames," Combust. Flame **159**(8), 2563–2575 (2012).

32. D. Meshulach and Y. Silberberg, "Coherent quantum control of two-photon transitions by a femtosecond laser pulse," Nature **396**(6708), 239–242 (1998).

33. A. A. Lanin, I. V. Fedotov, A. B. Fedotov, D. A. Sidorov-Biryukov, and A. M. Zheltikov, "The phase-controlled Raman effect," Sci. Rep. **3**(1), 1842 (2013).

34. U. Gaubatz, P. Rudecki, S. Schiemann, and K. Bergmann, "Population transfer between molecular vibrational levels by stimulated Raman scattering with partially overlapping laserfields. A new concept and experimental results," J. Chem. Phys. **92**(9), 5363–5376 (1990).

35. S. Zhdanovich, E. A. Shapiro, M. Shapiro, J. W. Hepburn, and V. Milner, "Population transfer between two quantum states by piecewise chirping of femtosecond pulses: Theory and experiment," Phys. Rev. Lett. **100**(10), 103004 (2008).

36. C. H. Camp, Y. J. Lee, J. M. Heddleston, C. M. Hartshorn, A. R. H. Walker, J. N. Rich, J. D. Lathia, and M. T. Cicerone, "High-speed coherent Raman fingerprint imaging of biological tissues," Nat. Photonics **8**(8), 627–634 (2014).

37. F. Mazza, N. Griffioen, L. Castellanos, D. Kliukin, and A. Bohlin, "High-temperature rotational-vibrational O_2-CO_2 coherent Raman spectroscopy with ultrabroadband femtosecond laser excitation generated in-situ," Combust. Flame **237**, 111738 (2022).

38. S. Rostami, J.-C. Diels, and L. Arissian, "Polarization evolution of ultrashort pulses in air," Opt. Express **23**(3), 3299–3307 (2015).

39. A. H. Sheinfux, E. Schleifer, J. Papeer, G. Fibich, B. Ilan, and A. Zigler, "Measuring the stability of polarization orientation in high intensity laser filaments in air," Appl. Phys. Lett. **101**(20), 201105 (2012).

40. E. T. J. Nibbering, D. A. Wiersma, and K. Duppen, "Ultrafast Nonlinear Spectroscopy with Chirped Optical Pulses," Phys. Rev. Lett. **68**(4), 514–517 (1992).

41. Y. J. Yan and S. Mukamel, "Pulse shaping and coherent Raman spectroscopy in condensed phases," J. Chem. Phys. **94**(2), 997–1005 (1991).

42. T. Hellerer, A. M. K. Enejder, and A. Zumbusch, "Spectral focusing: High spectral resolution spectroscopy with broad-bandwidth laser pulses," Appl. Phys. Lett. **85**(1), 25–27 (2004).

43. F. Théberge, N. Aközbek, W. Liu, A. Becker, and S. L. Chin, "Tunable ultrashort laser pulses generated through filamentation in gases," Phys. Rev. Lett. **97**(2), 023904 (2006).

44. A. Mysyrowicz, A. Couairon, and U. Keller, "Self-compression of optical laser pulses by filamentation," New J. Phys. **10**(2), 025023 (2008).

45. V. V Toro, A. V Mokhov, H. B. Levinsky, and M. D. Smooke, "Combined experimental and computational study of laminar, axisymmetric hydrogen–air diffusion flames," Proc. Combust. Inst. **30**(1), 485–492 (2005).

46. L. Gong, W. Zheng, Y. Ma, and Z. Huang, "Higher-order coherent anti-Stokes Raman scattering microscopy realizes label-free super-resolution vibrational imaging," Nat. Photonics **14**(2), 115–122 (2020).

47. F. Grisch, P. Bouchardy, and W. Clauss, "CARS thermometry in high pressure rocket combustors," Aerosp. Sci. Technol. **7**(4), 317–330 (2003).